Top_Fuel 2006

2006 INTERNATIONAL MEETING ON LWR FUEL PERFORMANCE

"NUCLEAR FUEL: ADDRESSING THE FUTURE"

22-26 October 2006
Salamanca, Spain

Transactions

Organised by
European Nuclear Society (ENS)

In cooperation with
American Nuclear (ANS)
Society and Atomic Energy Society of Japan (AESJ)
International Atomic Energy Agency
Spanish Nuclear Society
Nuclear Energy Agency (NEA)

TABLE OF CONTENTS

POSTER SESSION I

POST-IRRADIATION EXAMINATION OF HIGH BURNUP SBR MOX FUEL

M.A.BARKER
Nexia Solutions Ltd
Sellafield, Seascale, CA20 1PG – United Kingdom

E.C.MATTHEWS, K.STEPHENSON
British Nuclear Group Ltd
Sellafield, Seascale, CA20 1PF – United Kingdom

S.BRÉMIER, D.PAPAIOANNOU, C.T.WALKER
Institute for Transuranium Elements
Postfach 2340, D-76125, Karlsruhe – Germany

Y.PARMAR
NOK
Parkstrasse 23, 5401 Baden – Switzerland

ABSTRACT

Results are presented from the PIE of fuel which represents the highest burnup experienced by commercially irradiated BNFL Short Binderless Route (SBR) MOX. These results show the benign performance of SBR MOX up to 54MWd/kgHM. Favourable behaviour with respect to both PCI and fission gas release are demonstrated.

1 Introduction

In 1994 BNFL supplied four assemblies of Short Binderless Route (SBR) MOX to the Swiss utility, NOK. The fuel was in a Westinghouse 14×14 PWR design clad in low-tin Zr-4. These assemblies, denoted M501 to M504, were irradiated in Beznau-1 for three cycles to an average burnup of 34.5MWd/kgHM.

Seven rods were extracted from assembly M501 in 1998, and sent for a comprehensive post-irradiation examination (PIE) programme at the Institute for Transuranium Elements (ITU) of the European Commission, Germany. The results from this programme have been extensively reported in the open literature and previous TopFuel and ANS LWR conferences [1-5]. After PIE, segments of the M501 rods were ramp tested in the Petten High Flux Reactor. The rodlets retained their integrity during power ramps up to 50kW/m terminal rating and were subjected to further PIE [6,7].

The three remaining assemblies, M502 – M504, were irradiated for a further 16 months. In 2001, four rods, with burnups in the range 37 to 44MWd/kgHM, were removed from assembly M504 for PIE. Results from non-destructive examination and puncture of these rods were presented at TopFuel 2003 [8].

In July 2001, assembly M502 was re-loaded into the reactor in a central position and irradiated in cycle 30 for a further year to an average burnup of ~49MWd/kgHM. The lead rod, M502-F2, achieved a rod average burnup of ~54MWd/kgHM. This is the highest burnup reached by SBR MOX in commercial irradiation. From assembly M502, six rods were selected for PIE. The current paper presents results from the non destructive testing (NDT) and puncture of these rods.

2 Rod Selection

Data on the rods selected for PIE from assembly M502, including results from rod puncture, are shown in Table I. Each rod is referred to hereafter by the Rod ID. Rod C1 has medium enrichment (3.72%Pu/HM) while the remaining five rods are high enrichment (5.54%Pu/HM). The lead rod is F2 with a rod average burnup of 54MWd/kgHM. The power histories with respect to burnup for F2 and C1 are shown in Figure 1. The rod powers are greatest during the second cycle of irradiation when the assembly is brought nearer the core centre and the fuel still has a high reactivity. For the final cycle of irradiation the assembly was at the very centre of the core to ensure a significant increase in burnup. At no time during the assembly's life did the average power exceed 25kW/m in any rod.

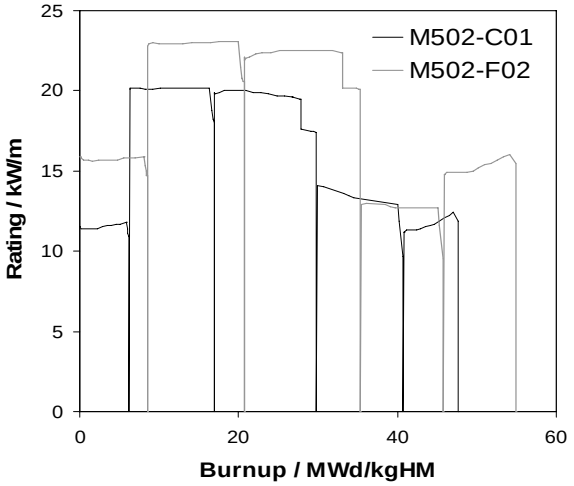

Figure 1: Typical power histories.

Rod ID	Burnup† in MWd	Enrich.*	FGR/%	He/cc
F2	54.0	5.54	2.5	-2.2
E4	53.7	5.54	1.3	12.0
I2	53.6	5.54	1.7	27.8
K3	52.8	5.54	1.1	5.1
C1	48.9	3.72	0.7	7.9
E8	48.3	5.54	0.8	-4.9

† Rod average burnup
*% Pu with respect to HM

Table I: Rods selected for PIE.

3 Results

Visual examination of the rods showed that the pellet-pellet interfaces are visible as circumferential lines on the outside of the cladding. Occasional marks due to the spacer grid and from handling are also visible. All rods exhibit an oxide layer, which in some cases shows local spalling close to the regions of maximum thickness. Numerous areas are seen with oxide patterns suggestive of galvanic corrosion of second phase particles, destructive testing will investigate these further.

Gamma scanning was performed on all six rods. In general, the gamma profiles were regular with no significant gaps in the fuel stack indicated. In all rods, pellet-pellet interfaces have reduced levels of gamma activity showing that no significant migration of volatile fission products, such as Cs, had occurred.

Profilometry and eddy-current oxide thickness (ECT) measurements were made on rods F2, E4 and C1. The results for oxide thickness are shown in Figure 2(a) for rods F2 and C1 along with measurements from three and four cycle SBR MOX. The ECT measurements on F2 show that the peak oxide thickness is ~80μm. This contrasts with ~45μm from the four cycle measurements (rod average burnup 44.1MWd/kgHM) which were made on a high-enrichment rod that had a similar location within its parent assembly to that of F2. The plot demonstrates the significant growth in oxide that has occurred in M502 compared with earlier fuel. It is also apparent that as the burnup of the fuel is increased, the peak in the oxide thickness becomes more distinct relative to the thickness at the lower portions of the rod. This is due to a feedback mechanism whereby as oxide thickness increases, the thermal conductance of the oxide layer is reduced. An increased metal-oxide interface temperature results and leads to increased corrosion rates which produces both a sharply peaked oxide profile and an increase in oxide growth rate with burnup.

Profilometry measurements found that rods E4 and F2 have the largest diameters, and this is expected from the fact that these two high enrichment rods have higher burnup and power ratings than the low enrichment rod C1. Figure 2(b) shows oxide-corrected profiles from commercial irradiations of BNFL SBR MOX. Each plotted point is an average of several measurements along the respective rod's length in order to remove fluctuations. The effect of oxide growth on the clad surface has been removed using the Pilling-Bedworth ratio to account for the oxide/clad density difference. The plot demonstrates the gross evolution of clad profile with irradiation. All three rods had an as-fabricated outside diameter of 10.72mm. The three-cycle results (M501) show how, after the fuel has densified and the clad has crept down in early irradiation, solid-fission product swelling has now begun to increase the fuel-stack diameter, and expand the cladding. Swelling continues to increase in the four cycle (M504) measurements. M502 represents the highest burnup fuel and shows that in F2, the lead rod, swelling has yet to raise the clad diameter to the as-fabricated diameter. It should be noted that in the irradiated condition the fuel-clad gap is expected to be closed, so although the clad-diameter is less than in the as-fabricated state, the actual fuel stack diameter is greater, as would be expected from fuel swelling.

Figure 3 shows details of the diameter profile from four regions of rod F2. Note that the diameter profiles shown here have not had the oxide thickness removed. Figures 3(a) to 3(c), are taken from grid spans 2 to 4 and are typical of most of the rod length. The outlines of pellets are clearly visible in these profiles, each pellet being ~10mm in length, with local-minima of up to ~20μm depth separating pellets. In Figure 3(d), taken from grid span 5, the local minima in the diameter profile have become indistinct: it is no longer possible to identify individual pellets in the profile.

Oxide measurements have shown that a small part (typically about 10%) of the depth of each local minimum in Figures 3(a) to 3(c) is due to thinning of the oxide: a result of temperature reduction at pellet-pellet interfaces. However, the dominating mechanism for formation of the minima is clad creep onto the fuel stack, revealing the pellet shapes in the clad profile. Therefore, the profiles suggest that along the majority of the fuel stack the pellets remain largely as either right-circular or oblate cylinders, rather than adopting the prolate-cylindrical (*wheatsheaf* shape*)* more usually seen in fuel of moderate or high burnup. The apparent change in profile behaviour in Figure 3(d) compared with 3(a) to 3(c) may be due to oxide growth filling the clad profile minima or changes to pellet swelling; these possibilities are to be investigated in destructive testing. The general lack of primary ridging in SBR MOX implies a resistance to PCI failure modes which are associated with the pellet wheatsheafing seen frequently in UO_2. The different behaviour is possibly due to a combination of higher creep rate and higher fission gas swelling in SBR MOX. Measurements by Caillot [10] showed that AUC and ADU MIMAS had higher creep rates than UO_2. Additionally, ADU derived MOX showed less primary ridging than AUC, suggesting higher creep in ADU compared to AUC. That SBR MOX shows no primary ridging implies a further increase in creep rate above that of ADU, which may be linked to the fractional volume of fuel occupied by a $(U,Pu)O_2$ solid solution phase.

Puncture results from the six M502 rods are shown in Figure 4, measurements of fission gas release and helium release are shown in Figure 4(a) and 4(b), respectively. In each plot, results from two, three and four cycle MOX have been added along with, in Figure 4(a), comparative measurements for MIMAS AUC and UO_2. Fission gas release in SBR MOX is found to be generally favourable when compared with other fuels although differences in power histories make direct comparisons difficult. Results from ramp testing of three cycle SBR MOX have previously demonstrated its propensity for retaining gas on grain boundaries, evident from fuel swelling and ceramography [6,7]. Fission gas swelling may actually be beneficial in promoting oblate rather than cylindrical pellet shapes and therefore reducing PCI at pellet edges.

Negative values for helium release indicate that absorption of the as-fabricated helium fill gas has occurred. Helium release is seen to increase with burnup. Measurements prior to M502, which were all at burnups below 45MWd/kgHM mainly showed net helium absorption. Some of the M502 results continue to show net absorption; however, a net helium release up to a volume of almost $30cm^3$ STP is also seen. This volume of helium is a significant fraction of the total gas (fission and helium) released

from the fuel. In the most extreme case, M502-I2, the volume of helium released is equivalent to 54% of the volume of released fission gas.

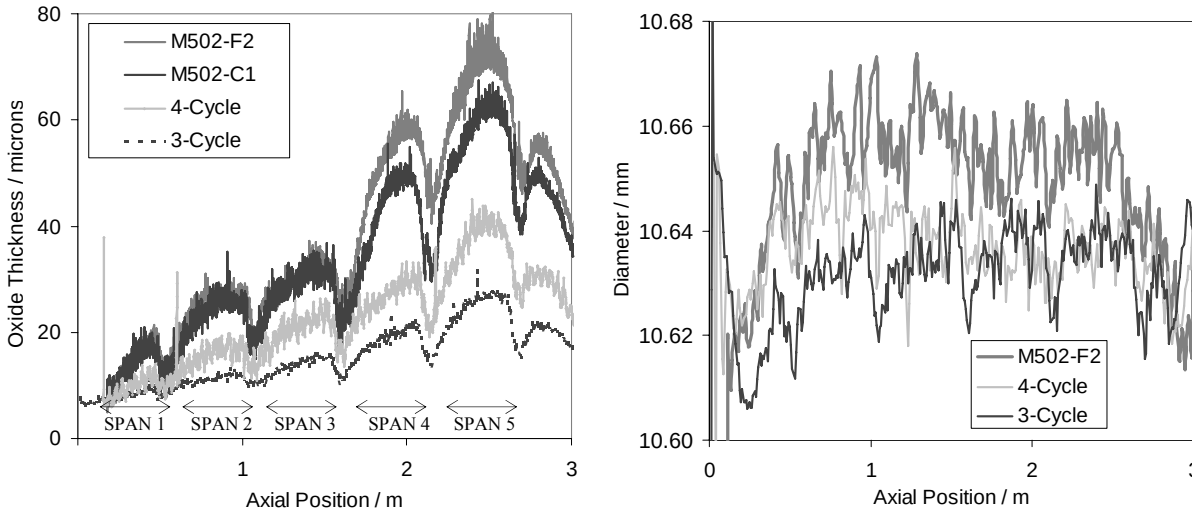

(a) **(b)**

Figure 2: Oxide thickness and corrected clad diameter for BNFL SBR MOX rods.**(a)** Growth in oxide thickness from 3-cycles to 5-cycles; **(b)** Clad diameter corrected for oxide thickness, results for 3- to 5- cycles.

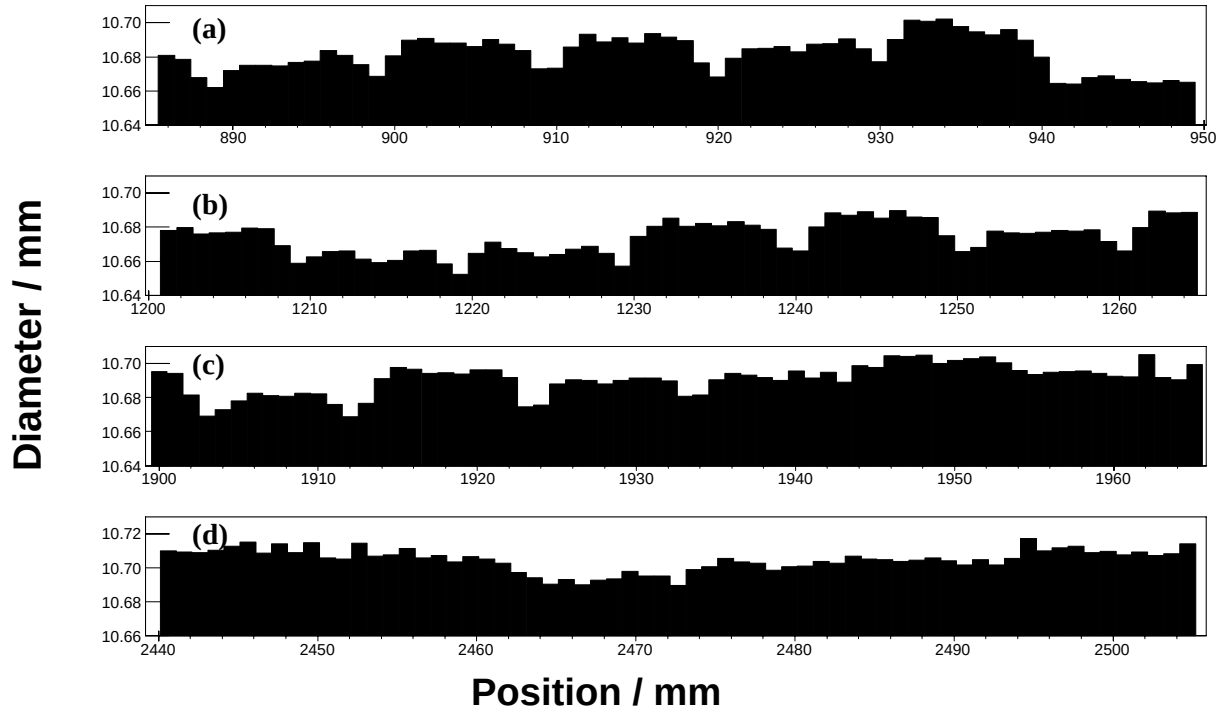

Figure 3: Expanded segments of M502-F2 profile along 0-degree axis. Data are shown without any oxide correction; **(a)** to **(c)** taken from grid spans 2 to 4 respectively; **(d)** taken from grid span 5.

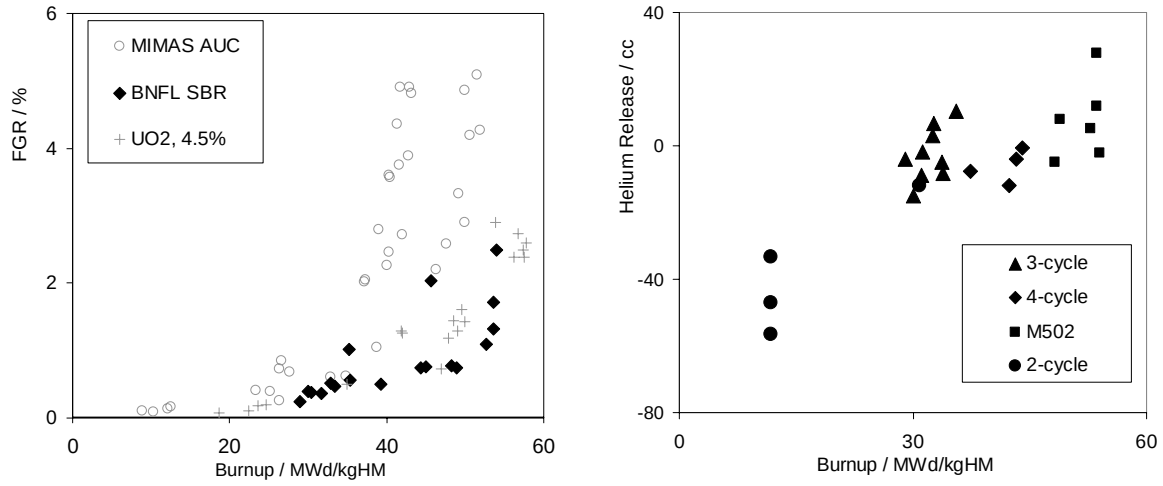

(a) **(b)**

Figure 4: (a) Fission gas release from BNFL SBR MOX, MIMAS MOX [9] and UO_2; **(b)** Helium release from SBR MOX.

4 Conclusions

NDT and Puncture results from five cycle SBR MOX have demonstrated its benign performance up to rod average burnups of 54MWd/kgHM. A thick oxide growth was observed on the Zr-4 cladding, reaching 80μm in the lead rod.

Profilometry measurements have shown that SBR MOX is expected to have greater resistance to PCI failure modes than UO_2 and other fuels. This is likely to be due to enhanced creep rates of the relatively homogeneous solid solution of $(U,Pu)O_2$ achieved by SBR along with the generally oblate shape of pellets caused by retention of fission gas and the associated swelling.

The quantity of helium released to the free volume is seen to steadily increase over the range of burnups examined although even at five cycles the rod internal pressure remains well within acceptable limits. Puncture measurements show that fission gas release compares favourably with other fuel types, the retention of fission gas on grain boundaries may also be a contributory factor in the lack of primary ridging.

References

[1] Cook P., et al., 'PIE of BNFL's First Commercially Irradiated SBR MOX Fuel,' in IAEA Symposium, Vienna, Austria, 1999, Paper No. IAEA-SM-358-16, p.42
[3] Cook P., Stratton R & Walker CT, 'Post Irradiation Examination of BNFL MOX Fuel,' in ANS LWR Topical Meeting 2000, 10-13 April 2000, Park City, Utah, USA, p.653
[4] White R., et al., J.Nucl.Mater. **288** (2001) 43
[5] Fisher S., et al., J.Nucl.Mater. **306** (2002) 153
[6] Barker M.A., et al., 'Ramp testing of SBR MOX fuel' in International seminar on PCI in LWR Fuels, Cadarache, March 2004
[7] Cook P., et al., 'Post-irradiation examination and testing of BNFL SBR MOX fuel' in ANS international topical meeting on LWR fuel performance, Orlando, Florida, September 2004
[8] Cook P., et al., 'Performance of BNFL MOX Fuel', in TopFuel 2003, Germany, March 2003
[9] Guerin Y., et al., 'Microstructure evolution and in-reactor behaviour of MOX Fuel', in ANS 2000, Park City, USA
[10] Caillot, L., et al., 'Out-of-pile and in-pile viscoplastic behaviour of mixed-oxide fuels', in International seminar on PCI in LWR Fuels, Cadarache, March 2004

DEVELOPMENT OF EXPERIMENTAL TECHNIQUE FOR SIMULATION OF RADIAL CRACKING OF HIGH BURNUP FUEL CLADDING TUBES

K. SAKAMOTO, M. NAKATSUKA
Global Nuclear Fuel - Japan Co., Ltd., Fuel Technology Group
2163, Narita-Cho, Oarai-Machi, Higashi Ibaraki-Gun, Ibaraki-Ken, 311-1313– Japan

ABSTRACT

An experimental technique has been developed to obtain the simulated radial incipient crack at the outer surface of the fuel cladding tubes by using the unirradiated fuel cladding tubes. It has been confirmed that the radial incipient crack is successfully formed at the outer surface of the fuel cladding tube. The specimens having the incipient outer crack have been applied to the burst test and the DHC test. The results have demonstrated that the technique developed in the present study is applicable to the measurements focusing on the radial fracture from the outer surface, such as a mechanical test and a DHC test of high burnup fuel cladding tubes.

1. Introduction

An understanding of fracture mechanism for the fuel cladding tubes having a radial crack at the outer surface is essential to assess the outside-in type failure in the high burnup fuel cladding tubes.[1] However, in most experimental studies, the mechanism was examined by the cracking in the axial direction or in the radial direction from the inner surface of the fuel cladding tubes.[2]-[11] The main reason for the lack of the experimental data on the fracture in the radial direction from the outer surface of the cladding tubes seems to be the difficulty to get the sharp radial incipient crack at the outer surface of the tube specimens.

In the present study, a development of an experimental technique was made to obtain the simulated radial incipient cracks at the outer surface of the fuel cladding tubes by using unirradiated fuel cladding tubes. In order to demonstrate the applicability of the proposed method, the specimens with the incipient outer crack were applied to the burst test and the delayed hydride cracking (DHC) test.

2. Experimental

2.1. Materials

Unirradiated cold-worked Zry-2 fuel cladding tubes were used. The chemical composition of the tubes is shown in Table 1. In both the burst test and the DHC test, tubes of 11.2 mm diameter, 0.71 mm thickness and 60 mm long were used. Some of the tubes were charged with hydrogen (CH-type specimen), and followed by the hydride reorientation treatment to the tube radial direction (RH-type specimen). The circumferential hydrides reoriented by five thermal cycles between 663 K and 423 K at the hoop stress of 160 MPa. The hydrogen concentration of specimen was approximately 200 ppm.

Table 1 Chemical composition of Zircaloy-2 cladding used (mass%)

Sn	Fe	Cr	Ni	Fe+Cr+Ni	O	Zr
1.36	0.18	0.11	0.07	0.36	0.122	bal.

2.2. Making of Incipient Cracks at Outer Surface of Fuel Claddings

The line of 10 mm long in the axial direction was scratched on the outer surface of specimen. At which, the periodic compressive load was applied together with the iodine methanol solution (I_2/CH_3OH).[12] This treatment resulted in the initiation and the propagation of the incipient crack at the outer surface of the specimens in the tube radial direction.

2.3. Non-destructive Measurement of Crack Depth

The non-destructive measurement of the crack depth is essential to use the specimen having the radial incipient crack because the depth of the incipient crack is a key parameter to determine the experimental condition. For instance, in the DHC test, the stress intensity factor *K* to be applied during crack propagation is a function of the crack depth. The applicability of eddy current test (ECT) was examined by measuring the incipient crack at the outer surface of the specimens for the burst test. The gap of 0.2 mm was kept between the detector of ECT and the surface of the specimen, and the DC output signal was recorded successively along the length of the specimen.

2.4. Rapid Burst Test

The rapid burst test was performed by applying an internal pressure at the room temperature to examine the effect of the incipient crack on the circumferential mechanical property of the fuel cladding tubes. The effects of the hydride and its orientation were also examined with NH- (as-received), CH- and RH-type specimens. The specimen was set as illustrated in Fig. 1. The high-pressurized water is sealed into the specimen with O-rings until the specimen fractures. The diameter and the internal pressure of the specimen were recorded at a frequency of 10 kHz to obtain the circumferential deformation and the hoop stress of the specimen.

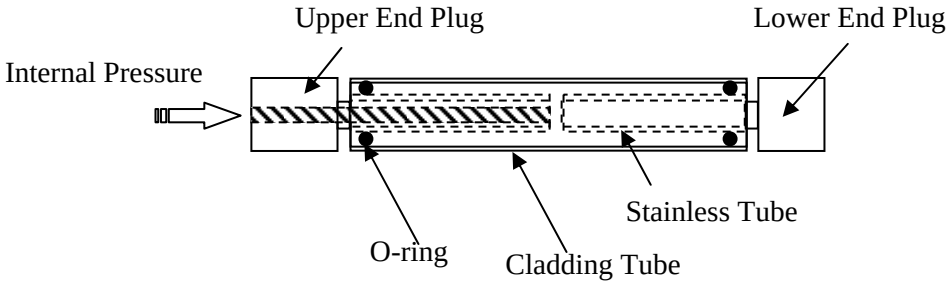

Figure 1 Schematic drawing of burst test specimen

2.5. DHC test

RH-type specimen was welded with plugs as illustrated in Fig. 2. The internal pressure and the thermal cycle applied in the DHC test are shown in Fig. 3. The bulk of hydrides should dissolve in heating up to 613 K and re-precipitate in the cooling to 573 K. After reaching 573 K, the temperature was kept for 5.5 h and cooled down to the room temperature. The internal pressure increased form 10.5 MPa to 24.7 MPa after the holding of 30 min at 573 K. The DHC test was performed in the air.

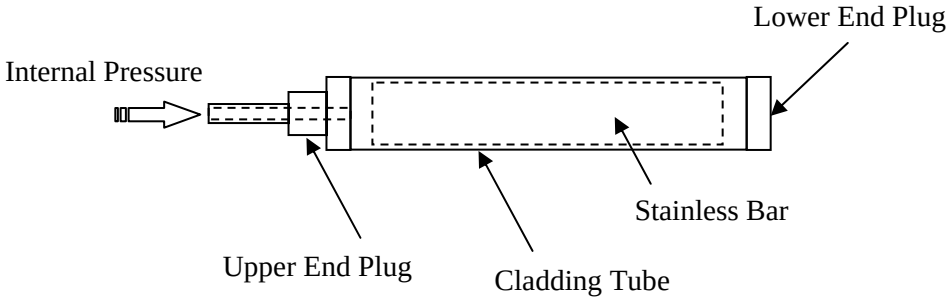

Figure 2 Schematic drawing of DHC test specimen

2.6. Observation of Fracture Surface

The fracture surface of specimen was observed with an optical microscope (OM) and a scanning electron microscope (SEM). The depth of the incipient and the DHC crack were evaluated by the SEM fractographs.

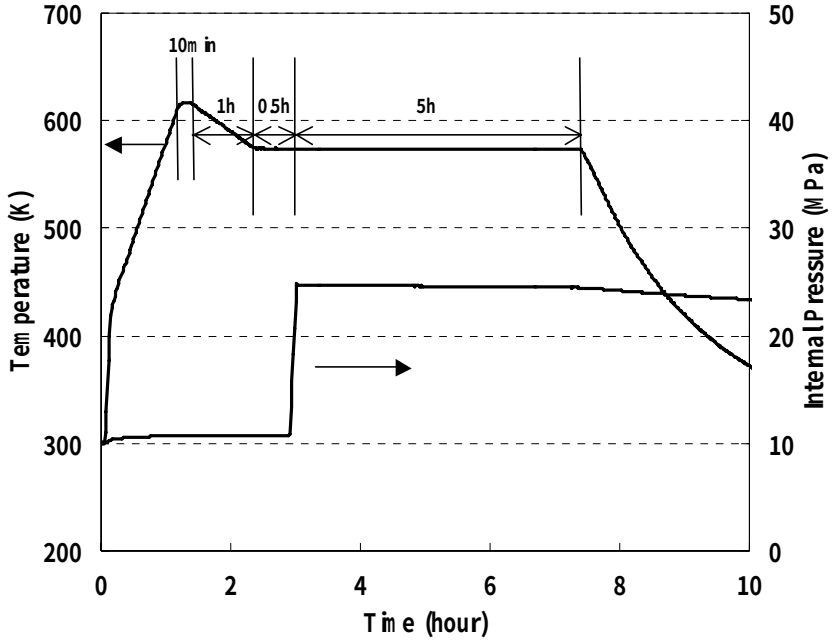

Figure 3 Internal pressure and thermal cycle applied in DHC test

3. Results and Discussion

3.1. Fractographs of Incipient and DHC Cracks

The fracture surface was observed with OM and SEM. As an example, the fracture surface of the DHC test specimen is shown in Fig. 4. In the OM fractograph, the incipient crack is surrounded by a blue band and the DHC crack is brown because of the oxidation during the DHC test in the air. The brittle surfaces are observed on the SEM fractographs of the incipient and the DHC cracks but the surface of the DHC crack is rougher than that of the incipient crack. According to the fractographs of the burst test specimens, it was confirmed that NH- and CH-type burst test specimens fractured in a ductile manner during the burst test. In the case of RH-type burst test specimen, the specimen fractured in a brittle manner.

The radial-circumferential plane was also observed by cutting at the middle of the crack or at the point of the maximum depth of the crack in the axial direction. Figure 5 is the OM micrographs of the DHC test specimen. The hydrides orient mainly in the circumferential direction, whereas before the DHC test the radial hydrides precipitated as RH-type burst test specimen. This is because that the thermal treatment of heating up to 613 K and cooling down to 573 K under the low hoop stress resulted in the hydrogen reorientation from the radial direction to the circumferential direction. By comparing with the fractographs in the radial-axial plane, it is confirmed that the radial incipient crack is successfully formed at the outer surface of the fuel cladding tube. The DHC crack propagates in the radial direction to the depth of approximately 0.5 mm. In the case of the burst specimen, the radial incipient crack propagated in the radial direction during the burst test to the depth of approximately 0.5 mm in RH-type specimen and 0.3 mm in NH- and CH-type specimens.

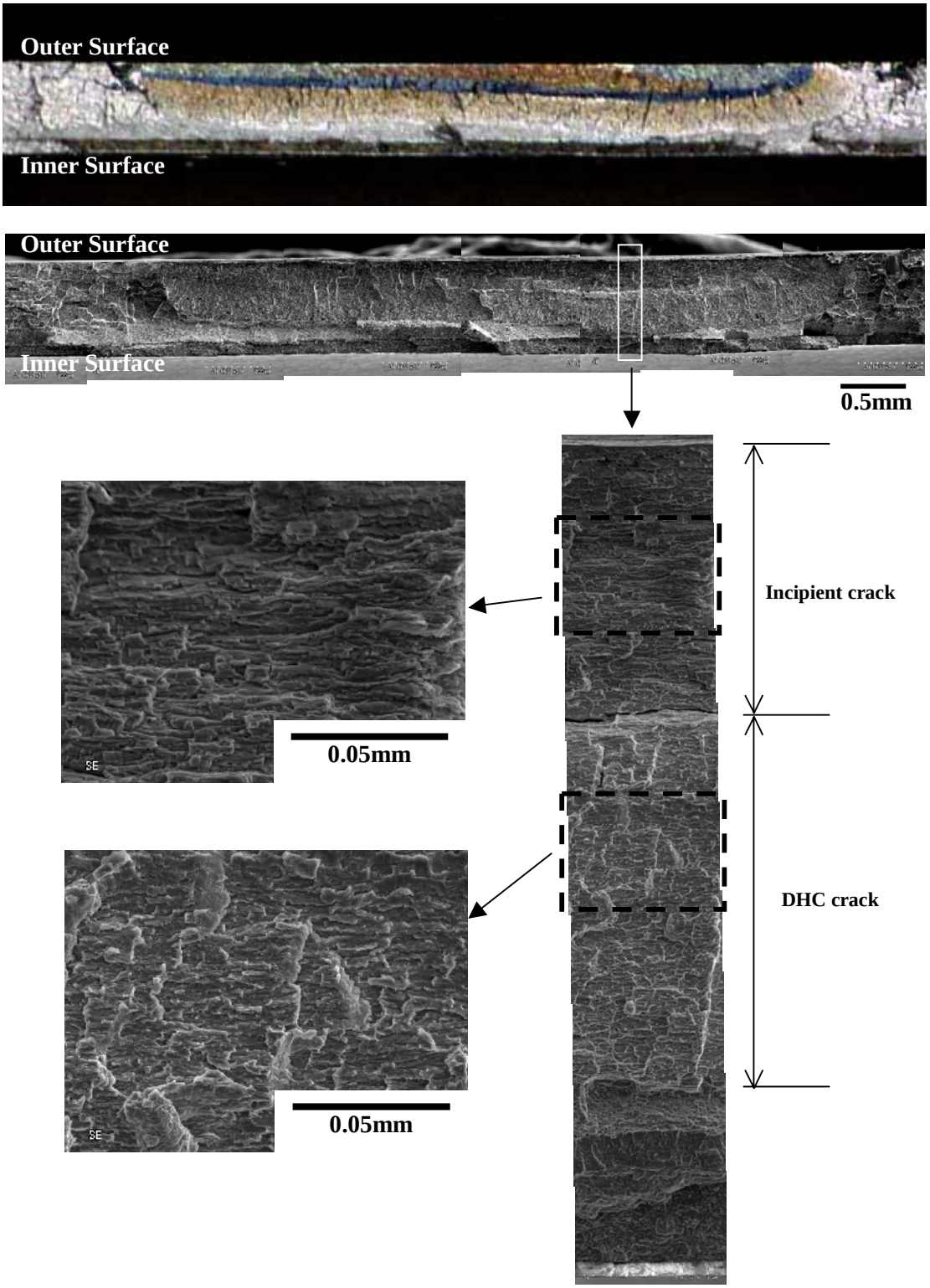

Figure 4 OM and SEM fractographs of DHC test specimen

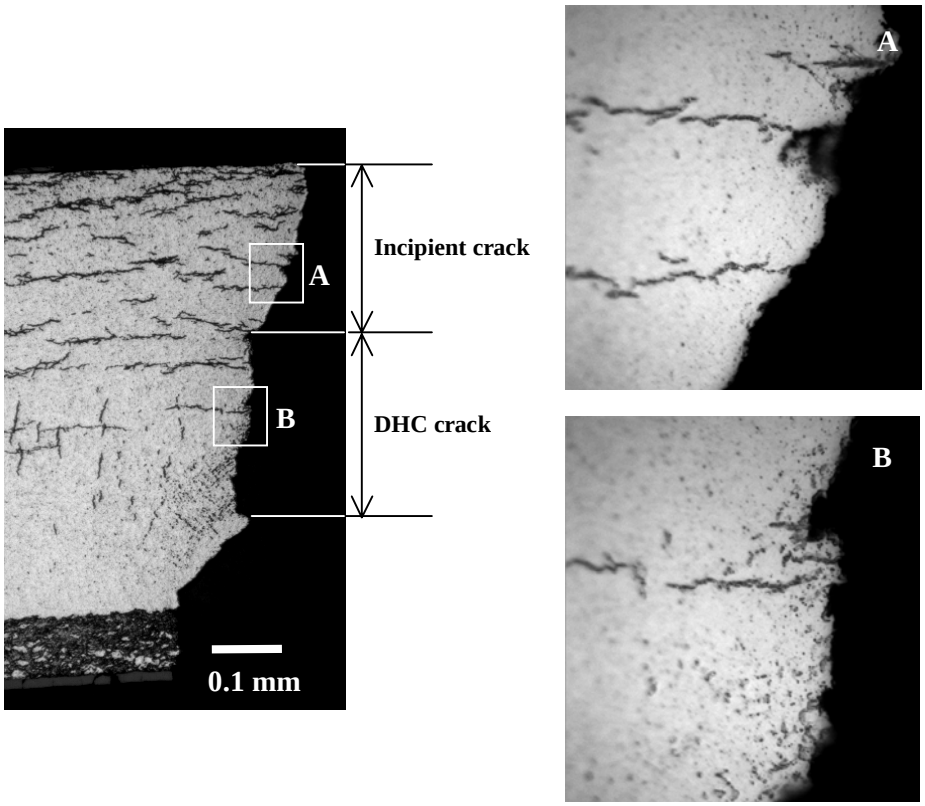

Figure 5 OM fractographs of DHC test specimen

3.2. Crack Depth Measurement by ECT

The result of the ECT is summarized in Fig. 6, in which the strength of ECT signal is compared with the depth of the incipient crack evaluated from the SEM fractographs. A good correlation between ECT and SEM observation implies the validity of the adoption of ECT to the non-destructive measurement of the depth of incipient crack formed by the proposed technique.

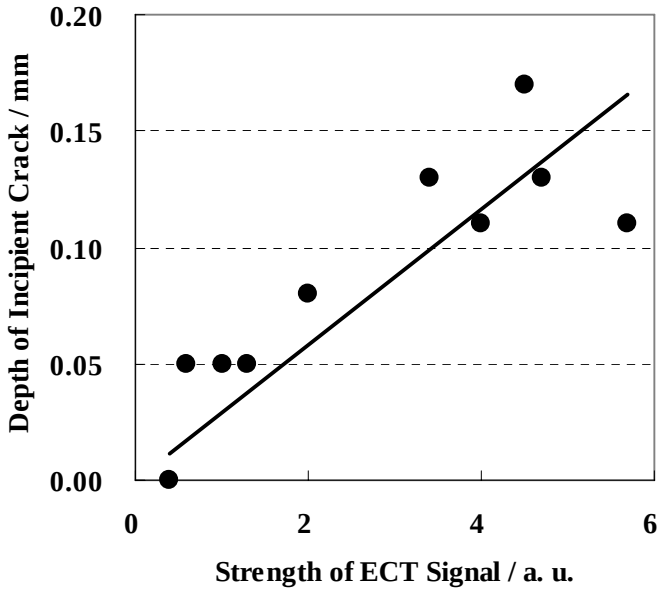

Figure 6 Comparison of ECT and fractography

3.3. Circumferential Mechanical Property at Room Temperature

The relationship between the hoop stress and the hoop strain was obtained from the changes of the diameter and the internal pressure of tubes recorded in the burst test. Figure 7 shows the effect of the incipient outer crack on the strain energy density (SED) of the fuel cladding tubes. The incipient crack degrades SED of all types of specimen: SED decreases with the depth of incipient crack up to $b/t \sim 0.15$. Here, b is the depth of the incipient crack and t the wall thickness of the fuel cladding tube (0.71 mm). It can be also seen in Fig. 7 that the direction of hydrides strongly affects the circumferential mechanical property.

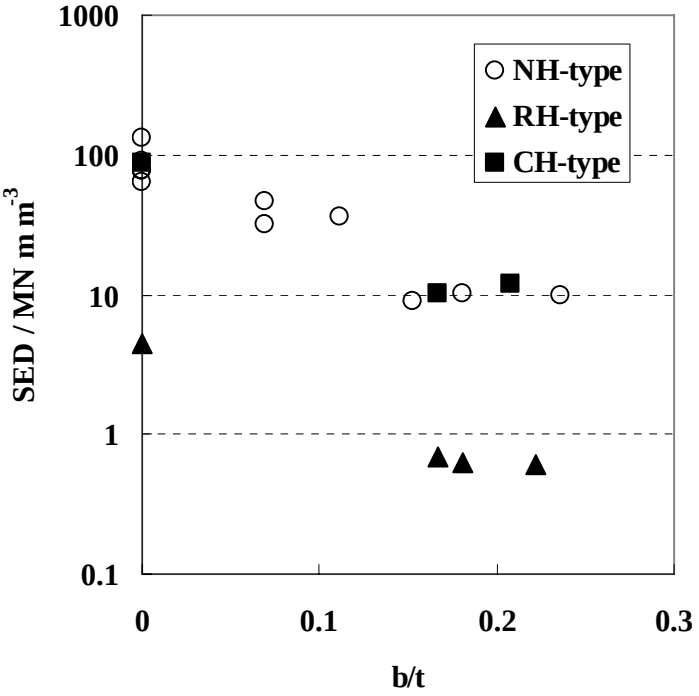

Figure 7 Effect of outer incipient crack on SED

3.4. Velocity of DHC (V_{DHC})

In the present study, because the crack propagation of the DHC test specimen was not measured continuously, V_{DHC} at each time could not be obtained. Hence, the mean value of V_{DHC} was evaluated from the SEM fractographs in Fig. 4. It is known that there is the incubation time of DHC in zirconium alloys,[4][6][10][11] so the mean value of V_{DHC} is lower than V_{DHC} obtained by an in-situ measurement. Assuming that the DHC occurred at the internal pressure of 24.7 MPa and 573 K, the crack propagated 0.31 mm for 5.0 h; the mean value of V_{DHC} was 1.7×10^{-8} m/s. This value is in the range of V_{DHC} in zirconium alloys (1×10^{-8} m/s -5×10^{-7} m/s),[2]-[11] but the direct comparison requires the further experimental data concerning the incubation time of DHC.

4. Conclusions

An experimental technique has been developed to obtain the simulated radial incipient crack at the outer surface of the fuel cladding tubes by using the unirradiated fuel cladding tubes. It has been confirmed that the radial incipient crack is successfully formed at the outer surface of the fuel cladding tube. The specimens having the incipient outer crack have been applied to the burst test and the DHC test. The mean value of V_{DHC} at 573 K has been evaluated as 1.7×10^{-8} m/s. And the radial incipient crack at the outer surface has degraded the circumferential mechanical property at the room temperature. These results have demonstrated that the technique developed in the present study is applicable to the measurements focusing on the radial fracture from the outer surface, such as a mechanical test and a DHC test.

5. References

(1) S. Shimada, E. Etoh, H. Hayashi, Y. Tukuta, A metallographic and fractographic study of outside-in cracking caused by power ramp tests, J. Nucl. Mater., 327 (2004) 97-113.
(2) S. Sagat, C. E. Coleman, M. Griffiths, B. J. S. Wilkins, The effect of fluence and irradiation temperature on delayed hydride cracking in Zr-2.5Nb, ASTM STP 1245 (1994) 35-61.
(3) Z. L. Pan, S. S. Lawrence, P. H. Davies, M. Griffiths, S. Sagat, Effect of irradiation on the fracture properties of Zr-2.5Nb pressure tubes at the end of design life, J. ASTM inter., 2, 9 (2005) 759.
(4) P. Efsing, K. Petterson, Delayed hydride cracking in irradiated Zircaloy cladding, ASTM STP 1354 (2000) 340-355.
(5) V. Grigoriev, R. Jakaobsson, Delayed hydrogen cracking velocity and J-integral measurements on irradiated BWR cladding, J. ASTM Inter., 2, 8 (2005) 711.
(6) G. K. Shek, D. B. Graham, Effects of loading and thermal maneuvers on delayed hydride cracking in Zr-2.5Nb alloys, ASTM STP 1023 (1989) 89-110.
(7) Y. S. Kim, S. C. Kwon, S. S. Kim, Crack growth pattern and threshold stress intensity factor, KIH, of Zr-2.5Nb alloy with the notch direction, J. Nucl. Mater., 280 (2000) 304-311.
(8) L. A. Simpson, C. F. Clarke, Application of the potential-drop method to measurement of hydrogen-induced sub-critical crack growth in zirconium-2.5 wt% niobium, AECL-5815 (1977).
(9) J. H. Huang, C. S. Ho, Subcritical crack growth behaviour for hydrided Zircaloy-4 plate, Mater. Chem. Phys., 47 (1997) 184-192.
(10) P. Efsing, K. Petterson, The influence of temperature and yield strength on delayed hydride cracking in hydrided Zircaloy-2, ASTM STP 1295 (1996) 394-404.
(11) IAEA, Delayed hydride cracking in zirconium alloys in pressure tube nuclear reactors, IAEA-TECDOC-1410 (2004).
(12) M. Nakatsuka, K. Sakamoto, Patent Pending JP2005-106531A.

FUMEX-II RESULTS OF HIGH BURNUP PERFORMANCE CODE INFRA

YONG SIK YANG, CHAN BOCK LEE, DAE HO KIM, SUN KI KIM, JE GEON BANG

P.O. Box 150, Yuseong, Daejeon, Korea, 305-600
Korea Atomic Energy Research Institute
Tel: 82-42-868-8689, E-mail: yys@kaeri.re.kr

ABSTRACT

The major objective of the IAEA CRP FUMEX-II program is to improve the high burnup fuel performance code prediction capabilities. In Korea, the INFRA(INtegrated Fuel Rod Analysis) code, which was developed by KAERI, has participated in the FUMEX-II verification programme. Among the FUMEX-II selected cases, except CANDU and other inadequate cases, a total of 22 database cases were used for the verification of the INFRA code. These 22 database cases contain important fuel performance information such as fission gas release, fuel centerline temperature, rod internal pressure, clad creep and radial FP distribution measurement data. In this paper, especially, the fission gas release verification results are summarized and, if possible, the fuel centerline temperature and radial FP distribution data is shown at the same time.

1. FUMEX-II program

A LWR fuel burnup extension requires a suitable fuel analysis model and code system which can predict a high burnup fuel in-reactor performance. A proper performance database is essential for the development of a high burnup fuel model and code system. The major objective of the IAEA Coordinated Research Programme FUMEX-II is to improve the predictive capabilities of fuel performance codes for a extended burnup above 50MWd/kgU. As we know, a extended burnup fuel behaviour modelling requires a number of key models which could predict the fuel and cladding in-reactor behaviour during a irradiation up to a high burnup. For the high burnup cladding behaviour, the important issue is a cladding corrosion and creep. But a cladding corrosion and creep model verification is a very difficult matter because the cladding corrosion and creep phenomena are strongly dependent on their characteristics such as material composition, heat treatment and operating condition. So, the FUMEX-II program is concerned with a high burnup pellet and a integrated fuel behaviour such as a fission gas release and a fission product radial distribution including rim microstructure behaviour. This work summarizes the fission gas release prediction results of the INFRA code which were performed by using the FUMEX-II steady-state and power ramp fission gas release test database. In most cases, if the data exists, fuel centreline temperature and radial fission gas distribution results have been compared at the same time due to the close relationship with a fission gas release prediction.

2. Fission gas release and rim microstructure formation model of INFRA

In the INFRA fission gas release model(MEGA model), a grain is assumed as a sphere and the fission gas atom diffusion to the grain boundary is calculated by using the suggested diffusion coefficient by Turnbull[1]. When the grain boundary bubble fission gas density exceeds the saturation density, the grain face becomes open to external surface and forms a open channel. This opened bubble(surface) may remain open during a irradiation and therefore, the fission gas atoms which diffuse to this opened surface later are instantaneously released to fuel rod. The open bubble or surface fraction may increase with a burnup and enhanced fission gas release can occur at a high burnup. Several important model coefficients were determined from the high burnup fuel fission gas release test results. In addition to the steady-state diffusional fission gas release model, a transient(or ramp) FGR model was inserted to calculate a burst fission gas release[2]. The transient FGR model can calculate a burst release as a function of the grain boundary fission gas concentration, increased power rate and terminal power level.

A rim microstructure formation is the most unique feature of a high burnup fuel performance. In the INFRA code, if the local region burnup exceeds a certain threshold burnup, that region is determined as a rim region and all the remaining fission gases in grain matrix are added to the intra-granular bubbles. C.B. Lee et al.[3] suggested a threshold burnp model to predict the starting burnup for a rim microstructure formation as a function of the local burnup, temperature, fission density and grain size. In the INFRA code, the fuel radial local burnup which was calculated by RAPID model[4] and the time averaged local fuel temperature were used to predict a rim microstructure formation. But, the transition region which means a rim microstructure formation is in progress can't be predicted by the threshold burnup model.

3. FUMEX-II cases and input preparation

The IAEA offered 27 fuel performance database cases to the participants and their code verification results were returned to the IAEA. Due to a incongruity and limitation between the database and INFRA, only 14 cases were calculated and measured data was compared with the predicted fission gas release. The reviewed and compared test cases are listed in Table 1. In Table 1, group B was subjected to no power ramp or transient during a normal operation and group A experienced a power ramping once or more during its life. The transient fission gas release model was operated during the group A calculation.

Group	Case	Test rod	Bu ($MWd/kgUO_2$)	FGR (%)	FCT	Radial FP
A	1	IFA 534.14 rod 8	52	4.68	N	N
	2	IFA 534.14 rod 9	52	8.89	N	N
	3	IFA 597.2/3 rod 8	60	15.8	Y	N
	4	Riso-3 rod AN2	37	29.7	N	Y
	5	Riso-3 rod AN3	37	38.3	Y	N
	6	Riso-3 rod AN4	37	40.9	Y	N
	7	REGATE	47	10.2	N	N
B	8	HBEP rod BK363	67	3.8	N	N
	9	HBEP rod BK365	69	2.4	N	Y
	10	HBEP rod BK370	51	1.4	N	Y
	11	TRIBULATION rod BN1/3	52	1.4	N	N
	12	TRIBULATION rod BN1/4	51	5.5	N	N
	13	TRIBULATION rod BN3/15	51	5.6	N	N
	14	EDF/CEA/FRA rod H09	46	0.8	N	Y

Tab 1: FUMEX-II selected cases for the INFRA code fission gas release verification

For the input preparation, detailed test conditions were reviewed such as a power rating(including a axial power variation), the test rod dimension & characteristics and irradiation condition. In general, FUMEX-II database contains cladding outside wall temperature data which is derived from power and test rod dimensions during a test period and some databases suggest their own correlation which can calculate a clad wall temperature as accurately as possible. In most cases, this correlation was used directly in the INFRA code, but the INFRA default model (Dittus-Boelter or Jeans-Lottes) was used if there was not suggested correlation. A fuel swelling and densification can affect a fuel temperature and consequently affects the fission gas release. In some verification cases, suggested swelling rate and densification values which were determined by a post irradiation examination were used for the calculation but in other cases the INFRA default swelling rate and densification model were used. The Halden model[5] was used for the fuel thermal conductivity calculation.

4. Results and Discussion

The first comparison was performed by using test cases 3, 5 and 6 which contained fuel temperature and fission gas release data . Figures 1 (a) and (b) show the verification results of the fuel centreline

temperature and fission gas release of test case 3. In the Fig 1(a), the predicted temperatures during the power ramp tests show slightly lower values than the measured ones. As can be seen in Fig 1(b), the burst release option was operated during the BOL ramp period and the total release was calculated as about 14%.

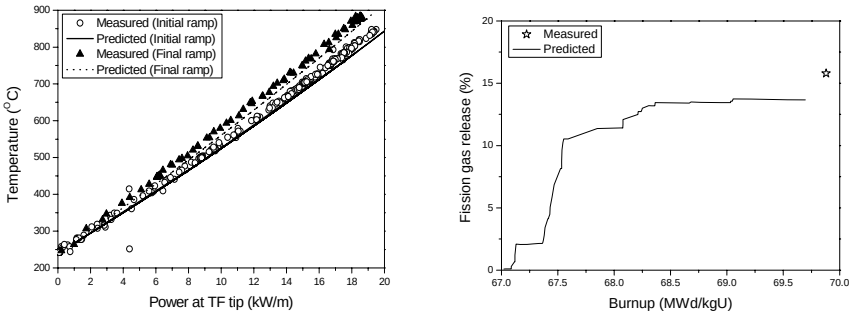

Fig 1. Comparison results for the case 3: (a) fuel temperature; (b) fission gas release

Figures 2 and 3 show the comparison results of the fuel centreline temperature and FGR of cases 5 and 6. These two tests were performed under very similar power histories and rod designs except for the initial filling gas composition (He vs. Xe). During two ramp periods (~ 50 and 70 hr), burst FGR observed by the rod pressure measurement data and the predicted FGR were calculated. In Fig 2 (b), the measured fission gas data shows the initial burst release. Mogensen et al.[6] reported that there were some athermal releases during the tests at a low power level (~11kW/m). In the INFRA code prediction, such a athermal release can't be considered and initial prediction error occurred.
The measured fuel centreline temperature difference between case 5 and 6 is caused by initial filling gas effect and the predicted temperature shows a slight under-estimating tendency of both cases.

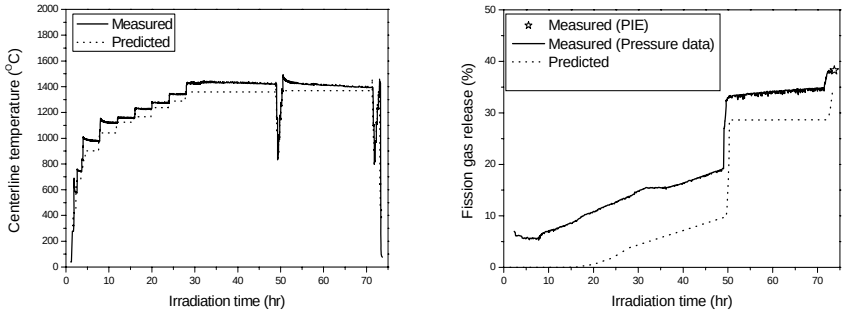

Fig 2. Comparison results for the case 5: (a) fuel temperature; (b) fission gas release

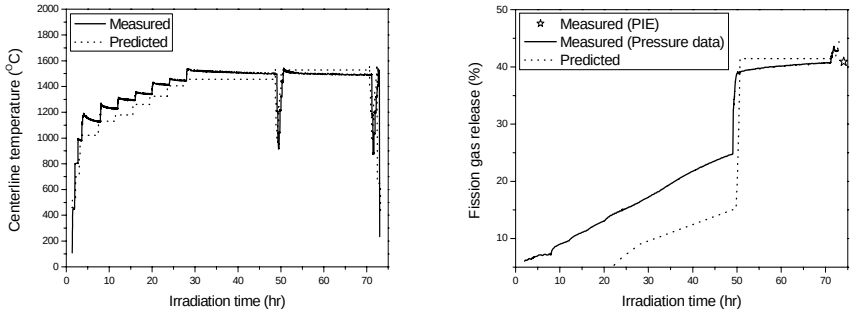

Fig 3. Comparison results for the case 6: (a) fuel temperature; (b) fission gas release

Because other FGR data contains no fuel centreline temperature information or in-pile FGR data which is measured from the rod internal pressure, the predicted EOL FGR data was compared to the measured data by PIE. Figure 4 shows the all the FGR comparison results including the group A and B databases

and indicates reasonable agreement with the measured data. The radial fission product distribution data, especially Xe distribution, was compared with predicted value. Figure 5 shows the radial Xe profile of cases 4, 10 and14 respectively. In Fig 5 (a), case 4 result shows a large amount of Xe release from the fuel centre to intermediate(r/r0=~0.6) region due to a power ramping but a very small amount of produced Xe was released from the outer region of pellet. Case 10 result shows that almost all the produced Xe remained in the pellet and no remarkable fission gas release could be found. In Fig 5 (b), the Xe depletion due to a rim microstructure formation was observed at the pellet's surface region. In the INFRA code calculation, this region was also determined as a rim region. In all the cases, the predicted Xe depletion showed a very small difference to the measured Xe profile.

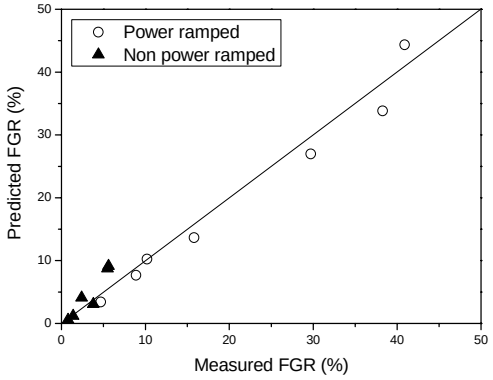

Fig 4. Overall results of fission gas release verification

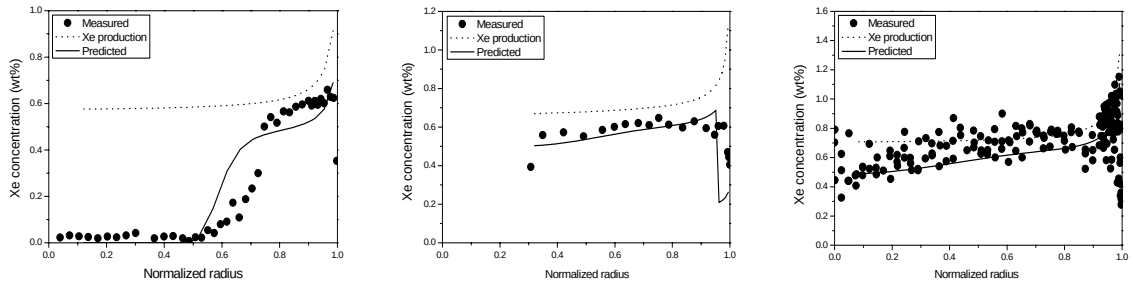

Fig 5. Radial Xe distribution: (a) case 4; (b) case 10; (c) case 14

5. Conclusion

The fission gas release and radial Xe distribution prediction capabilities of the INFRA code were examined by using the FUMEX-II database. For the fission gas release comparison, a careful input preparation was performed and, if possible, the fuel centreline temperature prediction results were compared with measured data in advance. Total of 14 fission gas release data cases were divided into two groups as a ramp or transient test group and steady-state one. In the ramp FGR calculation, a transient model option was operated during the calculation. In all the comparison results, the predicted fission gas release value showed a good agreement with measured data and radial Xe distribution prediction results showed very small difference within a reasonable error range. Other FUMEX-II comparison results will be published by IAEA and a detailed INFRA fission gas release model and verification results will be published soon.

Acknowledgements

This work has been carried out under the Nuclear R&D Program supported by Ministry of Science and Technology in Korea

6. References

[1] J.A. Turnbull, R.J. White, C. Wise, in : Proc. of the IAEA TCM on Water Reactor Fuel Element Computer Modelling, Preston, UK, 1988.
[2] Y. S. Yang et al., “Transient Fission Gas Release Model of the INFRA Code”, KNS Topical Meeting, May, 2006.
[3] C. B. Lee, Y. H. Jung, “An attempt to explain the high burnup structure formation mechanism in UO_2 fuel”, J. Nucl. Mater., Vol. 279, p207, 2000
[4] C. B. Lee, et al., “RAPID model to predict radial burnup distribution in LWR UO_2 fuel”, J. Nucl. Mater., Vol. 282, p196, 2000.
[5] W. Wiesenack, "Assessment of UO_2 conductivity degradation based upon in-pile temperature data", Proc. of Int. Top. Mtg. on LWR Fuel Performance, Portland, Oregon, 1997.
[6] M. Mogensen, et al., J. Nucl. Mater. 202 (1993) 199

ZIRCONIUM MATRIX ALLOYS FOR HIGH URANIUM CONTENT DISPERSION TYPE FUEL

A. SAVCHENKO, I. KONOVALOV, S. ERSHOV, A. LAUSHKIN,
G. KULAKOV, S. MARANCHAK, Y. KONOVALOV, E. MALAMANOVA
A.A. Bochvar All-Russian Scientific Research Institute of Inorganic Materials
123060 Moscow, P.O.BOX 369, Russia

ABSTRACT

A novel class of zirconium alloys having the melting temperature of 690-860°C has been developed. They are intended for use as a matrix of dispersion high uranium content fuel (CERMET and METMET) for fuel elements fabricated by impregnation method. Investigations have been carried out on the structure and properties of the alloys as well as the specific technologies of their fabrication, in particular via induction furnace melting. The alloys may be also produced in the amorphous state as granules and strips. It is shown that thanks to their capillary properties they might be applied in brazing dissimilar materials. Based on novel zirconium matrix alloys high uranium content fuel compositions were developed having high thermal conductivity and uranium content of 8.5-9.5 g·cm^{-3}. Their properties have been investigated. The first results on in-pile testing the fuel compositions are presented.

1. Introduction

One of the routes of upgrading fuels involves the application of high uranium content fuel. Its use is most efficient in dispersion type fuel elements that demonstrate high irradiation resistance, reliability, serviceability under transient conditions and high burnupability. The application of high uranium content fuel in reactors of the PWR and BWR types might be put into practice only with the use of zirconium or its alloy matrices. The pressurized impregnation method is technologically usable for fabricating this type of dispersion fuel element (Fig. 1) [1]. Therefore, as applied to this technology, novel matrix alloys on the basis of zirconium, the melting temperature of which is 1860 °C, had to be designed with relatively low melting temperatures (up to 900 °C) as well as the impregnation process had to be updated with account for the novel alloys and the high uranium content fuel.

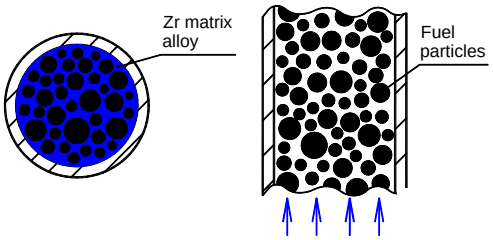

Fig. 1. Schematic presentation of dispersion fuel element and its fabrication via impregnation. The arrows show the motion direction of the molten matrix alloy in the fuel element fabrication process

2. Structural features of Zr matrix alloys

The accomplished investigations resulted in developing novel zirconium alloys of several classes [2, 3]. They are deep ternary or quaternary eutectics having relatively low melting point in comparison with pure zirconium, i. e. from 690 °C to 860 °C. The alloy compositions, the temperatures of melting and impregnation (brazing) are summarized in Table 1.

№ of group	Contents of alloying elements, % mass						Melting T, °C	Impregnation T, °C
	Zr	Ti	Fe	Cu	Be	Nb		
1	base	5-20	4-7	1-3	1.5-2.5	-	690-720	780-810
2	base	-	4-8	0.5-3.0	2-3	1-3	780-810	850-870
3	base	5-10	8-14	8-14	-	-	810-820	880-900
4	base	-	6-12	6-12	-	-	850-860	900-910

Tab 1: Alloy compositions, melting and impregnation temperatures (T)

Figures 2 and 3 illustrate the surface of the liquidus of the Zr-Fe-Be system and the microstructures of Zr-Fe-Cu and Zr-Fe-Be based alloys [3] The main phase in the alloy structures is a phase of the $Zr_2(Fe,X)$ type having the body centered tetragonal crystal lattice, where X is elements Cu, Be, Ni, Nb, Al, Si etc. Depending on the compositions of the alloys the other phases are α-Zr, Zr_2Cu, $ZrBe_2$ etc.

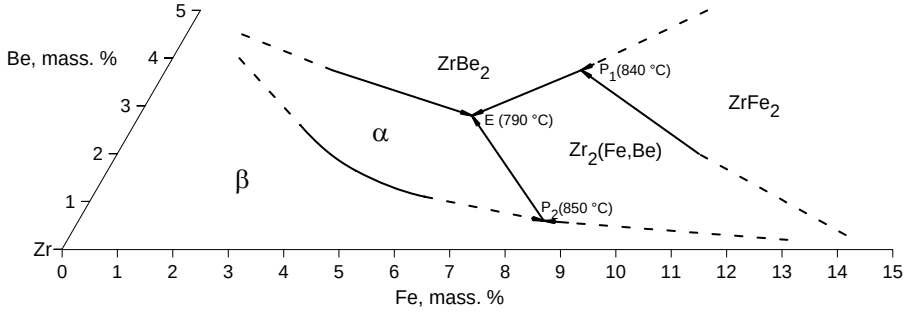

Fig. 2. Liquidus surface near zirconium angle of Zr-Fe-Be phase diagram

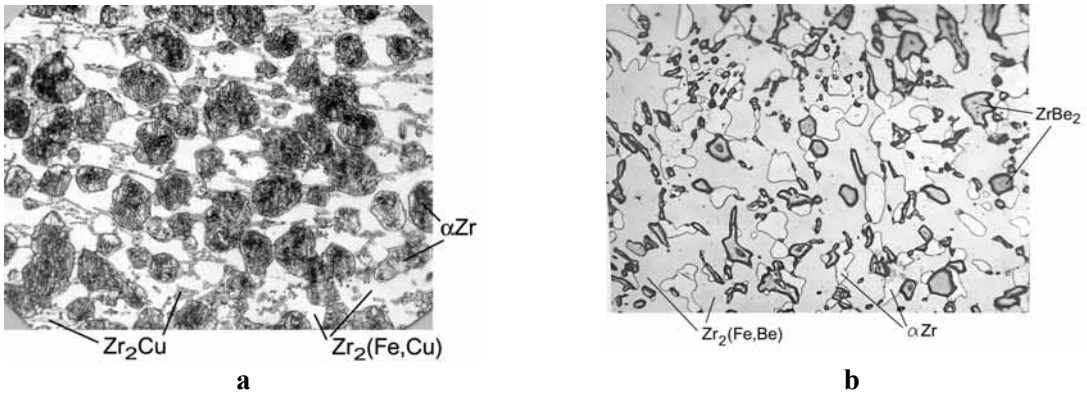

Fig. 3. Microstructures of alloys of systems: (a) Zr-Fe-Cu, (b) Zr-Fe-Be

3. Properties of zirconium matrix alloys

The melting temperatures for all the groups of the alloys are summarized in Table 1; the properties of the alloys of the Zr-Fe-Be system are tabulated in Table 2.

Density, $g \cdot cm^{-3}$	6.1-6.3		
Temperature coefficient of linear expansion (100-500 °C),	$9\text{-}11 \times 10^{-6}\ K^{-1}$		
Aqueous corrosion rate at 350 °C, $g \cdot m^{-2} \cdot h^{-1}$	0.002-0.004		
Steam corrosion rate at 550 °C, $g \cdot m^{-2} \cdot h^{-1}$	0.2-0.5		
Thermal conductivity, $W \cdot m^{-1} \cdot K^{-1}$	100 °C	300 °C	500 °C
	12-13	16-18	22-26
Compression strength, $\sigma_в$, MPa	100 °C	300 °C	500 °C
	700	650	500

Tab 2: Properties of Zr-6.4Fe-2.7Be alloy

Due to low melting temperatures the alloys were not fabricated by arc melting like conventional zirconium alloys, but by induction melting in graphite or ZrO_2 crucibles. The temperature of the melting process did not exceed 1300 °C since higher melting components gradually dissolved in low melting eutectics that formed at the onset of melting. At these temperatures no reaction with the crucible materials took place. The appearance of the alloy ingots is illustrated in Fig. 4a. The maximal ingot mass was 15 kg [3].

a **b**

Fig. 4. Appearance of ingots of Zr-Fe-Cu alloy (a) and granules, amorphous strips and amorphous items produced from alloy of Zr-Ti-Fe-Cu-Be system (b)

The alloys were also produced as granules or amorphous strips. When rapidly quenched the alloys, particularly those of the Zr-Ti-Fe-Be-Cu system, easily become amorphous. The ultimate thickness of the amorphous strip was 250 μm at the width of 50 mm (Fig. 4b).

The alloys feature high capillary properties in molten state and enter the sites where practically no gap was available [2-3]. This property is used to braze dissimilar materials, viz., ceramics - metal, graphite – metal, metal – metal (Be – Cu, Zr – stainless steel, etc) and to impregnate porous graphite etc. In all instances the molten alloy spontaneously entered micrometer size gaps [3, 4]. It is also possible to use them as hydrides to accumulate hydrogen. The attained hydration coefficient made up 1.6 – 1.8.

4. Properties of Fuel Compositions

Owing to the low melting points of zirconium matrix alloys the fuel compositions were produced by impregnating fuel granules loaded into a fuel element cladding with a molten matrix alloy. Since zirconium forms the base of the matrix alloys the alloys are compatible with the high uranium content fuel both upon fabricating fuel elements and after long-term isothermal anneals of fuel compositions at 750 °C for 6000 hours (Fig. 5).

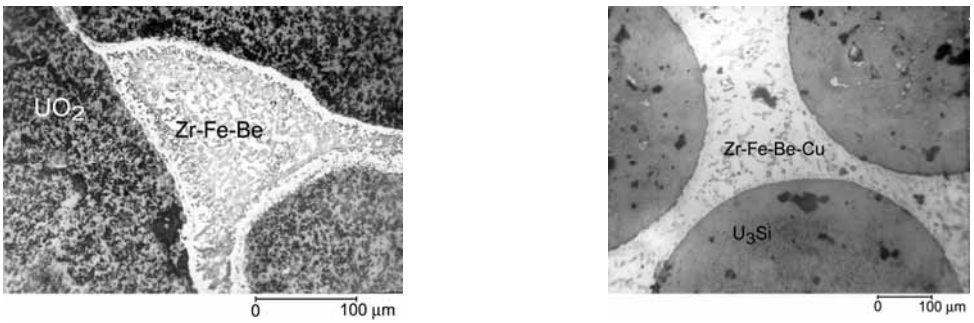

a **b**

Fig. 5. Microstructure of isothermally annealed (750 °C - 6000 h) fuel composition; (a) UO_2 + Zr-Fe-Be, (b) U_3Si + Zr-Fe-Be-Cu

The properties of the fuel composition containing alloys of the Zr-Fe-Be system are shown in Table 3.

Fuel composition	U density, $g \cdot cm^{-3}$	Thermal conductivity at 500 °C, $W \cdot m^{-1} \cdot K^{-1}$	Aqueous corrosion rate at 350 °C, $g \cdot m^{-2} \cdot h^{-1}$	Interaction layer after annealing at 750 °C for 6000 h, μm
UO_2+(Zr-Fe-Be)	5.7	12	-	25
(U5Nb5Zr)+(Zr-Fe-Be-Cu)	8.5	20	0.02-0.04	10
U_3Si+(Zr-Fe-Be-Cu)	8.7	23	-	10
U9Mo+(Zr-Fe-Be-Cu)	9.5	26	-	10

Tab 3: Properties of fuel compositions containing alloys of Zr-Fe-Be system

The high thermal conductivity of the novel high uranium content fuel compositions promotes the ultimate temperature in the VVER-1000 fuel element centre not higher than 450 °C at the linear heat rate of 400 $W \cdot cm^{-1}$. At the expense of the tight diffusion bond to the zirconium cladding and the unavailability of brittle intermetallic compounds at the cladding – fuel interface (Fig. 6) the specimens of the fuels have demonstrated the high stability under thermal cycles (more than 300 cycles of thermal shock: heating to 500 °C – cooling in water), which promotes serviceability of fuels in transient conditions.

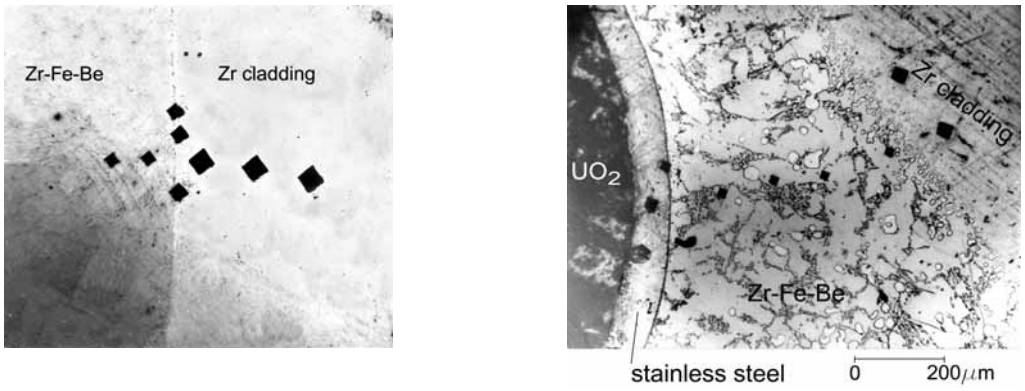

Fig. 6. Microstructure of fuel element after pressurized impregnation with Zr-Fe-Be alloy; (a) zirconium cladding – matrix (no etching), (b) zirconium cladding –matrix - stainless steel cladding of mini-elements

The UO_2, U5Nb5Zr and U_3Si fuel compositions clad in zirconium alloy E110 within (loaded into) liquid sodium containing ampoules have been successfully in-pile tested at the fuel composition temperatures of 250-300 °C up to the burnup of 0.8, 0.4 and 0.3 $g\text{-}fiss \cdot cm^{-3}$ respectively, without any indications of loss of tightness or shape changes. In this case the heat flux from the surface made up 2.0, 1.0 and 0.8 $MW \cdot m^{-2} \cdot K^{-1}$, respectively.

RBMK type UO_2 fuels with Zr-Fe-Be and Zr-Fe-Be-Cu alloy matrix 13.6 mm in the diameter and 1000 mm long were tested in the AM reactor (Obninsk) under the RBMK operating conditions (the water temperature of 280 °C, the heat flux from surface of 1.0 $MW \cdot m^{-2} \cdot K^{-1}$). The cycle was 5 years, the maximal burnup was 0.4 $g\text{-}fiss \cdot cm^{-3}$. The fuels retained the integrity. After irradiation neither the structure nor the fuel composition volume changed.

VVER-440 type dispersion UO_2 fuel elements clad in E110 alloy 9.1 mm in the diameter and Zr-Fe-Be alloy matrices were tested in MIR reactor (Dimitrovgrad) under the VVER-440 operating conditions (linear heat generation rate of 325 $W \cdot cm^{-1}$, coolant temperature of 270 °C, coolant pressure of 12.5 MPa) [5]. The maximal temperature in the fuel element centre made up 442 °C. The achieved

burnup was 0.4 g-fiss·cm^{-3} which as recalculated for the standard UO_2 pelletized fuel rod corresponds to 50 MWd/kgU. The tests are in progress.

Thus, the preliminary in-pile tests of the fuels and the fuel compositions with zirconium matrix alloys have demonstrated their applicability in various types of water reactors.

Basing on the capillary properties of the novel zirconium matrix alloys both the fuel composition fabrication process and the structure of the high uranium content fuel compositions are being updated. Instead of impregnating the internal space of a fuel element with molten Zr alloy in the novel process the zirconium matrix alloy granules, mixed with the fuel granules are loaded into the fuel cladding and then heated to a temperature 50 °C higher than the melting temperature of the alloy [1, 6, 7]. Under the action of capillary forces the molten zirconium alloy coats the fuel granules and the cladding and penetrates into the gaps between the fuel granules and the cladding - forming so-called bridges which provides for the high thermal conductivity of the fuel meat.

5. Conclusion

A novel class of zirconium alloys having the melting temperature of 690-860°C has been developed. They are intended for use as a matrix of dispersion high uranium content fuel (CERMET and METMET) for fuel elements fabricated by impregnation method.

Investigations have been carried out on the structure and properties of the alloys as well as the specific technologies of their fabrication, in particular via induction furnace melting. The alloys may be also produced in the amorphous state as granules and strips. It has been shown that owing to their strong capillary properties the alloys are usable for brazing dissimilar materials.

On the basic of the novel zirconium matrix alloys high uranium content fuel compositions have been developed that have high thermal conductivity of 20-26 W·m^{-2}·K^{-1} and uranium content of 8.5 – 9.5 g·cm^{-3}. Their properties have been studied. The first results on in-pile testing the fuel compositions are presented.

6. References

[1] ISTC Project No 173-95 Designing New Generation Fuel Elements for Water Reactors of Different Purposes (1995-1996).

[2] Zr-base alloy. Patent of Russia 2009239, 31.01.1992 (VNIINM).

[3] A.M. Savchenko, I.I. Konovalov, S.A. Ershov, A.V. Laushkin, G.V. Kulakov, S.V. Maranchak, Y.V. Konovalov, E.K. Malamanova, Novel zirconium alloys as matrix for high uranium content dispersion type fuel, in: Proceedings of the E-MRS 2006 Spring Meeting, Nice, France, 29.05-03.06.2006.

[4] A.M. Savchenko, A.V. Vatulin, A.V. Morozov, I.V. Dobrikova, S.A. Ershov, S.V. Maranchak, Z. N. Petrova, Y.V. Konovalov, IMF with low melting point zirconium brazing alloys, J. Nucl. Mater., 352 (2006) 334-340.

[5] V.Y. Shishin, V.A. Ovchinnikov, A.E. Novoselov, Behaviour of CERMET fuel compositions in inert matrices (review of experiments), in review disposition of weapons-grade plutonium with inert matrix fuels, NRG, Petten, 2004.

[6] A.M. Savchenko, I.I. Konovalov, A.V. Vatulin, S.A. Ershov, G.V. Kulakov, S.V. Maranchak, Z.N. Petrova, Dispersion type zirconium matrix fuels fabricated by capillary impregnation method, in: Proceedings of the E-MRS 2006 Spring Meeting, Nice, France, 29.05-03.06.2006.

[7] A.M. Savchenko, I.I. Konovalov, S.A. Ershov, A.V. Laushkin, S.V. Maranchak, Y.V. Konovalov, E.K. Malamanova, Capillary impregnation technology for novel types of fuel, these Proceedings

RELATIONSHIP BETWEEN RELEASE BEHAVIOR OF CESIUM AND SINTERED PELLET DENSITY IN DUPIC FUEL FABRICATION WITH HIGH BURN-UP SPENT PWR FUEL

G.I. PARK, D.Y. LEE, JUNG WON. LEE, J.W. LEE, M.S.YANG
Dry Process Nuclear Fuel Development, Korea Atomic Energy Research Institute
150 Deokjin-dong, Yuseong, Daejeon, 305-353, Korea

ABSTRACT

Key parameters influencing the DUPIC fuel fabrication characteristic in a wide range of spent PWR fuel burn-ups would be both the powder properties and the amount of fission products in a spent fuel. The release fraction of cesium from a green pellet under different sintering conditions was obtained. Based on these results, the relationship between a release characteristic of cesium during a sintering step and a sintered pellet density was evaluated to analyse the influence of the DUPIC fuel fabrication with a high burn-up spent fuel of 65,000 MWd/tU. It was identified that a sintering temperature history, to completely remove the fission product of cesium, affected the sintered pellet density due to the intermediate sintering stage when considering three stages of a sintering process. Possible sintering mechanism affecting the decrease in the sintered density was suggested when a high burn-up fuel is processed.

1. Introduction

The dry process, known as DUPIC(Direct Use of spent PWR fuel in CANDU reactor), for fabricating fuel pellets from spent fuel as a recycling technology has been well demonstrated by establishing an optimization process for a fuel fabrication through a number of batch processes using typical PWR spent fuel [1]. When considering a strategy for extending the burn-up in a LWR fuel, an experimental verification for analyzing the effect of a spent fuel burn-up on a fuel fabrication is necessary from some respects as one of the key parameters influencing the fuel fabrication characteristics would be the amount of fission products contained as impurity elements in a spent fuel. A high burn-up spent fuel has a higher amount of fission products compared with typical spent fuel irradiated at about 27,000 MWd/tU. A preliminary study showed that the sintered pellet density fabricated with a high burn-up fuel has a lower value than that of common fuel burn-ups of about 30,000 MWd/tU. To provide a better understanding of remote fuel fabrication characteristics from the aspect of a wide range of spent fuels generated from PWR reactor, the influence of a fission products release on the fabrication characteristics of the dry processed fuel with a high burn-up fuel of 65,000 MWd/tU were experimentally evaluated.

It is expected that a key fission product affecting the fabrication characteristics in the dry process is the cesium isotope due to its boiling point of 670^{o}C and the low dissociation temperature of its oxides(<700^{o}C) [2]. Cesium as a semi-volatile fission product has been a major concern during a spent fuel treatment due to its high content, long half-life (Cesium-137: 30.2 years), and high heat generation. Cesium exists in a spent fuel matrix as solid chemical compounds such as Cs, CsI, $Cs_2UO_{3.56}$, Cs_2UO_4, Cs_2MoO_4, which depend on the O/M ratio of a spent fuel. Especially, the release fraction of semi-volatile fission products depends on the chemical species of the corresponding fission products in various gas atmospheres. For example, cesium monoxide (Cs_2O) is one of the chemical forms of cesium that could be present in a spent fuel. However, it is confirmed that a major chemical form released from a spent fuel in a steam condition is cesium iodide (CsI) by a stoichiometric reaction with iodine.

This study focused on analyzing the relationship between a release characteristic of cesium from green pellets fabricated with a variation of the compaction pressure and sintered density under different

sintering conditions using a tubular furnace in the IMEF M6 hot cell.

2. Experimental

The spent PWR fuel with a high burn-up of 65,000 MWd/tU(**K23-M03**) and a short decay time of 2.8 years in the K23 assembly from Uljin # 2 in 2001 was used for fabricating the green pellets as raw materials for the study of the release behavior of cesium during the sintering step. Fuel pellets were fabricated in accordance with the optimized fuel fabrication process flow [3]. The process parameter of each step was established from both the pre-qualification test and the qualification test. The optimized process conditions were applied for the fabrication of the OREOX (Oxidation and Reduction of Oxide fuel) powder and green pellet. U_3O_8 powder oxidized at 500°C for 5 hrs was treated by the OREOX process which is composed of 3 cycles of a oxidation at 450°C in air and a reduction at 700°C in 4%H_2/Ar. After the milling and precompaction steps, the green pellet was fabricated by a final compaction process with a pressure range from 88 MPa to 150 MPa. The typical sintering conditions by using the as-fabricated green pellet in an Ar-4%H_2 atmosphere are summarized in Table 1. After each sintering experiment, a sintered density was measured from the geometric data.

Test No.	Compaction pre.(MPa)	Sintering conditions	Wt. (g)
ST-1	88	Heating to 1,650°C → Cooling	12.2
ST-2	88	Heating to 1,650°C(5 hrs holding) → Cooling	11.6
ST-3	88	1,350°C(1.2 hr holding) → Reheating to 1,650°C → Cooling	12.1
ST-4	88	1,350°C(1.2 hr holding)→ Reheating to 1,650°C(5 hrs holding) → Cooling	12.1
ST-5	102	Heating to 1,650°C → Cooling	13.6
ST-6	102	1,350°C(1.2 hr holding) → Reheating to 1,650°C → Cooling	13.4
ST-7	102	1,350°C(1.2 hr holding)→ Reheating to 1,650°C(5 hrs holding) → Cooling	12.6
ST-8	120	Heating to 1,650°C → Cooling	12.8
ST-9	120	1,350°C(1.2 hr holding) → Reheating to 1,650°C → Cooling	12.3
ST-10	120	1,350°C(1.2 hr holding)→ Reheating to 1,650°C(5 hrs holding) → Cooling	13.4

Table 1 : Sintering conditions for the evaluation of release behavior of cesium from green pellets.

The supplementary experiments to analyze a release behaviour of fission products during various sintering conditions were carried out. The gamma spectrometer system (GAMMA-X^{TM} HPGE, Coaxial Photon Detector System, ORTEC Gamma Vision 32 GMX Series) was aligned to a green pellet located in a tubular furnace for obtaining the gamma spectrum due to the release of cesium from the green pellets. The cumulative release fraction of cesium during the sintering step was calculated from a comparison of the count rates measured during each test with the initial count rate of cesium from the green pellet before the test. Fig. 1 shows the schematic diagram of the equipment for the fission products release evaluation.

3. Results and Discussion

3.1 Fabrication of green pellets

The green pellets were fabricated by using the OREOX powder of K23-M03 spent fuel in a range of 80~ 160 MPa of the compaction pressure, as shown in Fig. 2. The geometric density of the green pellets increased with the compaction pressure. But in a high compaction pressure over 150MPa, some cracks

on the green pellet were identified. Therefore, the green pellets fabricated in a range of 80 ~ 120MPa were used for the sintering experiments.

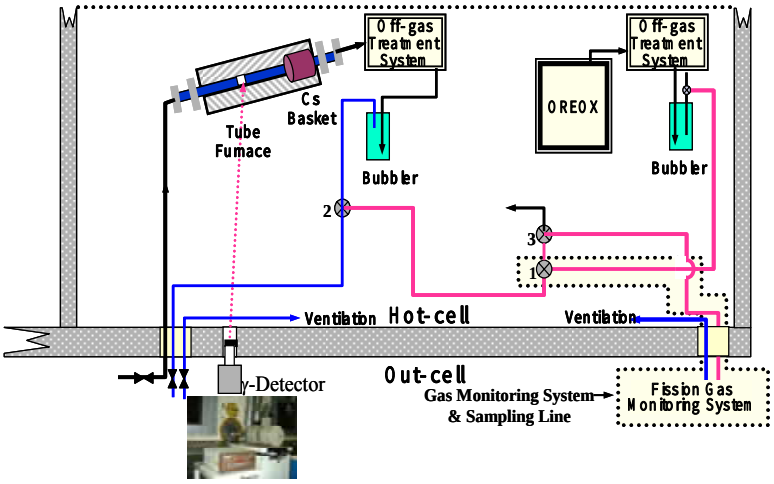

Fig 1. Schematic diagram of the equipment for the fission products release evaluation.

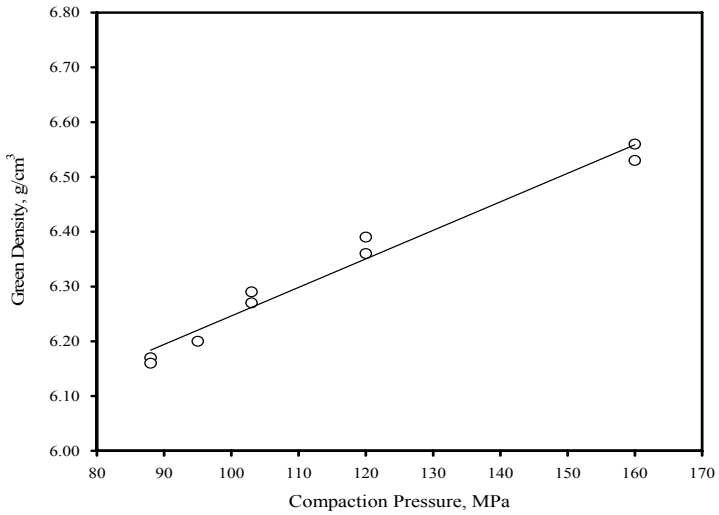

Fig.2. Geometric density of the green pellets with the compaction pressure.

3.2 Release characteristics of cesium from a green pellet

Fig. 3 shows the release characteristics of cesium from the green pellets under different sintering conditions. Fig. 3(A) is typical release behaviour of cesium under a direct heating to 1,650°C in test number ST-1,5,7. in Table 1, and Fig.3(B) is from test number ST-3,6,7 that was heated to 1,350°C, followed by a 1.2 hr holding time and reheated to 1,650°C. A difference between test ST-1 and ST-3 is the temperature history during the sintering step. Regardless of the sintering temperature history, cesium was released in a temperature range of 1,100°C to 1,450°C during the sintering step. The sintering process is generally divided into three stages : (a) Initial stage of a sintering (Neck formation and growth), (b) Intermediate stage of a sintering (Interconnected pores), (c) Final stage of a sintering (Isolated pores). The onset of a real densification for a sintering occurs above 1,100 ~ 1,150°C and a relative density percent during an intermediate sintering stage corresponds to 60 to 90 % [4]. It is clear that the temperature range for a cesium release from a green pellet corresponds to the intermediate sintering stage. It was reported that cesium is gaseous above 1,200°C, thus the release of cesium occurs by an axial migration in the grain boundary porosity in the central region of the fuel [2]. Especially, a marked migration of cesium to the pellet rim region for a high burn-up fuel was observed and

the micro-structure changes resulted in a decrease in the grain size and the formation of numerous small pores [5]. Therefore, a milled powder from the rim region of a high burn-up fuel for the fabrication of a green pellet would contain a high content of cesium. Based on these results, it is expected that a gaseous cesium release during an intermediate sintering stage affects the network formation of the pores, followed by a formation of residual pores in a green pellet.

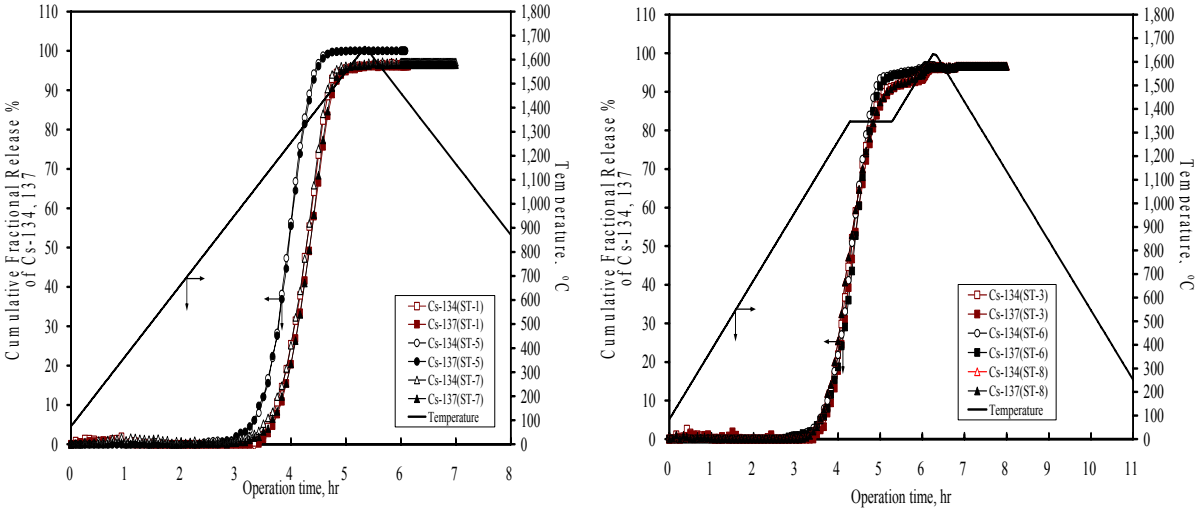

(A) Test No : ST-1,5,7 (B) Test No. : ST-3,6,8

Fig.3. Cumulative release fraction of Cs-134 and Cs-137 from the green pellets with the sintering time under a different sintering temperature history.

3.2 Variation of sintered density with sintering conditions

The influence of the sintering temperature history on a sintered pellet density was evaluated. Fig. 4 shows a variation of the sintered pellet density measured from each test, as represented by % of T.D.(Theoretical Density). As described in Table 1, final sintering temperature in this study was 1,650°C which is somewhat lower when compared to a normal sintering temperature of about 1,800°C. But some trends in the sintered pellet density with a variation of the sintering temperature history would be identified, even though the absolute values of the sintered density were not so high.

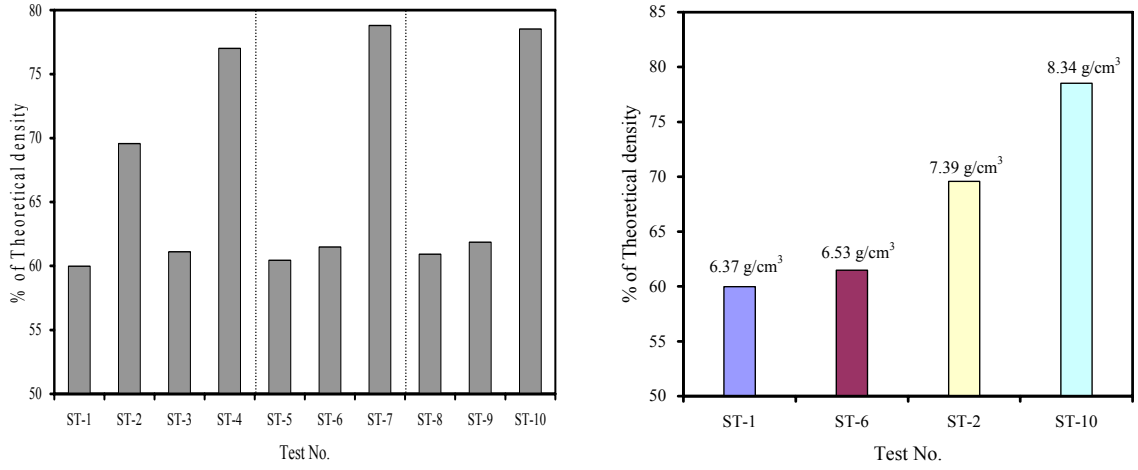

Fig.4. Variation of sintered pellet density measured from each test.

No influence of the compaction pressure on the sintered pellet density under the same sintering temperature history was observed, but the sintering temperature history had a significant effect on the

sintered density. In the case of ST-1 and ST-6, the holding time at 1,350°C for a complete removal of cesium during the intermediate sintering stage caused a slight increase in the sintered density. However, a holding time at a sintering temperature of 1,650°C was 5 hrs such as ST-2 and ST-10 to completely remove cesium during the intermediate sintering stage at around 1,350°C made a significant increase in the sintered density when compared to a direct heating to 1,650°C. These results imply that the degree of interconnection of the pores from a result of a cesium release at the holding temperature stage of 1,350°C would be a key parameter because the sintered pellet density increased from 7.4 g/cm^3(ST-2) to 8.3 g/cm^3(ST-10).

4. Conclusion

The release characteristics of cesium from the green pellets fabricated with a high burn-up spent fuel of 65,000 MWd/tU were evaluated for the analysis of the effect of the fission products release on the sintering process. Cesium as a gaseous phase was released in a temperature range of 1,100°C to 1,450°C during the sintering step. It was also identified that temperature range to completely remove cesium affected the sintered pellet density due to the intermediate stage of the sintering process. When a holding time at a sintering temperature of 1,650°C was 5 hrs, a complete removal of cesium during the intermediate sintering stage at around 1,350°C caused a significant increase in the sintered density when compared to direct heating to 1,650°C. The influence of a complete removal of cesium during the intermediate sintering stage which resulted in an increase of the sintered density would be suggested that a cesium release during this stage would cause a rapid formation of interconnected pores, followed by an easy formation of the isolated pores in the sintered pellet.

5. Acknowledgement

This project has been carried out under the Nuclear R&D Program by MOST

6. Reference

1) J.W. Lee, G.I Park, et al., Proliferation-resistant Fuel Technology Development : Development of Nuclear Fuel Remote Fabrication Technology, KAERI/RR-2524/2004, Korea Atomic Energy Res. Inst., (2004).
2) C.T. Walker, C. Bagger and M. Mogensen, “Observation on the release of cesium from UO2 fuel”, J. of Nuclear Materials, 240, 32-42 (1996).
3) G.I. Park, et al., Development of Manufacturing and Operating Procedure for Fabrication of DUPIC Fuel, KAERI/TR-2382/2003, Korea Atomic Energy Res. Inst., (2003).
4) T.R.G. Kutty, et al., “Densification behavior of UO_2 in six different atmospheres”, J. of Nuclear Materials, 305,159-168 (2002).
5) K. Une, M. Hirai, K. Nogita, et al., “Rim structure formation and high burnup fuel behavior of large-grained UO_2 fuel”, J. of Nuclear Materials, 278,54-63 (2000).

R&D innovations at AREVA NC - Recycling Business Unit(1)

AREVA NC Recycling Business Unit is the world leader in MOX(2) production, and manufactures MOX fuel assemblies for nuclear power plants at the MELOX Plant.

NEW R&D OBJECTIVES IN AN EVOLVING MARKET

> Adaptation to new product requirements
> Ongoing development to improve the overall performance of MOX fuel
> Improvement of plant performance relating to productivity and safety

>> MELOX plant

>> MELOX control room

THE MEANS TO MEET THESE CHALLENGES

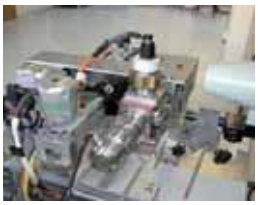

>> Rod welding workshop equipment

>> Small scale industrial test line

>> AREVA NC CDA view

MOX rod welding R&D workshop

> The rod welding workshop at the AREVA NC Cadarache site uses all the welding processes used on the MELOX plant plus comprehensive examination techniques (corrosion, RX, metallographic, etc.).
> This workshop makes it possible to anticipate changes in the MELOX rod manufacturing line due to new rod and plug designs and the effect on the welding parameters, to improve the welding process before implementation on the MELOX main line, and to define optimized welding parameters based on parametric tests.

MELOX small scale industrial test line

The small scale industrial line includes the full range of technologies used in MELOX fabrication lines, on a small industrial scale (except sintering, performed in the production furnaces).

The main objectives of the MELOX test line:

> Testing of potential processes or technological optimizations before industrial implementation
> Manufacturing of specific pellets for calibration of measurement devices
> Support to other R&D partners to develop new pellet products

Cadarache UO_2 workshop

The UO_2 workshop tests scale 1 equipment for MOX industrial plants. Global testing of industrial systems at AREVA NC Cadarache R&D Activities (CDA), combined with a close relationship between R&D and engineering studies has produced savings in time and money.

Main advantages of Cadarache UO_2 workshop:

> Technical, mechanical and instrumentation choices are validated in representative conditions
> Technical issues can be identified and solved early in the project
> In-site testing can be minimized
> Prototypes can be used to validate changes prior to implementation on industrial equipment

PRACTICAL ILLUSTRATIONS

Chromox program

> R&D is already preparing to improve MOX fuel performance to the same level as UO2 the standard fuel for the future (60 GW d/t).
> Using the small scale industrial test line, MELOX is presently manufacturing chrome doped pellets. The fuel rods using M5 cladding will be inserted into two assemblies to be irradiated in an EDF reactor. These test rods will be extracted after 3, 4 and then 5 cycles for post irradiation examinations.

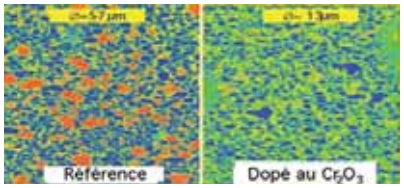

>> Standard fuel pellet >> Chromox pellet

>> Reinforced Glove

>> Cleaner robot

>> Radiashield cloth

>> New generation of vacuum cleaner

Safety of glove box operation

> With 30 years of experience in MOX glove box operation, AREVA NC is continuously maintaining its R&D efforts to improve glove box working conditions and safety. Important new innovative solutions have been developed in the last few years.

(1) AREVA NC Recycling Business Unit consists of the MELOX Plant and the Cadarache site
(2) MOX is a mixture of uranium and plutonium oxides

RAJ-II AND NPC SHIPPING CONTAINERS DEVELOPMENT AND LICENSING STATUS

A. LANGSTON, R. STACHOWSKI
Global Nuclear Fuel
3901 Castle Hayne Road, Wilmington, NC 28402 – USA

ABSTRACT

GNF has replaced its fuel bundle and drum type containers with the new generation RAJ-II and NPC packages. Both packages are constructed of stainless steel and engineered impact absorbing and fire insulating materials. The RAJ-II is currently licensed as a Type B(F) container for shipping BWR fuel bundles, mixed oxide, and channeled fuel bundles. The NPC is licensed as Type A(F) used to ship homogeneous or heterogeneous uranium bearing material that is enriched up to 5% U^{235}. To meet the growing demands for the NPC container, an expansion of current authorized contents is being evaluated.

1. RAJ-II Shipping Container

GNF has replaced its fleet of wood and carbon steel RA-3 and RA-3D fuel bundle shipping containers with the new stainless steel RAJ-II [Ref. 1]. The RAJ-II is used to transport Boiling Water Reactor (BWR) fuel assemblies containing both Type A and Type B fissile material and accommodates two bundles. The NRC Certificate of Compliance for the RAJ-II was received in November of 2004 and complies with the new "-96" IAEA regulations. Unlike the previous generation of container, the RAJ-II is licensed to ship mixed oxide fuel assemblies and pre-channeled fuel. The RAJ-II package is comprised of an inner container and an outer container both made of stainless steel.

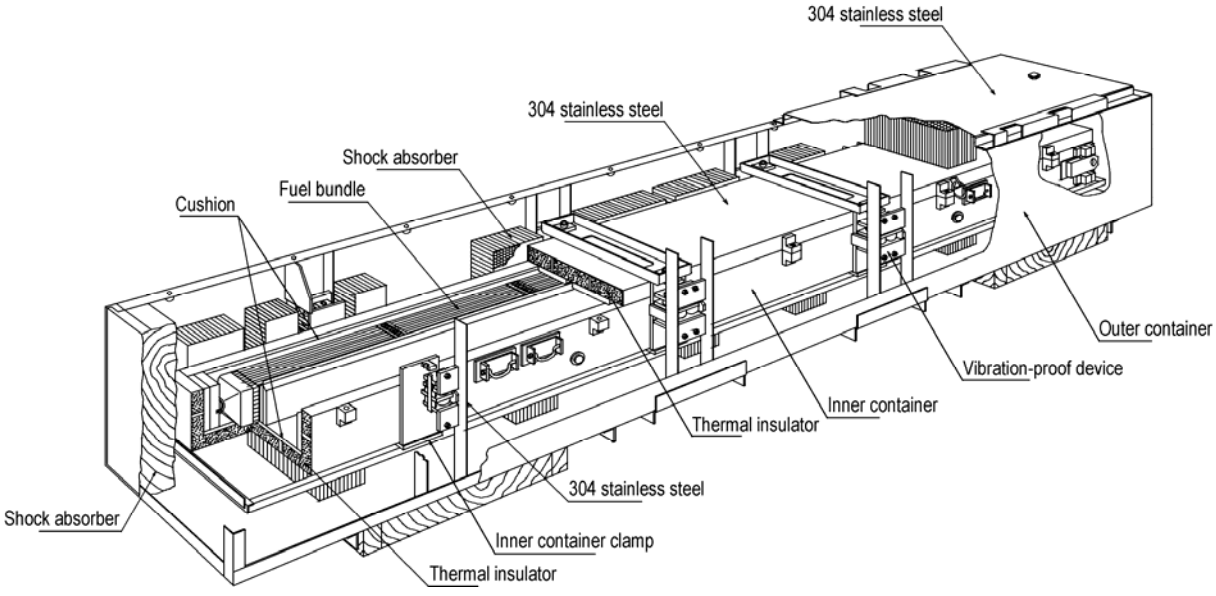

Fig 1: RAJ-II Shipping Container

1.1 Inner Container (IC)

The inner container is comprised of three parts: an inner container body, an inner container end lid (removable), and an inner container top lid (removable). These components are fastened together by

bolts made of stainless steel through tightening blocks. The inner container body is fitted with six sling fittings and the inner container lid is fitted with four sling fittings.

The inner container is a double-wall stainless steel sheet structure with alumina silicate thermal insulation filling the gap between the two walls. Polyethylene foam cushioning material is placed on the inside of the inner container for protection of the fuel assembly.

The outer wall is made of a 1.5 mm (0.0591 in) thick stainless steel sheet formed to a U-shape that constitutes the bottom and sides of the inner container body. A total of 14 stainless steel tightening blocks are attached on the sides of the outer wall, seven per side, to fasten the inner container lid and the inner container end lid by bolts. Additionally, six stainless steel sling fittings are attached on the sides (three on each side) for handling.

The inner wall of the inner packaging is formed into U-shape with 1.0 mm (0.0391 in) thick stainless steel sheet. The inner packaging is partitioned down the center with 2.0 mm (0.0787 in) thick stainless steel sheet welded to the bottom of the packaging. Foam polyethylene is placed on the inner surface of the inner wall where the fuel assemblies are seated.

1.2 Outer Container (OC)

The outer container is comprised of three parts: a container body, a container lid and inner container hold clamps made of stainless steel and fastened together using stainless steel bolts. Two tamper-indicating device attachment locations are provided, one on each end, of the outer container.

The outer container is made from a series of 50 mm (1.97 in) stainless steel angles that make the framework. Welded to the framework is a bottom plate and side plates made of 2 mm (0.079 inch) thick stainless steel. Sling holding angles for handling with a crane and protective plates for handling with a forklift are welded on the outside of the container body.

Eight sets of support plates are welded on the inside of the outer container body for installing the inner container hold clamps. Additionally, shock absorbers made of 146 mm (5.75 in) wood are attached to each end and paper honeycomb shock absorbers are attached to the bottom and sides for absorbing shock due to a drop. The shock absorbers are 157 mm (6.18 in) thick and 108 mm (4.25 in) thick.

The outer container lid is comprised of a lid flange and a lid plate made of stainless steel. Stainless steel lid sling fittings are welded four places on the top surface of the outer container lid. A paper honeycomb shock absorber, 157 mm (6.18 in) thick by 160 mm (6.30 in) wide and 380 mm (14.96 in) long is attached to the bottom side of the lid similar to the attachment at the bottom of the container. The outer container lid has holes for bolts in its flange so that it can be fastened to the outer container body by the stainless steel bolts.

The inner container hold clamp consists of an inner container receptacle and a vibro-isolating device. The inner container receptacle consists of an inner container support plate; a support frame, a bracket and an inner container hold clamp fastener made of stainless steel. The receptacle guides the inner container to the correct position. The inner container receptacle is fitted with the vibro-isolating device through the gusset attached to the bracket. The vibro-isolating material is attached on the upper and lower side of the gusset. Shock mount fastening bolts go through the center of each piece of vibro-isolating rubber. The bolts at both ends are tightened so that the vibro-isolating rubber pieces press the gusset. There are four sets (eight pieces) of the vibro-isolating devices mounted on the outer container.

1.3 Gross Weight and Dimensions

The maximum gross shipping weight of a RAJ-II package is 1,614 kg (3,558 pounds) maximum. A summary of the major component weights and dimensions are given in Table 1.

Tab 1: Summary of RAJ-II Weights and Dimensions

Component	Item	RAJ-II
Contents	Number of assemblies per package	Maximum 2 Assemblies
	Number of fuel rods per package	See Table 6-2 RAJ-II Fuel Rod Loading Criteria (Reference 1)
	Maximum weight	684 kg (1,508 lb)
Inner Container	Body	200 kg (441 lb) [1]
	Lid	101 kg (223 lb)
	End lids	7 kg (15.4 lb)
	Dimension	Length: 4,686 mm (184.49 in) Width: 459 mm (18.07) Height: 286 mm (11.26)
	Maximum weight	308 kg (679 lb)
Outer Container	Body	485 kg (1,069 lb)
	Lid	137 kg (302 lb)
	Dimension	Length: 5,086 mm (199.53 in) Width: 720 mm (28.35) Height: 742 mm (29.21)
	Maximum weight	622 kg (1,371 lb)
Packaging	Maximum weight	930 kg (2,050 lb)
Package	Maximum weight	1,614 kg (3,558 lb)

2. NPC Shipping Container

GNF has replaced its drum type containers with the new stainless steel New Powder Container (NPC) [Ref. 2]. The packaging consists of a stainless steel sheet metal Outer Confinement Assembly (OCA) body and lid that encases ceramic fiber insulation and rigid polyurethane foam, and nine equally spaced, individually sealed stainless steel Inner Containment Canister Assemblies (ICCAs). The closure of each canister is provided by a closure lid with a silicone rubber gasket and a standard stainless steel bolted band clamp assembly.

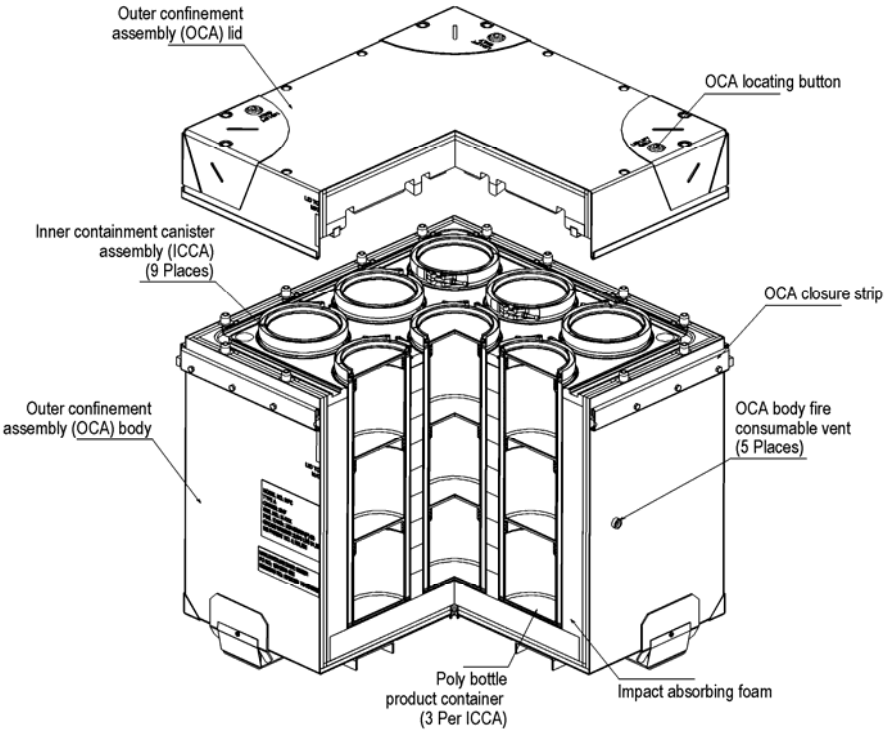

Fig 2: NPC Shipping Container

The NPC packaging is a Type A(F) package designed for transportation of homogeneous or heterogeneous uranium bearing material that is enriched up to 5% U^{235}. The maximum gross weight of the package is 2,870 pounds (1,302 kg).

2.1 Outer Confinement Assembly

The Outer Confinement Assembly (OCA) consists of an OCA lid and OCA body, each primarily comprised of an outer stainless steel sheet structure, a layer of ceramic fiberboard, and a layer of rigid polyurethane foam. The polyurethane foam provides thermal insulation, energy absorption for the normal and hypothetical accident conditions of transport and neutronic isolation. Nine sealed individual canister assemblies, which provide containment of the uranium bearing material, are located within the interior of the OCA. The canisters are positioned such that their center-to-center spacing is fixed.

The OCA lid has nominal external dimensions of 1,099 mm × 1,099 mm × 2225 mm (43 1/4-in × 43 1/4-in × 8 7/8- in). The OCA body has nominal external dimensions of 1,118 mm × 1,118 mm × 981 mm (44-in × 44-in × 38 5/8-in). In its assembled configuration, the OCA has approximate nominal external dimensions of 1,140 mm × 1,140 mm × 1,122 mm (44 7/8-in × 44 7/8-in × 44 3/16-in).

The OCA lid is secured to the OCA body with (16) 1/2-13UNC socket head cap screws, with four bolts installed on each edge of the OCA lid. At the joint between the OCA lid and OCA body, a stainless steel closure strip is attached between the OCA lid and OCA body. The closure strip is secured with (24) 7/16-14UNC hex head bolts that are screwed into a 5/8-inch thick stainless steel bar, which is welded to the OCA body. The purpose of the closure strip is to provide additional structural strength to the OCA closure.

The outer skin of the OCA is fabricated using a 10-gauge (3 mm) thick Type 304L austenitic stainless steel sheet. Behind the outer skin, two layers of 12.7 mm (1/2-inch) thick ceramic fiberboard are positioned around the sides, bottom, and top of the OCA. Polyurethane foam is then installed between the ceramic fiberboard and the containment canisters. A 25.4 mm × 25.4 (1-in × 1-in) ceramic fiber braided rope is installed in the polyurethane foam around the circumference of the OCA body to provide additional thermal protection of the OCA lid/body joint. Nine individual canister silos, fabricated of 22-gauge (0.74 mm) thick Type 304L austenitic stainless steel sheet, are located within the OCA body interior. These canister silos provide the receptacle for the Inner Containment Canister Assemblies (ICCAs). A 1.6 mm × 229 mm diameter (1/16-in thick × 9-in diameter), silicon rubber pad is placed in the bottom of each canister silo to provide cushioning of ICCA during transport.

2.2 Inner Containment Canister Assembly

The Inner Containment Canister Assembly (ICCA) consists of a closure lid and body, which are fabricated with Type 304L austenitic stainless steel sheet. The closure lid and body are fabricated using 16-gauge (1.5 mm) and 18-gauge (1.2 mm) material respectively. An austenitic stainless steel band clamp assembly, which uses a 5/16-inch T-bolt, is utilized to secure the canister closure lid to the cylindrical canister body. The band clamp assembly includes a silicone rubber gasket between the canister closure lid and canister body. To provide criticality control, the outer cylindrical surface of each canister is wrapped with a minimum 0.5 mm (20-mil) cadmium sheet, and then a 0.4 mm (15-mil) High Density Polyethylene (HDPE) sheet wrapped to a thickness of 12.7 mm (½-in) minimum. A 24-gauge (0.6 mm) austenitic stainless steel sheet is wrapped around the cadmium/HDPE materials to secure these materials to the canister body.

The ICCA has a nominal external diameter of 248 mm (9 3/4-in) and a nominal overall length of 816 mm (32 1/8-in). The band clamp assembly has a nominal external diameter of 260 mm (10 1/4-in). The payload contents in an ICCA are limited to a maximum of 60 kg (132.2 lb), which is to include the weight of packing material (receptacles, etc.) in the ICCA.

2.3 Contents of Packaging

The NPC packaging is designed to transport a maximum of 540 kg (1,190 lb) of uranium bearing payload, including receptacles and packing material (e.g. bags, bottles, cans) in the ICCA in accordance with the table below. The radionuclide content is uranium from natural sources, which is commercially enriched. The payload within an NPC may be distributed in any ratio within the nine Inner Containment Canister Assemblies (ICCAs), if the content of any one ICCA never exceeds 60 kg (132.2 lb), and the maximum uranium payload of the following table are met.

Tab 2: Type, Form and Maximum Quantity of Material per NPC

Material Form* **(≤ 5.00 wt.% U-235)**	**Particle Size Restriction: Minimum OD (Inches)**	**Maximum Loading per ICCA (kg)**		**Maximum Loading per NPC (kg)**	
		Net	Uranium	Net	Uranium
Homogeneous Uranium Oxides/Compounds	N/A	60.0	52.89	540.0	476.1
Heterogeneous UO_2 Pellets (BWR)	0.342	60.0	48.48	540.0	436.3
Heterogeneous UO_2 Pellets (PWR)	0.300	60.0	46.71	540.0	420.4
Heterogeneous Uranium Compounds	Unrestricted particle size	60.0	40.54	540.0	364.8

*The Material Form within any NPC must be the same.

Note: Uranium-bearing contents may be moderated by water or carbon to any degree and may be mixed with other non-fissile materials with the exception of deuterium, tritium and beryllium. Materials such as uranium metal and uranium metal alloys are not covered by this analysis.

3. Licensing Status

The RAJ-II is currently licensed in the United States as a Type B(F) container and Japan as Type A(F). Application for license is currently in review in Spain, France, Germany, Switzerland, Belgium, UK, Canada, Sweden, and Finland.

The NPC is currently licensed in the United States, Canada, Russia, and Japan as a Type A(F) container. Application for license is currently in review in Spain, France, Germany, Sweden, Belgium, and UK. To meet the growing demands for the NPC container, an expansion of current authorized contents is being evaluated.

4. References

1. "Safety Analysis Report for the Model Number RAJ-II Package," USA/9309/B(U)F-96, Docket Number 71-9309, Rev. 6, Global Nuclear Fuel-Americas, Wilmington, April 2006.
2. Safety Analysis Report for the Model Number NPC Package," USA/9294/AF-85, Docket Number 71-9294, Rev. 4, Global Nuclear Fuel-Americas, Wilmington, October 2005.

ALCYONE: THE PLEIADES FUEL PERFORMANCE CODE DEDICATED TO MULTIDIMENSIONAL PWR STUDIES

G. THOUVENIN, J.M. RICAUD, B. MICHEL, D. PLANCQ
DEC/SESC/LSC, Commissariat à l'Energie Atomique
Centre d'Etudes de Cadarache, 13108 St Paul Lez Durance – France

P. THEVENIN
Electricité de France
Centre d'Etudes de Cadarache, 13108 St Paul Lez Durance – France

ABSTRACT

Within the framework of a collaboration between CEA and EDF, the PLEIADES project has been built to create a new simulation platform for the study of any reactor concept fuels behavior. In this new environment, the multi-scale application ALCYONE has been developed for studies on fuel rods for Pressurized Water Reactors. Indeed, a general three dimensional modeling of the thermo-mechanical problem is obviously the best way to recreate the most accurate representation of the pellet/cladding system interaction problem, but is not appropriated to model an entire rod, where a mono-dimensional representation of the rod cut by slices is used for a low CPU time cost. The paper gives a global overview of the ALCYONE application, showing tools and models shared between different scale schemes.

1. Introduction

ALCYONE is the new CEA multi-scale application dedicated to the study of fuels rods under PWR conditions, built using the PLEIADES platform resources [1]. In the same way, the current EDF industrial code named CYRANO3 [2] has been reorganized in a new architectural design to join the PLEIADES platform and then progresses within the ALCYONE modeling environment. To carry out studies on fuel behavior, a general three dimensional modeling of the thermo-mechanical problem is obviously the best way to recreate the most accurate modeling. Nevertheless, as in most physical domains, the three dimensional modeling of an entire rod is costly forbidden even with the increasing power of calculation. Most of the fuel performance studies can be well performed assuming a mono-dimensional representation of the whole rod cut by slices for a low CPU time cost.

Until now, two distinct numerical codes are used by the CEA to perform PWR studies: the overall behavior of the rod is evaluated using the METEOR one-dimensional code [3], whereas the interaction between pellet and cladding is modeled thanks to the TOUTATIS tri-dimensional code [4]. These codes do not focus on the same scale and the same geometry dimension (the whole fuel rod in 1D or the Pellet Clad Interaction in 3D), and a major difference can be found in their implementation language and numerical tools.

As the ALCYONE application has to be an integrated tool to allow multi-scale studies for PWR reactors, it necessary needs to be at least as effective as the existing codes. The application has then been developed inside the PLEIADES platform with the ambitious purpose to aggregate all the potentialities of both codes, and to give the possibility for a user to perform one-, two- and three dimensional multi-scale studies using a common database of physical models and material laws.

2. Thermo-mechanical analysis in relation with fuel rod and cladding discretization

As the temperature, strain and stress distributions in the rod are the main pilots of the dimensional changes of the fuel rods during its irradiation, the fuel element behavior in a fuel performance code is usually and mainly defined by the thermo-mechanical description of the fuel rod and the cladding. Spatial discretizations of the fuel element and associated restrictive assumptions like generalized plane strain or axisymmetry must be performed in a way to obtain sufficient accuracy for a given problem without being discriminating with regards to the CPU time cost. Most of the fuel performance studies can be well performed assuming a mono-dimensional representation of the whole rod cut by slices for a low CPU time cost, but a local three dimensional description reduced to the representation of a particular pellet in its cladding is required to treat the tri-axial problem of the Stress Corrosion Cracking by Pellet Cladding Interaction.

2.1 Mono-dimensional representation of the whole rod

The mono-dimensional representation is inspired by the previous 1D METEOR fuel performance code in which the fuel element is represented as a series of axial regions (slices on which a loop is performed at each discretization time) for which an axisymmetric, isotropic and 'generalized' plane strain analysis is performed. The basic assumption of this approach is that there is no significant axial variation of external loadings along a slice. This representation of the fuel rod has been enriched by a fuel cracking modeling, the so called MEFISTO model [5], in order to relief the stresses through the crack propagation: it allows to equilibrate the stresses in the direction perpendicular to a crack with the internal rod pressure, as well as modeling the fact that a cracked pellet expands more than a monolithic cylinder under a temperature gradient

Even if the 1D discretization is often sufficient to model the mechanical behavior of the fuel rod, it restrains by construction the modeling to the behavior of the medium pellet plane. In particular, it does not model kinematical effects such as hour-glassing in the pellet induced by radial thermal gradient, primary and secondary ridges appearing in the cladding as well as the evolution of the dishing filling and its capabilities to accommodate fuel creep and fission gas swelling.

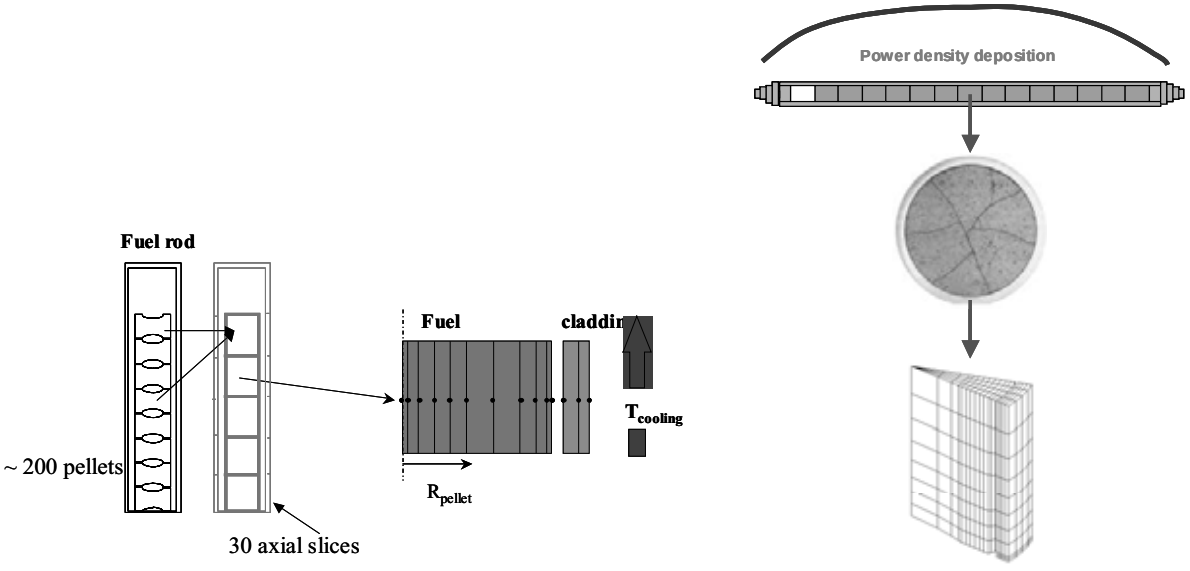

Fig 1. Idealized 1D view of a fuel rod and 3D view of the pellet/clad system

2.2 Three-dimensional representation of the pellet/clad system

For several years, a three dimensional thermo-mechanical description of a pellet/clad system has been investigated using the TOUTATIS program based on the Finite Element Code CAST3M. Such a

refined description of the fuel is proposed to study the local effects of a fractured pellet on the cladding. It is of great interest for Stress Corrosion Cracking (SCC) by Pellet Cladding mechanical Interaction. Indeed, it is assumed that the high tensile stresses located between two fragments at the inter-pellet plane combined with a chemically aggressive environment is responsible for the rupture by PCI/SCC.
In this type of representation, the fuel pellet is assumed to be pre-fractured into equal fragments (typically eight fragments) by radial cracks extending to the fuel central line (see figure 1). This hypothesis is acceptable since fuel fracture occurs at early stage of irradiation when thermal and irradiation enhanced phenomena have not yet occurred. One could argue that an axial fragmentation is also detected but an extended study has concluded that this fragmentation had low effects on the mechanical behavior.

2.3 Intermediate two-dimensional approaches

The 1D ALCYONE application can be extended in the same way to a 2D one. Such a new approach provides further modeling elements in comparison with a 1D application with a low cost of development. Replacing the 1D mesh by a 2D one in the modeling of a slice of the rod, which can be still seen as an average pellet description, allows to take into account dishings and different status between median and inter pellet planes with a 2Drz approach, or introduces an explicit fracturation of pellet with a 2Drθ. This is of importance to obtain a better accuracy in stress fields and PCI evolution.

3. Physical models and thermo-mechanical modules description

The sequence of physical models, thermal and mechanical modules into the time-dependent and thermo-mechanical convergence loop is described in figure 2. Only two physical models are called implicitly in the convergence loop: the URGAP model, which evaluates a global exchange coefficient between the pellet and the cladding due to radiation, conduction in the gas and eventually by direct contact when the pellet-cladding interaction has been activated; and a model which calculates the fission gas production and its distribution inter or intra grains, as well as the gaseous porosity variation.

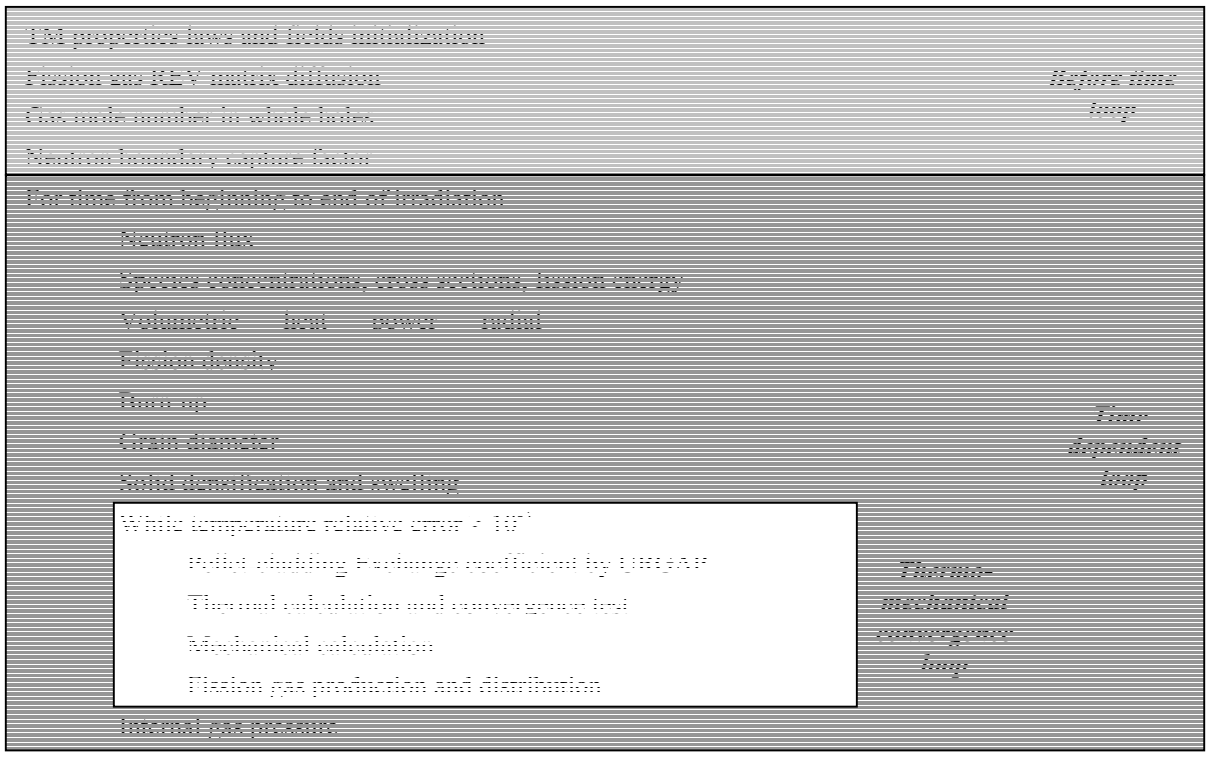

Fig 2. Sequence of physical models and thermo-mechanical modules inside ALCYONE application

The URGAP model is associated with the thermal and the mechanical modules. The thermal module resolves a steady state diffusion of temperature in the pellet and the cladding; thermal loading is due to volumetric heat power inside pellet, with particular radial distribution. The boundary conditions traduce a fixed external cladding temperature and heat exchange between pellet and cladding. Concerning the mechanical module, the mechanical loading described in figure 3 is completed by a thermal one linked to the dilation of the pellet, and by imposed strains due to the solid swelling-densification and gaseous swelling.
Before the time-dependent loop, a set of models initialize all the fields and material laws which will be used during the time loop, as well as some time independent variables, i.e. the fission gas diffusion matrix in a representative elementary volume, the gas mole number in the whole holes (gap, chamfer and dishing) and the neutron boundary capture factor. All the others models are called explicitly in the time loop, and deals with the evaluation of the neutron flux, species concentrations, cross sections, fission energy, burn-up, volumetric heat power, densification and swelling of solid and gas, and finally, the internal gas pressure after the thermo-mechanical convergence loop.

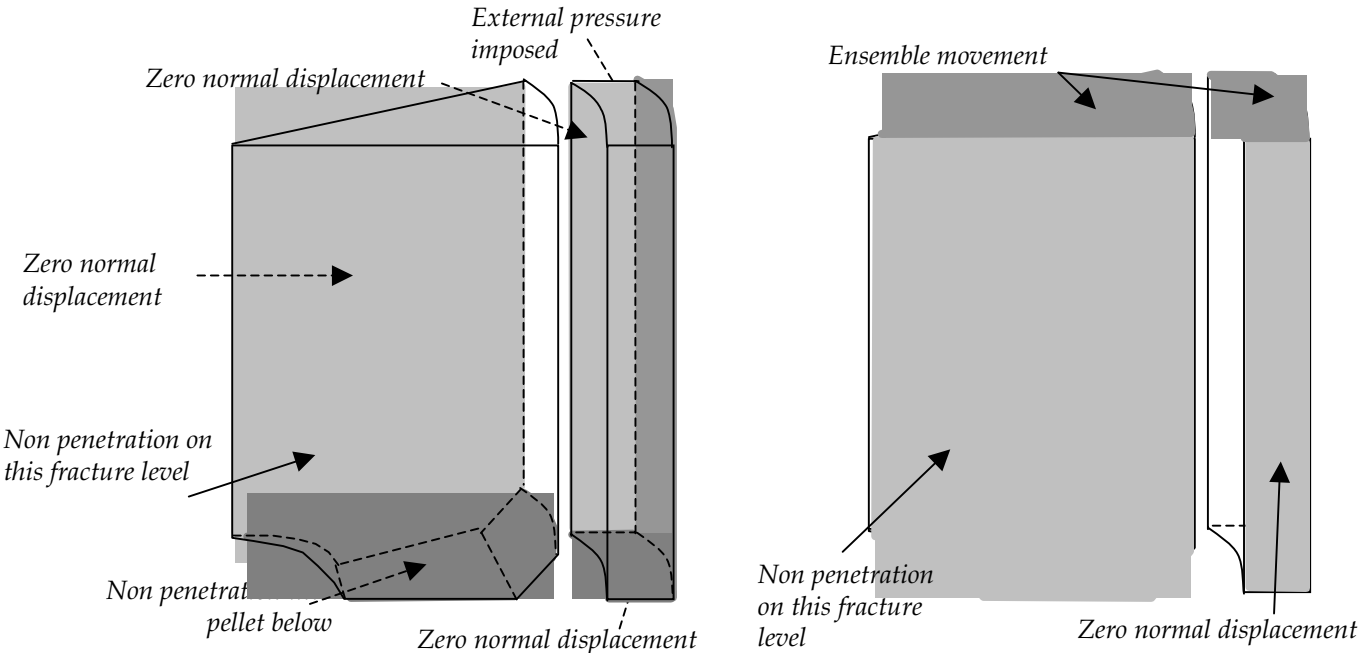

Fig 3. Mechanical boundary conditions in 3D case

4. An example of modeling for the 5108-I04 rod

The input data relative to a fuel rod irradiation are extracted from the CRACO database thanks to an GUI tool which allows to easily create a complete data file. The selection of a rod leads to the creation of a set of new toolboxes grouping all the characteristics of the fuel rod, the pellet and the cladding, as well as the irradiation history and all the options the user chose through the GUI tool.

The output of the calculations have to preview as good as possible the experimental measurements. A useful criterion is the outer cladding radius which can be measured after irradiation and the shape of the evolution of this radius along the cylindrical axis, with its primary and secondary ridges, is very characteristic. And the prediction of ALCYONE is quite good as shown in figure 4, since a good agreement of the ridges shape has been obtained, as well as a their range.

In addition to classical time-dependent evolutions, ALCYONE allows to post-process output data as 3D-fields on the actual deformed mesh for a given time.

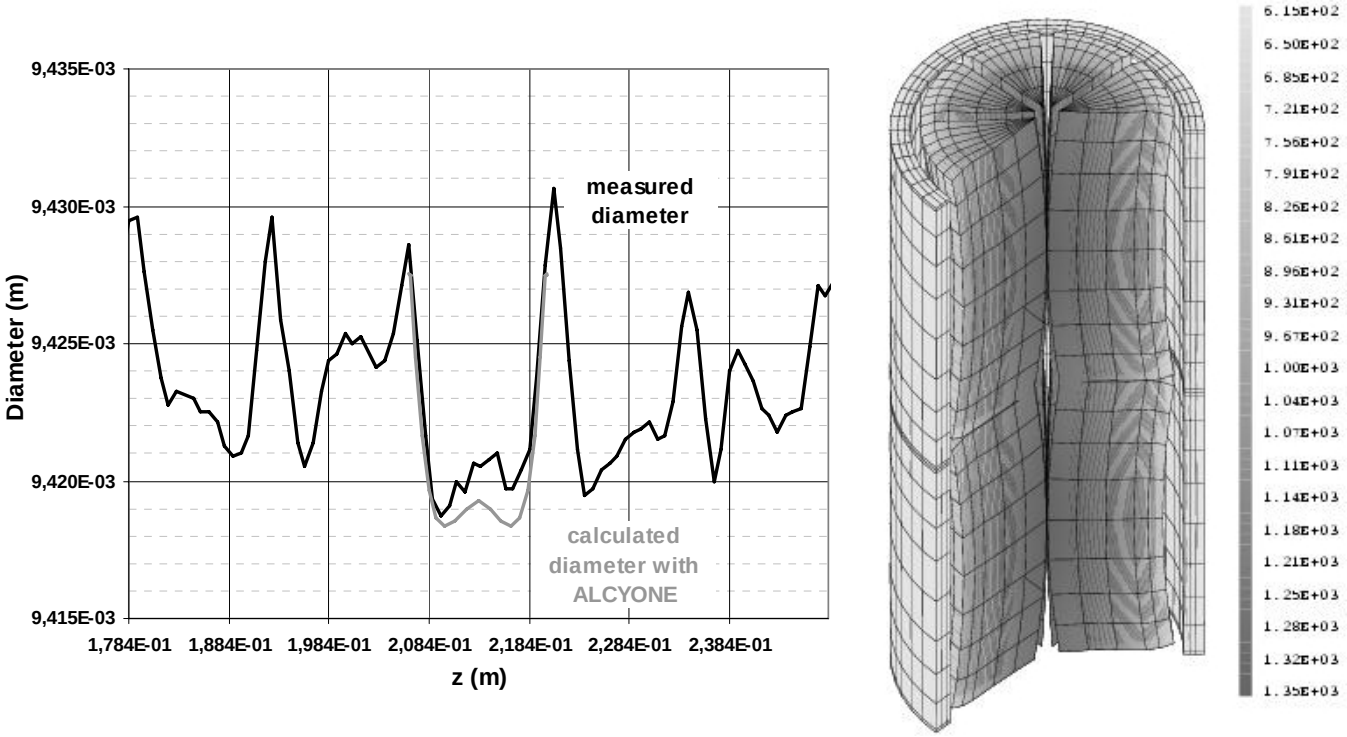

Fig 4. a) Comparison between calculated and measured outer cladding radius. B) 3D view of temperature (in K) on deformed mesh of two pellet/clad systems piled up.

5. Conclusion

The ALCYONE application tends today to reach its first goal, namely to be at least as effective as both existing codes, METEOR and TOUTATIS, and to allow one-, two- and three dimensional multi-scale studies using a common database of physical models and material laws. The validation is being performed from validation database of each codes.

The second goal, which is definitely more ambitious, is to do better than existing codes. In this way, a quite sophisticated transient swelling gas model only validated on 1D modeling with METEOR has been introduced in ALCYONE. This model has been first validated in comparison with METEOR on similar 1D modeling, then extended and used for 3D studies. Furthermore, another interesting way of development is investigated to represent the whole fuel rod always cut by slices but modeled with 2D meshes. This approach would not be much more expensive in computing times and should allow to combine pellet/clad local effects and whole fuel rod studies.

References

[1] D. Plancq et al. PLEIADES : A unified environment for multi-dimensional fuel performance modelling, proceedings of the International meeting on LWR Fuel Performance, Orlando (2004).

[2] R. Masson et al. CYRANO3 : the industrial PLEIADES fuel performance code dedicated to advanced fuel products studies for EDF PWR, TopFuel2006, Salamanca (2006).

[3] P. Garcia, C. Struzik & M. Moyne. Modelling the Steady State and Transient Mechanical Behaviour of Fuel Rods, SMIRT 14 Conference proceedings, Lyon (1997).

[4] F. Bentejac & N. Hourdequin. Toutatis: An application of the Caste3M Finite Element Code for PCI Three-dimensional Modelling, Pellet-Clad Interaction in Water Reactor Fuels Conference proceedings, Aix-En-Provence (2004).

[5] P. Garcia et al. Mono-dimensional mechanical modelling of fuel rods under normal and off-normal operating conditions, Nuclear Engineering and Design, 216, 183-201 (2002).

1 D NEUTRONIC MODEL IN THE FREQUENCY DOMAIN AND ITS COUPLING TO THE STABILITY CODE LAPUR

J.L.Muñoz-Cobo, C.García, A.Escrivá
Departmento de Ingeniería Química y Nuclear
Polytechnic University of Valencia
Camino de Vera 14 Valencia 46022 (Spain)
email: jlcobos@iqn.upv.es, aescriva@iqn.upv.es

José Melara
Iberdrola Ingeniería y Construcción
José Bardasano Baos 9, Madrid 28016 (Spain)

ABSTRACT

The version 5.2 of LAPUR uses a table of point kinetics density reactivity coefficients tabulated as function of the relative water density to compute the feedback reactivity.
The way in which 1D kinetics is used in the new version of the LAPUR-6 code proceed as follows: for each unit perturbation of inlet mass flow rate, power or inlet sub-cooling temperature the code solves the conservation equations of mass, energy and momentum in the frequency domain and computes the void fraction, and the coolant temperature distribution. Once we know the new values of the perturbed void fractions we compute the new cross section values at the axial nodes, and we solve the 1D eigenvalue equation obtaining the fast and thermal fluxes along the axial nodes. After that step we are able to obtain the reactivity changes produced by these perturbations using the expression of the reactivity variation in terms of the cross section variations and the fluxes. The new version provides more consistent values of the DR and the oscillation frequency.

1. Introduction

Reactor stability codes in the frequency domain, like LAPUR 5, NUFREQ [1, 2, 3], solve the linearized equations of mass, energy and momentum of both phases in the frequency domain. Usually these codes use point kinetics to compute the reactivity to power transfer function. These codes can perform predictions of the reactor stability parameters like the global decay ratio and the oscillation frequency. Some of these codes, as LAPUR, incorporate also the reactivity to power transfer function of the first sub-critical mode and are able to predict the decay ratio of the reactor for out of phase oscillations.

Recently, the LAPUR code has been upgraded for the new fuel type designs [4]. The main improvements performed in the code are the following ones: i) the geometry of the channels simulated by the code has been changed from constant area to variable area, in order to simulate more precisely the partial length fuel rods; ii) the local losses due to the spacers have also been incorporated; iii) the irreversible pressure drops produced by the area changes have been incorporated; iv) also the code has the possibility to simulate contractions if necessary along the channels; v) finally 1D kinetics has been added to the code. In addition to these improvements the new version of the code incorporates a more precise description of the recirculation loop. These previous changes have been performed in the steady state equations and in the linearized frequency domain conservation equations.

This paper deals with the development of a 1D kinetics model and its connection to the LAPUR code. To understand the way in which the 1D kinetics has been implemented into the LAPUR code we first explain the way in which the point kinetics is implemented in LAPUR 5.2, then we explain the development of the 1D kinetics and its coupling with the LAPUR code. Finally we discuss the results of LAPUR using point kinetics and 1D kinetics and the main conclusions of the paper.

2. Comparison between the reactivity calculation using point kinetics and 1D kinetics in LAPUR

2.1 The reactivity calculation and the block diagram of LAPUR 5

In LAPUR 5.2 the calculation of the flow to density reactivity feedback coefficient e_{ix} at a specified channel type (ix), is computed in the FREQ subroutine performing a unit perturbation of normalized flow $\delta\bar{y}_{in}$ at the channel inlet, while the power and the inlet subcooling temperature perturbations are set to zero:

$$e_{ix} = \left[\delta\bar{\rho}_{fb}^{ix}\right]_{\substack{\delta\bar{y}_{in}=1 \\ \delta\bar{q}=0 \\ \delta T_{in}=0}} \tag{1}$$

where e_{ix} gives the feedback reactivity change $\delta\bar{\rho}_{fb}^{ix}$ that it is produced when a unit perturbation of normalized flow $\delta\bar{y}_{in}$ is performed in the flow entering to the ix-channel. The LAPUR 5 code solves the linearized and discretized mass, energy and momentum equations in the frequency domain and computes the void fraction perturbations $\delta\bar{\alpha}_{ix}(i)$ and also the liquid enthalpy perturbations in the nodes of the channel ix. Finally it also solves the heat conduction equations in the frequency domain to compute the perturbations in the fuel temperature. Then the transfer function e_{ix} is computed in the FREQ subroutine by means of the following expression:

$$e_{ix} = \sum_{i=1}^{NN}\left(\frac{\partial\rho_{fb}}{\partial\rho'_{dens}}\right)_i W_i \left[\delta\bar{\rho}'_{dens,i}\right]_{\substack{\delta\bar{y}_{in}=1 \\ \delta\bar{q}=0 \\ \delta T_{in}=0}} \tag{2}$$

where $\left(\frac{\partial\rho_{fb}}{\partial\rho'_{dens}}\right)_i$ is the density reactivity coefficient for the i-th channel node. The value of this coefficient for the i-th node in LAPUR 5 is obtained from a set of tabulated density reactivity coefficients in terms of the average relative water density $\left(\rho'_{dens}/\rho'_f\right)_{a,i}$, the way to obtain these coefficients have been explained in Muñoz-Cobo et al. [5]. W_i is the reactivity weighting factor that depends on the square of the power distribution, and is given by:

$$W_i = \frac{P_i^2}{\sum_{i=1}^{NN} P_i^2} \tag{3}$$

where P_i is the power in the i-th node, and the summation runs over all the NN thermal-hydraulic axial nodes of the channel. Finally $\left[\delta\bar{\rho}'_{dens,i}\right]_{\substack{\delta\bar{y}_{in}=1 \\ \delta\bar{q}=0,\delta\bar{T}_{in}=0}}$ is the density variation in the i-th node of the ix channel produced by the unit flow perturbation $\delta\bar{y}_{ix}$. For the nodes belonging to the subcooled-boiling region, the average density variation in the i-th node is given by:

$$\delta\bar{\rho}'_{dens,ai} = \left(\frac{\partial\rho'_l}{\partial H}\right)_i (1-\delta\bar{\alpha}_{a,i})\delta\bar{H}_{a,i} + (\rho'_s - \rho'_f)_{ai}\,\delta\bar{\alpha}_{a,i} \tag{4}$$

where ρ'_s and ρ'_f are the densities of the steam and saturated liquid respectively, the subindex a refers to the average value of a physical magnitude in the i-th node; $\delta\bar{H}_{a,i}$ is the liquid enthalpy variation produced in the i-th node by the unit flow perturbation. In the bulk boiling region we set $\delta\bar{H}_{a,i} = 0$, in equation (4), while in the nodes of the non-boiling region we have only variations in the liquid enthalpy.

The calculation of the power to density reactivity feedback coefficient f_{ix} at a specified channel type (ix), is computed also in the TRANS subroutine performing a unit power perturbation $\delta\bar{q}$:

$$f_{ix} = \left[\delta\bar{\rho}_{fb}^{ix}\right]_{\substack{\delta\bar{y}_{in}=0 \\ \delta\bar{q}=1 \\ \delta\bar{T}_{in}=0}} \tag{5}$$

where f_{ix} gives the feedback reactivity change $\delta\bar{\rho}_{fb}^{ix}$ that it is produced when a unit perturbation of normalized power $\delta\bar{q}$ is performed in the fuel power of the ix-channel. The LAPUR 5 code solves the linearized mass, energy and momentum equations of that channel in the frequency domain and computes the void fraction perturbations $\delta\bar{\alpha}_{ix}(i)$, and the liquid enthalpy perturbations $\delta\bar{H}_{a,i}$ in the nodes of the channel ix, produced by the power perturbation, it also solves the heat conduction equations in the frequency domain to compute the perturbations in the fuel temperatures. Then, the transfer function f_{ix} is computed in the FREQ subroutine by means of the following expression:

$$f_{ix} = \sum_{i=1}^{NN}\left(\frac{\partial\rho_{fb}}{\partial\bar{\rho}'_{dens}}\right)_i W_i \left[\delta\bar{\rho}'_{dens,i}\right]_{\substack{\delta\bar{y}_{in}=0 \\ \delta\bar{q}=1 \\ \delta\bar{T}_{in}=0}} \tag{6}$$

The calculation of the inlet temperature to density reactivity feedback coefficient h_{ix} at a specified channel type ix, is also performed in the FREQ subroutine. To obtain h_{ix} we perform a unitary perturbation in the inlet temperature of the subcooled liquid entering to one channel of the ix type. Then the program solves the linearized mass, energy and momentum conservation equations in the frequency domain and obtains for each channel node the perturbations in the flow, void fraction and liquid enthalpy, i.e. $\delta\bar{y}_{a,i}$, $\delta\bar{\alpha}_{a,i}$, $\delta\bar{H}_{a,i}$, produced by this particular perturbation. Finally, this feedback coefficient is also computed in the FREQ subroutine by means of the following expression:

$$h_{ix} = \sum_{i=1}^{NN}\left(\frac{\partial\rho_{fb}}{\partial\bar{\rho}'_{dens}}\right)_i W_i \left[\delta\bar{\rho}'_{dens,i}\right]_{\substack{\delta\bar{y}_{in}=0 \\ \delta\bar{q}=0 \\ \delta\bar{T}_{in}=1}} \tag{7}$$

The density reactivity change $\delta\bar{\rho}_{dens,fb}$ in the entire reactor core produced by the set of perturbations $\delta\bar{y}_{in}(ix)$, $\delta\bar{T}_{in}$ and $\delta\bar{q}$, performed in the reactor channels, can be recasted in terms of the density reactivity feedback coefficients as follows:

$$\delta\bar{\rho}_{dens,fb} = \sum_{ix} e_{ix}\, N_{ch}(ix)\,\delta\bar{y}_{in}(ix) + \sum_{ix} f_{ix}\, N_{ch}(ix)\,\delta\bar{q} + \sum_{ix} h_{ix}\, N_{ch}(ix)\,\delta\bar{T}_{in} \tag{8}$$

where $N_{ch}(ix)$ is the number of channels of the ix-type, and we have assumed perfect mixing of the fluid in the lower plenum i.e. $\delta\bar{T}_{in}(ix) = \delta\bar{T}_{in}$.

From the linearized momentum equation in the frequency domain we can relate, according to Otaduy [1], the normalized pressure perturbations $\delta\bar{\pi}_{in}$, $\delta\bar{\pi}_{ex}$ in the lower and upper plena respectively, with the total inlet flow perturbation $\delta\bar{Y}$ to the reactor core, the inlet flow temperature perturbation $\delta\bar{T}_{in}$, and the power perturbation $\delta\bar{q}$. This relation is given by the following equation [1]:

$$\delta\bar{\pi}_{in} - \delta\bar{\pi}_{ex} = Z_Y\ \delta\bar{Y} + Z_Q\,\delta\bar{q} + Z_T\,\delta\bar{T}_{in} \tag{9}$$

where Z_Y, Z_Q and Z_T are the flow, power and temperature impedances respectively.

The total inlet flow perturbation $\delta\bar{Y}$ can be related to the inlet flow perturbations $\delta\bar{y}_{in}(ix)$ to the reactor channels by means of the following obvious equation:

$$\delta\bar{Y} = \sum_{ix} g_{ix}\, N_{ch}(ix)\ \delta\bar{y}_{in}(ix) \tag{10}$$

where g_{ix} is the fraction of the total flow which goes through one particular channel belonging to the ix-type.

The recirculation loop transfer function, denoted by R_{clp}, is defined as the normalized differential pressure to total inlet flow transfer function. If we have an external perturbation $\delta\bar{Y}_{ex}$ to the flow, see figure 1, we can write on account of this definition the following expression for the total inlet flow perturbation:

$$\delta\bar{Y} = R_{clp}\,(\,\delta\pi_{in} - \delta\pi_{ex}\,) + \delta\bar{Y}_{ex} \tag{11}$$

where the recirculation loop transfer function it is expressed in term of the recirculation loop constants. The simplest model of the recirculation loop express this transfer function in term of two loop constants which are the gain G_{clp} and the time constant τ_{clp} of the loop:

$$R_{clp} = \frac{G_{clp}}{1 + \tau_{clp} s} \tag{12}$$

Combining equations (9) and (11), it is deduced after some algebra the following expression for the total inlet flow perturbation to the reactor core:

$$\delta\bar{Y} = \frac{R_{clp}\, Z_Q}{1 - Z_Y\, R_{clp}}\,\delta\bar{q} + \frac{R_{clp}\, Z_T}{1 - Z_Y\, R_{clp}}\,\delta\bar{T}_{in} + \frac{1}{1 - Z_Y\, R_{clp}}\,\delta\bar{Y}_{ex} \tag{13}$$

Next we define the pressure to flow transfer function in the non-boiling region for the ix-channel type, as follows:

$$a_{ix} = \left(\frac{\partial\bar{y}}{\partial\bar{\pi}_{nb}}\right)_{ix} \tag{14}$$

that can be obtained integrating the linearized momentum equation in the non-boiling region from the entrance to the channel to the boiling inception point z_1, where begins the subcooled boiling. Therefore we can write down that the flow perturbation at the channel inlet is related to the difference between the inlet pressure perturbation $\delta\bar{\pi}_{in}(ix)$ to the channel and the pressure perturbation $\delta\bar{\pi}_{z1}(ix)$ at the inception point by:

$$\delta\bar{y}_{in}(ix) = a_{ix}\,\left(\delta\bar{\pi}_{in} - \delta\bar{\pi}_{z1}(ix)\right) \tag{15}$$

where we have assumed that the pressure field is uniform at the channel's entrance and therefore $\delta\bar{\pi}_{in}(ix) = \delta\bar{\pi}_{in}$.

Next we define the following transfer functions: i) inlet flow to pressure at the inception point transfer function denoted by *b(ix)*; ii) power to pressure at the inception point transfer function denoted by *c(ix)*; iii) inlet temperature to pressure at the inception point transfer function denoted by *d(ix)*. These transfer functions can be obtained by solving the linearized and discretized mass, energy and momentum equations in the frequency domain when unit perturbations of flow, power and fluid temperature are performed:

$$b(ix) = \left(\frac{\partial\bar{\pi}_{z1}}{\partial\bar{y}}\right)_{ix} = \left[\delta\bar{\pi}_{z1}\right]^{(ix)}_{\delta\bar{y}=1,\delta\bar{q}=0,\delta\bar{T}_{in}=0} \tag{16}$$

$$c(ix) = \left(\frac{\partial\bar{\pi}_{z1}}{\partial\bar{q}}\right)_{ix} = \left[\delta\bar{\pi}_{z1}\right]^{(ix)}_{\delta\bar{y}=0,\delta\bar{q}=1,\delta\bar{T}_{in}=0} \tag{17}$$

$$d(ix) = \left(\frac{\partial\bar{\pi}_{z1}}{\partial\bar{T}_{in}}\right)_{ix} = \left[\delta\bar{\pi}_{z1}\right]^{(ix)}_{\delta\bar{y}=0,\delta\bar{q}=0,\delta\bar{T}_{in}=1} \tag{18}$$

Therefore the pressure perturbation at the boiling inception point can be recasted in term of these transfer functions as follows:

$$\delta\bar{\pi}_{z1}(ix) = b(ix)\,\delta\bar{y}_{in}(ix) + c(ix)\,\delta\bar{q} + d(ix)\,\delta\bar{T}_{in} \tag{19}$$

To obtain equation (19) we have assumed a perfect mixing of the fluid at the lower plenum of the reactor core, i.e $\delta\bar{T}_{in}(ix) = \delta\bar{T}_{in}$.

The next step is to eliminate the pressure perturbations $\delta\bar{\pi}_{z1}(ix)$ and $\delta\bar{\pi}_{in}(ix)$, with the help of equations (9), (10), (15) and (19), in order to relate the inlet flow perturbation $\delta\bar{y}_{in}(ix)$ to a particular

channel with the total flow perturbation $\delta\bar{Y}$ to the core, the power perturbation $\delta\bar{q}$, and the inlet temperature perturbation $\delta\bar{T}_{in}$. After some algebra it is obtained the following result:

$$\delta\bar{y}_{in}(ix) = L(ix)\,\delta\bar{Y} + M(ix)\,\delta\bar{q} + N(ix)\delta\bar{T}_{in} \tag{20}$$

where the channel dependent coefficients L(ix), M(ix), and N(ix) are given by :

$$L(ix) = \frac{a(ix)}{1 + a(ix)b(ix)}\ Z_Y \tag{21}$$

$$M(ix) = \frac{a(ix)}{1 + a(ix)b(ix)}\ \left(Z_Q - c(ix)\right) \tag{22}$$

$$N(ix) = \frac{a(ix)}{1 + a(ix)b(ix)}\ \left(Z_T - d(ix)\right) \tag{23}$$

Direct substitution of equation (20) for the inlet flow perturbation into equation (8) for the density feedback reactivity yields the following result:

$$\begin{aligned}\delta\bar{\rho}_{dens,fb} &= \left\{\sum_{ix} e_{ix}\, N_{ch}(ix) L(ix)\right\}\delta\bar{Y} + \left\{\sum_{ix} N_{ch}(ix)\left(e_{ix} M(ix) + f_{ix}\right)\right\}\delta\bar{q} + \left\{\sum_{ix} N_{ch}(ix)\left(e_{ix} N(ix) + h_{ix}\right)\right\}\delta\bar{T}_{in} \\ &= R_{\rho'}\,\delta\bar{Y} + Q_{\rho'}\,\delta\bar{q} + S_{\rho'}\,\delta\bar{T}_{in}\end{aligned} \tag{24}$$

The expressions inside the curly brackets define the following transfer functions: $R_{\rho'}$ is the core total flow to density reactivity transfer function; $Q_{\rho'}$ is the power to density reactivity transfer function; and finally $S_{\rho'}$ is the inlet temperature to density reactivity transfer function.

The perturbations in the flow to the channels, the power, and the inlet subcooling temperature also provoke changes in the fuel temperature and therefore in the feedback reactivity. This fuel temperature feedback reactivity is known as the Doppler feedback reactivity. Proceeding with the same steps that for the density feedback reactivity, it is obtained the following expression:

$$\begin{aligned}\delta\bar{\rho}_{D,fb} &= \left\{\sum_{ix} d_y(ix) N_{ch}(ix) L(ix)\right\}\delta\bar{Y} + \left\{\sum_{ix} N_{ch}(ix)\left(d_y(ix) M(ix) + d_q(ix)\right)\right\}\delta\bar{q} + \\ &+ \left\{\sum_{ix} N_{ch}(ix)\left(d_y(ix) N(ix) + d_{T_{in}}(ix)\right)\right\}\delta\bar{T}_{in} = R_D\,\delta\bar{Y} + Q_D\,\delta\bar{q} + S_D\,\delta\bar{T}_{in}\end{aligned} \tag{25}$$

where $d_y(ix)$ is the channel flow to Doppler feedback reactivity transfer function for a single channel of type ix, $d_q(ix)$ is the power to Doppler feedback reactivity transfer function for a single channel of type ix, and $d_{T_{in}}$ is the inlet temperature to Doppler reactivity transfer function for a single channel of type ix. Finally the frequency dependent parameters R_D, Q_D, and S_D, define the total flow to Doppler reactivity transfer function, the power to Doppler reactivity transfer function and inlet temperature to Doppler reactivity transfer function respectively.

Finally the total feedback reactivity perturbation will be given by the addition of the density and the Doppler contributions so we will write down the following expression for the total feedback reactivity perturbation:

$$\begin{aligned}\delta\bar{\rho}_{fb} &= \delta\bar{\rho}_{dens,fb} + \delta\bar{\rho}_{D,fb} = (R_{\rho'} + R_D)\,\delta\bar{Y} + (Q_{\rho'} + Q_D)\delta\bar{q} + (S_{\rho'} + S_D)\delta\bar{T}_{in} \\ &= R\ \ \delta\bar{Y} + Q\ \ \delta\bar{q} + S\,\delta\bar{T}_{in}\end{aligned} \tag{26}$$

Figure (1) displays the block diagram of LAPUR 5 transfer functions where G is the open-loop transfer function for neutron kinetics i.e the total feedback reactivity to normalized power transfer function given by the standard expression:

$$G = \frac{\delta \bar{n}(s)}{\delta \bar{\rho}_{fb}(s)} = \frac{1}{s\left(\Lambda + \sum_{j=1}^{6} \frac{\beta_j}{\lambda_j + s}\right)} \tag{27}$$

where Λ is the neutron mean generation time.

Next we explain how is computed the feedback transfer function H of the block diagram displayed in figure (1), and given in simplified form in figure (2). First, we substitute equation (13) into equation (26), for the feedback reactivity, after some rearrangements it is obtained the following result

$$\delta \bar{\rho}_{fb} = \left(Q + \frac{R\ R_{clp}}{1 - Z_Y\ R_{clp}} Z_Q\right)\delta \bar{q} + \left(S + \frac{R\ R_{clp}}{1 - Z_Y\ R_{clp}} Z_T\right)\delta \bar{T}_{in} + \left(\frac{R}{1 - Z_Y\ R_{clp}}\right)\delta \bar{Y}_{ex} \tag{28}$$

From equation (28), it is obtained that the power to reactivity transfer function H is given by:

$$H = Q + \frac{R\,R_{clp}}{1 - Z_Y\ R_{clp}} Z_Q = \left(\frac{\partial \bar{\rho}_{fb}}{\partial \bar{q}}\right) + \left(\frac{\partial \bar{\rho}_{fb}}{\partial \bar{Y}}\right)\left(\frac{\partial \bar{Y}}{\partial \bar{q}}\right) \tag{29}$$

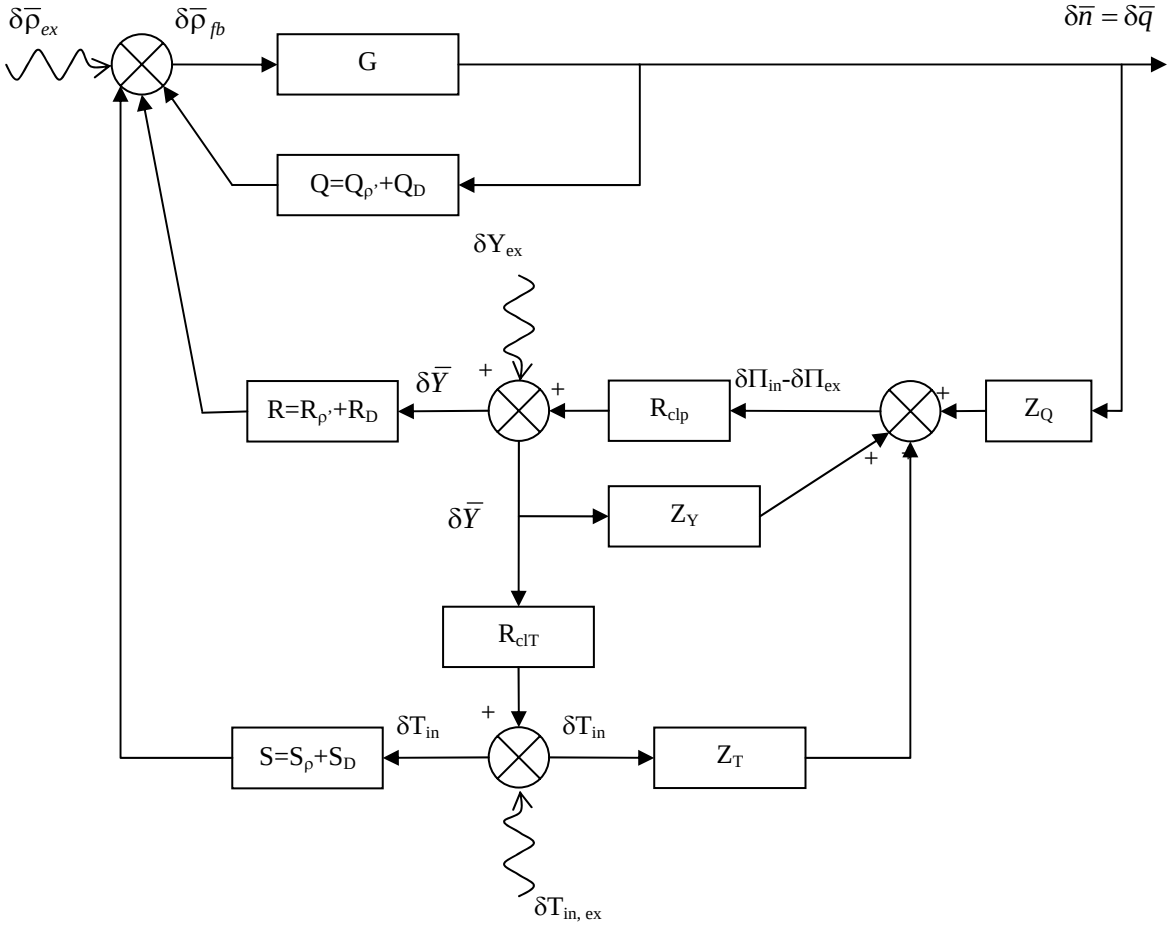

Fig 1. Block diagram of LAPUR5.2 transfer functions. G is the neutron kinetics open loop transfer function. R_{clp} is the core differential pressure to inlet flow transfer function. Q is the power to feedback reactivity transfer function. R is the total flow to feedback reactivity transfer function. S is the inlet temperature to feedback reactivity transfer function.

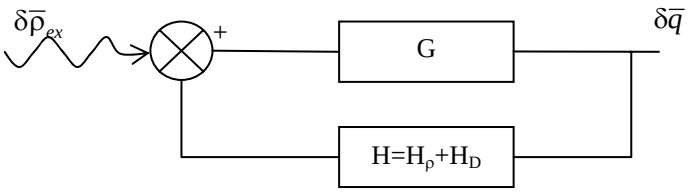

Fig 2. Block diagram of LAPUR 5 transfer functions in compact form.

2.2 The calculation of the density feedback reactivity coefficients in the improved version of LAPUR

The calculation of the flow to density reactivity feedback coefficients at a specific channel ix is performed in the new TRANS subroutine. In this subroutine we calculate the reactivity change due to de following flow perturbation:

$$\delta\bar{y}_{ix} = 1,\ \delta\bar{q} = 0,\ \delta\bar{T}_{in} = 0 \tag{30}$$

Then the flow to density reactivity feedback coefficient e_{ix} is computed by means of expression (1). The calculations at a first stage proceed as in LAPUR 5, i.e. the code calls to the FREQ subroutine where it solves the linearized mass, energy, and momentum equations for this particular type of perturbation, and this particular type of channel, obtaining as an output the void fraction perturbations $\delta\bar{\alpha}_{ix}(i)$ at the nodes of channel ix. Then, from TRANS subroutine the code calls to the new subroutine ONEKIN (One D Kinetics) and computes the cross section changes, produced by the void fraction changes:

$$\delta\Sigma_x^{(ix)}(i) = \Sigma_x\left(\alpha_0^{ix}(i) + \delta\bar{\alpha}_{ix}(i)\right) - \Sigma_x\left(\alpha_0^{ix}\right) \qquad i = 1, NAXN \tag{31}$$

where $\alpha_0^{ix}(i)$ are the void fractions at steady state unperturbed conditions at channel ix, the sub-index x denotes the cross-section type, $\delta\bar{\alpha}_{ix}(i)$ is the void fraction perturbation at the ith-axial node of the channel, and NAXN is the total number of axial nodes.

In subroutine ONEKIN, the following cross section set is computed for the flow perturbed case (*P*):

$$\begin{aligned} &D_1^P(i) \equiv D12(i), && D_2^P(i) \equiv D22(i) \\ &\Sigma_{a1}^P(i) \equiv SIGA\ 12(i), && \Sigma_{a2}^P(i) \equiv SIGA\ 22(i) \\ &\nu\Sigma_{f1}^P(i) \equiv SGNF\ \ 12(i), && \nu\Sigma_{f2}^P(i) \equiv SGNF\ \ 22(i) \\ &\Sigma_{r1}^P(i) \equiv SIGR\ 12(i) \end{aligned} \tag{32}$$

The next step is to compute the reactivity changes produced by the cross-section variations, in the new subroutine REACT. Several approximations can be used to compute the reactivity variation. First we compute the base case, for a given region ix. The program calls the KTRAC subroutine that solves the 1D two groups eigenvalue equation using the analytical nodal method [6], with the cross-section set $\Sigma_x\left(\alpha_0^{(ix)}(i)\right)$, where $\alpha_0^{(ix)}(i)$ is the steady state void fraction axial distribution at region (ix). From KTRAC, we get the eigenvalue $k^{B(ix)}$, and the unperturbed fast and thermal fluxes $\left(\phi_1^{B(ix)}(i), \phi_2^{B(ix)}(i)\right)$, and the fast and thermal adjoint fluxes $\left(\phi_1^{*B(ix)}(i), \phi_2^{*B(ix)}(i)\right)$. To compute the reactivity change produced by a perturbation, the user can select several approximations; in this paper we discuss the simplest one, i.e. first order perturbation theory. In this approximation the reactivity is computed by means of the well known expression:

$$\delta\rho_{ix} = \sum_{i=1}^{NAXN} \delta\rho_{ix}(i) \approx \frac{\sum_{i=1}^{NAXN} \left\{ -\phi_1^{*B}\,\delta D_1\,B_1^{2P}\,\phi_1^{B} - \phi_1^{*B}\,\delta\Sigma_{t,1}\,\phi_1^{B} + \frac{1}{k^B}\phi_1^{*B}\,\delta\nu\Sigma_{f,1}\,\phi_1^{B} - \phi_2^{*B}\,\delta D_2\,B_2^{2P}\,\phi_2^{B} + \frac{1}{k^B}\phi_1^{*B}\,\delta\nu\Sigma_{f,2}\,\phi_2^{B} - \phi_2^{*B}\,\delta\Sigma_{a,2}\,\phi_2^{B} + \phi_2^{*B}\,\delta\Sigma_{r,1}\,\phi_1^{B} \right\}_i^{(ix)}}{\sum_{j=1}^{NAXN} \left(\phi_1^{*B}\,\nu\Sigma_{f,1}{}^{P}\,\phi_1^{B} + \phi_1^{*B}\,\nu\Sigma_{f,2}{}^{P}\,\phi_2^{B} \right)_i^{(ix)}} \tag{33}$$

This approximation will give good results if the perturbations are small because we have neglected the correction to the flux.

The main difference with the previous version of LAPUR to compute e_{ix} is the way to compute the density feedback reactivity perturbation. The LAPUR 5 code use expression (2), that is based in a set of tabulated density reactivity coefficients $\left(\frac{\partial\rho_{fb}}{\partial\rho'_{dens}}\right)_i$. The value of this coefficient for the i-th node in

LAPUR 5 is obtained from a set of tabulated density reactivity coefficients as a function of the average relative water density $\left(\rho'_{dens} \big/ \rho'_{dens,f}\right)_{a,i}$. These coefficients used in LAPUR 5 are frequency independent and are real.

The calculation of the power to density reactivity feedback coefficient f_{ix} at a specified channel type ix, is performed in the new TRANS subroutine. In this subroutine we calculate the density feedback reactivity change due to the following power perturbation:

$$\delta\bar{y}_{ix} = 0,\ \delta\bar{q} = 1,\ \delta\bar{T}_{in} = 0 \qquad (34)$$

The steps followed to compute the density feedback reactivity change produced by this perturbation are the same ones that the ones we have performed to compute e_{ix}. Finally in a similar way we have computed the inlet temperature to density feedback reactivity transfer function $h_{ix.}$ Therefore the only existing difference between LAPUR 5 and LAPUR 6 feedback reactivity calculation is the method used to obtain the coefficients e_{ix}, f_{ix}, h_{ix}. The density feedback reactivity is calculated from the same expression in both codes, i.e. from equation (24) in both codes.

Therefore, e_{ix}, f_{ix}, and h_{ix} are computed by different methods in LAPUR 5 and the revised version of LAPUR. In the new version, the inlet perturbations produce void fraction perturbations along the channels that influence the cross-sections, inducing macroscopic cross-sections changes. From these cross-section changes, the code computes the reactivity changes. The calculation of the Doppler Feedback reactivity has not been changed, due to the negligible impact of this feedback on BWR instabilities.

3. Results, discussion and main conclusions

In order to have an estimation of the reactivity changes versus the frequency computed using point and 1D kinetic respectively, we display in table 1, the reactivity change $\delta\rho_{fb}$ computed using point kinetics and 1D kinetics for different frequencies when a unit perturbation of inlet subcooling temperature is introduced at the entrance of the average channels of a BWR typical nuclear power plant.

Frequency (Hz)	$h_{ix} = \lfloor \delta\rho_{fb} \rfloor_{\delta T_{in}=1}$ point kinetics	$h_{ix} = \lfloor \delta\rho_{fb} \rfloor_{\delta T_{in}=1}$ 1D kinetics
0.01	-2.612E-4+j 3.802E-5	-1.238E-3+j1.741E-4
0.1	-8.876E-5+j 2.099E-4	-4.529E-4+j 9.871E-4
0.5	-2.667E-5-j 4.732E-5	-8.320E-5-j 3.816E-4
1	1.995E-5-j 5.443E-6	2.276E-4+j 7.501E-5
10	1.472E-7+j 2.005E-8	7.387E-7+j 1.400E-6
100	-7.705E-8+j 9.053E-8	-1.847E-7+j 3.154E-7

Tab 1: Reactivity change computed using point kinetics and 1D kinetics when a unit perturbation of inlet sub-cooling temperature is performed at the inlet of the average channels of a BWR reactor.

We observe that the real parts of the reactivity changes $\left[\delta\rho_{fb}\right]_{\delta\bar{T}_{in}=1,\delta\bar{q}=0,\delta\bar{y}_{in}=0}$ diminish at high frequencies for the same perturbation, while the imaginary parts increase starting from zero at very low frequencies up to a maximum and then decrease with the frequency.

To validate the new 1D kinetics model, we have compared the results obtained with the new version of the code denoted as LAPUR 6-1D kinetics with the results of the old version of LAPUR 5, and the experimental data obtained by autoregressive model analysis from the APRM and LPRM neutron detector signals of Cofrentes nuclear power plant. In tables 2 and 3 we display the stability results (Decay Ratio and Frequency), for two cases the 1991 instability event of Cofrentes NPP, and a start up of Cofrentes NPP.

	In-Phase		Out-of-Phase	
	DR	Frequency (Hz)	DR	Frequency(Hz)
Experimental	0.918	0.48		
LAPUR-5	0.86	0.42	1.14	0.41
LAPUR-6-1D	0.99	0.59	1.01	0.51

Tab 2: Case 1, Cofrentes out-of-phase instability event.

	In-Phase		Out-of-Phase	
	DR	Frequency (Hz)	DR	Frequency(Hz)
Experimental	0.44	0.48		
LAPUR-5	0.62	0.35	0.44	0.36
LAPUR-6-1D	0.43	0.55	0.54	0.49

Tab 3: Case 2, Cofrentes start up.

For low values of the decay ratio, case 2, the new version of the LAPUR code predicts better the DR and the oscillation frequency than the older one. The oscillation frequencies of a typical BWR at start–up conditions are very close to 0.5 Hz. The LAPUR 5 code has under-predicted this value for many years, the new version gives according to table 3 values that are closer to the typical oscillation frequency for in-phase and out-of phase oscillations. Concerning the DR at start-up conditions the values predicted by LAPUR 6 for case 2 are closer to the experimental ones than the old version. For the instability event both codes give good predictions of the DR with an error less than 10%.

As conclusion we can say that the estimations of the Decay Ratio and the oscillation frequency with the new version of the LAPUR code seem to be much closer to the experimental one than the old version, there is a clear effect of the 1D kinetics on the real and imaginary parts of the reactivity changes for the different types of perturbations.

Acknowledgments: This research has been performed under the sponsorship of IBERDROLA GENERACIÓN inside the framework of a R&D project called DROP (Decay Ratio On-line Predictor) to develop a predictive stability tool to couple with the BWR Core Monitoring System. The authors are particularly grateful to Manuel Albendea, for the project coordination and support.

5. References

1- Otaduy, P.J. “Modeling of the dynamic behaviour of large boiling water reactor cores”, PH-D Thesis. University of Florida (1979)

2- Escrivá, A., March-Leuba, J.. “LAPUR 5.2 verification and user´s manual”. NUREG/CR-6696, ORNL/TM-2000/340. (2001)

3- Park, G.C., Podowski, M., Becker, M., Lahey, R.T., “The development of NUFREQ-N, an analytical model for the stability analysis of nuclear coupled density-wave oscillations in BWR reactor”. NUREG/CR-3375 (1983)

4-Escrivá, A., Muñoz-Cobo, J.L., Melara, J. “Upgrade of the thermal-hydraulic capabilities of the stability code LAPUR 5, for the new fuel type designs”. NURETH-11. 11 Conference on Nuclear Reactor Thermal-hydraulics, Avignon, France, paper-085, (2005).

5- Muñoz-Cobo, J.L., Escrivá, A., García, C., “Consistent generation and point feedback reactivity parameters for stability and thermal-hydraulic codes”. Annals of Nuclear Energy (2006), doi:10.1016/j.anucene.2006.07.006.

6- Nigg, D.W. “One dimensional neutronic routines for the TRAC-BD1 program”. Report INEL EGG-PBS-6379 (1984).

ANALYSIS OF FRAPCON-3 MODELS RELATED TO HIGH BURNUP FUEL

M.T. DEL BARRIO, I. VALLEJO, L.E. HERRANZ
Unit of Nuclear Safety Research, CIEMAT,
Avda. Complutense, 22. 28040 Madrid - Spain

ABSTRACT

The present trend towards reaching higher fuel burnup requires qualifying fuel performance codes to consistently simulate fuel and clad behaviour under the whole irradiation period. This involves both the introduction of models for new phenomena appearing during long irradiation times and to test others that were developed to deal with shorter irradiations and, as a consequence, have been validated up to lower burnup levels.

This paper reviews some fundamentals of the models encapsulated in the FRAPCON-3 code and, whenever possible, their performance is illustrated through comparison to available data. Two groups of models have been addressed: fission gas release and fuel-to-clad heat transfer. Moreover, an axial gas transport model could be potentially missing.

Regarding FGR, the evaluation highlights that a model not so heavily dependent on fitting parameters would be desirable and a first approach is presented. The review of heat transfer models suggests that the available database should be updated to high burnup in order to can carry out a proper validation. Moreover, the lack of axial fission gas transport in the code could be translated in non-conservative situations. In short, further work is still needed.

1. Introduction

FRAPCON-3 code has been extended to can deal with fuels burnt to 65 GWd/tU under steady-state conditions (1). Because of its importance in fuel performance at high burnup conditions, two groups of models have been addressed: fission gas release (FGR) and fuel-to-clad heat transfer. The evaluation includes an extended database than that used in the code assessment.

The paper is structured in two main sections. The first evaluates the two models assessed: FGR and clad-to-fuel heat transfer models. A simpler approach for FGR is proposed, and has been contrasted to an extended database with regard to that of the code model validation. The fuel-to-clad heat transfer model and the evolution of the thermal resistances in the fuel rod up to high burnup under prototypical irradiation conditions are also presented. Moreover, the solid-solid conductance model has been assessed and compared to that used by others fuel safety codes. The second section evaluates the expected fuel temperature evolution after FGR whether axial gas transport along the longitudinal fuel rod direction is considered or not, to point out the temperatures differences which could be reached.

This work is framed within the CSN-CIEMAT agreement on “Thermo-Mechanical Behaviour of the Nuclear Fuel at High Burnup”.

2. Review of some FRAPCON-3-3 models

2.1 FGR

Fission Gas Release plays an important role in the fuel rod performance at high burnup. Therefore, FGR should be properly estimated by fuel rod codes.

2.1.1 Model fundamentals and shortcomings

The named Massih model is included in FRAPCON-3 to simulate steady state and slow-power ramps. This model is based on the original Forsberg&Massih formulation (2) that considers the diffusion towards grain boundaries, including the resolution process to fuel matrix in the proximities of grain

boundaries. The original model is modified to be implemented in the code with some parameters and alternative correlations to fit with the validation database. Besides, the FGR model considers that the resolved gases are not incorporated to the matrix inventory. So, in FRAPCON-3 the resolved gas is not used for diffusion and only when the saturation condition for release is achieved, both resolved and accumulated gases in grain boundaries are released. In addition, the code does not consider grain growth and a fixed value of 10 μm for grain size is applied.

2.1.2 Outline of a simpler approach

The proposed approach does not consider fitting parameters or burnup dependent correlations. It also includes a new approximation to simulate the resolution of the fission gases and the possibility of gas growth at high temperatures (3). The new resolution approach gives the possibility that resolved grain could return inside the grains increasing the bulk grain concentration when the saturation condition is not reached, instead of FRAPCON-3 approach which does not incorporate the resolved gas to the matrix inventory. Moreover, the initial grain size used corresponds to that of the specific fuel rod analysed.

2.1.3 Comparative assessment

The analysis is mainly performed on the database used for the steady state assessment of the fission gas release model, comprising rods irradiated in test and commercial reactors, with fission gas release values up to 50 %. Fig 1 compares the FRAPCON-3 estimations with the current model and modified approach to the experimental data. As conclusion, when the database is extended the absolute error worsens, because the model fitted to a restricted database. In fact, when all the fitting parameters are removed, the model estimations deviate noticeably from measurements.

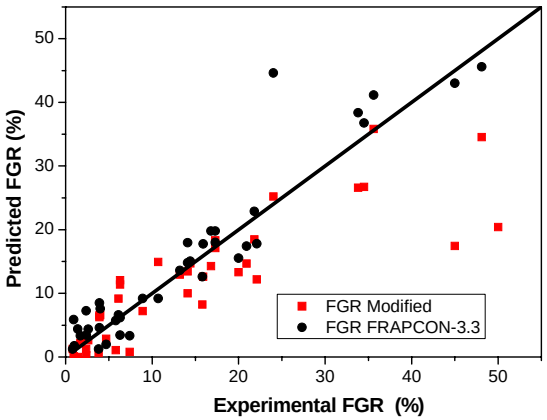

Fig 1. Predicted and Experimental FGR comparison

Commercial Fuel rods usually present FGR lower than 10%. As can be seen in Fig 1, no significant difference for FGR lower than 20% between the code model and the modified one is found and that is only noticeable at values higher than 30%. Such divergence is mainly due to new approach for gas resolution, because decrease significantly the amount of available gases to be released. In short, the modified approach does not provide a better FGR estimation compared to that of the code. However, it must be highlighted that the model modification is less dependent of fitting parameters. A new FGR approach is currently in progress.

2.2 Fuel-to-clad heat transfer

Two topics related to fuel-to-clad heat transfer have been analysed: the burnup evolution of thermal resistances, with special attention to the oxide resistance and, the solid-solid conductance.

2.2.1 Model fundamentals

Fuel temperature is dependent upon linear heat rate generation ($\dot{q}'$), coolant temperature (T_{cool}) and total thermal resistance (R_{tot}) as shown in equation 1.

$$T(r) = -\frac{\dot{q}'}{4\,k_{fuel}\,A_{fuel}}\left(r_{fuel}^2 - r^2\right) + R_{tot}\cdot\dot{q}'\cdot L + T_{cool} \qquad (1)$$

Heat rate generation and coolant temperature are control variables of the reactor, whereas the total thermal resistance, which corresponds to the sum of the individual thermal resistances from the gap to the coolant (equation 2), evolves during irradiation.

$$R_{tot} = R_{gap} + R_{Zry} + R_{oxide} + R_{cool} \qquad (2)$$

2.2.2 Burn-up effect on thermal resistances

The evolution of the thermal resistances in a fuel rod up to near 70 GWd/tU under typical operation conditions were studied in (4). As illustrates Fig 2, it was observed that gap resistance dominates at the beginning of the irradiation (until closure) and becomes again the major contributor at high burnup as a consequence of the significant gap conductivity reduction.

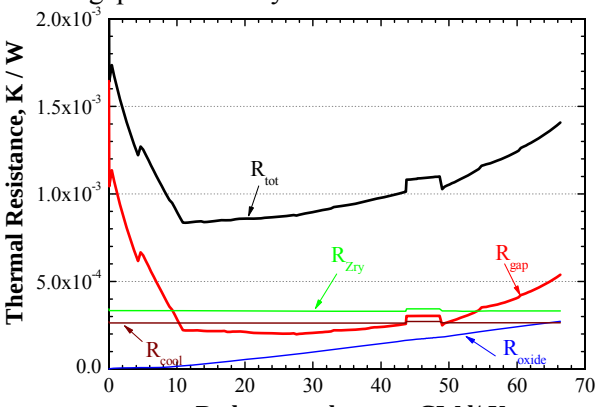

Fig 2. Thermal resistances evolution along irradiation.

In addition, it was also studied conservative assumption of FRAPCON-3 regarding the evolution of the clad thermal resistance when the oxide increases. FRAPCON-3 does not consider that when the metallic layer is oxidised a fraction of the metallic Zr disappears to form ZrO_2. So, FRAPCON-3 code estimates total clad thickness as an addition of two fully independent layers and, as a consequence, it overestimates the clad thickness and then overestimates the total thermal resistance. However, relative differences to FRAPCON-3 approach were estimated to be lower than 1% (4).

2.2.3 Assessment of solid-solid conductance model

The solid-solid conductance (h_{solid}) models used in FRAPCON-3 and other nuclear safety codes have been studied to analyse its capability to deal with high burnup conditions (5). h_{solid} depends on the material properties, the surface topology and the contact pressure. Most of the models encapsulate similar variable dependences.

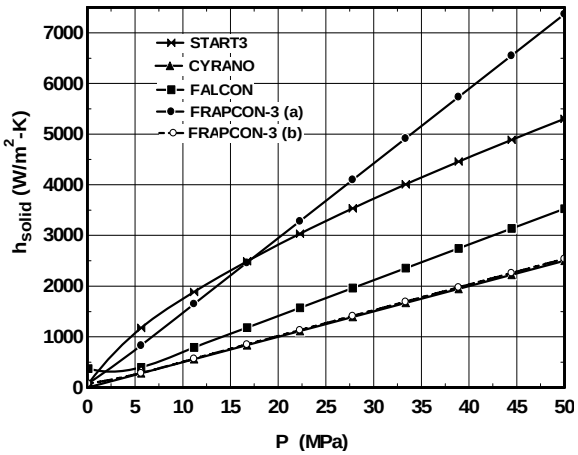

Fig 3. h_{solid} as a function of the interfacial pressure

A comparison of absolute values of h_{solid} shows that the discrepancies between different models, that Fig 3 presents, result from the different dataset used for validation of the correlations. Two different FRAPCON-3 calculations have been included, depending on whether the multiplicative factor used by the model when the ratio of interfacial pressure to cladding Meyer hardness is greater than 0.003, is considered (a) or not (b). As conclusion, in spite of the large scattering and scarcity of data under conditions anticipated at high burnup, the FRAPCON-3 estimations seem to be accurate enough and, anyway, the closest ones to data among all the models assessed.

3. A potential missing model in FRAPCON-3: axial fission gas transport

The thermal conductivity of the released gases is significantly lower than the filling gas. So, the FGR worsens the pellet-cladding heat transfer and the fuel temperature is increased. Moreover, the higher fuel temperature could cause a FGR enhancement through a thermal feedback process.

Two extremes strategies can be considered to model the gas transport in the gap during a rapid FGR. The first and simpler is to assume that the released fission gases are instantaneously mixed with the filling gas. The second supposes that the mixing is so slow, that the gap stays contaminated by only fission gases.

Experimental evidences have shown that the gas mixing is not instantaneous and a certain time is required to achieve the homogeneity of species in the gap. However, the most of the fuel codes, as FRAPCON-3 does, assume that the released gases to the gap are instantaneously mixed. So, that assumption is non-conservative from the safety point of view because significantly underestimates the local fuel temperature, and likely also then, the FGR as consequence of the thermal feedback (6).

Fig 4 shows the centre fuel temperature evolution after a power ramp in a short (experimental) rod (7). The measured fuel temperature increases immediately due to the released gases and gradually decreases about 200^{o}C in the course of 5-8 minutes. So, the gas transport in the gap has a significant impact on the fuel performance, because it determines the time that fuel is exposed to high temperature. The increase in fuel temperature will be more considerable during power ramps, since the amount of fission gas released is greater.

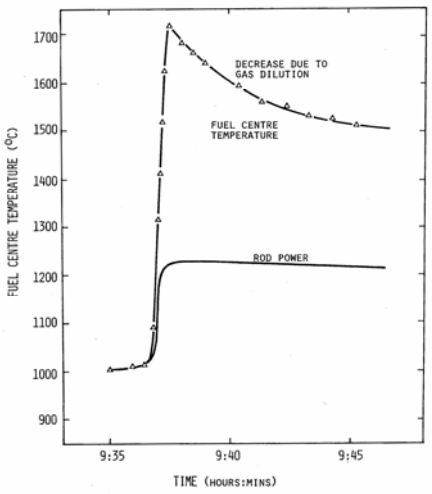

Fig 4. Centre fuel temperature behaviour after a power ramp

The released gases generate gradients of concentration and pressure between the zone of release and the plenum. Both are considered the main driving forces to balance the species in the gap. Experiments on this issue have shown that the transport kinetics is mainly affected by the axial region of release, the initial pressure of the rod, and the fuel activate length. Observations show that the worse situation happens when the gases are released from the fuel bottom, since the whole fuel stack will be affected by the varying gas concentration. The effect of release in pressurised rods will be less important once the balance is obtained, but the difference between the maximum temperature after the release and the equilibrium value will be greater. In addition, when the experimental data with short rod is translated

to commercial fuel rod is necessary to take into account that the diffusion time depends linearly with the square of the diffusion distance. So, whereas the time to dilute the gas to the 50% is about 13 minutes in a 30 cm rodlet, in a full length rod can be about 30 hours (7).

The burnup will also affect the gas transport, since the irradiation process modifies the gap size, the gas composition and the internal pressure. When the gap is open, it would be possible to apply directly the diffusion and convective mechanisms. However, at higher burnup, the amount of gases in the gap will increase and then, the relative poisoning will be less important. On the other hand, the internal pressure will also increase as consequence of the higher amount of gases and the gradual decrease of the gap size. The increase of the pressure results in a slowdown of the diffusion and convective processes. Once the gap is closed, the gas transport will be impeded and likely only the diffusion mechanism could happen, likely through the porous rim zone. An attempt to provide an approach for axial gas mixing, both in open and closed gap conditions, is currently in progress.

The lack of any axial transport of the released gases along the fuel-to-clad gap in the code could drive to inaccuracies in the fuel temperature estimation, and also, in the FGR estimated, because of the induced thermal feedback.

4. Final remarks

Overall, this study supports the FRAPCON-3 code performance up to burnup of 70 GWd/tU. Regarding FGR, the evaluation highlights that a model not so heavily dependent on fitting parameters would be desirable and it outlines initial steps taken in that direction. In addition, a peer review of the solid-solid conductance model suggests that the available database should be updated to high burnup in order to carry out a proper validation. Besides, discussion on axial gas transport could result in an inaccurate gain of FRAPCON-3 predictions under power ramps.

5. References

1. D. D. Lanning, D.D., Beyer, C. E. and Painter, C. L. (1997) “FRAPCON-3: Modifications to Fuel Rod Material Properties and Performance Models for High-Burnup Application” NUREG/CR-6534 PNNL-11513.
2. Forsberg, K. and Massih, A. R. (1985) “Fission Gas Release under time-varying conditions” Journal of Nuclear Materials, 127, 141-145.
3. Vallejo, I., del Barrio, M.T., Herranz, L.E. (2004) “Major Sensitivities of Fission Gas Release Modelling within the FRAPCON-3 Code”. Proceedings of the 2004 International Meeting on LWR Fuel Performance. Orlando, Florida, September 19-22, 2004.
4. Herranz, L.E., Vallejo, I., del Barrio, M.T. (2003) “Analysis of the effect of the FRAPCON-3 approximation regarding cladding thickness change onto fuel-coolant heat transfer under high burnup scenarios”. 10th International Topical Meeting on Nuclear Reactor Thermal Hydraulics (NURETH-10). October 5-9, 2003. Seoul, Korea.
5. Herranz, L.E., Tigeras, A. (2006) “Assessment of models for solid-solid conductance in nuclear fuel performance codes”. International Heat Transfer Conference IHTC-13. 13-18 August, 2006. Sydney. Australia.
6. del Barrio, M.T., Herranz, L.E. (2005) “Distribución axial de gases de fisión a lo largo de una barra combustible”. 31st Annual Meeting of the Spanish Nuclear Society. October, 2005. Logroño, Spain.
7. Vitanza, C., Johnsen, T., Aasgaard, J.M., (1983) “Interdiffusion of Noble Gases. Results of an Experiment to Simulate Dilution of Fission Gases in a Fuel Rod”. HPR-295. OECD Halden Reactor Project.

CONSISTENT MODELLING OF THRESHOLD CONDITIONS FOR BEGINNING OF HBS FORMATION IN HIGH BURNUP UO_2

V.V. LIKHANSKII, V.G. ZBOROVSKII
SRC RF TRINITI, Troitsk, Moscow Reg., 142190, Russia

YU.V. PIMENOV
JSC TVEL, 24/26 Bolshaya Ordynka st., Moscow, 119017, Russia

ABSTRACT

An approach to consistent modelling of dislocations and bubbles for the conditions of rim-structure formation in UO_2 fuel is considered. Point defects fluxes to finite size dislocation loop are calculated and fitted with simple models. Equilibrium interstitial concentration is found as function of loop radius. Formation and evolution of bubbles in large and small grains is considered. Gas bubbles overpressurization is considered as a criterion for onset of HBS formation. The model gives correct dependence of fuel restructuring threshold on grain size.

1. Introduction

In LWR fuel elements at average burnups over 40 MWd/kgU notable structural changes arise in the pellet outer zone [1,2]. Original grains with the size of about 6–10 μm subdivide into submicron grains (0.1-0.3 μm) and fuel porosity in that region grows up to 20%. This process is called restructuring and formed fuel structure is called rim-layer or high burnup structure (HBS). Such microstructure changes affect fuel thermal and mechanical properties. The problem of obtaining criterion that would determine rim-layer formation threshold is of special interest, because it would allow to determine dependence of restructuring start on initial fuel microstructure and irradiation conditions, i.e. temperature, fission rate and grain size.

At most present works concerned with modelling of fuel performance at the conditions of rim-structure formation dislocations parameters such as density and size are considered as external ones and are specified using correlation dependences, for example [2]. However, such approach does not suit well for consistent modelling which would establish the criterion for onset of HBS formation for fuels with various initial microstructure parameters and irradiation history. Therefore consistent modelling of dislocation kinetics is necessary. In the present work modelling of point defects behaviour near dislocation loops of finite size are considered as the first step of such modelling, as it would allow determining conditions of dislocation loops growth and coalescence. Point defects fluxes onto the unit length of dislocation loops are calculated for the conditions of HBS formation by the means of computational modelling and also approximated by simple analytic expressions. Equilibrium point defects concentration is also found as a function of dislocation loop radius and it is shown that coalescence of dislocation loops is possible.

Also in the present work concerns formation of large overpressurized bubbles as a criterion for onset of fuel restructuring first proposed in [3] and further investigated in [4]. Formation of non-destroyable bubbles is carried out using consistent modelling of point defects and fission gas behaviour near dislocation and in grain volume. Further evolution of non-destroyable bubbles is described with simple kinetic model. Results of modelling are in qualitative agreement with experimentally observed dependence of restructuring threshold on grain size.

2. Modelling of point defects kinetics near dislocation loop of finite size

Dislocation loops evolution can be described with kinetic equations, subject to point defects fluxes per unit length of dislocation loop can be obtained. In turn, these fluxes can be found as a solution of problem of point defects behaviour near dislocation loop.

The following processes taking place near edge dislocation should be accounted for: point defects generation on tracks of fission fragments, diffusion transport of the point defects, drift in the field of dislocation loop strain, point defects recombination, radiation-induced resolution of dislocation loops by fission fragments. These are the processes affecting point defects fluxes onto

dislocation loop and they can be described with the system of equations:

$$D_i \Delta c_i + D_i^{th} \nabla c_i \cdot \nabla (E/kT) - s_i c_i - \beta c_i c_v + A\dot{F} + P n_d = 0 \quad (1)$$

$$D_v \Delta c_v - D_v^{th} \nabla c_v \cdot \nabla (E/kT) - \beta c_i c_v + A\dot{F} = 0 \quad (2)$$

Dislocation loops in UO_2 are known to be circular prismatic loops. The interaction energy between such dislocation loop and point defect was derived in [5]. It is given by:

$$E = \frac{Gb\Omega}{3\pi} \frac{1+\mu}{1-\mu} \left((r+r_l)^2 + z^2 \right)^{-\frac{1}{2}} \times \left(\frac{r_l^2 - r^2 - z^2}{(r_l - r)^2 + z^2} E(k) + K(k) \right), \quad k^2 = \frac{4 r r_l}{(r+r_l)^2 + z^2}, \quad (3)$$

where E and K are the complete elliptic integrals of the first and the second kind correspondingly. r and z are cylindrical coordinates, with center of coordinate system corresponding to the center of dislocation loop. Z axis is perpendicular to dislocation loop plane. The energy has complex spatial dependence, and the expression for it can be simplified in the limiting case of small distance to dislocation core. In this case the energy can be expressed via distance from dislocation core ρ and "elevation angle" θ:

$$E \approx \frac{Gb\Omega}{3\pi} \frac{1+\mu}{1-\mu} \left(-\frac{\cos\theta}{\rho} - \frac{\sin^2\theta}{2r_l} + \frac{1}{2r_l} \ln \frac{8r_l}{\rho} \right). \quad (4)$$

The first term in parentheses corresponds to the interaction energy of infinite edge dislocation.

The process of radiation-induced resolution of dislocation loops is characterized by a parameter R, which generally takes the form $R \approx \frac{2\pi r_{tr}^3 l_{tr} \dot{F}}{a_0^2}(1-\alpha)$ [6], where α is the ratio of interstitial atoms which is knocked out in front of the dislocation and returns to it due to drift in the field of its strain. The value of α can be estimated in the following way. The regions of attraction and repulsion of point defects are determined by the sign of interaction energy E. Therefore, at the given distance to dislocation loop, one can find the critical angles at which repulsion changes to attraction. Since point defects are knocked out within the range smaller than typical dislocation loop radius, approximation (4) can be used and critical angles satisfy the following equation:

$$\frac{\cos\theta_c}{\rho} + \frac{\sin^2\theta_c}{2r_l} = \frac{1}{2r_l} \ln \frac{8r_l}{\rho}. \quad (5)$$

For the purpose of estimate, ρ can be substituted with characteristic track radius r_{tr}. α is related with θ_c as $\alpha = \theta_c / \pi$ and the approximate solution of (5) provided that $r_{tr} \ll r_l$ yields R as a function of loop radius:

$$R \approx \frac{\pi r_{tr}^3 l_{tr} \dot{F}}{a_0^2} \left[1 + \frac{r_{tr}}{\pi r_l} \left(\ln \frac{8r_l}{r_{tr}} - 1 \right) \right]. \quad (6)$$

The system of Eqs. (1), (2) is steady-state one. Effective sinks s_i were included to vary point defect concentrations $c_{i,v}$. Without effective sinks ($s_i = 0$) calculated point defects fluxes satisfy the flux balance condition: $J_i = J_v + R$ and therefore uranium interstitials are in equilibrium with dislocation loops.

Geometry for modelling of finite size dislocation loops should be chosen carefully. Toroidal reservoir is shown to be the most appropriate both for small and for large loops [7]. Inner torus corresponds to dislocation core and outer one corresponds to dislocation influence region. Interaction energy of point defects with the dislocation loops E does not depend on azimuthal angle and therefore the problem is reduced to two-dimensional one. The calculation region is chosen similarly to [7]. It is generally bounded by surfaces of tori and dislocation loop plane and may be also bounded with tori's axis of symmetry. The problem described above was solved numerically using 2D finite-difference method on regular non-uniform mesh. The equations after discretization were solved using various iteration techniques.

Calculated fluxes of uranium interstitials and vacancies were fitted in the following way: $J_i = A_i c_i + B_i$, $J_v = A_v \sqrt{c_v} \left(1 - B_v \sqrt{c_v} \right)$, fitting parameters $A_{i,v}$, $B_{i,v}$ depend on fission rate, temperature and dislocation loop radius. An example of fitting is presented in Fig. 1 ($r_l = 7.7 \cdot 10^{-6}$ cm). Point defects flux can be considered as consisting of two parts: absorption of point defects generated

near the dislocation core and drift and diffusion transport from outer regions. Fast absorption takes places for uranium interstitials due to drift in the field of dislocation strain and for vacancies due to formation of peak in vacancies distribution [6]. For interstitial atoms, the first part could be attributed to the term B_i, whereas the second part corresponds to $A_i c_i$. Indeed, calculations show that B_i is proportional to fission rate $\dot{F}$ and A_i does not show strong dependence on $\dot{F}$. Drift and diffusion transport prevails for sufficiently high concentration of interstitial atoms. Conversely, absorption from the region of peak predominates over diffusion transport for vacancies, so the term $A_v\sqrt{c_v}$ corresponds to flux due to peak and correction $B_v\sqrt{c_v}$ could stand for peak diminishing as average concentration of vacancies increase [4].

Dependence of coefficients $A_{i,v}$, $B_{i,v}$ on dislocation loop radius can be fitted with rather simple model: $y=\begin{cases} a\ln(r/r_{dist})+b, & r<r_{dist} \\ b, & r\geq r_{dist} \end{cases}$, where $r_{dist} \approx 0.5n_d^{-1/2}$ is average inter-dislocation distance. An example of fitting for coefficient A_v is shown in Fig. 2.

Equilibrium concentrations of point defects corresponding to flux balance condition were also calculated as a function of dislocation loop radius. Calculated uranium interstitials equilibrium concentration is shown in Fig. 3 along with its fitting by expression $c_i^{eq}=c_i^0\ln\left(K+r_{disl}/r_l\right)$. It can be seen that equilibrium concentration of interstitials is higher for smaller loops, which makes possible coalescence of dislocation loops at high burnups.

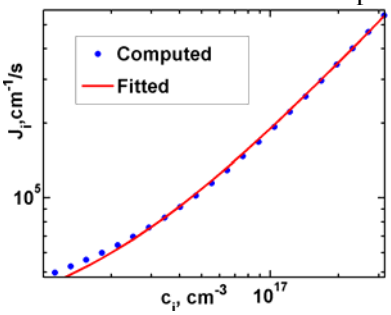

Fig.1. Interstitial atom flux as a function of concentration

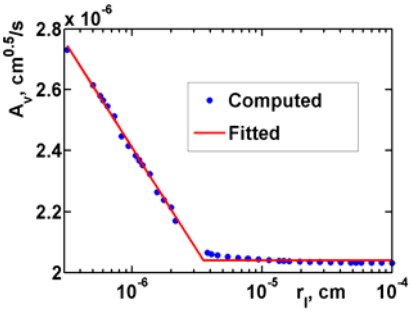

Fig.2. Fitting of coefficient A_v

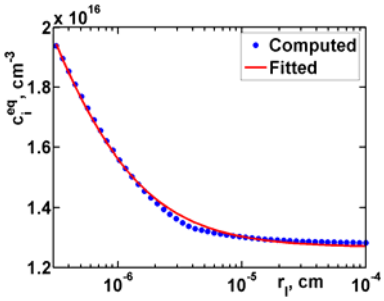

Fig.3. Equilibrium interstitial atom concentration

3. Modelling of large non-destroyable gas bubbles formation and evolution

In [4] it was shown that non-destroyable fission gas bubbles could at first form near the dislocation core due to formation of peaks in vacancy distribution. The magnitude of the peak is shown to depend on ratio of average concentrations of vacancies and interstitial atoms; namely, the peak diminishes as vacancy concentration grows. Average concentrations vary for the grains of different size and different irradiation history. Therefore modelling of bubbles development near dislocation loop requires consistent modelling of point defects and fission gas atoms behaviour both at the scale of one dislocation loop and in grain volume.

Preliminary consistent calculations [4] showed that in larger grains non-destroyable gas bubbles near dislocations form earlier than in smaller grains. However, rim-structure forms earlier in smaller grains. It can be related with development of intergranular bubbles due to accumulation of fission gas (in particular, Xe) at grains boundaries. So it is necessary to account for flux of Xe to the grain boundary and irradiation-induced resolution of Xe atoms from the grain boundary.

The approach to modelling of non-destroyable gas bubbles formation follows one in the work [4]. Bubbles nucleate in thermal spikes along the tracks of fission fragments and their radius is determined by local Xe concentration: $r_b=r_{sp}\left(\Omega_{Xe}c_{Xe}\right)^{1/3}$ for bubbles in grain bulk and $r_b=r_{sp}\left(3\Omega_{Xe}n_s/r_{sp}\right)^{1/3}$ for intergranular bubbles, where n_s is surface density of Xe on the grain boundary. The bubbles are then destroyed by fission fragments, unless their size is greater than critical, which approximately equals track radius. For consistent modelling of point defects and Xe atoms the spherical grain was divided into concentric zones. At each zone the following system of

equations for point defects and Xe atoms concentration near dislocation was solved:

$$\frac{\partial c_i}{\partial t} = D_i \Delta c_i + D_i^{th} \nabla c_i \cdot \nabla \frac{\Lambda_i \cos\theta}{r} - \beta_i c_i c_v + A\dot{F} + j_i , \quad (7)$$

$$\frac{\partial c_v}{\partial t} = D_v \Delta c_v - D_v^{th} \nabla c_v \cdot \nabla \frac{\Lambda_v \cos\theta}{r} - \beta_i c_i c_v + A\dot{F} + \alpha c_{Xe,v} - \beta_{Xe} c_{Xe,i} c_v - \eta_{in} c_{Xe,v} + 2\eta_{Xe,b} + j_v , \quad (8)$$

$$\frac{\partial c_{Xe,i}}{\partial t} = D_{Xe,i} \Delta c_{Xe,i} + D_{Xe,i}^{th} \nabla c_{Xe,i} \cdot \nabla \frac{\Lambda_{Xe,i} \cos\theta}{r} + \alpha c_{Xe,v} - \beta_{Xe} c_{Xe,i} c_v + \eta_{out} c_{Xe,b} + Q_{Xe}\dot{F} + j_{Xe,i} , \quad (9)$$

$$\frac{\partial c_{Xe,v}}{\partial t} = D_{Xe,v} \Delta c_{Xe,v} - D_{Xe,v}^{th} \nabla c_{Xe,v} \cdot \nabla \frac{\Lambda_{Xe,v} \cos\theta}{r} - \alpha c_{Xe,v} + \beta_{Xe} c_{Xe,i} c_v - \eta_{in} c_{Xe,v} + j_{Xe,v} , \quad (10)$$

$$\frac{\partial c_{Xe,b}}{\partial t} = \eta_{in} c_{Xe,v} - \eta_{out} c_{Xe,b} . \quad (11)$$

Xe atoms were considered in interstitial and vacancy state and in gas bubbles, Xe atom in bubble occupies two vacancies. Coefficient for capture and release of Xe atoms by bubbles are $\eta_{in} = 2N_{sp}\Omega_{sp}\dot{F}$ and $\eta_{out} = 2V_{\text{tr}}\dot{F}\left(1 + r_b / r_{\text{tr}}\right)^2$, where N_{sp} is amount of spikes per fission fragment track. Inter-zone fluxes j were calculated across the zones: $j = n_d D \Delta c$.

On the grain boundary zero boundary conditions were used, except for Xe in vacancy state. Concentration of Xe in vacancies on grain boundary is determined by balance of diffusion transport and irradiation-induced resolution from the grain boundary.

Calculations were carried out for two grain sizes and corresponding dislocations density: for large grain ($r_g = 40\mu$, $n_d = 10^9\,\text{cm}^{-2}$) and for small grain ($r_g = 10\mu$, $n_d = 10^{10}\,\text{cm}^{-2}$), in order to compare burnups at which non-destroyable bubbles form. One can see (Fig. 4) that at first non-destroyable bubbles form in large grains on dislocations and on grain boundaries. After the small delay, non-destroyable bubbles develop on grain boundaries in small grains and then formation of non-destroyable bubbles on dislocation in small grains takes place.

The following evolution essentially depends on bubbles and vacancies concentration after the stage of non-destroyable bubble formation. Processes of small bubbles nucleation and destruction can be neglected at this stage. Non-breakable bubbles are good sinks for vacancies and Xe atoms, and their absorption by bubbles increases bubble radius and accelerates the process further. If concentration of bubbles and vacancies is high enough, instability develops that could lead to overpressured bubbles formation. A fuel volume in which radius of bubbles exceeds the critical one determines concentration of non-destroyable bubbles. For small grains this region can be considerably large, since magnitude of peak in vacancies distribution is smaller and thus more bubbles simultaneously become non-destroyable. For the grains given above calculations show that concentration of bubbles in small grain is about $3 \cdot 10^3$ times higher than in large grain. Therefore one could expect slow growth of bubbles in large grains and rapid matrix cleanup from vacancies and Xe atoms in small grains. At the same time, bubbles in small grain before completion of matrix cleanup will grow faster than in large grains, due to larger supply for vacancies.

For evolution of non-breakable bubbles the following simplified model can be used. The distributions of point defects, Xe atoms and parameters bubbles are considered spatially uniform. Absorption of point defects and Xe and irradiation-induced resolution of Xe atoms are taken into account. Since uranium interstitials and Xe atoms can only occupy vacancies in bubbles, their flux is limited by the overpressure factor: $\varepsilon = (3N_{Xe}\Omega_v)/(2\pi r_b^3)$, where N_{Xe} is number of Xe atoms in bubble. Thus the system of equation describing these processes can be written as follows:

$$\dot{c}_i = A\dot{F} - \beta_i c_i c_v - 4\pi r_b c_b D_i c_i (1-\varepsilon) , \quad (12)$$

$$\dot{c}_v = A\dot{F} - \beta_i c_i c_v - 4\pi r_b c_b D_v c_v , \quad (13)$$

$$\dot{N}_{Xe} = 4\pi r_b D_{Xe} c_{Xe} (1-\varepsilon) - z \frac{\pi r_{tr}^3}{\Omega_v} r_b^2 l_{tr} \dot{F} \frac{D_v}{D_i (1-\varepsilon)} , \quad (14)$$

$$4\pi r_b^2 \dot{r}_b = 4\pi r_b \Omega_v \left[D_v c_v - D_i c_i (1-\varepsilon) \right] , \quad (15)$$

$$c_{Xe} = c_{Xe0} + Q_{Xe}\dot{F}t - c_b N_{Xe} . \quad (16)$$

Eq. (16) is simply conservation law of amount of Xe atoms. The second term in Eq. (14) stands

for irradiation-induced knock-out of Xe atoms. Parameters of bubbles and vacancies and Xe concentration calculated with consistent model up to the moment of non-destroyable bubbles formation were taken as initial values for the system of Eqs. (12)-(16). Kinetics of non-destroyable bubbles on grain boundary can be considered as a negligibly small perturbation to kinetics of bubbles, vacancies and Xe atoms in the grain bulk.

Calculations indicate two stages of kinetics of non-destroyable bubbles on grain boundary (Fig. 5). At first, rapid growth will take place while matrix is rich with vacancies and Xe atoms. Then non-breakable bubbles will form on dislocation and decrease of radius and increase of pressure will happen due to cleanup of matrix from excessive vacancies. As a result, radius and pressure of bubble in small grain can become larger compared with large grain, as illustrated in Fig. 5.

Punching of dislocation loops into matrix by bubble happens if the following criterion for pressure and radius of the bubble holds [8]: $P > P_{eq} + Gb/r$, where $P_{eq} = 2\sigma/r$ is equilibrium pressure of gas in bubble. So the threshold condition for onset of rim-structure formation is governed by parameter:

$$\xi = \frac{N_{Xe} r_b}{\frac{4\pi}{3} r_b^3 - \Omega_{Xe} N_{Xe}}. \qquad (17)$$

Calculated evolution of parameter ξ for large and small grains is shown in Fig. 6. It can be seen that according to this model HBS formation can start earlier for small grains, which is in accordance with experimental data.

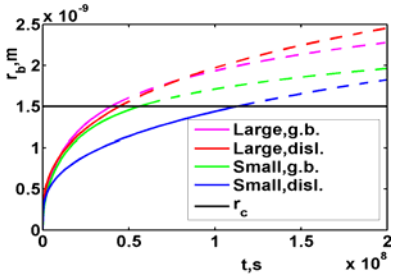

Fig.4. Evolution of bubbles radius up to attainment of critical value (black line).

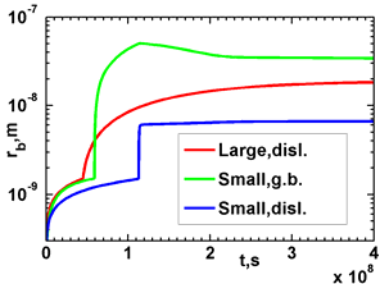

Fig.5. Evolution of bubbles radius

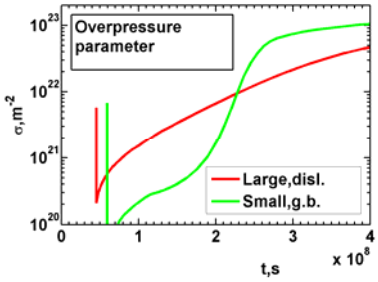

Fig.6. Evolution of overpressure parameter of gas bubbles

4. Conclusion

This paper concerns modelling of dislocation and bubble structures at conditions of high burnup fuel restructuring. Fluxes of point defects to unit length of dislocation loop as functions of point defects concentration and loop radius are found by the means of computer simulation and approximated by simple dependencies. Equilibrium interstitial concentration is also found and possibility of dislocation loops coalescence is proven possible. Consistent modelling of non-destroyable bubbles formation on dislocations and on grain boundaries are carried out. Further evolution of non-destroyable bubbles is treated with the use of simple kinetic model and punching of dislocation loops by overpressurized bubbles is considered, the results are in agreement with experimental data. In future it is planned to develop consistent models of dislocation and bubbles behaviour using obtained flux dependences.

5. References

[1] Hj.Matzke, M.Kinoshita, J. Nucl. Mater. 247 (1997), 108-115.
[2] K. Nogita and K. Une, J. Nucl. Mater. 226 (1995), 302-310.
[3] C.B.Lee, Y.H.Jung, J. Nucl. Mater. 279 (2000), 207-215.
[4] V.V.Likhanskii, V.G.Zborovskii. Modeling of Threshold Conditions for Beginning of Rim Formation in High Burnup UO2 Fuel. Proceedings of 2005 Water Fuel Reactor Performance Meeting, Kyoto, 2005.
[5] J. Bastecka, F. Kroupa, Chechoslov. J. Phys. [B] 14 (1964), 443.
[6] V.V.Likhanskii, V.G.Zborovskii. J.Nucl. Mater. 350 (2006), 1-8.
[7] V.I.Dubinko, A.S.Abyzov, A.A.Turkin, J.Nucl. Mater. 336 (2005), 11-21.
[8] G.W.Greenwood, A.J.E.Foreman, D.E.Rimmer, J.Nucl. Mater. 4 (1959), 305.

MODELING FISSION GAS EFFECTS ON HIGH BURNUP FUEL BEHAVIOR DURING RIA

WENFENG LIU AND MUJID S. KAZIMI
Center for Advanced Nuclear Energy Systems
Department of Nuclear Science and Engineering
Massachusetts Institute of Technology
77 Massachusetts Avenue, Cambridge MA 02139 – U.S.A.

ABSTRACT

Models are developed in FRATRAPN 1.3 accounting for: 1) Burst release of fission gas accumulated at the grain boundary and porosity in the rim structure; 2) Swelling of rim pores and expansion of intergranular bubbles. The fission gas induced deformation of the cladding is solved by two steps: 1) Predict the state of stress and strain by thermal expansion model; 2) Correct the prediction by calculating the incremental displacement due to fission gas swelling.

The models have been validated by experimental data from CABRI and NSRR simulated RIA tests concerning irradiated UO_2 fuel with enthalpy 37 ~ 200 cal/g and burnup 26 ~ 64 MWd/kgU. The predicted absolute error of fission gas release (FGR) is 5.6%. Majority of the fission gas comes from the grain boundary as indicated by analysis of Xe/Kr ratio. Results reveal that fission gas induced deformation in the early phase of RIA is small due to high interface pressure.

1. Introduction

Economic advantage and reduced spent fuel storage have been driving nuclear industry to pursue high burnup of LWR fuel. Safety concerns have been raised over performance of high burnup fuel during transient conditions. During a Reactivity Initiated Accident (RIA), one concern is the significant fission gas release of high burnup fuel. Current experimental observation in simulated RIA tests and post irradiation examination are not sufficient to precisely describe its role on loading to the cladding. Hence modeling efforts are directed towards development of fission gas release and swelling in integrated fuel performance code to better quantify the loading effect of fission gas. As part of our efforts to understand the behaviour of high burnup fuel during RIA and building on our previous modeling work [1-3], this paper highlights the improvement made in the FRAPTRAN 1.3 code and applies the models to expanded sets of test cases for validation.

Our models account for the transient burst release of fission gas accumulated at the grain boundary and porosity formed in the rim region of high burnup fuel. Fission gas inventory in the grain boundary is initialized from a simulation of base irradiation by the FRAPCON code. Fission gas in the rim pores is based on a high burnup structure model accounting for the depletion of fission gas from fuel matrix. The release mechanism assumes instantaneous flow of fission gas from the fragmented fuel into the plenum when the clad-fuel deformation creates an open gap. During the Pellet Cladding Mechanical Interaction (PCMI), the model takes into account the swelling of pores in the rim by a dislocation punching mechanism as well as the fission gas expansion after fuel fragmentation. A new set of cladding-coolant heat transfer correlation for high burnup fuel during RIA [3] has been implemented in this version of FRAPTRAN to improve prediction of cladding temperature during transient film boiling.

The models have been validated by experimental data from CABRI and NSRR simulated RIA tests concerning irradiated UO_2 fuel with enthalpy 37 ~ 200 cal/g and burnup 26 ~ 64 MWd/kgU. The absolute error of the FGR predicted by the model is 5.6% for validation cases. Results of the mechanical response of the fuel pin while applying the models reveal that early phase deformation by fission gas is small (less than 0.3% of hoop strain) due to high interface pressure. However in the later phase of RIA,

the combinational effects of decreased cladding yield stress at high temperature in the film boiling regime and plenum pressure increase due to fission gas release could cause large deformation, as observed in some NSRR tests.

2. Modeling fission gas release and swelling

2.1 Fission gas inventory

The Massih model in FRAPCON 3.3 is used to initialize the gas inventory in the grain boundaries. During the base irradiation of LWR fuel, fission gas diffuses towards grain boundaries and precipitates as intergranular bubbles. Thermal release is assumed to occur when the saturation condition, i.e. inter connection of bubble network to free volume, is met. Massih model is a two stage model accounting for the thermal diffusion and fission gas storage in grain boundary. In FRAPCON 3.3, Massih model partitions fission gas as: fission gas in fuel matrix, fission gas in intergranular bubbles, fission gas in resolution layer and fission gas released. For each test case, base irradiation is simulated by FRAPCON 3.3. Parameters concerning the fission gas quantity in the grain boundary, in the fuel matrix, and the grain boundary surface coverage are calculated at End Of Life (EOL) and are subsequently input into FRAPTRAN to initialize corresponding variables.

The rim region of LWR fuel at high burnup features: 1) high porosities, 2) high fission gas content, and 3) large pores surrounded by submicron grains. The amount of fission gas in the rim-zone in [%w] is given as xenon depletion [4].

$$Xe_c = \dot{c}BU - \dot{c}\left\{\frac{1}{a} + \left(BU_0 - \frac{1}{a}\right)e^{\left[-a\left(BU-BU_0\right)\right]}\right\} \tag{1}$$

where $\dot{c}$ is the xenon production rate in [%w / BU], BU_0 is a threshold burnup for the xenon depletion measured in [MWd / kgU], BU is the local burnup and *a* is a constant measured in the reciprocal of BU units related to the xenon equilibrium concentration.

2.2 Fission gas release

The burst release model assumes that open porosities connects the gas plenum to the percolated fuel as the fuel is fragmented. In the central region, fuel fragmentation is assumed to occur as a result of grain boundary separation with a criterion as follows: [5].

$$p > p_S + \frac{p_H}{f} + \left(\frac{1-f}{f}\right)\sigma_r \tag{2}$$

where *f* is the grain boundary surface gas coverage fraction, p_s [Pa] is the surface tension pressure and σ_r is the fracture stress of grain boundary in [Pa]. In the rim region, where quantification of the intergranular bubbles by Massih model is not applicable, an empirical threshold temperature is employed as the condition for fuel fragmentation.

2.3 Fission gas induced deformation

During RIA, the micrometer pores, at rapid heating, would punch dislocations into the surrounding fuel matrix to relieve the excess pressure. Detailed equations are described in [1] to compute the pore pressure and volume change by pores. After fuel fragmentation, either in the central region or the rim region, the fission gas expansion is calculated following the ideal gas law.

To couple the fission gas induced deformation with the rigid pellet model FRACAS-I in FRAPTRAN code, it's necessary to account for the constraint of the cladding on the expanded fuel. Though an iteration approach has been adopted in [1] and [6], this approach is flawed as the thin-walled solution is applied in a closed-gap regime, where the hoop to axial stress ratio is around 1.0 and may vary depending on the pellet cladding interfacial frictional force. A two step method is developed below [7]:

1) Predict the state of stress and strain of the cladding due to thermal expansion of pellet by the FRACAS-I rigid pellet model in the FRAPTRAN code,

2) Correct above solution by calculating the incremental displacement due to fission gas by linearization of the Generalized Hook's law and Prandtl flow rule using the state of stress and strain obtained in step 1).

In an open-gap regime, the existing models in FRAPTRAN are used to calculate the deformation of cladding due to plenum pressure change. A new set of cladding-coolant heat transfer correlation for high burnup fuel during RIA is implemented in FRAPTRAN to the compute the cladding temperature escalation during film boiling [3].

3. Model validation results

Test No	Burnup (MWd/kg)	Peak Fuel Enthalpy(cal/g)	Measured Cladding Permanent Hoop Strain (%)	Measured FGR (%)	Category (Validation or Fitting)
RepNa2	33	210	3.5	5.54	V
RepNa3	52.8	125	2	13.7	V
RepNa4	62.3	88	0.4	8.3	F
RepNa5	64.3	108	1.1	15.1	F
HBO2	50.4	37	0.41	17.7	F
HBO3	50.4	74	1.5	22.7	V
HBO4	50.4	50	0.17	21.1	V
HBO6	49	85	1.2	10	F
HBO7	49	88	2.23	8.5	V
OI2	39.2	108	4.8	10.2	F
GK1	42	93	2.23	12.8	F
GK2	42	90	1.05	7	V
MH1	38.9	47	0.02	3.5	F
MH3	38.9	67	1.6	4	V
TS2	26.6	66	0.4	12	V
TS3	26.6	88	0.5	10	V
TS4	26.6	89	0.4	15	V
TS5	26.6	98	0	8	F
FK1	45	130	0.9	8.2	F
FK2	45	70	0	3.1	F
FK3	41	145	1.5	4.7	V
FK4	56	140	1.25	15.7	F
FK5	56	70	0	9.6	V
FK6	61	130	-	16.9	V
FK7	61	129	-	17	V
FK8	61	65	0.02	11.3	V
FK9	61	90	-	16.6	V
FK10	61	102	-	16.1	V
FK12	61	89	-	17.8	V

Table 1: Test cases description

Test cases used for comparison with the model includes the UO_2 fuel in CABRI and NSRR simulated RIA tests given in Table 1. This set of test cases has been subdivided into two groups: one for model parameters fitting and the other for model validation. The FGR predicted by the fuel code gives good agreement with the experimental data (absolute error is 4.9% for fitting cases and 5.6% for validation cases), except for large under-prediction of HBO2, HBO3 and HBO4, as shown in Figure 1.

Figure 2 gives the prediction of the permanent hoop strain by the modified code as compared to the original FRAPTRAN code. The model predicts the fission gas induced deformation is less than 0.3%, which is small compared to the thermal expansion of the pellet. However in the later phase of an RIA, the decrease of cladding yield stress at high temperature, together with the fission gas release, could

cause a large deformation. For the example of GK1, the calculated peak cladding temperature (PCT) is 1061.8 K, and the cladding yield strength is 15.3 MPa at PCT, thus the pressure loading is sufficient to create large plastic strain. A sensitivity study of OI2 illustrates the possible large deformation at increased power level as shown in Figure 2.

The higher ratio of Xe/Kr from fission of plutonium isotopes than uranium isotopes has been considered as an indicator to track fission gas release from rim structure where there is high content of plutonium isotopes. Therefore, a calculation by the MCODE 1.0 [8], which couples the particle transport code MCNP 4c3 and isotope depletion code ORIGEN 2.1, is performed to generate the radial profile of Xe/Kr ratio for PWR fuel tested in NSRR. The Xe/Kr of fission gas release has been calculated by:

$$Xe/Kr = \frac{\sum_{i=1}^{N} n_i /(1+(Xe/Kr)_i)}{\sum_{i=1}^{N} n_i (Xe/Kr)_i /(1+(Xe/Kr)_i)} \tag{3}$$

where n_i is the quantity of total fission gas released at the i-th radial node, $(Xe/Kr)_i$ the Xe/Kr ratio at radial node i. The calculated Xe/Kr ratio is compared with that obtained from rod punctures in NSRR tests. Analysis of the Xe/Kr ratio of HBO2-HBO4 as shown in Table 2 indicates that the large under-prediction of fission gas release is partially due to under-prediction of the fission gas release from the rim region.

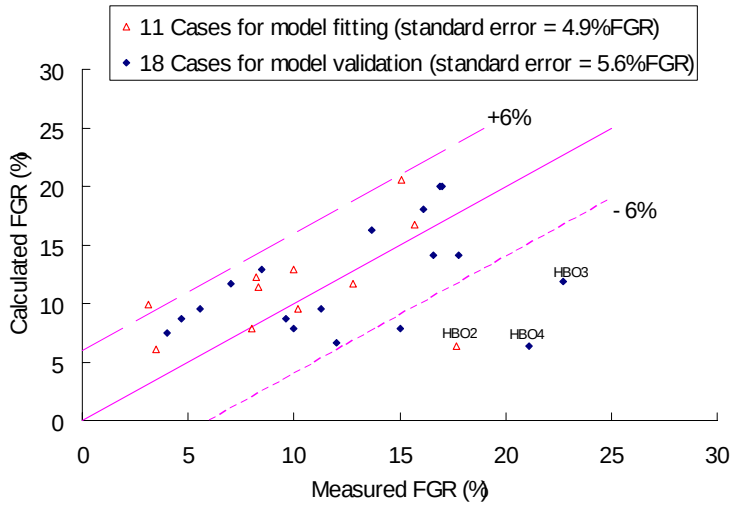

Figure 1 Prediction of fission gas release

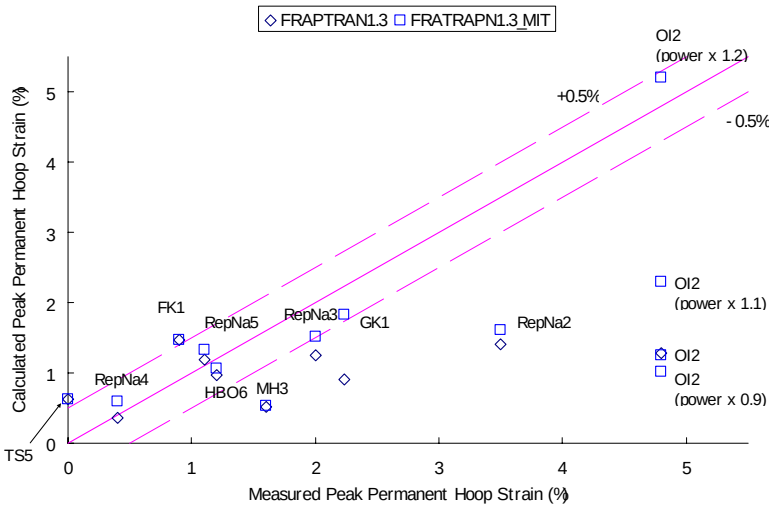

Figure 2 Prediction of permanent hoop strain

Test No.	Enrichment (%)	Xe/Kr		Rim (%)	GB (%)	Total (%)	Measured (%)
		Experiment	Calculated				
HBO2	3.2	10.4	9.5	0	6.3	6.3	17.7
HBO3	3.2	11.8	10.8	4.1	7.8	11.9	22.7
HBO4	3.2	11.7	9.5	0	6.3	6.3	21.1
HBO6	3.2	10.4	10.6	4	8.9	12.9	10
HBO7	3.2	10.5	10.6	4	8.9	12.9	8.5
MH3	2.6	10	9.5	0	7.4	7.44	4
GK1	3.4	10.6	8.9	0	11.7	11.7	12.8
OI2	3.2	9.2	9	0	9.5	9.5	10.2

Table 2: Fission gas release analysis for PWR fuel tested in NSRR

4. Conclusion

This paper summarizes the improved FRAPTRAN modeling at fission gas induced deformation during an RIA by initializing the fission gas inventory by FRAPCON code, validating rim gas contribution by Xe/Kr ratio, implementing heat transfer conditions at RIA conditions, and coupling fission gas swelling with the FRACAS-I model. Models are validated by NSRR and CABRI UO_2 fuel in terms of FGR, Xe/Kr, and permanent hoop strain. Fission gas induced deformation is predicted to be less than 0.3% in the early phase of RIA as revealed by application of models. This is attributed to the high interface pressure suppressing the gaseous swelling. Large deformation is due to decreased cladding strength at escalated temperature. Xe/Kr analysis indicates fission gas release is partly from rim region and majority of fission gas released is from grain boundary.

References

[1] W. Liu, A. Romano, and M. S. Kazimi. Modeling High-burnup LWR Fuel Fission Gas Release and Swelling during Fast Transients. *Proceedings of the 2004 International Meeting on LWR Fuel Performance*, Orlando, U.S., Sep 19-22, 2004.

[2] W. Liu, and M. S. Kazimi. Modeling High-burnup BWR Fuel Behavior during RIA. I*nternational Conference on LWR Fuel Performance*, Kyoto, Japan, Oct 2-6, 2005.

[3] W. Liu and M. S. Kazimi., Modeling Cladding-Coolant Heat Transfer of High-Burnup Fuel during RIA. *Proceedings of 14th International Conference on Nuclear Engineering*, Miami, U.S., July 17-20, 2006.

[4] K. Lassmann, C. T. Walker , J. van de Laar and F. Lindström, Modelling the High Burnup UO2 Structure in LWR Fuel, *Journal of Nuclear Materials*, **226**, *1-2*, 1-8 (1995).

[5] F. Lemoine, J. Papin, J. Frizonnet, B. Cazalis and H. Rigat, The Role of Grain Boundary Fission Gases in High Burnu-up Fuel under Reactivity Initiated Accident Conditions, *Proc. of the Fission Gas Behaviour in Water Reactor Fuels Seminar*, p.175-187, OECD, Cadarache, France, (2000).

[6] T. Nakamura, H. Sasajima, T. Fuketa and K. Ishijima, Fission Gas Induced Cladding Deformation of LWR Fuel Rods under Reactivity Initiated Accident Conditions, *Journal of Nuclear Science and Technology*, **33**, *12*, 924-935 (1996)

[7] W. Liu, Assessment of High-burnup LWR Fuel Response to Reactivity-Initiated Accident, Ph.D. Dissertation, Nuclear Science and Engineering Department of MIT (To be published)

[8] Z. Xu, M.J. Driscoll, M.S. Kazimi, Design Strategies for Optimizing High Burnup Fuel in Pressurized Water Reactors, Report by Center for Advanced Nuclear Energy Systems, MIT, MIT-NFC-TR-053, 2003.

CHARACTERIZATION TEST AND ANALYSIS OF LWR FUEL ASSEMBLY MECHANICAL BEHAVIOUR

H.-K. KIM[1], K.-H. YOON[1], K.-H. LEE[1], Y.-H. LEE[1], T.-H. CHUN[1], S.-S LEE[2]

1: Advanced LWR Fuel Development Division, Korea Atomic Energy Research Institute
150 Dukjin-dong Yuseong-ku, Daejeon 305-353 Korea (Rep. of)
2: School of Mechatronics Engineering, Korea University of Technology and Education
307 Gajeon-ri Byeongcheon-myeon, Cheonan Choongnam Province 330-708 Korea (Rep. of)

ABSTRACT

A fuel assembly mechanical characterization test facility, named FAMeCT, has recently been built at the Korea Atomic Energy Research Institute (KAERI). It is a robust column equipped with various devices for the vibration, stiffness and impact tests of an LWR fuel assembly. Among the available tests, a lateral vibration and a lateral stiffness test were carried out with a test fuel assembly (an improved design) of the Korea Standard Nuclear Power Plant type to verify the performance of the FAMeCT. As a result, the fundamental frequency and damping ratio were found to be 1.98 ~ 2.41 Hz and 3.45 ~ 4.54 %, respectively when a vibration force of 2 ~ 20 N was applied during the vibration tests. It was noted that the location of a vibration excitation needed to be different from the nodal points. The deflection at each grid was measured during a bending of the fuel assembly by 2 ~ 20 mm at the mid-grid during the stiffness tests. Reasonable curves of the force vs. displacement and the defection shapes were obtained. The stresses of the guide thimbles and upper/lower end pieces were also evaluated from the strains collected from over 100 locations in the fuel assembly. From the test results, it was concluded that the present test methods and the performance of the FAMeCT were verified. The test results enabled a simple modelling for the finite element analysis.

1. Introduction

A fuel assembly test is defined as a test with a full size fuel assembly. It is mandatory to check the reliability and compatibility of a fuel assembly after the completion of a fuel development. Data from the tests are also used for acquiring the license of the fuel use as well as for verifying the fuel assembly (finite element) model for a core structural analysis. During a fuel technology development phase in Korea, test equipment for the fuel components are developed and procured such as a grid impact tester, a fretting wear tester, a flow-induced vibration (FIV) tester etc. However, fuel assembly tests could not until recently be conducted since such test facilities have not been built in Korea. Without any doubt, it is mandatory for fuel vendors to conduct fuel assembly tests for a licensing as well as developing (or improving) a new design. To this end, the Korea Atomic Energy Research Institute (KAERI), although it is not a fuel vendor, started to develop fuel assembly test facilities under the Mid- and Long-Term Nuclear R&D program by the Ministry of Science and Technology of Korea to support the vendor in Korea and possibly in foreign countries. Another purpose of it is for fuel R&D works at the KAERI such as fuel failure and structural analyses.

The facilities under development consist of two: a mechanical tester and a hydraulic tester. The former characterizes the mechanical behaviour of a fuel assembly such as the stiffness, vibration and impact while the latter is used for investigating the hydraulic performances such as a pressure drop, an FIV and wear due to the FIV. In this paper, the mechanical tester, named the Fuel Assembly Characterization Tester (FAMeCT), is introduced. After its construction was complete, a performance verification tests were carried out through lateral vibration and stiffens tests of the test assembly. This paper presents the results of them. Besides, it is usually necessary to implement a sophisticated modelling to analyze a fuel mechanical behaviour by using a finite element method. This can be considerably simplified if actual test data is available. So, a finite element analysis was also carried out with a simple model in this paper. Its validity is also discussed.

2. Fuel Assembly Mechanical Characterization Tester (FAMeCT)

2.1 Fuel assembly mechanical test items

A brief description of the fuel assembly mechanical tests is as follows.

- Vibration test: the vibration test is conducted to obtain the vibration behaviour of a fuel assembly. It is a dynamic test to obtain natural frequencies, model shapes and critical damping ratios. These are used for a fuel assembly accident analysis being subjected to the seismic and LOCA conditions.
- Stiffness test: this test is basically to examine the static response of a fuel assembly while it is loaded laterally as well as axially. As for the data, deflection at each grid location and strain of the guide thimbles and upper/lower end pieces are measured during loading and unloading phases. The test results are used for verifying the fuel assembly model for the reactor analysis.
- Impact test: the purpose of this test is to evaluate the fuel assembly performance when being subjected to the lateral and axial impact conditions. Possible case of a fuel assembly impact is a banging of a fuel assembly against an adjacent one or a core baffle under the seismic and LOCA conditions. The structural integrity of a fuel assembly is of a major concern. Impact force, displacement and rebound height are measured.

2.2 Feature and structure of the FAMeCT

The most important requirements of the FAMeCT were a sufficient rigidity and a sufficient reliability. Reflecting on these, the FAMeCT was designed and constructed to have the following features (see Fig. 1 for an overall view).

- Concrete column, steel bed and work platform

Overall shape is like an "L" with the dimension of 1000×1600×6000 mm^3 (upper part) where the steel beds of 50 mm in thickness are attached to the 1000×2700×500 mm^3 (lower part) where the fuel assembly sits. The straightness, and the flatness as well as the perpendicularity of the panels were carefully controlled so that the tolerance of each was less than ±0.1 mm. A work platform, a truss structure surrounding the concrete column, was constructed for accessing the fuel assembly. Fuel storage area was also prepared in the work platform.

- Upper and lower core plate simulators

For simulating the loaded condition of a fuel assembly in a reactor, an upper and a lower core plate simulators were fabricated that fit the upper/lower end pieces of a test fuel assembly, respectively. Especially, the lower core plate simulator was attached to a loadcell for measuring the compressive and impact forces. So, the loadcell was installed on a rotary table, by which the fuel assembly could be rotated by a specified angle.

- Shaker and loader

For the vibration test, an electromagnetic shaker was procured. It was installed in a bracket that was attached to the steel bed of the concrete column. The frequency range of the shaker is up to 9 kHz so that all the natural frequencies of a fuel assembly can be covered. By a special controller, sine sweep and dwell tests are available. For the stiffness test, a loader that applied a screw jack is installed on the same bracket for the shaker installation. The movement of the loader is controlled by a remote controller and can provide continuous characteristic curves by an appropriate programming. Since the location of the bracket is adjustable along the fuel axis, various responses of the fuel assembly can be obtained.

- Linear gauges, loadcells and gauge brackets

More than 60 linear gauges and 10 loadcells with various measuring ranges were procured. These are installed in specially designed gauge brackets that are attached to a steel bed. The number of strain gauges for the test is more than 100. They are pasted on to every location of the guide thimbles as well as the upper/lower end pieces. Therefore, three junction boxes (each has 40 strain gauge terminals) were fabricated and installed on each story of the work platform to minimize the signal noises caused by the lengthy signal lines.

- Data acquisition and processing system (DAS)

A total of nine data scanners (7 static and 2 dynamic) were procured to collect and process all the data obtained during the tests. A commercial software StrainSmart® [1] is used for the data collection and processing. For the vibration analysis, IDEAS T-DAS [2] is additionally used for the analysis.

- Other facilities

Two cranes (capacity of 3 ton and 1 ton) were installed for handling the fuel assembly. A fuel assembly handling tool was procured to grip the fuel assembly. A fuel assembly container was fabricated to

transport the test fuel assembly. All the necessary appliances including the tools and fixtures were prepared including a self-propelled scissors lift.

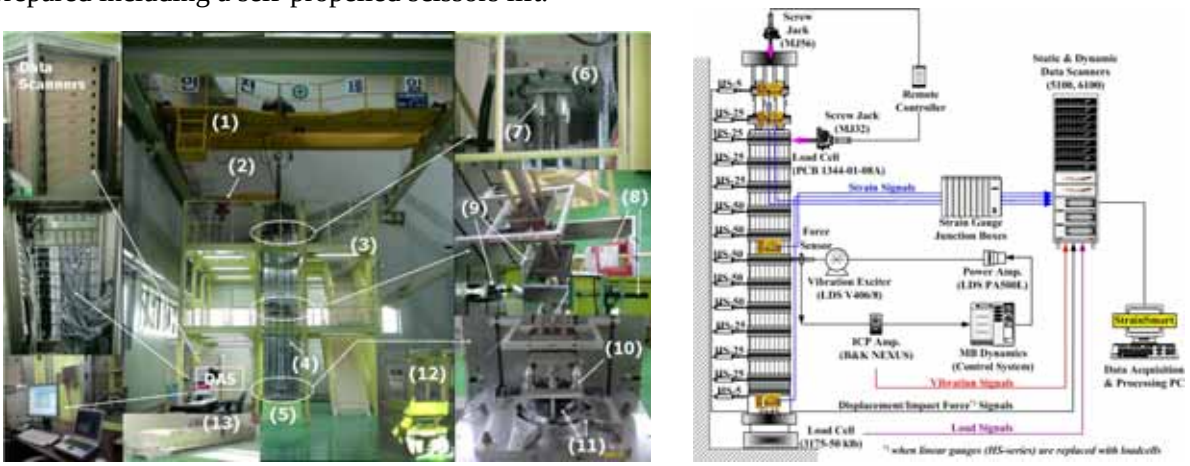

Fig. 1. The FAMeCT view and DAS configuration: (1) Overhead Crane (2) Jib Crane (3) Work Platform (4) Main Bed (5) Concrete Column (6) Carriage (7) UCP Simulator (8) Shaker & Loader (9) Linear Gauges & Loadcells (10) LCP Simulator (11) Loadcell & Rotary Table (12) Self-Propelled Scissors Lift (13) Test Fuel Assembly Shipping Container.

3. Fuel Assembly Vibration and Stiffness Tests using the FAMeCT

3.1 Fuel Assembly specimen

A test fuel assembly of an improved design for the Korean Standard Nuclear Power Plants was prepared, which has been tested once. The geometric dimensions and the materials of the test fuel assembly were exactly the same as the real one except the fuel rods were filled with lead pellets instead of the UO_2 pellets. The weight of the test fuel assembly was 628.6 kg, which was slightly lower than the actual one.

3.2 Vibration tests

There were two conditions for the fuel assembly preload in the axial direction: 7470 N to simulate an in-core BOL hot condition and a null force to simulate a release of an upper core plate. Strain gauge type linear gauges were used at each grid location to measure the lateral displacement. An electromagnetic shaker was attached to the 6th grid of the test assembly to apply a shaking force through a metal stinger for a sine sweeping test. The shaker input force was varied from 2 N to 20 N. For each force, the shaker output frequency was varied from 1.0 to 30 Hz at a log sweep rate of 1 octave/minute. The input from an electromagnetic shaker and the output from the linear gauges were stored on a data acquisition system (SYSTEM 6000) and they were analyzed by using I-DEAS TDAS [2].

Mode	2N		5N		7.5N		10N		15N		20N	
	ω_i (Hz)	ζ_i (%)	ω_i (Hz)	ζ_i (%)	ω_i (Hz)	ζ_i (%)	ω_i (Hz)	ζ_i (%)	ω_i (Hz)	ζ_i (%)	ω_i (Hz)	ζ_i (%)
1st	2.41	3.45	2.20	5.13	2.16	4.47	2.12	4.79	2.04	6.09	1.98	4.54
2nd	4.22	7.54	3.32	2.87	4.29	4.52	4.17	3.52	4.01	4.83	4.00	4.22
3rd	9.08	2.50	9.03	3.40	8.98	3.21	8.88	3.06	8.83	3.35	8.65	3.46
4th	11.80	3.37	9.96	4.47	11.88	4.64	11.26	4.55	12.50	3.76	10.94	8.30
5th	19.75	4.72	19.42	5.45	19.66	5.31	19.26	4.74	19.56	6.83	19.10	4.79

Tab 1: Natural frequencies (ω_i) and damping ratio (ζ_i) from the lateral vibration tests.

Table 1 shows the modal analysis results for the natural frequencies and the damping ratio up to the 5th mode. It is confirmed that the natural frequency decreases as the input force increases (the softening effect) except at the 2nd and 4th modes. They seem to be somewhat abnormal. The mode shapes are shown in Fig. 2 when the test assembly was vibrated with an excitation force of 7.5 N. The mode shapes at the odd numbers (Fig. 2(a); 1st, 3rd and 5th) look like a typical shape when a simply supported beam is vibrated. However, those at the even numbers (Fig. 2(b); 2nd and 4th) show somewhat distorted shapes.

This is attributed to the location of the input excitation as well as the nonlinear characteristic of a fuel assembly. It can be improved if the location of the excitation is altered from the nodal points.

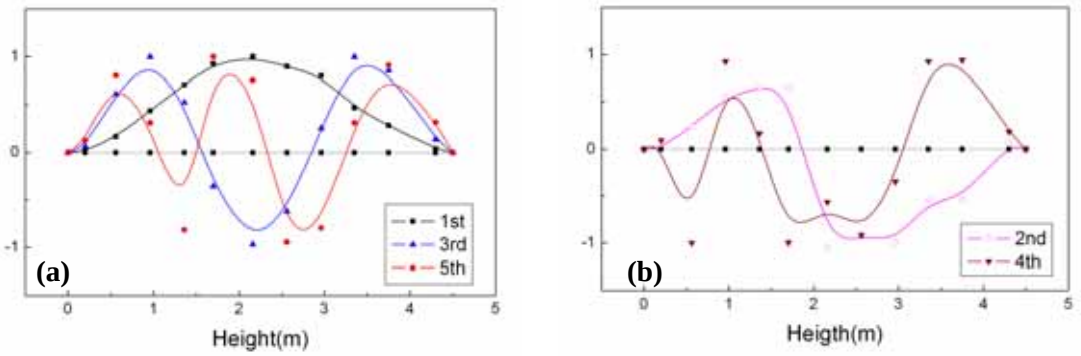

Fig. 2. Mode shapes from the lateral vibration tests: (a) for 1st, 3rd and 5th, (b) for 2nd and 4th.

3.3 Stiffness tests

In the stiffness test, a lateral load was applied at the 6th grid to deflect the test assembly. The deflections were varied as 2 ~ 20 mm. Fig. 3(a) shows the lateral load vs. deflection results at each spacer grid position. The force was measured at the 6th grid by a load cell (PCB 1344-01). The load vs. deflection characteristics was found to be non-linear mainly due to a fuel rod slippage at the grid-to-rod contacts. The fuel assembly did not return to its original position although it was fully unloaded due to the frictional forces of the fuel rods against the grids (i.e., springs/dimples). Also, Fig. 3(b) shows the FA deflection shape and magnitude along the FA height measured at the 6th grid.

Fig. 3 shows that the deflection of the upper part (higher than the 6th grid) was a little higher than that of the lower part (lower than the 6th grid). It may be caused by an upper end fitting assembly which is more flexible than a lower end fitting assembly. These characteristic behaviours (load vs. grid deflection, fuel assembly deflection shape) showed typical phenomena of a commercial fuel assembly. The strains of the guide tubes, instrumentation tube and the end pieces were monitored during the loading events. The membrane and bending stresses were calculated from the conventional formulae. It was confirmed that the bending and membrane stresses were within the elastic range of each material.

The test assembly may be somewhat deformed due to the previous tests. From the above vibration and stiffness test results with accommodating a possible deviation due to the pre-deformation, it was concluded that the FAMeCT was verified as a facility for a fuel assembly characterization.

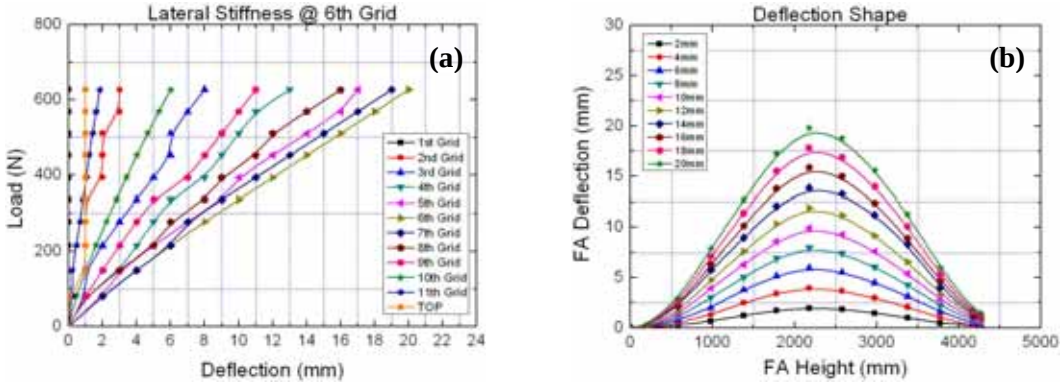

Fig. 3. Load vs. deflection results from the lateral stiffness tests: (a) stiffness, (b) deflection shape.

4. Finite Element Analysis

Fuel assembly is a sophisticated structure. It consists of a lengthy rod bundle which is in contact with a lot of supporting locations (i.e., more than 15500 spring and dimple contacts). It also has a lot of joints and connections with various clamping methods. Therefore, it is almost impossible to build a finite element (FE) model and boundary conditions to simulate the actual features of the aforementioned. It is true that the finite element analysis (FEA) can provide better results if the models and conditions are as close to the actual state as possible. So, the problem in the FEA for the fuel assembly behaviour is how to

build them with a consideration of a calculation economy and an acceptable error. This is only possible if the actual test data is available.

Since the fuel assembly test data was available, we attempted to tackle this task. In the present FEA, a 3-dimensional beam element was used for a fuel skeleton (without fuel rods) at first. Then, a rod which was equivalent to 59 fuel rods for a quarter of the fuel assembly cross section from the point of the 2nd moment of the inertia and its area. Resultantly, the model simplified the fuel assembly considerably. In the analysis, a commercial code, ANSYS [3] was used. The natural frequencies and the deflection shapes of a fuel assembly were obtained and compared with the vibration and the stiffness test results, respectively.

Table 2 shows the comparison of the natural frequencies obtained from the FEA and the vibration tests for the 1st ~ 3rd modes. It is found that the FEA results are closer to the test results at the lower modes. The increased discrepancy is due to the nonlinearity of the fuel structure. Fig. 4 illustrates the fuel assembly deflection shape by the FEA, which can be compared with Fig. 3(b). The overall shape is somewhat different from the test results. It was thought that the boundary conditions of the contacts needed to be amended. The FEA works are underway. Nevertheless, it is verified that the modelling works become much simpler due to the availability of our own test data when compared with the previous trials with an obscurity due to a lack of enough test data.

Mode	2N		5N		7.5N		10N		15N		20N	
	Test	FEA	Test	FEA	Test	FEA	Test	FEA	Test	FEA	Test	FEA
1st	2.41	2.39	2.20	2.27	2.16	2.16	2.12	2.13	2.04	2.06	1.98	2.03
2nd	4.22	4.63	3.32	4.34	4.29	4.07	4.17	3.98	4.01	3.79	4.00	3.67
3rd	9.08	9.94	9.03	9.01	8.98	8.27	8.88	8.03	8.83	7.47	8.65	7.13

Tab 2: Comparison of the natural frequencies obtained from the lateral vibration tests and FEA.

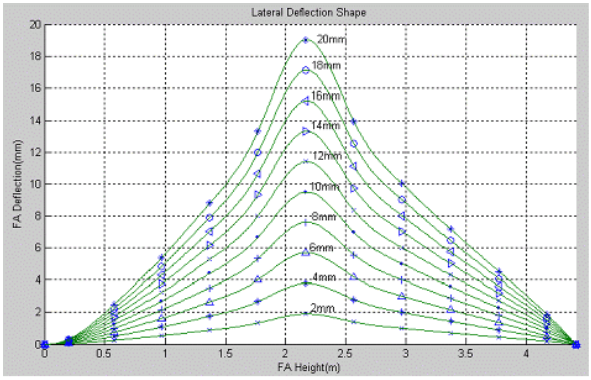

Fig. 4. Deflection shapes of a test fuel assembly evaluated from FEA.

5. Concluding Remarks

A fuel assembly characterization tester, the *FAMeCT* has been built at the KAERI, and the lateral vibration and stiffness tests were successfully completed for performance verification. It will be used for a licensing support and fuel R&D. It will also help in analysis works such as a finite element analysis.

6. Acknowledgements

This project has been carried out under the Nuclear R&D Program by MOST of Korea. Authors are grateful to Mr. Young-Ki Jang, Dr. Kyu-Tae Kim and their colleagues of the Korea Nuclear Fuel Co., Ltd. for their support on a test fuel assembly.

7. References

[1] Vishay Measurements Group Inc., 2001, “StrainSmart® User's Manual,” CT, USA.
[2] Structural Dynamics Research Corporation, 2002, "I-DEAS Master Series 9.0," OH, USA.
[3] ANSYS ver.5.7, “ANSYS User's Manuals”, ANSYS, Inc.

A SIMPLE MODEL OF THE ENHANCED CLADDING CORROSION IN PWRs

M. QUECEDO, A. SANCHEZ, J. ANDRES
Product Engineering, ENUSA Industrias Avanzadas S.A.
Santiago Rusiñol 12, 28040 Madrid-Spain

ABSTRACT

This paper proposes a simple model of Zr alloy corrosion under PWR conditions focusing on the prediction of the enhanced corrosion that may be observed under high burnup/duty operation. Based on the current knowledge of the mechanisms for the corrosion acceleration, the model is based on a mixing law of the corrosion rates of the Zr alloy and the hydrides that precipitate at the cladding metal-oxide interface. To calculate the hydride volumetric fraction at this interface a simplified model is proposed. The neutron effects on corrosion are incorporated in the Zr alloy corrosion rate using lower oxide thickness measured in a number of rods. Finally, the overall model capabilities to predict the enhanced uniform cladding corrosion sometimes observed in high burnup/duty rods are verified as well as the key role of the precipitated hydride corrosion in the overall cladding corrosion kinetics.

1. Introduction

The fuel cycle cost-effectiveness has been improved over the last decade in PWRs by reactor power uprate, higher peaking factors and coolant temperatures, longer residence times and higher lithium duties, among others. Under these severe irradiation conditions, even the improved Zircaloy-4 fuel rod cladding experiences an enhanced uniform corrosion, beyond the post-transition rate, that places significant limitations for an optimized fuel operation. Therefore, Zircaloy-4 has been gradually replaced by high corrosion resistance alloys such as ZIRLO.

In parallel, the industry has dedicated significant efforts to better understand the reasons of this enhanced uniform corrosion and references on these efforts abound. In this way, cladding materials may be further improved for the future operation conditions and the relevant phenomena incorporated in the predictive models used for fuel performance assessments and licensing calculations.

A number of mechanisms have been already proposed for this enhanced corrosion, among them, the detrimental effect of the hydrides precipitated in the metal-oxide interface has been pointed out as one of the key reasons. Indeed, the autoclave corrosion tests performed by several researchers, such as the pioneering work of Kido [1,2] and Garde[3], substantiated the detrimental role of the precipitated hydrogen in the corrosion performance of the zirconium alloys and proposed a model incorporating this effect.

Based on these early observations on the effect of hydrogen, this paper describes a tentative model to explain the acceleration, beyond the post-transition rate, of the in-reactor PWR uniform cladding corrosion.

For this purpose, the overall corrosion is modelled by considering a mixing law, based on the volumetric hydride fraction, of the corrosion rates of the zirconium alloy and the zirconium hydrides; the neutron irradiation effects being incorporated into the Zr alloy corrosion rate. While the thermal corrosion rates are obtained from autoclave tests, the determination of the hydride volume fraction at the metal-oxide interface, where the corrosion reaction takes place, requires solving the partial differential equation describing the thermally, under heat flux, assisted diffusion of hydrogen as well as its precipitation and dissolution. This equation solution should be coupled to the corrosion rate equation integration. However the necessary computer time for this equations solution is a drawback for industrial applications. Therefore, the authors have devised a simplified model of the hydrogen/hydride distribution in the cladding that can be solved using a combination of an analytical and a numerical method.

Once the neutron irradiation enhancement factors are incorporated into the Zr alloy thermal corrosion rate by using measured low thickness in-reactor data, the resulting model capability to predict oxide thicknesses is verified using further oxide thickness data obtained in the fuel inspections carried out on ZIRLO cladding in different Spanish PWRs. In this way, the model capabilities and the detrimental role in the cladding corrosion of the hydrides precipitated at the metal/oxide interface are verified.

2. Cladding corrosion model description

2.1 Model Equation

The cladding corrosion reaction produces hydrogen that is partially picked by the cladding. This absorbed hydrogen migrates through the cladding wall due to the existing concentration and thermal gradients. The thermally assisted migration of the hydrogen may be mathematically described using the principles of the non-equilibrium thermodynamics. However, as the heat of transport for a dilute zirconium alloy-hydrogen system is positive, the thermal transport pushes the hydrogen towards the cooler cladding waterside. As the solubility of the hydrogen in zirconium alloys is limited and drops with temperature, the precipitation terminal solid solubility may be reached at the cooler cladding outer side and zirconium hydride platelets may first precipitate at the metal-oxide, M/O, interface, where the cladding corrosion reaction takes place. Therefore, once hydrides precipitate the corrosion reaction involves a composite of the initial zirconium alloy, containing some hydrogen in solid solution, and the zirconium hydrides platelets.

Thus, the overall cladding corrosion rate may be described as

$$\frac{dw}{dt} = (1-f)\left.\frac{dw}{dt}\right|_{Zr\ alloy} + f\left.\frac{dw}{dt}\right|_{Zr\ Hydrides}$$

where f is the volumetric fraction of hydrides at M/O interface.

Now, assuming that the irradiation conditions, i.e. fast neutron flux/fluence, lithium content, etc., only affects the corrosion rate of the base alloy, the overall corrosion rate may be described as

$$\frac{dw}{dt} = (1-f)\,g(\Phi, Li, ..)\,h(Css)\,K\,e^{-\frac{Q}{RT}} + f\left.\frac{dw}{dt}\right|_{Zr\ Hydride}$$

where

- the g function brings the dependence of the Zr alloy corrosion on the relevant irradiation parameters. The simplest possibility is a multiplicative law of linear functions

$$g(\Phi, \phi, Li, ..) = \left(1 + A_{fluence}\Phi\right)\left(1 + A_{flux}\phi\right)\left(1 + A_{Li}\left[Li\right]\right)..$$

- the base alloy corrosion rate is determined by temperature, assuming an Arrhenius type dependence, and the hydrogen in solid solution, C_{ss}, at the M/O interface as brought by the function h(Css). A simple possible function is

$$h(Css) = (1 + A_{Css}Css)$$

Assuming the above mentioned dependencies on the irradiation parameters, the dependence on the dissolved hydrogen, A_{Css}, and the hydride corrosion rate may be determined from autoclave tests on cladding charged with different concentrations of hydrogen as it will be presented in a later section. Besides, it should be noted that the hydride corrosion rate should be independent of the Zr alloy composition, thus it may be used for the different dilute zirconium alloys.

2.2 Hydride fraction determination

A key variable in the proposed corrosion rate model is the hydride fraction, *f,* at M/O interface. The value of *f* may be calculated by solving the thermally assisted hydrogen migration differential equations, complemented by the boundary conditions, *i.e.* inward hydrogen flux, and temperature field.

As the hydrogen flux depends on the corrosion rate through the pick-up fraction, *F*, and the temperature field varies with time due to the heat flux history and the oxide layer growth, the hydrogen migration equations should be solved along the fuel rod life in a couple manner with the cladding corrosion rate integration. As this is a computer demanding task, the actual hydride fraction in the corrosion rate equation is approximated in this work by the one calculated assuming that the hydrogen flux inside the cladding

$$\vec{J} = -D\left(grad\, C_{ss} + \frac{Q^* C_{ss}}{RT^2} grad\, T \right)$$

is zero. From this assumption, the hydrogen profile is determined by the temperature field as

$$C_{ss}(r) = C_o\, e^{\frac{Q^*}{RT(r)}}$$

where the C_o integration constant is calculated to result in the total amount of hydrogen absorbed by the cladding up to that time (oxide thickness)

$$C_o = \frac{\frac{4}{123.2} F\, \rho_{ox} w \left(R_o - 0.67w\right)}{\rho_{Zr} \int_{Ri}^{R_o - 0.67w} r\, e^{\frac{Q^*}{RT(r)}} dr}$$

where R_o and R_i are the cladding outer and inside diameter respectively and the 0.67w term accounts for the metal loss in the corrosion reaction.

Once the hydrogen concentration becomes larger than the Zr-H precipitation solid solubility limit at a radial position R_{pr}, the above profile is only valid for $r \leq R_{pr}$. Considering a constant *f* for $r > R_{pr}$, the total hydrogen mass in the cladding may be calculated as

$$\frac{4}{123.2} F\, R_o\, w\, \rho_{ox} = R_o\, \delta\, f\, C_{hydride} \rho_{Zr} + C_o \rho_{Zr} \int_{Ri}^{R_o - 0.67w - \delta} r\, e^{\frac{Q^*}{RT(r)}}\, dr$$

where

- δ is the hydride rim thickness, R_o-0.67w-R_{pr}, and
- the integration constant Co may be calculated from the precipitation condition

$$C_o\, e^{\frac{Q^*}{RT(R_{pr})}} = A_{TSSpr} e^{-\frac{\Delta H}{RT(R_{pr})}}$$

Then, there are three unknowns, δ (or R_{pr}), *f* and C_o and two equations. Therefore, a relationship between the hydride rim thickness and the hydride fraction is assumed

$$f = 1 - e^{-k\delta}$$

where the parameter *k* is determined from the hydride rim characteristics (hydrogen content and thickness) measured in PWR irradiated rods. These three equations can be solved iteratively to determine the hydride volumetric fraction and, as a by-product, the hydride rim thickness.

3. Corrosion kinetics

The different material parameters involved in the model presented above have been obtained from autoclave test and from oxide thickness measured on PWR irradiated rods as presented next. Those material properties independent of the corrosion reaction have been taken from [4] and [5]. It should be noted that due to the very limited experimental available for the hydrogen heat of transport and for the $TSS_{pr,}$ this work considers unirradiated values.

3.1 Autoclave tests

In the absence of irradiation, the proposed corrosion rate model reduces to

$$\frac{dw}{dt} = \left(1 - f\right)\left(1 + A_{C_{ss}} C_{ss}\right) K\, e^{-\frac{Q}{RT}} + f \left.\frac{dw}{dt}\right|_{Zr\ Hydride}$$

For as-fabricated tubing, $C_{ss} \approx 0$ and f=0, this equation is the standard post-transition rate of a Zr alloy tested in autoclave. From the existing possibilities [6], the EPRI-KWU/CE [7] for Zr-4 has been selected with a reduced corrosion rate constant, K, to incorporate the lower corrosion rate for ZIRLO measured in autoclave tests [8].

The solid solution hydrogen enhancement, parameter A_{Css}, and the corrosion rate of the hydride have been determined from the autoclave test on pre-hydrided Zr-4 performed by Kido [1-2]. For this purpose, those samples with an initial hydrogen concentration below to the terminal solid solubility for precipitation, *i.e.* with f=0, are used to calculate A_{Css}. Then, the samples with the maximum initial

charged hydrogen were used to determine the hydride corrosion rate, keeping intermediate hydrogen charged samples for an independent verification of the fitting.
In this way, in the range of temperature and conditions of the tests (340ºC-400ºC)

- $A_{Css}=3.16\ 10^{-4}$ $[1/ppm]$
- $\left.\frac{dw}{dt}\right|_{Zr\ Hydride} = 4952\, e^{-\frac{4482}{T}} \left[mg/dm^2 - day\right]$

The calculated A_{Css} value suggests that the hydrogen in solid solution has only a reduced contribution to the overall cladding corrosion. However, the corrosion rate of the zirconium hydride is much larger than the corrosion rate of the Zr-4, up to a factor of 6 at 370ºC, and much less dependent on temperature. Therefore, for low hydride fractions, *f*, the overall corrosion rate remains basically the same as for the base alloy while as *f* increases, the overall corrosion rate becomes dominated by the hydride corrosion.

3.2 In-reactor enhancement factors

The in-reactor enhancement factors, *i.e.* attributed to the fast neutron fluence/flux and Litihum, have been quantified using the oxide profiles measured in a number of fuel rods irradiated in three different Spanish PWRs. The maximum measured oxide thickness on these rods is limited to 10-40 μm. In this way, based on the expected hydrogen content in the cladding and the typical cladding temperatures in a PWR, it may be expected that the hydride fraction at M/O interface is null or sufficiently low to prevent a significant contribution from the hydride rim. Thus, hydride acceleration is not expected to start or it is not significant for these rods. In this way, the enhancement factors will be attributed solely to the neutron irradiation effects.
The fuel under consideration is 16x16 and 17x17 standard diameter with standard ZIRLO cladded rods, achieving burnups of 35-45 MWdkgU and one rod at a lower, 15 MWd/kgU, burnup. Considering the thermal-hydraulic models used in [9] to calculate the coolant and cladding surface temperatures, the flux/fluence dependency factors have been determined to provide a best estimate of the rod maximum measured oxide thickness.

4. Extrapolation to higher oxide thickness

The model parameters determined as presented above have been used to predict the oxide thickness measured in two Spanish PWRs. In this case, the measured oxide thickness when extrapolated from the values measured in previous cycles indicated an enhanced corrosion.
Figure 1 depicts the model prediction for a representative 17x17 rod from the first plant and the measured oxide thickness on the set of rods. Also shown it is the model prediction removing the effect of the hydride corrosion on the overall corrosion, making evident the overall corrosion acceleration due to the hydride corrosion.
Figure 2 presents the model predictions for 16x16 rods measured in two set of fuel assemblies irradiated in symmetrical core positions during their first three cycles of irradiation while, during the last cycle, one fuel assembly was loaded at the core periphery and the other one in the core centre. Thus, the power histories of the concerned rods are significantly different during the last cycle. Again, there is a clear change in the predicted corrosion kinetics from the lower oxide thickness and the model adequately predicts the measured data.

5. Summary and conclusions

This paper describes a simple model of PWR in-reactor corrosion. The main feature of the model is the separation of the hydride and base alloy corrosion using a simple mixing law and an approximate calculation of the hydride content at the metal-oxide interface. Based on existing autoclave corrosion information on prehydrided samples, the hydride corrosion rate has been determined and confirmed to be, as expected, larger than the base alloy corrosion.
Using measured oxide thickness on rods irradiated in different Spanish PWRs, below or at the second transition point, the fast neutron flux/fluence enhancement factors have been determined. Then, the resulting model has been used to predict in-reactor measured data beyond this second transition point. The analyses of the results seem to indicate that the hydride rim in the metal-oxide interface is an explanation for the corrosion acceleration of the third stage of the in-reactor Zr-alloys corrosion process.

Further knowledge of the thermally assisted migration and dissolution/precipitation kinetics of hydrogen in Zr-alloys under irradiation as well as on the hydride corrosion rate would help for further modelling efforts.

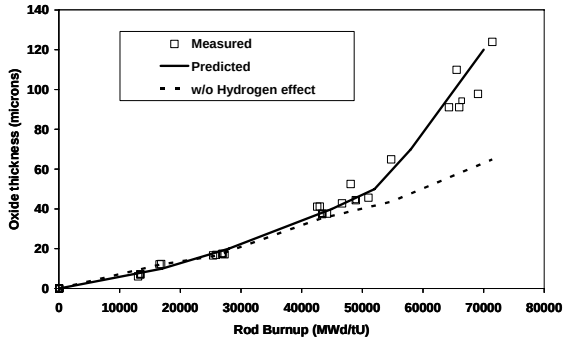

Fig. 1.- Model predictions of high burnup 17x17 rods.

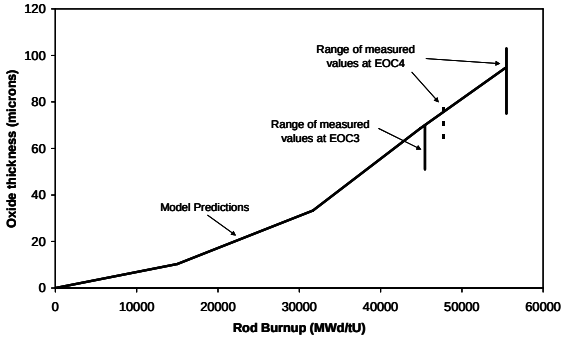

Fig. 2.- Model predictions on high duty 16x16 fuel.

6. Acknowledgments

The authors appreciate the excellent collaboration of ANAV and CNAT in the on-site inspection campaigns that have provided valuable experimental data to improve the understanding of Zr-alloys corrosion in PWR conditions.

7. References

1. Kido,T., "A study on enhanced uniform corrosion of Zircaloy-4 cladding during high burnup operation in PWRs", *Proceedings of the Sixth International Symposium on Enviromental Degradation of Materials in Nuclear Power Systems*, sponsored by TMS, ANS and NACE., San Diego, August 1-5, 1993.
2. Kido, T., Kanasugi, K., Sugano, M., Komatsu, K., "PWR Zircaloy cladding corrosion behaviour: quantitative analyses", J. Nuc. Mat. 248 (1997) 281-287.
3. Garde, A.M., "Enhancement of aqueous corrosion of Zircaloy-4 due to the hydride precipitation at the metal-oxide interface", *Zirconium in the Nuclear Industry: Ninth International Symposium, ASTM STP 1132*, C.M. Eucken and A.M. Garde, Eds. ASTM, 1991, pp. 566-594.
4. Kammenzind, B.F., Franklin, D.G., Peters, H.R., Duffin, W.J., "Hydrogen pickup and redistribution in alpha-annealed Zircaloy-4", *Zirconium in the Nuclear Industry: Eleventh International Symposium, ASTM STP 1295*, E.R. Bradley and G.P. Sabol, Eds. ASTM, 1996, pp. 338-370.
5. "SCDAP/RELAP5-3D Code Manual, Vol. 4: MATPRO-A library of materials properties for light-water reactor accident analysis", INEEL/EXT-02-00589 rev.0, May 2002.
6. "Waterside corrosion of zirconium alloys in nuclear power plants", IAEA-TECDOC-996, 1998.
7. Garzarolli, F., Jorde, D., Manzel, R., Parry, G.W., Smerd, P.G., "Review of PWR Fuel Rod Waterside Corrosion Behaviour", EPRI NP-1472, 1980.
8. Sabol , G.P., Kilp, G.R., Balfour, M.G., and Roberts, E.,"Development of a cladding Alloy for High Burnup", *Zirconium in the Nuclear Industry: Eight International Symposium*, *ASTM STP 1023*, L.F.P. Swam and C.M. Eucken, Eds. ASTM, Philadelphia, 1989, pp. 227-244.
9. Quecedo, M., Serna, J.J., Weiner, R.A., Kersting, P.J., "A systematic approach for development of a PWR cladding corrosion model", in "Nuclear fuel behaviour modelling at high burnup and its experimental support", IAEA-TECDOC-1233, July 2001.

CALCULATION WITH MCNP OF REACTIVITY AND POWER DISTRIBUTION OF ATRIUM-10XP DESIGN AND COMPARISON WITH ISOTOPICS OBTAINED WITH MONTEBURNS, MCNP-ACAB AND CASMO4

P. ORTEGO, C. TÖRE
SEA, Ingeniería y Análisis de Blindajes
Av. Atenas 75, 28232 Las Rozas, Madrid –Spain

A. CRESPO
IBERINCO
Av. Burgos 8B, 28036, Madrid –Spain

P. MATA, L. GARCIA-DELGADO
IBERDROLA Generación
C/ Tomás Redondo 1 , 28033, Madrid –Spain

O. CABELLOS, N. GARCIA-HERRANZ, J. SANZ
Instituto de Fusión Nuclear, Universidad Politécnica de Madrid
José Abascal 2,28006 Madrid –Spain

ABSTRACT

GIRALDA methodology, used routinely for BWR fuel reload design of Cofrentes NPP, licensed by CSN, includes the requirement of performing a comparison of the reactivity and power distribution computed with the code used by the fuel supplier and with other independent code. This is applied to every new fuel design inserted in the core. The reference code should have been qualified with power distribution measurements and with critical experiments.

This requirement has been met for cycle 16 of Cofrentes NPP by using MCNP as the neutronic code of reference, modelling in full detail the physical characteristics of the ATRIUM-10XP design. The isotopic evolution along the fuel depletion has been obtained with two different codes, MONTEBURNS and MCNP-ACAB.

The reactivity and power distribution results obtained with CASMO4 for different burnup steps are compared with those obtained by MCNP by using the main isotopics provided by MONTEBURNS. The comparison is performed at different void fraction and control conditions. The differences between MONTEBURNS and MCNP-ACAB for some transuranic elements are highlighted, and those for Americium isotopes are detailed.

1. Introduction

GIRALDA methodology, presently used for the licensing of BWR fuel reload with the Spain regulatory authority (CSN), requires the verification of reactivity and power distribution results by comparison with a reference calculation code, usually that used by the fuel manufacturer. In the case of the introduction of ATRIUM-10XP in Cofrentes NPP, this requirement has been satisfied by comparing CASMO-4 results with Los Alamos MonteCarlo code MCNP.

In order to perform an independent comparison also in the isotopics evolution with burnup, different depletion systems based on MCNP are used. These are the code Los Alamos code MONTEBURNS and the code system MCNP-ACAP developed in Madrid Polythecnic University based on the ACAB code, a well known reference in the area of neutron activation in fusion reactors.

2. Description of calculation codes and of the fuel assembly

CASMO-4 [1] is a well known proprietary code routinely used for PWR and BWR fuel design. MCNP is a family of codes well known in different applications such as criticality and fixed source neutron transport, gamma shielding and photon-electron interaction. Version MCNP-4B [2] has been extensively benchmarked by SEA with a wide set of critical experiments including those of ICSBEP Handbook. MONTEBURNS [3] is a combination of MCNP and ORIGEN codes, which calculates the one-group cross-sections to be used by ORIGEN and updates the isotopic composition for MCNP.

MCNP-ACAB [4] is a system that links MCNP and the inventory ACAB code [5] using a coupling procedure similar to that MONTEBURNS. However, ACAB is able to compute the isotopic inventory dealing with all nuclear processes that can occur (with ORIGEN only six different neutron reactions are treated if no additional ones are specified by the user). For that, the activation cross sections for the reactions and nuclides not provided by MCNP are obtained by collapsing the activation cross section library with the MCNP flux spectrum. Moreover, by means of ACAB capabilities, the system enables to assess the impact of neutron cross-section uncertainties on the inventory and other inventory-related responses.

The ATRIUM-10XP fuel assembly design is the most advanced AREVA fuel design for BWR reactors. It has an array of 10x10 fuel rods with a central channel occupying 9 rod positions. Two different regions are distinguished along its height due to the presence of 10 part length rods. Pellet enrichment is constant axially for each different rod.

3. Reactivity and fission density results for fresh fuel

Eigenvalue calculations have been performed with CASMO-4 and MCNP-4B for both axial regions of the ATRIUM-10XP design inserted in cycle 16 of Cofrentes NPP. Results of k-effective are obtained at full power with different void fractions, at hot standby conditions and at cold conditions with control rods either inserted or withdrawn. The results are presented in Tables 1 and 2. It is seen the good agreement in reactivity, especially for the highest void fraction. Except for the case of 0% void, all the differences are lower than 0.8%. The results for radial distribution of fission density are compared in Table 3.

Condition	CASMO-4	MCNP4B	diff.
Hot full power 0%VF	1.0404	1.0509	1.05%
Hot full power 40%VF	1.0223	1.0289	0.66%
Hot full power 80%VF	1.0000	1.0009	0.09%
Zero power 0%VF, CRin	0.8460	0.8503	0.43%
Cold, All Rods Out	1.1013	1.1077	0.64%
Cold, CRin	0.9310	0.9345	0.35%

Tab 1: Reactivity comparison for lower region

Condition	CASMO-4	MCNP4B	diff.
Hot full power 0%VF	1.0015	1.0125	1.10%
Hot full power 40%VF	0.9862	0.9943	0.81%
Hot full power 80%VF	0.9656	0.9688	0.32%
Zero power 0%VF, CRin	0.8083	0.8138	0.55%
Cold, All Rods Out	1.0564	1.0623	0.59%
Cold, CRin	0.8883	0.8917	0.34%

Tab 2: Reactivity comparison for upper region

-0.3									
-0.1	-0.3								
0.1	-0.4	-1.2							
1.0	-0.6	-0.2	-0.3						
1.6	-0.1	-0.8	-0.8						
1.4	0.1	-0.5	-0.6						
1.1	0.0	-0.1	-0.5						
0.4	-0.6	-0.9	0.5	-0.3	-0.3	0.1	-0.9		
0.2	0.1	-0.2	-0.5	-0.3	-0.5	-0.6	-0.3	-0.4	
-0.1	-0.2	0.3	0.6	1.4	1.4	0.5	0.3	-0.2	0.1

Table 3: Differences in fission density for lower region at HFP, 40% VF

4. Calculations for burnt fuel

Comparison calculations between CASMO-4 and MCNP-4B have been performed at different burnup steps for the lower region of the assembly. The isotopic composition used in MCNP-4B has been obtained with the use of MONTEBURNS. It has been run in a PC for 3 days with 60 depletion steps and 24000 neutrons per step. Fuel has been depleted at hot full power with a fixed void fraction of 40%. Except for the gadolinium rods where some lumping was required, the fuel rods are modelled individually. The differences in K-effective are presented in Table 4. The differences are very small even for the burnup steps where the depletion of gadolinium is more critical.

The differences in fission density distribution are presented in Tables 5 to 7 for different burnup steps and with an instantaneous void fraction of 40%. It is seen a small difference in rod-by-rod power even for the gadolinium rods (marked in bold characters).

Burnup (GWd/tU)	**HFP 0% VF**	**HFP, 40% VF**	**HFP 80% VF**	**HZP, CRin**	**CZP ARO**	**CZP CRin**
5	-0.46	-0.20	0.44	-0.14	-0.01	0.14
10	-0.21	0.13	0.74	0.12	0.28	0.42
15	-0.60	-0.23	0.43	-0.16	-0.05	0.08
20	-0.55	-0.19	0.60	-0.01	-0.06	0.21
30	-0.26	0.13	0.83	0.03	0.44	0.46
40	-0.18	0.21	0.95	-0.05	0.34	0.38
50	-0.29	0.11	0.82	-0.33	0.09	-0.05
60	-0.54	-0.09	0.69	-0.70	-0.38	-0.49

Table 4: Differences in reactivity along burnup (CASMO – MCNP, in %)

-1.6									
-0.2	-0.9								
0.4	0.4	0.4							
0.7	**-1.8**	0.6	**0.0**						
1.5	1.2	0.4	0.4						
1.0	1.0	**-0.7**	0.7						
0.7	0.2	0.9	**0.4**						
1.0	**-2.4**	0.0	0.6	0.5	0.3	0.3	**-3.7**		
-0.4	0.2	0.2	**-1.9**	0.6	0.1	**-2.2**	-0.5	-0.8	
-0.9	-0.6	-0.2	0.2	0.8	0.6	0.0	0.2	-0.7	-1.0

Table 5: Fission density differences at 15 GWd/MTU

-1.6									

-1.2	-0.3								
0.8	0.5	0.4							
0.6	**-2.6**	0.1	**-0.4**						
0.6	1.4	0.6	-0.2						
1.6	1.3	**-1.1**	0.0						
0.8	-0.3	0.7	**-0.8**						
0.3	**-1.0**	0.6	0.7	0.6	-0.2	0.4	**-1.6**		
-0.2	0.3	0.4	**-0.1**	0.5	-0.2	**-2.6**	0.0	-0.3	
-0.6	-0.5	0.4	-0.1	0.8	0.1	0.6	0.1	-0.5	-1.2

Table 6: Fission density differences at 20 GWd/MTU

-3.1									
-1.5	-0.6								
-0.9	0.3	1.4							
-1.1	**1.5**	2.3	**3.0**						
-0.9	3.2	2.0	1.3						
0.4	2.4	**0.5**	0.9						
0.0	-1.6	1.9	**-2.1**						
-0.7	**-0.9**	2.1	1.7	0.6	1.1	0.9	**1.5**		
-0.1	-0.4	1.2	**0.8**	2.5	-0.7	**-1.3**	-0.4	-1.2	
-2.9	-2.9	-1.1	-0.6	0.4	-1.0	-1.5	-1.8	-2.8	-3.3

Table 7: Fission density differences at 60 GWd/MTU

5. Comparison of isotopics from MCNP-ACAB and MONTEBURNS

All the MCNP-ACAB system has been run under linux, in a 4 CPU cluster. The MCNP code (version 4C3) has been compiled in parallel with PVM. The sequence of alternating neutron flux spectrum and burnup step calculations is being also parallelized. The complete calculation (60 burnup steps) has taken 9.5 hours with 200 000 neutron histories per step.

For comparison purposes, MCNP-ACAB has been run using the same nuclear data that MONTEBURNS. Then, a MCNP-ACAB calculation has been performed taking the nuclear libraries used by MONTEBURNS, both transport cross-section and one-group activation libraries. That is, in the burnup calculations performed by ACAB, the one-group cross sections not provided by MCNP are taken from the ORIGEN one-group cross section library BWRU.LIB and the decay data are taken from DECAY.LIB. This means that the same cross sections, fission yields and decay data are used.

The comparison of k-eff shows a very good agreement with MONTEBURNS, being the maximum eigenvalue difference +0.007. The isotopic evolution predicted by both codes is very similar for most nuclides. There are no important differences in calculated densities of ^{235}U, ^{239}Pu or ^{241}Pu. However, differences in the inventory of some actinides reach up to 90% (^{244}Cm). These differences are due to a bad treatment of the isomeric transitions by MONTEBURNS, where the cross sections for ORIGEN leading to ground states are updated with the MCNP-total cross sections.

To confirm this issue, the concentration of ^{243}Am is represented along burnup. The depletion of ^{243}Am is mainly due to: $^{243}Am(n,\gamma)$ and $^{243}Am(n,\gamma\text{-}m)$. Taking into account proper branching ratios in the ^{243}Am capture reaction, MCNP-ACAB predicts an isotopic concentration 37% higher than MONTEBURNS at 60 GWd/tU. MONTEBURNS overestimates the $^{243}Am(n,\gamma)$ reaction, resulting in an underestimated ^{243}Am concentration. Consequently, a correct branching evaluation is needed to predict accurately the isotopic inventory produced via isomeric transitions.

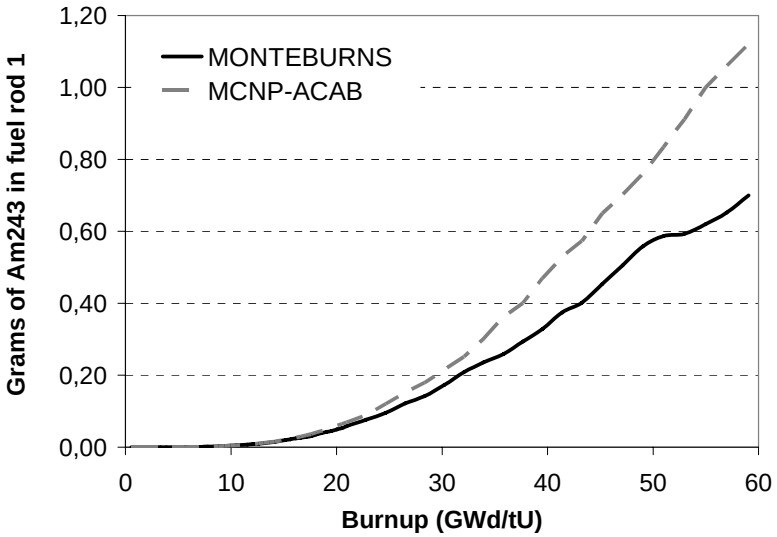

Fig 1. Difference in Am-243 concentration between MONTEBURNS and MCNP-ACAB

6. Conclusions

CASMO-4 slightly underestimates the reactivity of fresh fuel, when compared with MCNP. Along burnup CASMO-4 underestimates reactivity for low void fraction and opposite for high void. Differences are very small and always lower than 1%. The distribution of fission density is very similar even for the gadolinium rods, where significant differences have been found before [6]. This successful result has been obtained by segmenting the gadolinium rods in radial layers (onion rings).

Comparisons between MCNP-ACAB and MONTEBURNS, using the same nuclear data libraries, show a good agreement. Discrepancies in results can be attributed to the different modelling of reaction paths, and to the different branching ratios treatment.

7. References

1. STUDSVIK/SOA-95/1 “CASMO-4. A fuel assembly burnup program. User´s Manual”

2. J.F. Briesmeister, Ed. “MCNP - A General Monte Carlo N-Particle Transport Code” Version 4B. Los Alamos National Laboratory. 1991.

3. D. Poston, H. Trellue. “User`s Manual, Version 2.0 for MONTEBURNS, Version 1.0, Los Alamos National Laboratory Report LA-UR-99-4999, September 1999.

4. N. García-Herranz, O. Cabellos, J. Sanz. “Applicability of the MCNP-ACAB System to Inventory Prediction in High-Burnup Fuels: Sensitivity and Uncertainty Estimates” Internacional Conference on Mathematics and Computation, Supercomputing, Reactor-Physics and Biological Applications (MC2005), Avignon (France), Sept. 12-17th, 2005.

5. J. Sanz. “ACAB Activation Code for Fusion Applications: User’s manual V5.0” UCRL-MA-143238, Lawrence Livermore National Laboratory (Feb. 2000).

6. M. Anttila, A. Ranta-aho “Burnup Calculations for a 10x10 BWR Assembly – Comparison of CASMO-4, Monteburns 1.0 and MCB Results”. CMS European Users Group Meeting, Turku, Finland, 19-21st April, 2004.

IMPROVEMENTS IN THE FISSION GAS RELEASE MODULE OF THE FUEL BEHAVIOUR CODE FUROM

K. KULACSY, Á. GRIGER
MTA KFKI Atomic Energy Research Institute
29-33 Konkoly Thege Miklós út, H-1121 – Hungary

ABSTRACT

The code FUROM (FUel ROd Model) is a fuel behaviour code based on the Czech code PIN MICRO and improved at the MTA KFKI Atomic Energy Research Institute. Several features have been added to the code lately, e.g. an up-to-date rim model, but so far only the release of the thermo-mechanically relevant stable or very long-lived fission gases was taken into account.
In the present work we extend the release model to the gaseous radioactive species of interest.

1. Introduction

The fission gas content of the fuel-to-cladding gap of PWR fuel rods is of great importance, since it has a major effect on the thermal conductivity of the gap, therefore on the temperature of the fuel. As the thermo-mechanical properties of the fuel rods are mainly determined by the stable or very long-lived fission gases, only these are taken into account in most of the fuel behaviour codes, including the code FUROM. In the case of a fuel failure, however, the activity of the primary coolant is determined by the activity of the fuel-to-cladding gap, which thus becomes the source term for all further calculations. A series of improvements has therefore been started to extend the fission gas release model of the code FUROM to radioactive species, and to make it more accurate.

2. The original model

The fission gas release model of the code FUROM [1] is based on the MacDonald-Weisman model [2]. The fuel pellet is considered to consist of spherical grains, and the gas released from these grains appears at once in the fuel-to-cladding gap, i.e. no intergranular processes are taken into account. The amount of gas released from the grain within a time interval Δt is

$$\Delta m = \beta\left[\Delta t - \tau_s(1-k')\left(1-e^{-\Delta t/\tau_s}\right)\right] + \bar{c}_n\left(1-e^{-\Delta t/\tau_s}\right), \tag{2.1}$$

where

Δm is the amount of gas leaving the grain within a time interval Δt,

k' is the proportion of the gas that reaches the grain boundary directly,

k'' is the probability per unit time that gas trapped in the intragranular bubbles is resolved,

$1/\tau_s \equiv k \equiv k'k''$, and

$\bar{c}_n$ is the local average concentration of the gas (in solution + in bubbles).

This leads to a stepwise formula for the fractional release f_i:

$$f_{n+1} = 1 + f_n \frac{FA_n}{FA_{n+1}} e^{-\Delta t/\tau_s} - \frac{FA_n}{FA_{n+1}} e^{-\Delta t/\tau_s} - (1-k')\left(1-\frac{FA_n}{FA_{n+1}}\right)\frac{1-e^{-\Delta t/\tau_s}}{\frac{\Delta t}{\tau_s}}, \tag{2.2}$$

where

FA_i is the inventory of the given isotope in time step *i*

This model corresponds more or less to the quadratic approximation

$$c(r,t) = b(t)\left(a^2 - r^2\right)$$

to the solution of the diffusion equation

$$\frac{\partial c}{\partial t} = D\left(\frac{\partial^2 c}{\partial r^2} + \frac{2}{r}\frac{\partial c}{\partial r}\right) + \beta\,, \tag{2.3}$$

where

c is the concentration of the gas in the fuel (in solution + in bubbles),

D is the effective (measured) diffusion coefficient

β is the production rate of the given isotope per unit volume.

The exact solution of this equation was worked out by Booth [3] and contains infinite series. Moreover, it is difficult to use for varying power histories, since it does not yield a stepwise algorithm. On the other hand, the MacDonald-Weisman model is known to give lower releases than the exact solution. This lower release is compensated for by a higher numerical value of the diffusion coefficient. The overall performance of the model is surprisingly good when tested against measured data.

3. Extension to radioactive species

For radioactive species, the diffusion equation (2.3) becomes

$$\frac{\partial c}{\partial t} = D\left(\frac{\partial^2 c}{\partial r^2} + \frac{2}{r}\frac{\partial c}{\partial r}\right) + \beta - \xi c\,, \tag{3.1}$$

where

$\xi = \lambda + \nu$ is the “disappearance” (decay + activation) constant of the given isotope.

We then apply the same quadratic approximation to this equation and calculate the concentration of the gas released from the fuel. This time, however, the concentration of the gas in the gap obeys the balance equation

$$\frac{dg}{dt} = \frac{dm}{dt} - \xi g\,, \tag{3.2}$$

where

g is the concentration of the gas in the gap and

$\frac{dm}{dt}$ is the release rate of the gas from the grain.

The resulting fractional release is

$$\begin{aligned} f_{n+1} = {} & f_n \frac{FA_n}{FA_{n+1}} e^{-\Delta t/\tau_r} - \frac{FA_n}{FA_{n+1}}\left(e^{-\Delta t/\tau_r} - e^{-\xi\Delta t}\right) + \\ & + \frac{1}{FA_{n+1}}\beta\left[(1-k')\tau_r e^{-\Delta t/\tau_r} - \frac{1}{\xi}e^{-\xi\Delta t} + \tau_r\left(\frac{1}{\xi\tau_s} + k'\right)\right], \end{aligned} \tag{3.3}$$

where

$$\tau_r = \frac{\tau_s}{1+\xi\tau_s} \text{ and}$$

$$\beta = \frac{FA_{n+1} - FA_n}{\Delta t} + FA_n\xi\,.$$

4. The precursor effect

The release of a given isotope is not the same when it comes directly from fission as when from the decay of a precursor atom. If there is a relatively long-lived precursor in the decay chain leading to the given isotope, it also diffuses towards the grain boundary, which leads to a higher release of the

daughter isotope. Within the framework of the Booth model, a precursor factor can be introduced [4]. In our quadratic approximation, however, the precursor effect has to be calculated by solving the coupled equations

$$\begin{aligned}\frac{\partial c_1}{\partial t} &= D_1\left(\frac{\partial^2 c_1}{\partial r^2}+\frac{2}{r}\frac{\partial c_1}{\partial r}\right)-\xi_1 c_1+\beta_1\\ \frac{\partial c_2}{\partial t} &= D_2\left(\frac{\partial^2 c_2}{\partial r^2}+\frac{2}{r}\frac{\partial c_2}{\partial r}\right)-\xi_2 c_2+\lambda_1 c_1+\beta_2\end{aligned}, \tag{4.1}$$

where the indices 1 and 2 denote the precursor and the daughter, respectively. Fortunately in the decay chains of the isotopes of interest, there is never more than one long-lived precursor, two coupled equations are therefore sufficient for the calculations. Following the same procedure as in Section 3, the set of equations can be solved, then the decay of the gas in the gap can be taken into account, and the result for the fractional release of the daughter becomes

$$\begin{aligned}f_{2,n+1} = {} & f_{2,n}\frac{FA_{2,n}}{FA_{2,n+1}}e^{-\Delta t/\tau_2}+f_{1,n}\frac{FA_{1,n}}{FA_{2,n+1}}U+\frac{FA_{2,n}}{FA_{2,n+1}}\left(e^{-\xi_2\Delta t}-e^{-\Delta t/\tau_2}\right)+\\ & +\frac{FA_{1,n}}{FA_{2,n+1}}\left[\frac{\lambda_1}{\xi_2-\xi_1}\left(e^{-\xi_1\Delta t}-e^{-\xi_2\Delta t}\right)-U\right]+\frac{\beta_1}{FA_{2,n+1}}V+\frac{\beta_2}{FA_{2,n+1}}W\end{aligned}, \tag{4.2}$$

where

$$\begin{aligned}U = {} & (1-k')\frac{\lambda_1\tau_1\tau_2}{\tau_1-\tau_2}\left(e^{-\xi_2\Delta t}-e^{-\Delta t/\tau_2}\right)-\\ & -\frac{1}{\xi_2-\frac{1}{\tau_1}}\left[(1-k')\frac{\lambda_1\tau_1\tau_2}{\tau_s(\tau_1-\tau_2)}-\lambda_1\right]\left(e^{-\Delta t/\tau_1}-e^{-\xi_2\Delta t}\right),\end{aligned}$$

$$\begin{aligned}V = {} & -\frac{\lambda_1}{\xi_1(\xi_2-\xi_1)}\left(e^{-\xi_1\Delta t}-e^{-\xi_2\Delta t}\right)+\\ & +(1-k')^2\lambda_1\tau_1\tau_2\left[\frac{\tau_1}{\tau_1-\tau_2}-1\right]\left(e^{-\xi_2\Delta t}-e^{-\Delta t/\tau_2}\right)+\\ & +\frac{(1-k')\lambda_1\tau_1}{\xi_2-\frac{1}{\tau_1}}\left[(1-k')\frac{\tau_1\tau_2}{\tau_s(\tau_1-\tau_2)}+1\right]\left(e^{-\Delta t/\tau_1}-e^{-\xi_2\Delta t}\right)+\\ & +\frac{\lambda_1\tau_1}{\xi_2}\left[(1-k')^2\frac{\tau_2}{\tau_s}+\frac{1}{\xi_1\tau_s}+k'\right]\left(1-e^{-\xi_2\Delta t}\right),\end{aligned}$$

$$W = -\frac{1}{\xi_2}e^{-\xi_2\Delta t}+\tau_2 e^{-\Delta t/\tau_2}+\frac{\tau_2}{\tau_s}+k'\tau_2\left(1-e^{-\Delta t/\tau_2}\right),$$

$$\tau_i = \frac{\tau_s}{1+\xi_i\tau_s}.$$

The fractional release of the precursor is given by Eq.(3.3).

5. Comparison of the quadratic approximation to the exact solution

The following figure [5] demonstrates an example for the approximation made when applying the MacDonald-Weisman model.

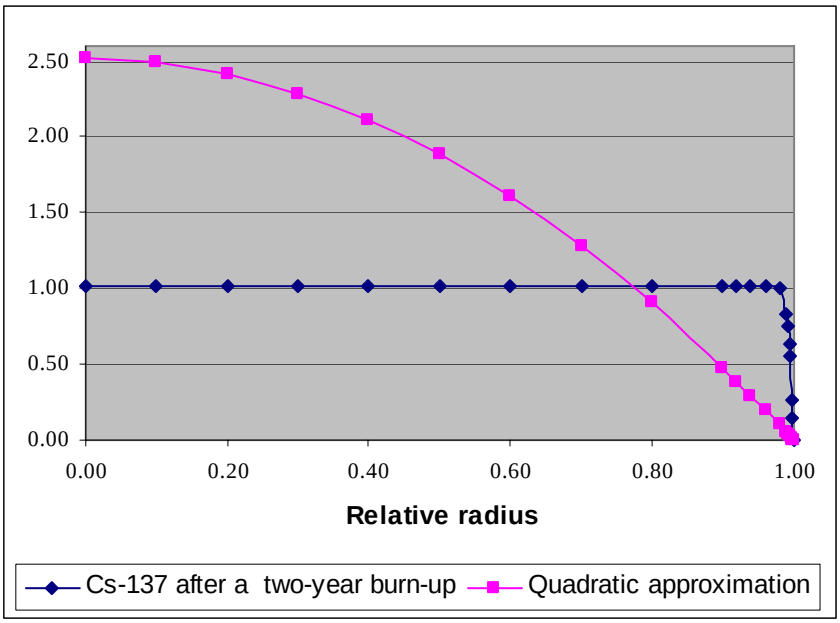

Fig. 1. Normalised radial distributions within the grain (constant power history)

It is clear that the gradient of the concentration, which determines the flux of atoms leaving the grain, is much smaller for the quadratic curve than for the true one. This is balanced by a higher value of the diffusion coefficient to yield results in line with the measurements. A more accurate model is nevertheless necessary.

6. Future work

A two-step release model is under development at AEKI, including a more accurate diffusion model as well as an intra-granular module, which will account for the incubation phenomenon.

7. Summary

The MacDonald-Weisman model is suitable for modelling the fission gas release with a diffusion coefficient higher than in reality. It has been extended to radioactive species as well, including the special case when a long-lived precursor affects the release rate of a certain isotope.

8. References

[1] Á. Griger, J. Gadó: Description of the code FUROM-1.2, AEKI-FRL-2006-719-1.2, Budapest, March 2006 (in Hungarian)
[2] J. Weisman, P.E. Macdonald, A. Miller, H.M. Ferrari, ANS Trans. 12 (1969) 900
[3] A.H. Booth: A method of calculating fission gas diffusion from UO_2 fuel and its application to the X-2-f loop test, AECL, CRDC-721, Chalk River, Ontario, September 1957
[4] B.J. Lewis, C.R. Phillips, M.J.F. Notley: A model for the release of radioactive krypton, xenon, and iodine from defective UO_2 fuel elements, Nucl. Techn. 73, pp. 72-83 (1986)
[5] Courtesy of A. Keresztúri

3D FEM BASED FUEL ROD SIMULATOR FRA-TF

M. DOSTÁL, M. VALACH, J. ZYMÁK
Reactor technology department, Nuclear Research Institute Řež plc
Husinec-Řež 130, 250 68 Husinec-Řež – Czech Republic

R. SVOBODA
ČEZ a.s., NPP Temelín

ABSTRACT

Paper briefly describes first phase of industry oriented development of FEM based Fuel Rod Analyser - FRA - TF (TF for thermo-physical part). Simulator is designed to calculate 3D steady state and transient temperature field in Temelín VVANTAGE Fuel Rod with all temperature dependent material properties, 3D thermal power sources and anisotropic initial and boundary conditions.
Paper summarizes modelling approach used in the COSMOSM/COSMOSDesignSTAR S.R.A.C. FEM software from mesh generation in separate objects to the materials properties libraries.
Practical implementation and fuel rod behaviour simulations are presented on detailed studies of fresh and highly burned fuel rod configurations, and the typical Temelín Fuel Rod irradiation history simulation.
In conclusion are summarised practical experience and limitations from development and implementation phases.
Practical examples are prepared for fresh and burned fuel rod configurations. Modelling of real length of fuel rod and local effects on temperatures are graphically presented as our approach to "real" 3D modelling at poster.

1. Introduction

Condition of raised loading is thermophysically and mechanically expressed in higher probability of cladding failure especially during power manoeuvring. Paper briefly presents development of 2D and 3D FEM based models partially dealing with this problem. Industrial application – 3D model of the whole fuel rod for simulation of thermo-physical behaviour is demonstrated.

2. Development from 2D to 3D models

Papers presented earlier at different conferences [9], [10], [11] and [12] documented our development from particular 2D models to the more complex 3D models.
The problem has been solved by means of the COSMOSM [6] and COSMOSDesignSTAR [7] software systems. It is a complete, modular finite element system, which includes various modules for thermal heat transfer and structure mechanics problems.

2.1 „3D anizotropic" steady state thermal calculations with 3D half pellet model

Advanced („more realistic") 3D configuration model of the half pellet with cladding was natural next development step to simulate behaviour of fractured pellet. Model of the pellet is created by rotation of 2D half-pellet-region, that consists of three equal volume fractured parts bonded together in the middle two thirds of radius and with three radial cracks at the outer third of radius. At the bottom of the pellet there is a tangential crack representation also. All gaps are filled with helium or mixture of

gases (in case of burned configuration). Optionally, inner and outer ZrO_2 layer on cladding is also incorporated.
For finite element mesh were used 8-node solid elements. In the radial direction there are 33 elements in the pellet, 1 in the gap and 13 in the cladding and in the axial direction 50 in all substances. Total number of elements thus reaches almost 75 000.

2.2 Parametric 3D calculations

The postulated nominal case has heat sources that correspond to the linear heat rate of 300 W/cm. This value is considerably higher than average LHR in the NPP Temelín (158,6 W/cm). The maximum temperature in the middle of the pellet is 1721 K. All parametric calculations are related to this value.
Results of this calculation are presented on the following figures (Figure 1-4) that show graphical possibilities of the COSMOSM system also.

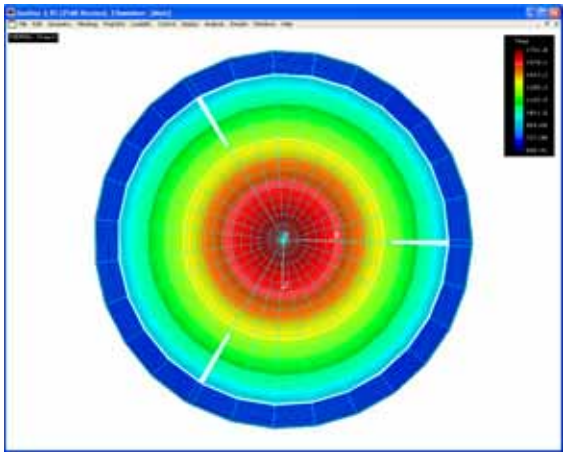

Fig 1. 3D nominal calculation – LHR 300 W/cm – top view

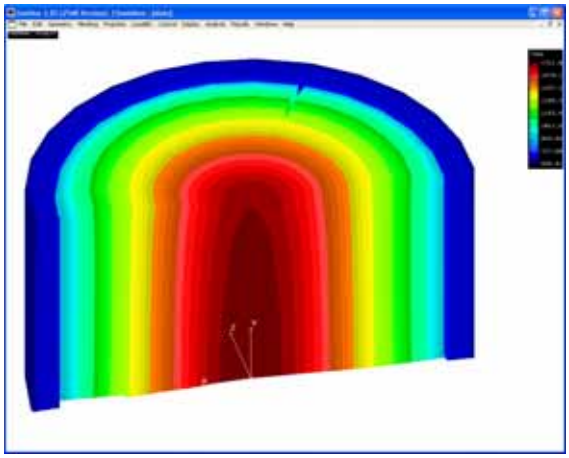

Fig 2. 3D nominal calculation – LHR 300 W/cm – 3D view on the cuted object

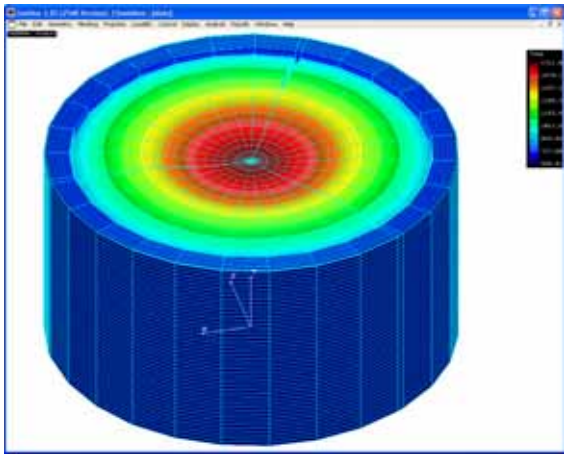

Fig 3. 3D nominal calculation – LHR 300 W/cm – izometric 3D view

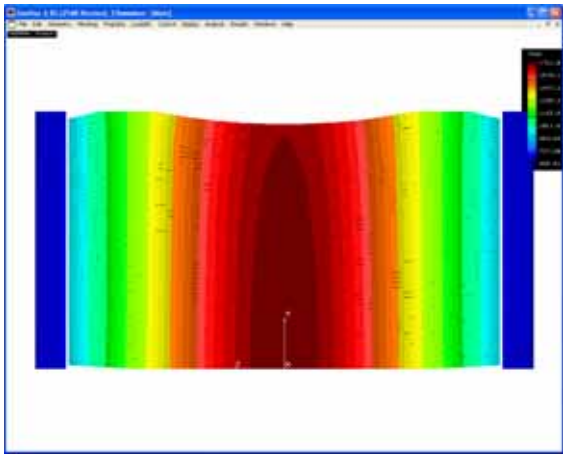

Fig 4. Longitudonal section of 3D model

Computations were done with different: oxide layer sizes, gas composition, heat sources in individual fragments, heat transfer coefficient and coolant temperature, coefficient of thermal conductivity of pellet, fragments position, finite element mesh.
We may conclude, that the highest influence to the maximum temperature was in the case of higher heat source in one fragment. The influence of the heat transfer appears to be not so significant in comparison with other examined parameters.

3. Practical industry oriented application

3.1 COSMOSM

The application designed to calculate 3D steady state temperature field in the Temelin VVANTAGE Fuel Rod was finished in COSMOSM 2.85.
3D model consists of lower and upper end plug and cladding in the real dimensions. The spring is for thermophysical calculation replaced with a hollow cylinder. Fuel pellets were modelled in so way to stay within software meshing limits. After this simlification the pellet stack consists of 35 so called macro-pellets with preserved stack height. Dishing, chamfering and all radial dimensions are same as in the real pellet. Upper and lower macropellet is without heat sources (that corresponds with end pellets with naturaly enriched uranium).
Thanks to macropellets the fuel rod is axially divided into 35 segments and boundary condition for heat transfer (bulk temperature and heat transfer coeficient) can be effectively defined for each segment. It is also possible to input 3D thermal sources and anisotropic initial and boundary conditions. All used materials are temperature dependent.
Simulation of burned situation is made in two levels. First, the geometry is changed according to burn-up. Secondly, the material characteristics are changed to agree with the burn-up also. Special excel sheets are created and user can easy generate temperature dependent properties by changing the burn-up level. These material sets are exported into the COSMOSM working files. We assume three „typical“ axial shapes: uniform, sinus axial profile, deformed – axial profile is deformed by the control rod. The following figures (Fig 5-10) document results of thermal calculations of steady-state „fresh“ and „burned“ models.

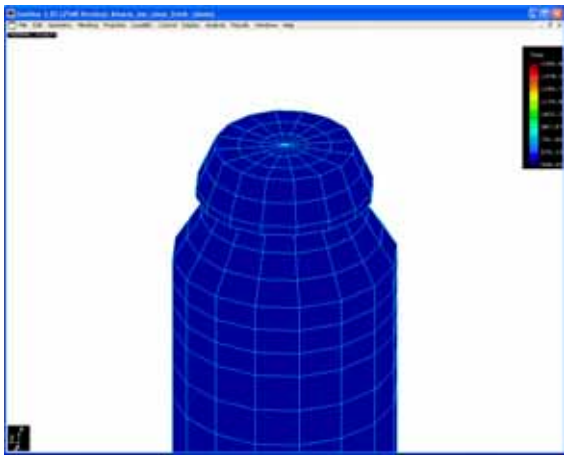

Fig 5. Temperature field in upper end plug

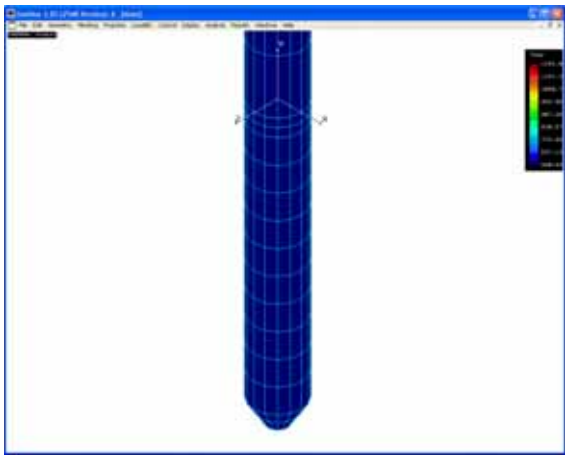

Fig 6. Temperature field in lower end plug

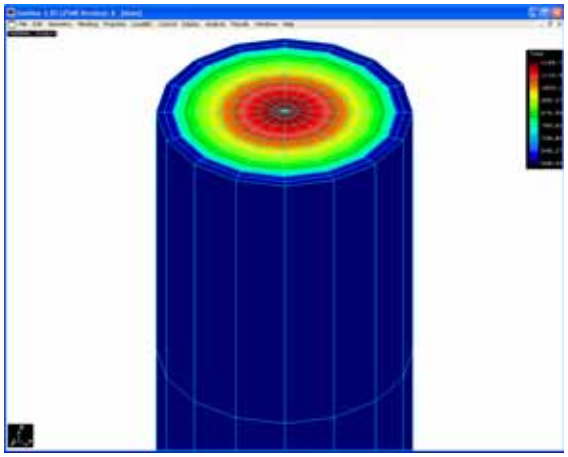

Fig 7. Temperature field in the fuel rod - cross-section

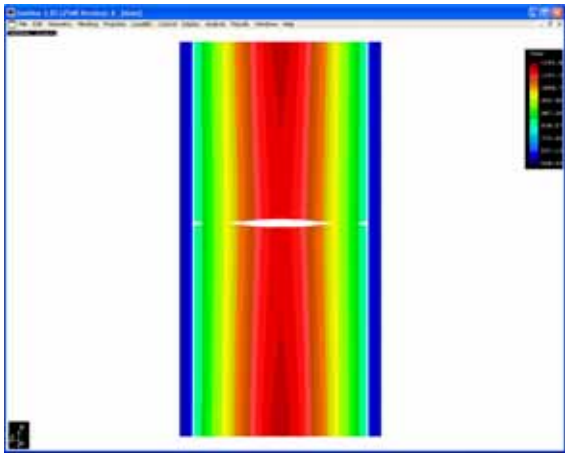

Fig 8. Interface between two macropellets and cladding (example of temperature profile).

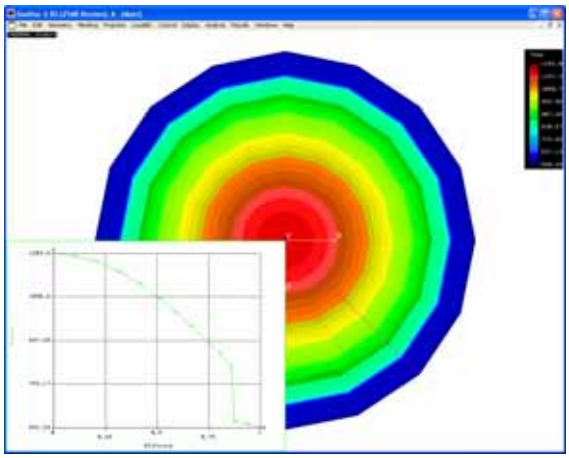

Fig 9. Temperature profile in cross-section

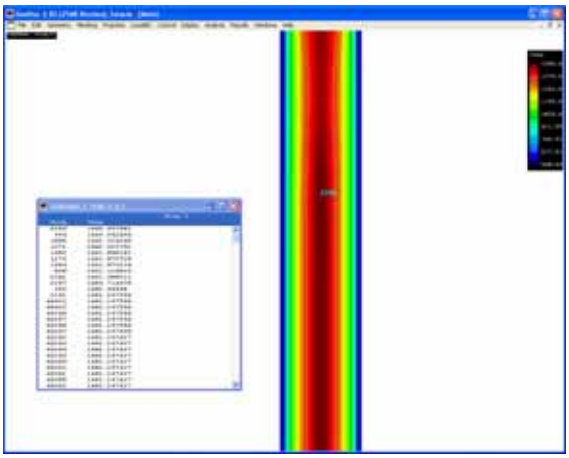

Fig 10. Maximum temperature

3.2 COSMOSDesignSTAR

Very similar effort was done in the COSMOSDesignSTAR 4.0 (parallel program to COSMOSM). This software is able to import CAD geometry and use very sophisticated mesh generator to create an adaptive mesh in arbitrarily shaped body. This we found very useful for modelling of upper and bottom end plugs and the spring. Limitation was fact, that boundary conditions can be prescribed only on surfaces, edges, lines and volumes.
Hardware and software allowed us to model only 7 pellets with the real end plugs and spring.

Example of thermophysical calculations of fuel rods of NPP Dukovany (VVER-440) and NPP Temelin (VVER-1000) is presented below (Figures 11-12).

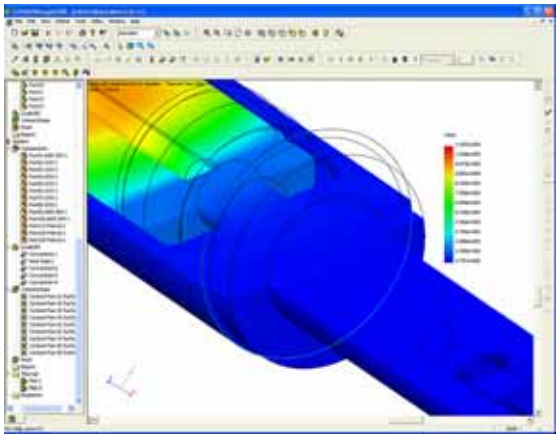

Fig 11. Thermal calculation result of lower end plug

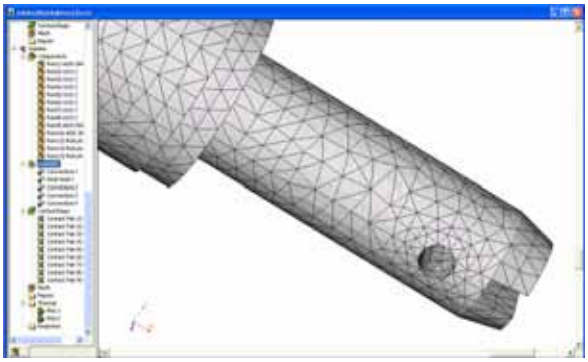

Fig 12. FE mesh of lower end plug

4. Conclusions

The poster presents in comprised graphical form more than 6 years of development, testing, solution of step by step problems in various levels of complexity and difficulty. The global task postulated at the start of our work was to develop simulator of PWR/VVER fuel rod using modern FEM based software with adaptive/scalable possibilities. The particular development steps are documented by 2D (r-z, r-φ) models, 3D models (level of pellet) up to the global full length fuel rod 2D and 3D models. Practically we delivered to our industrial customer various types of thermo-physical models, which have to be accompanied by boundary conditions and precalculated material properties sets to accommodate the problem of burning/irradiation processes in the reactor core. The most

painful/difficult problem still unresolved is the incorporation of several feedback loops with FGR gas generation, transport, release and flow/movement in the inner volumes.

5. References

[1] Belytschko, T., Liu, W. K.,Moran, B.:Nonlinear Finite Elements for Continua and Structures. J. Wiley & Sons Ltd., 2000.

[2] Hughes,T.J.R.: The Finite Element Method: Linear Static and Dynamic Analysis. Prentice Hall, Inc., Englewood Cliffs, New Jersey 1987.

[3] Timošenko, Š. P.: Strength of Materials I., II. Praha: Technicko-vědecké vydavatelství, 1951. (in Czech)

[4] Hlaváček, I., Haslinger, J., Nečas, J., Lovíšek, J.: Solution of Variational Inequalities in Mechanics. Bratislava: Alfa, 1982. (in Slovak)

[5] Hinton, E., Owen, D. R. J.: Finite Element Programming. London: AP, 1977.

[6] COSMOSM 2.8 for Windows - online manuals, SRAC 2003.

[7] COSMOSDesignSTAR 4.0 for Windows - online manuals, SRAC 2002.

[8] Suzuki, M.: FEMAXI-V manual, Japan, Jaeri 2000.

[9] Valach, M., Zymák, J., 2D Pellet-Cladding Modelling using FEM at NRI Rez plc., International seminar on pellet-clad interactions with water reactor fuels, Aix-en-Provence, France, 9-11 March 2004.

[10] Valach, M., Zymák, J., Dostál, M.: 2D Pellet-Cladding Modelling using FEM at NRI Rez plc.– High Burnup Fuel Simulation. 2.-3. March 2005, Fuel Safety Research Meeting 2005. Tokio, Japan.

[11] Valach, M., Zymák, J., Dostál, M., Hejna, J., Svoboda, R.: First attempts to simulate contact problem using FEM based systém COSMOS/M for analyses of three pellets in non-symetrical oxidized cladding in 2D and 3D configuration. 2005 Water Reactor Fuel Performance Meeting, Kyoto, Japan, October 2-6, 2005.

[12] Belac, J., Valach, M., Zymák, J., Influence of azimuth and radial neutron and thermal sources anisotropy on cotact problem simlation in real fuel pellet-cladding configuration using FEM, SMiRT-18, Beijing, China, August 7-12, 2005.

POROSITY AND GASEOUS SWELLING EFFECTS ON FUEL ROD BEHAVIOUR DURING CLASS 2 POWER RAMP TRANSIENT

J. JULIEN, R. MASSON
EDF-R&D, MMC/T25
Site des Renardières, 77818 Moret-sur-Loing – France

B. MICHEL, L. NOIROT, J.M. GATT
CEA Cadarache, DEN/DEC/SESC/LSC
Bât 151, 13108 Saint Paul-Lez-Durance – France

ABSTRACT

To better understand (and predict) effects of fuel behaviour on Pellet Cladding Interaction, tri-dimensional thermo-mechanical analysis are needed. This analysis stands on a new creep fuel law [3] which takes into account additional creep strains associated with porosity volume fraction's evolutions. This improvement provokes as main consequence a decreasing of middle external clad diameter. Then, a physical model uses data predicted by mechanical simulations to describe the fuel's microstructure. Corresponding results show two main conclusions: the pores are pressurized (contrary to the mechanical hypothesis) and a new population of cavity (pressurized bubbles) appears at a lower size scale. This last population of cavity must be taken into account for next simulations.

1 Context

To assess Pressurized Water Reactors (PWR) fuel rods behaviour under class 2 transients, experimental power ramps are imposed on rods during qualification programs. Tri-dimensional thermo-mechanical analysis (see [1]) are also needed to better understand pellet-cladding interaction (PCI) induced by these experimental power ramps. To correctly derive cladding strains, fuel thermal creep as well as gaseous swelling has to be taken into account. Up to now, these two phenomena have been modelled independently while they are coupled at the grain scale. This work aims at better understanding this coupling during PCI.

This paper shows in the first part how the porosity is taken into account in a tri-dimensional simulation. Results derived with these simulations underline the effects of porosity on mechanical behaviour and especially on the cladding external diameter. Thus, with thermo-mechanical data predicted by this simulation, a physical model allows to establish a sketch of micro-structure of fuel pellet.

2 Modelling the effect of porosity

2.1 The tri-dimensional modelling

During the first power increase, thermal stresses induce fuel pellet fragmentation. As a result; the displacement field displays significant axial (and tangential) dependencies throughout the rod illustrated by the so-called "hourglass effect" observed on irradiated fuel rods. Therefore, a tri-dimensional analysis is needed to simulate experimental power ramp imposed on rods during

qualification programs. This simulation is limited to the rod's axial position which experiences the maximum power level during the power transient.

Radial cracks are supposed to be distributed periodically around the rod axis (8 radial cracks regularly spaced). Additional symmetry considerations reduce the Finite Element mesh to a quarter of fragment of fuel pellet and the associated part of clad. The figure 2 shows the structure used in the simulation.

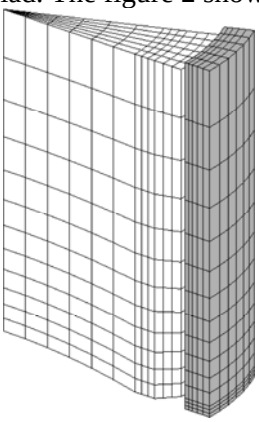

FIG.2 : the FE mesh

This structure is meshed by 864 elements for the pellet and 450 elements for the clad. These elements are linear cubic elements. The boundary conditions of the pellet are :

- for the side in front of, a stress free surface with a positive tangential displacement (pellet-pellet contact conditions)
- for the side behind, a symmetric plan with a null tangential displacement (pellet tangential symmetry plane)
- for the side bellow, a stress free surface with a positive axial displacement (pellet–pellet contact conditions)
- for the side above, all nodes have the same axial displacement (pellet axial symmetry plane)

The boundary conditions of the clad are :

- symmetric condition for the sides in front of, behind and bellow
- all nodes have the same axial displacement for the side above (the displacement of clad and of pellet are different while they are not in contact).

Between the pellet and the clad, finite element of contact with friction are introduced. All free pellet sides are submitted to the internal rod pressure while the external clad side is submitted to the coolant pressure.

The figure 1 shows the power history which is modelled hereafter. First, the rod is irradiated during two cycles in a power reactor. Then, a power ramp is imposed to the rod in experimental reactor. The modelled ramp reaches maximal power at 464 W/cm with a 12 hours holding time.

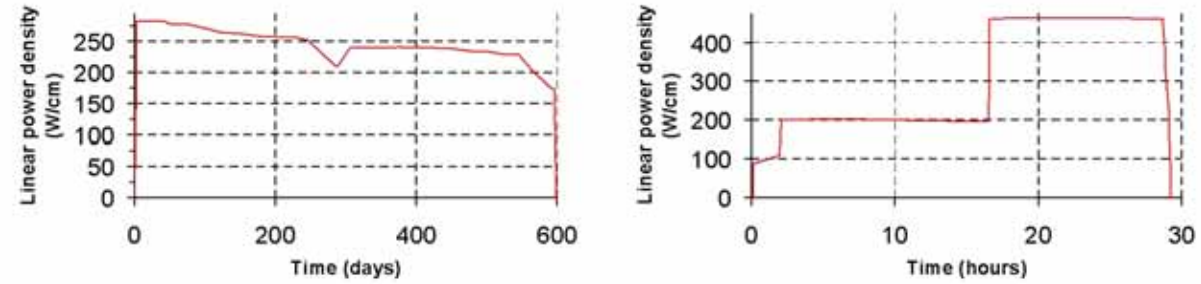

FIG.1 : Evolution of linear power density (Watt/cm) as a function of time during nominal conditions (figure on the left) and transient conditions (figure on the right).

2.2 The creep law

Fuel pellets are porous ceramics of UO_2. These cavities are due to fabrication process which are classically modelled as voids (porosities without internal pressure). These voids being sensitive to the pressure, they significantly modify the fuel creep: flow stresses depend on pressure and creep strain display a compressible component. Indeed, denoting by f the porosity volume fraction and $tr(\underline{\underline{\dot{\varepsilon}}}^{fl})$ the trace of the creep strain rate, the volume conservation read :

$$\dot{f} = (1-f)tr(\underline{\underline{\dot{\varepsilon}}}^{fl}).$$

According to this expression, a few percents of initial porosity should potentially induce compressible creep strain of similar magnitude. That's the reason why for the fuel considered hereafter (initial porosity equal to 5%), porosity effects can't be neglected. To describe pores effect on the creep behaviour of fuel pellet, we adopt the model developed by Monerie and Gatt [3]. During the nuclear reaction, the phenomenon of densification appears and modifies the porosity, namely :

$$\dot{f} = (1-f)[tr(\underline{\underline{\dot{\varepsilon}}}^{fl}) + tr(\underline{\underline{\dot{\varepsilon}}}^{densif})]$$

To study the effect of the porosity, next results will be compared to simulation based on a purely deviatoric creep law (i.e. depending only on the deviatoric stress). The porosity volume fraction being only sensitive to the pressure, it won't vary with this purely deviatoric model.

3 Results

3.1 Effect of pores on cladding external diameter

The prediction of the cladding external diameter is of great interest given that it can be directly compared to available experimental results. To compare the two models (compressible model and purely deviatoric one), we compare the cladding external diameter at two particular instants (see figure 3).

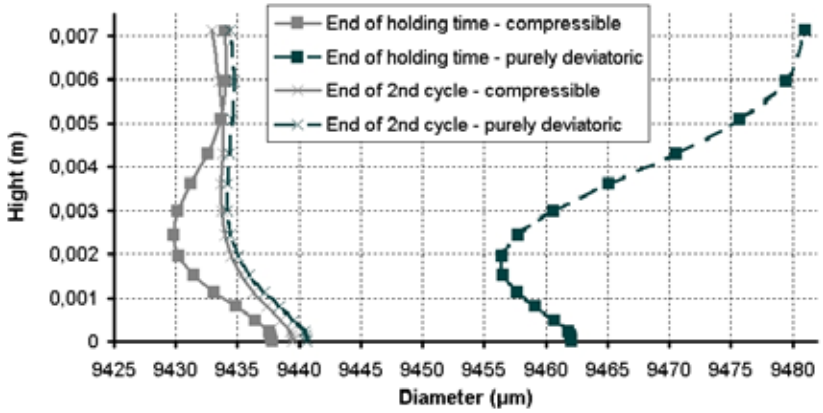

FIG.3 : external diameter as a function of the axial position. Results derived with compressible model (continuous Lines) are compared to the ones derived by the "purely deviatoric model"(doted Lines) at the end of the second cycle (cross Symbols) as well as the end of the holding time (square Symbol).

While the two models give similar results at the end of the second cycle in the reactor,. they appear to be very different at the end of the power ramp. Indeed, results derived with the compressible model display a middle external clad diameter lower than the ones computed by the purely deviatoric model.

This discrepancy can be explained with the introduction of the porosity volume fraction as new internal variable. The figure 4 shows the porosity volume fraction in the fragment at the end of power ramp according to the two models.

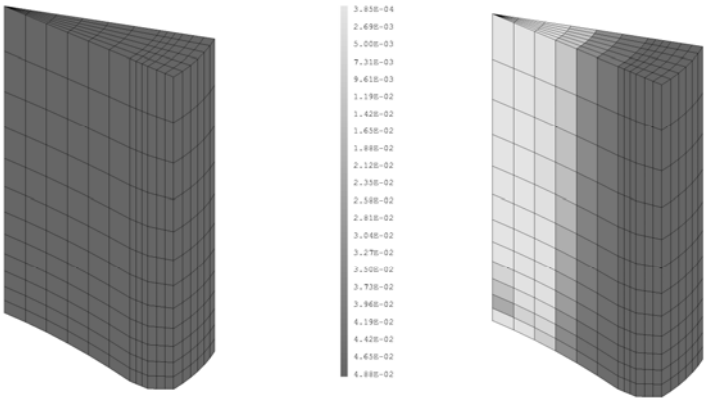

FIG.4 : Field of porosity throughout the fuel pellet as predicted by the purely deviatoric model (figure on the left) and the compressible model (figure on the right).

As expected the porosity volume fraction doesn't evolve with the purely deviatoric model while it decreases in the center of pellet with the compressible model. This diminution provokes a phenomenon of mechanical densification and the consequence is a lower increase of external clad diameter.

Now, we can extract thermo-mechanical data in order to use them in a post-processing physical model named MARGARET [4]. This model allows us to assess microstructure evolution under irradiation.

3.2 Physical simulation

For a given temperature and pressure, MARGARET models several physical micro-mechanisms like the apparition and the migration of fission products in the pellet. Diffusion phenomena being activated by temperature, we focus on the pellet's centre hereafter.

During the power ramp, fission products migrate toward cavities at the fuel's grain scale. This flux of fission products brings atoms in pores and, so, increases the pressure. The resulting pressure reaches an unrealistic high value at the end of the power ramp (because the pore volume given by the model tends to zero). Therefore, the mechanical hypothesis is questioned: the cavities can't be considered as voids (i.e. non-pressurized pores). Taking into account this pressurization in next calculation should prevent the porosity volume fraction from decreasing until zero.

Moreover, the physical simulation shows that a second type of cavities appears very early in the irradiation. This new cavities are named bubbles and they are pressurized too. Physical characteristics of these two kind of cavities, like volume fraction as well as internal pressures, appear to be different. The figure 5 shows a possible representation of micro-structure. For this sketch, we have supposed that the pores's radii remain approximately constant, the local hydrostatic pressure being equilibrated by the internal pressure. Future calculations should introduce the effect of internal pressure on the fuel's creep law to confirm this assumption.

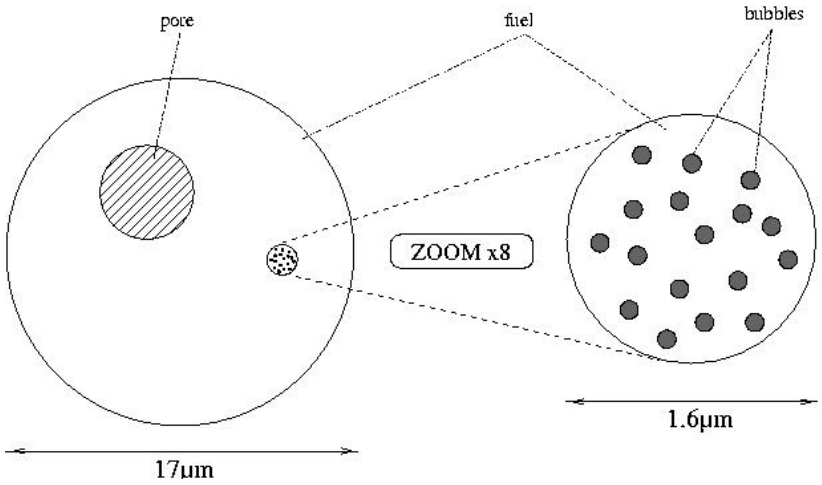

FIG.5 : Sketch of an estimation of micro-structure of fuel pellet at the end of the holding time

Although it exists a separation of scale at size level, this sketch shows that the two populations of cavities should be considered to model the mechanical behaviour. Indeed, with the hypothesis of a constant pore's radius, the pore volume fraction is always at the initial value (5%) whereas the physical simulation evaluates the bubble volume fraction at 9%.

4 Conclusion

In this paper, we show that initial porosity should play a significant role on pellet and cladding strains during experimental power ramp. However, internal pressure of pores have to be taken into account to derive simulations consistent with diffusion processes of fission products. Moreover, ours simulations underline that porosity and bubbles must be modelled simultaneously at two separate scales.

To improve the description of fuel behaviour, we develop currently a new mechanical model with two populations of pressurized cavities. This model will allow to realise a first coupling between mechanics and physics to derive a consistent constitutive law of the fuel.

5 Acknowledgements

The authors acknowledge J.C. Michel and M. Garajeu for their help in the mechanical part of this work. The authors also acknowledge T. Helfer for his useful help and his contribution in the simulations.

6 References

[1] D. Plancq and al. "PLEIADES : A unified environment for multi-dimensional fuel performance modelling" Proceeding of the 2004 International Meeting on LWR Fuel Performance, Orlando, Florida, paper 1060 (September 2004)

[2] J. Julien and al. "Modélisation multi-échelle du couplage physico-chimie – mécanique des combustibles REP" Colloque National MECAMAT, Aussois, France (janvier 2006)

[3] Y. Monerie, J.M. Gatt "Overall viscoplastic behavior of non-irradiated porous nuclear ceramics" Mechanics of Materials, Volume 38, Issue 7, July 2006, Pages 608-619

[4] L. Noirot "MARGARET An advanced mechanistic model of fission gas behavior in nuclear fuel" Water Reactor Fuel Performance Meeting, Kyoto, Japan (October 2005)

EXPERIMENTAL VERIFICATION OF WATER CHEMISTRY INFLUENCE ON AOA

N. DONCEL
Fuel Product Engineering Department, ENUSA Industrias Avanzadas SA
Santiago Rusiñol, 12. 28040 Madrid – Spain

G. RUBIO *(ASOCIACIÓN NUCLEAR ASCÓ-VANDELLÓS II A.I.E.);* M. NOVO *(A.I.E. CCNN ALMARAZ-TRILLO);* P. MATA, B. REMARTINEZ *(IBERDROLA GENERACIÓN S.A.);* J. DESHON *(ELECTRIC POWER RESEARCH INSTITUTE);* J. CHEN *(STUDSVIK NUCLEAR AB)*

ABSTRACT

Maintaining awareness of potential conflicts between water chemistry and anomalous core behaviour and fuel performance is an important element of PWR operation. A cosponsored experiment to verify the influence of water chemistry on the Axial Offset Anomaly phenomenon has been developed for these areas (water chemistry, core behaviour and fuel performance). The main purpose of the experiment is to identify the boron-containing species in a previously deposited layer of corrosion products (crud) under certain sub-cooled boiling and water chemistry conditions (pH, Ni concentration). These parameters have been postulated to be important in the initiation of the Axial Offset Anomaly phenomenon. This paper describes the most relevant advances of the experiment from 2000 to 2006, the potential industry implications as well as future plans for the work.

1. Introduction

1.1 Background

Axial Offset Anomaly (AOA) or Crud Induced Power Shift (CIPS) are both names for describing an abnormal core power shift that occurs in some Pressurized Water Reactors (PWR). It has been postulated [1,2] that this phenomenon is caused by the precipitation of some boron-containing species in fuel crud under certain sub-cooled boiling and water chemistry conditions (pH, Ni concentration).
The occurrence of AOA drove the need to identify and verify the mechanism by which the phenomenon occurs, as well as the speciation of the boron precipitate under proto-typical PWR conditions. Therefore, ENUSA in collaboration with IBERDROLA GENERACIÓN S.A, ASOCIACIÓN NUCLEAR ASCÓ-VANDELLÓS II A.I.E., A.I.E. CCNN ALMARAZ-TRILLO has carried out a test program at Studsvik Nuclear AB beginning in 2000. The ELECTRIC POWER RESEARCH INSTITUTE joined the program in 2003.

1.2 Objectives

The objectives of the project have been modified during the course of the program and updated to account for theories or ideas about the phenomenon. Currently, the objectives of every phase of the project can be described as: (1) determination of the existence of a threshold pH for co-precipitation of boron and lithium compounds, (2) determination of the impact of the crud presence prior to precipitation and (3) search for AOA mitigation solutions. In every phase, there are specific sub-objectives or tasks which are subjected to modification depending on the outcome of the previous test results.

2. Experimental

2.1 Pre-crudding procedure

The experiments use a zirconium-based (ZIRLO™) rod mounted with an electrical heater. The axial length of the heated zone is approximately 0.055m. For the experiments using a pre-crudded rod, the rod cladding is made to boil in degassed ultra pure water in a separate autoclave into which iron and nickel are injected. In order to avoid preferential precipitation of nickel oxide the pre-crudding is conducted in two steps. Iron is injected first and made to precipitate on the heated cladding surface for approximately one day. Thereafter, only nickel is injected into the autoclave for another day.

The oxide precipitates formed on the rod surface have a layered structure. The inner layer is tenacious and consists of nickel oxide and iron oxides. The outer layer is loose and consists mainly of iron oxides. Depending on the pre-crudding conditions, the crud thicknesses varies from a few tenths of a micron to over 1000 microns.

2.2 Autoclave exposure

The exposures under simulated PWR water chemistry conditions are conducted in an autoclave system shown schematically in Fig. 1.

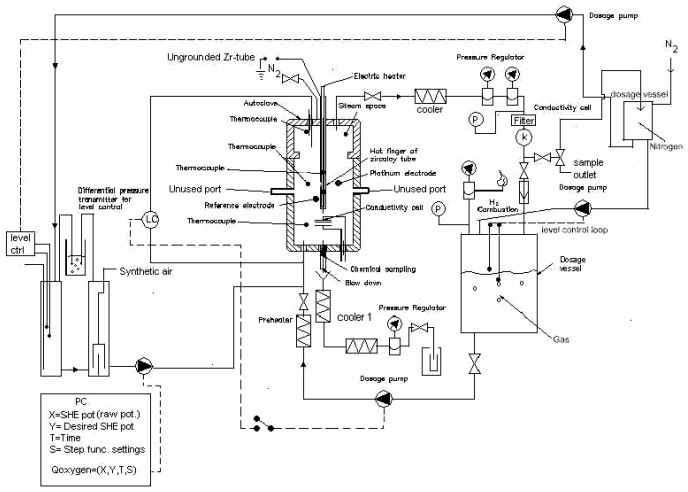

Fig. 1 A schematic illustration of the autoclave system.

The system consists of an autoclave main body made of Inconel 600, a hydrogen vessel of a nickel-based alloy, a large loop water reservoir made of high-density polyetene, a main circulation pump and dosage pumps, a sub-system for rapidly forcing water out of the autoclave main body, and some units for controlling temperature, pressure, corrosion potential and flow-rates. System data acquisition is largely computerised.

The rod is positioned vertically in the centre of the autoclave. To achieve the required water temperatures, the loop water is heated with a pre-heater before it enters the autoclave. An additional heater was placed around the lower part of the autoclave main body. The loop water is further heated by the electrically heated rod to achieve the desired sub-cooled boiling condition.

The applied heat flux is approximately 80% of the average heat flux that could be expected in a commercial PWR, 50% of a typical maximum local heat flux and 30% of the maximum limit for the local heat flux.

Table 1 below shows the operational conditions used throughout the different tests. It is pointed out that the experiment focuses on reproducing as representative operational PWR conditions as possible.

Test Phase	Phase 1	Phase 2	Phase 3

	1A	1B	1C	2A	2B		2C		3A	3B	
P (bar)	130	130	135-150	130	155		155		155	155	
T_{sat} (°C) phases 2 & 3 T_{rod} (°C)	330	330	330	330	344 363	344 330	344 357	344 357	344 362	344 352	344 379
Flow-rate (ml/min)	20-30	20-30	20-30	20-30	20-30		30		30	30	
Heat flux (W/cm^2)	≈5	≈30	≈20	≈12	≈48	≈48	≈48	≈48	≈49	≈50	≈48
ECP (mV SHE)	-	-	-	-300	-300		-300		-500	-500	
Boiling conditions	Net boiling	Sub-cooled	No boiling	Sub-cooled					Sub-cooled		
Exposure time (w)	≈2	≈4 - ≈2	≈2	≈2.5	≈2	≈6	≈2	≈2	≈2	≈2	≈4
Pre-crudded rod	No	No	No	Yes	No	No	Yes	Yes	Yes	Yes	Yes
[B], ppm	1200	1200	1200	1200	1200	(**)	1200	1200	1200	1200	1200
[Li], ppm	2.2	2.2	2.2	2.2	2.2	(**)	6.0	0.6	6.0	0.6	6.0
pH $_{at\ Tsat}$ (*calc.*)	7.4	7.4/4.0 (*)	7.4	7.4	7.7	(**)	8.1	7.2	8.1	7.2	8.1
[H_2], ppm (*calc.*)	2.8-3	-	3	3	3		3		3	3	

(*) An additional test at low pH was done by adding $4 \cdot 10^{3}$M of HNO_3 to reduce the pH at Tsat.
(**) Four tests: pH $_{at\ Tsat}$ 6.9 – 7.2 – 7.7 and 7.2, were performed varying the Boron and Lithium concentrations.

Tab 1: The main autoclave exposure conditions

Where:
P: Pressure of the main autoclave.
T_{rod}: Temperature measured at the upper and inner wall of the heated zone of the rod, available since phase 2B, when modifications were performed to further approximate PWR conditions.
ECP: Corrosion potential measured near the central part of the heated zone of the rod.

Prior to conducting phase 2B some modifications were implemented in the autoclave to improve the preservation of the deposited material, as well as to further approach PWR operational conditions. The corrosion potential (ECP) is determined using both platinum and Cu/CuO reference electrodes. During autoclave exposure, the ECP value is kept constant by adjusting the hydrogen and oxygen contents of the injected solution. Moreover, the nickel concentration is approximately 1ppb as dosed to the autoclave system, whereas the measured nickel concentrations in the autoclave are 3 to 7 times higher during the autoclave (Inconel 600) exposures.

After the rod is mounted in the autoclave system, the heat flux of the rod is raised incrementally until stable sub-cooled boiling conditions are reached and kept constant over the entire exposure period. At the end of an exposure period, drainage of the autoclave is performed. When the drainage is started, the rod power is turned off simultaneously. Since phase 2B, the drainage has been performed "instantaneously" while pressure inside the autoclave is maintained with the help of pressurized nitrogen gas connected to the autoclave. The drainage lasts for approximately 6s while flowing nitrogen gas is kept circulating inside the autoclave loop to keep the crud dry before it is taken out for various analyses.

2.3 Analytical techniques

The crud formed on the heated rod surface is divided axially into three zones, i.e. low, mid and upper. Crud is collected by scraping the rod surface with a knife made from the same rod material. In the low zone the outer loose crud and inner tenacious crud are scraped separately. However, the boundary between the inner and outer crud layers is not strictly defined.

The crud specimens are weighed and the scraped areas measured to obtain the crud density (in mg/cm2). The scraped samples are analyzed by Laser Raman Spectroscopy, X-Ray Power Diffraction (XRD), Scanning Electron Microscopy (SEM), Scanning Transmission Electron Microscopy (STEM) and Inductively Coupled Plasma Mass Spectrometry (ICP-MS) analyses.

3. Results and discussions

3.1 Phase 1

During the first phase of the testing program the results clearly showed that net-boiling or sub-cooled boiling promotes the formation of lithium - and boron -containing precipitates.

Under non-boiling conditions, only a small amount of boron could be detected on the cladding surface. Under boiling conditions there were differences in the amount of boron measured as a function of both pH and boiling conditions.

The formation of $LiBO_2$ was confirmed under boiling conditions and at high pH during phase 1B:1 (Fig. 2).

Fig. 2 Phase 1B, $LiBO_2$ appearance

3.2 Phase 2

During the second phase of the program, parametric studies were carried out. The effects of pH and crud thickness on the formation of the precipitates were examined under sub-cooled boiling conditions and, for the first time, under a preset ECP value. During phase 2A, the need for making modifications to the autoclave system was identified. This led to obtaining higher heat flux, pressure and temperature, i.e. more prototypical PWR conditions, and to preserve the crud deposited on the rods. An instantaneous drainage of the autoclave was successfully implemented for phase 2B and all subsequent phases.

Phase 2B was conducted using clean rods and the obtained results showed deposition of boron and lithium under representative PWR pressure and temperature conditions after several weeks with variable water pH values. The crud layers formed were 2-3μm and 4-20μm in thickness, respectively.

Pre-crudded rods were used again in phase 2C with the appearance shown in Fig. 3.

Fig. 3 A photo of the pre-crudded rod before autoclave exposure in phase 2C:1.

During phase 2C, the pre-crud thickness had significant variation along the rod length and an accelerated boron deposition was observed in the thick deposits, particularly for those deposits thicker than about 100μm. Moreover, more extensive boron deposition was observed at a high pH than at a low pH, also at comparable crud thickness. At low and high pH, there was a correlation between the presence of nickel oxide and the presence of boron in the crud, although this could also have been associated with the pre-crudding procedure. Upon further analysis, it was concluded that the crud thickness and composition have a significant influence on boron deposition at both low and high pH.

3.3 Phase 3

From phase 2 to phase 3 an improvement of the pre-crudding procedure was achieved by carefully controlling the different steps of the precipitation process. The improvement was confirmed by thorough characterization of the pre-crud. Fig. 4 shows the last pre-crud with controlled conditions of thickness and Ni/Fe ratio.

Fig. 4 Appearance of the 3B:1 pre-crudded cladding surface before the autoclave exposure.

The most recent phases 3A and 3B have been carried out at relatively low ECP (lower oxygen concentrations), which avoids the presence of Fe_2O_3 that was measured in the pre-crud used for the phase 2C tests under higher ECP.

However, a general conclusion from phase 2C, 3A and 3B was the detection of a considerable amount of Li and B elements formed in the crud under sub-cooled boiling conditions at various pH and ECP. In order to determine the phase composition of those boron - and lithium - containing compounds, it was decided to use STEM for identifying the boron containing phases in the crud samples obtained earlier. This study confirmed the presence of crystalline $Li_2B_4O_7$ [3] in the crud sample (Fig. 5). It was also confirmed that the needle-like crystals, as previously found by SEM, were crystalline NiO as has been observed in real crud samples from PWRs [2].

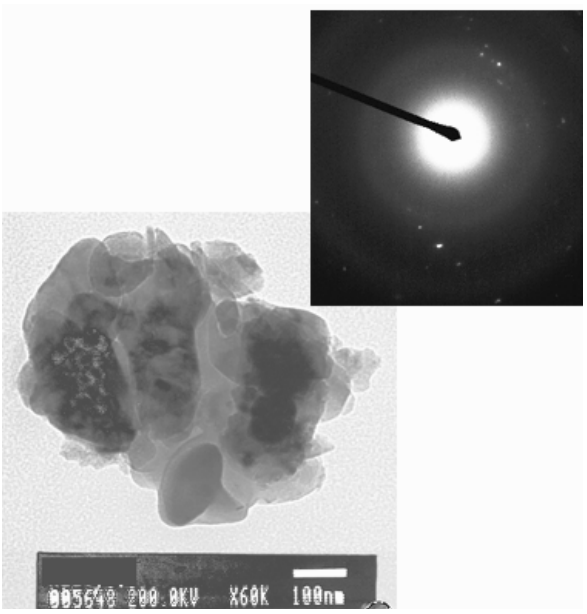

Fig. 5 $Li_2B_4O_7$ Transmission Scanning Electron Diffraction

With other experimental conditions remaining the same, the phase 3B:2 exposure was performed for four weeks, twice as long as in phase 3A:1. The amount of boron and lithium deposited in the crud was similar to that in phase 3A:1. In both tests, the presence of $Li_2B_4O_7$ crystals in the crud was confirmed. This observation suggests: (1) a rapid kinetics for the formation of lithium- and boron-containing compounds; (2) the deposition reached a maximum value rapidly.

4. Summary and future plans

The most interesting conclusion from the experiment has been the deposition and identification of boron-lithium compounds on both clean rods and pre-crudded rods under similar conditions of commercial PWRs. A number of experiments have been performed, and some other are foreseen, to study the effects of chemical conditions (pH, Ni concentration, ECP), exposure time in the autoclave and the crud thickness on boron deposition. A current on-going test (phase 3C:1) is being performed to study the effect of pH and boron concentration on the deposition process. This experiment will help inform us whether the use of EBA (Enriched Boric Acid) is a viable mitigation strategy for AOA. The high pH value from previous tests (pH_{Tsat} 8.1) is being maintained but by using EBA the boron concentration is significantly lower.

5. References

1. TARIN F., *Experimental Verification of pH and Nickel Influences on AOA*. Proceedings of the International Symposium on the Nuclear Fuel Cycle (TOPFUEL 2003) on CD-ROM. Trade 1, p. 209. Würzburg (2003).
2. *PWR Axial Offset Anomaly (AOA). Guidelines, Revision 1,* EPRI TR-1008102, Palo Alto, CA, June 2004
3. DONCEL, N. and CHEN J., *Verification of AOA Mechanism. Spanish investigation at Studsvik.* Presentation to the EPRI Fuel Reliability Program Meeting (FRP, WG1 Meeting February 21-22, 2006). San Diego (2006)

FRETTING WEAR EXAMINATION ON THE GUARDIAN™ FUEL FOR OPR1000 PLANTS

H.K. KIM, J.S. YOO, J.I. KIM, J.S. LEE, Y.K. JANG, K.T. KIM
Nuclear Fuel Design Department, Korea Nuclear Fuel Co., LTD.
493DeokJin-Dong Yuseong-gu Daejeon – Korea

ABSTRACT

This paper presents the main results of the poolside examination with regard to fuel rod diameter and fretting wear of the ZIRLO cladding irradiated for three cycles. The examination has been performed using specially designed examination equipment. As a result, the rod diameter change of the ZIRLO cladding showed a good agreement with design expectation value and the measured fretting wear depth was below the established design limit without any excessive fretting wear mark. The creep rate of the ZIRLO shows slightly faster than that of conventional partially recrystallized low-tin Zircaloy-4 at the early stage of irradiation. However, the creep rate difference seemed not to impact on the wear behaviour in the Guardian fuel assembly. Therefore, the introduction of the ZIRLO cladding into the Guardian fuel was successfully accomplished without any unexpected irradiation behaviour.

1. Introduction

The OPR1000 plant is the commercial Korean Standard Nuclear Power Plant being operated at 8 sites in Korea. The Guardian fuel assembly for the OPR1000 plants has utilized the low-tin Zircaloy-4 alloy having partially recrystallized microstructure (hereafter referred to as low-tin Zircaloy-4) as its cladding tube, since the plants started commercial operation. However, the OPR1000 plants were requested to operate with extended burnup up to 60,000 MWD/MTU and longer cycle length. In order to fulfil the requests, it was considered for the first time to introduce the ZIRLO cladding into the Guardian fuel assembly. For the introduction, a feasibility study has been carried out with fuel design point of view including safety analysis. During the study, it has been found that the creep rate of the ZIRLO cladding is slightly faster than that of the low-tin Zircaloy-4 cladding. Even though the results of the feasibility study were satisfactory, however, licensing authority recommended the examination on the fuel rod diameter and the in-reactor fretting wear behaviour in order to confirm the effect of the changed creep rate of the fuel rod. As per the recommendation, out-of-pile fretting wear test using the ZIRLO and the low-tin Zircaloy-4 cladding had been performed and a poolside examination (PSE) plan for three cycles had been established. And according to the plan, the diameter and the fretting wear of the ZIRLO cladding have been measured at each end of cycle using the LVDT and ECT devices, respectively.

This paper describes the main results of the PSE performed for 3 cycles on the fuel assemblies with the ZIRLO cladding. The examination has been carried out using some representative fuel rods extracted from 2 fuel assemblies.

2. Examination

2.1 Description of Examination Equipment

The cladding creep and fretting wear marks on the Guardian fuel were measured using specially designed examination equipment. The equipment consists of manipulator control system controlling sensor, motor and encoder, eddy current system, and calibration rod. The eddy current system consists of one rotating eddy current probe and two LVDT to measure fretting wear and fuel rod diameter,

respectively. The upper bound measurement uncertainty for the eddy current probe and LVDT is ±10μm and ±5μm, respectively. The configuration of the system is shown in Fig. 1.

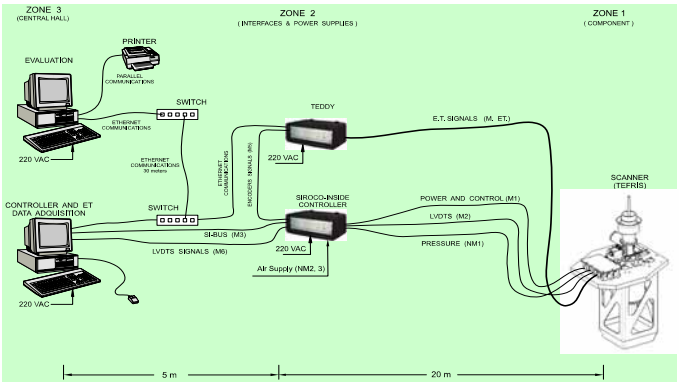

Fig. 1 Schematic diagram of fuel rod examination equipment

2.2 Description of Fuel Assembly

The schematic configuration of the Guardian fuel assembly is shown in Fig.2. The fuel assembly consists of 236 fuel rods (16x16 array), 4 guide tubes, 1 instrumentation tube, 11 spacer grids (10 Zircaloy-4 grids and 1 Inconel grid), and upper and lower end fittings. The outer guide tubes, spacer grids, and end fittings form the structural frame of the assembly. The general specifications are shown in Table 1.

Table 1. General specification of the Guardian fuel

	Specification
Fuel Assembly	
Type	16x16
Grid material	Zircaloy-4@top and mid Inconel @ bottom
Length	4528 mm
Fuel Rod Assembly	
Material	ZIRLO
Outer Diameter	9.7 mm
Inner Diameter	8.4 mm
Active Length	3810 mm
Pellet OD	8.255 mm

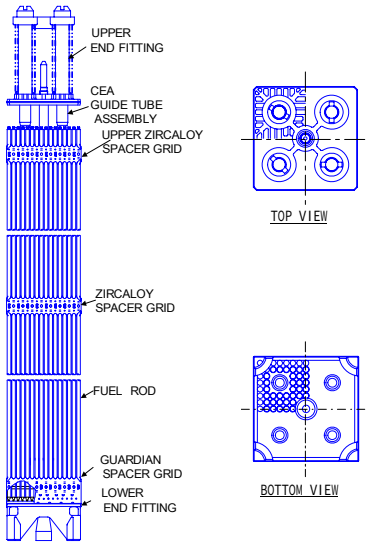

Fig. 2 Configuration of the Guardian fuel assembly

2.3 Irradiation and Examination History

The Guardian fuel assemblies with the ZIRLO cladding had been irradiated in YGN unit 4 from May 2001 to Oct. 2005 for three cycles under normal operation conditions. The assembly average burnup was in a range of 43,700 MWD/MTU to 48,000 MWD/MTU and the rod average burnup of the examined rods was in a range of 40,400 MWD/MTU to 55,000 MWD/MTU after three cycle operation.

For the examination after the 1st cycle irradiation, total eight fuel rods from two assemblies were selected under consideration of hydraulic condition, fuel burnup, and representativeness of fuel rods in the assembly and examined during fuel outage campaign. After that, sixteen fuel rods including previously examined eight fuel rods from the fuel assemblies were examined again after the 2nd cycle irradiation. And finally, eighteen fuel rods from other two fuel assemblies which had been burnt for three cycles were examined, since the fuel assemblies examined previously had been discharged after the two cycle

irradiations. In this case, furthermore, another two Guardian fuels with conventional low-tin Zircaloy-4 cladding were also examined for the comparison with results of the ZIRLO cladding.

3. Results

3.1 Visual Inspection

All of the fuel assemblies with the ZIRLO cladding as well as low-tin Zircaloy-4 cladding were inspected visually at the end of each cycle. In this inspection, all of the fuel components were in quite a good condition. Especially in the fuel rods, although typical oxide spots were found along the fuel rod, there were no unusual appearances like thick crud deposit and excessive deformation like bow. The typical photographs from the visual inspection of the Guardian fuel assemblies with the ZIRLO cladding and low-tin Zircaloy-4 cladding are shown in Fig.3.

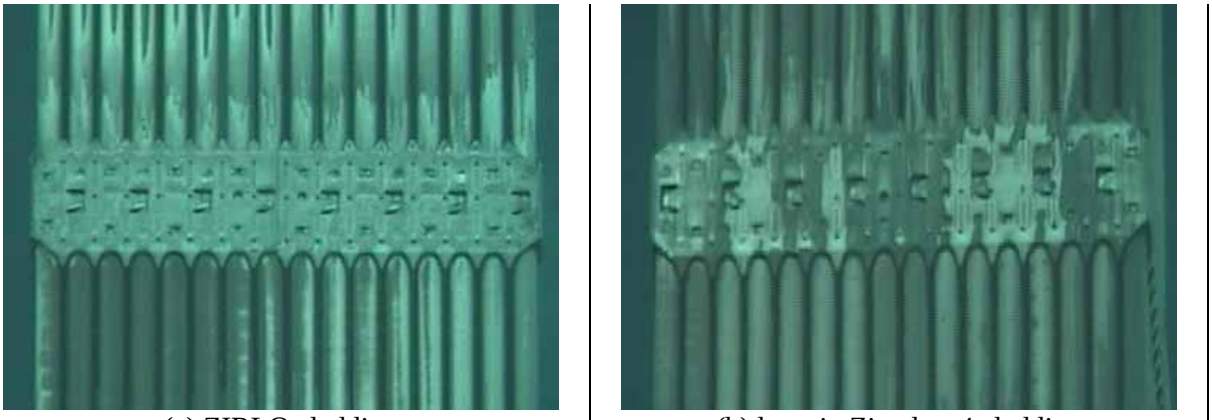

(a) ZIRLO cladding (b) low-tin Zircaloy-4 cladding

Fig. 3 Visual inspection of the Guardian fuel assembly (EOC3)

3.2 Clad Creep Measurement

The outer diameter of the ZIRLO fuel rod was measured using two LVDT. For the measurement, the diameter at 0° and 180° direction was measured with 0.5 mm interval along the fuel rod axial length and measured again at 90° and 270° direction. The diameter was determined from the arithmetic mean of the two. An averaged creep-down behaviour of the rod at active region as a function of the fuel rod average burnup is shown in Fig.4. In this figure, the x-axis represents axial elevation which is compatible with design node of fuel rod design code and spacer grid location as well. In this figure, the diameter of the Guardian fuel rod was crept down to about 40 MWD/MTU and then swelled. The diameter change has been about 70 μm at the upper part and about 50 μm to 60 μm in mid-area since the irradiation began. This result showed a good agreement with predicted result using fuel rod design code, although not shown here.

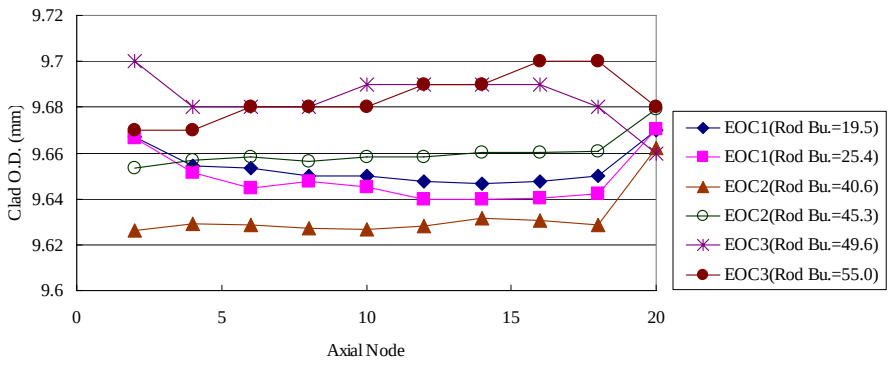

Fig. 4 Fuel rod outer diameter change during irradiation

3.3 Fretting Wear Measurement

Fretting wear was measured using the specially designed equipment with ECT device at the end of each cycle. For the measurement, the ECT probe rotates 10 rps and fuel rod moves axially with the speed of 5 mm/s.

After the 1st cycle irradiation, total eight fuel rods from two assemblies were measured. Since the creep rate behaviour of the ZIRLO cladding showed a little faster than that of the low-tin Zircaloy-4 cladding, the grid-to-rod interference of the ZIRLO cladding would be reduced comparatively faster at this stage of irradiation. However, any significant wear marks weren't detected during this period. In this measurement, total 9 of slight wear marks were measured from eight fuel rods.

After the 2nd cycle irradiation, total sixteen fuel rods including previously examined eight fuel rods from the two fuel assemblies were measured. As shown in Fig. 4, maximum creep down would occur during the 2nd cycle irradiation, and therefore, the grid-to-rod gap size could be maximized during this period. In this measurement, total 24 of wear marks were measured from sixteen fuel rods. However, the ZIRLO cladding maintained its integrity with enough margin against fretting wear.

Finally, after the 3rd cycle irradiation, eighteen fuel rods from other two fuel assemblies which had been burnt for three cycles were measured. In this measurement, total 44 of wear marks were detected from eighteen fuel rods. Fig. 5 shows a recognizable wear shape obtained from the measurement equipment. All of the measured wear depths were still less than design limit of the Guardian fuel.

The comparison of fuel rod average burnup versus detected wear number after the 2nd and the 3rd cycle irradiation is shown in Tables 2 and 3, respectively. Fig. 6 shows measured fretting wear evolution at the upper spacer grid locations (above the 7th grid). These tables and Fig. 6 show that detected wear number is steadily increased in proportion to the increase of the burnup. As a result, the ZIRLO cladding maintained its integrity during the three cycle irradiation, because all of the measured wear depths were below the established design limit.

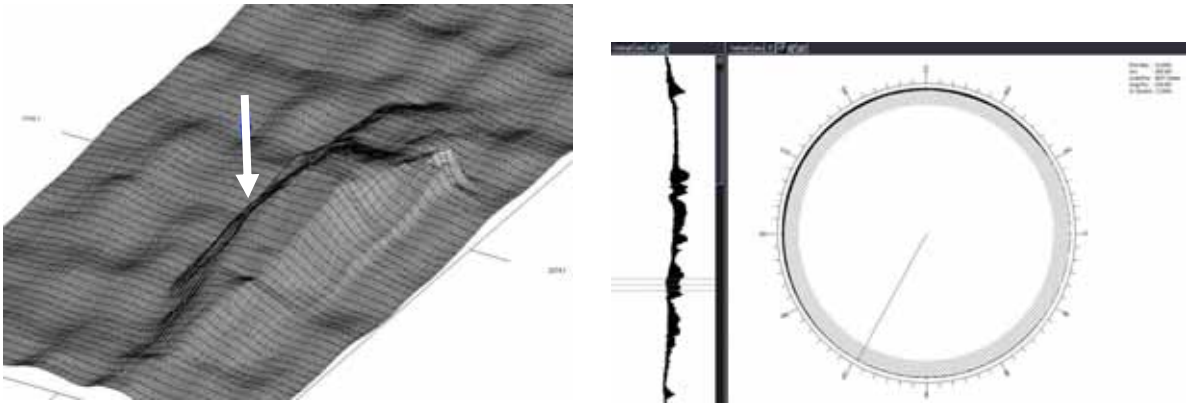

Fig. 5 ECT signals from the three cycle burnt fuel rod

Table 2. Number of wear marks vs. rod average burnup after the 2nd cycle irradiation

Rod Avg. burnup (MWD/MTU)	35,000~40,000	40,000~45,000	45,000~46,000
No. of wear mark	1	12	11
No. of measured rod	3	7	6

Table 3. Number of wear marks vs. rod average burnup after the 3rd cycle irradiation

Rod Avg. Burnup (MWD/MTU)	40,000~45,000	45,000~50,000	50,000~55,000
No. of wear mark	12	12	20
No. of measured rod	8	4	6

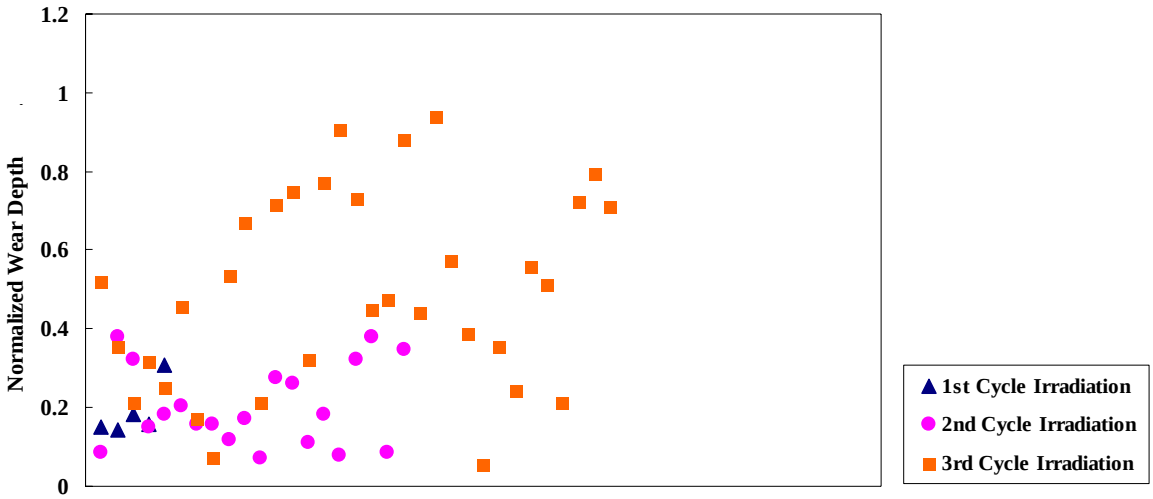

Fig. 6 Measured fretting wear evolution at the upper spacer grid locations(above the 7th grid)

For comparison with the low-tin Zircaloy-4 cladding, fretting wear of the low-tin Zircaloy-4 cladding was also measured after three cycle operations. In this comparison, the number of wear marks was somewhat similar, the low-tin Zircaloy-4 cladding had a little bit more though, but the locations of the wear mark were appreciably different. In the case of the low-tin Zircaloy-4 cladding, lots of the wear marks were detected at lower part of the cladding, while in the case of the ZIRLO cladding, they were at mainly upper part. This biased tendency seems to come from the difference of fuel rod supporting condition due to different creep rate of the both claddings. Because the results of the feasibility study on the supporting condition of the fuel rods showed that interference between fuel rod and spacer grids for the low-tin Zircaloy-4 cladding showed larger gap than that for the ZIRLO cladding at lower part and vice versa at upper part.

4. Conclusions

The results of the PSE showed the integrity of the ZIRLO cladding in the Guardian fuel assembly and a little bit less wear marks of the ZIRLO cladding than previous low-tin Zircaloy-4 cladding having partially recrystallized microstructure. Although the creep rate of the ZIRLO shows slightly faster than that of conventional partially recrystallized low-tin Zircaloy-4 at the early stage of irradiation, the creep rate difference seemed not to impact on the wear behaviour in the Guardian fuel assembly. Finally, because all of the measured wear depths were still below the established design limit, the introduction of the ZIRLO cladding into the Guardian fuel was successfully accomplished without any unexpected irradiation behaviour.

Acknowledgements

Several people have been participated in present examination work. All the authors represent gratitude to them all.

ULTRASONIC FUEL CLEANING SYSTEM (UFCS)

PEDRO ALVAREZ & HUMBERTO MARTA
ENUSA ENWESA A.I.E.
Santiago Rusiñol 12, 28040 Madrid - Spain

DAVE ARGÜELLES
DOMINION ENGINEERING
Reston VA - USA

ABSTRACT

The Ultrasonic Fuel Cleaning System (UFCS) is designed to remove corrosion products from fuel using ultrasonic energy. There are multiple benefits using this technique, which improves the performance of the fuel and the core management and also reduces the dose and crud inventory at NPP.
(EPRI Licence. Equipment design Proprietary to Dominion Engineering)

1. Introduction

The Ultrasonic Fuel Cleaning System (UFCS) is designed to remove corrosion products from fuel using ultrasonic energy.

Nowadays nuclear industry is improving core operation implementing longer cycles. Also new chemical programs are being developed and implemented in most of NPP´s: modification of pH, zinc injection, etc. These new programs are affecting to the fuel and core performance:

- Increasing of fuel corrosion due to the crud products
- Appearance of crud induced power shift causing Axial Offset Anomaly (AOA)

These effects must be mitigated and reduced using the Ultrasonic Fuel Cleaning System.

Other benefits of fuel cleaning are:

- Control particulate inventory to minimize personnel radiation during refuelling
- lower risk to fuel rod integrity
- Improve fuel cladding inspection
- Reduce risk of contamination during dry storage
- Reduce crud inventory to maintain fuel pool clarity
- Reduce risk of spread of contamination during transport and potentially ease reprocessing requirements.

2. Description of the system

The ultrasonic fuel cleaning system is designed to remove corrosion products from fuel using ultrasonic energy. It is a high throughput system that consists of a dual-chamber cleaning fixture that cleans one fuel assembly while another fuel assembly is moved into the adjacent chamber. Corrosion products that are removed from the fuel are pumped into a filtration skid where they are captured on filters that are later disposed of.

The ultrasonic cleaning process removes all transportable corrosion products and has been demonstrated at several plants to be safe for the fuel (see fig. 1)

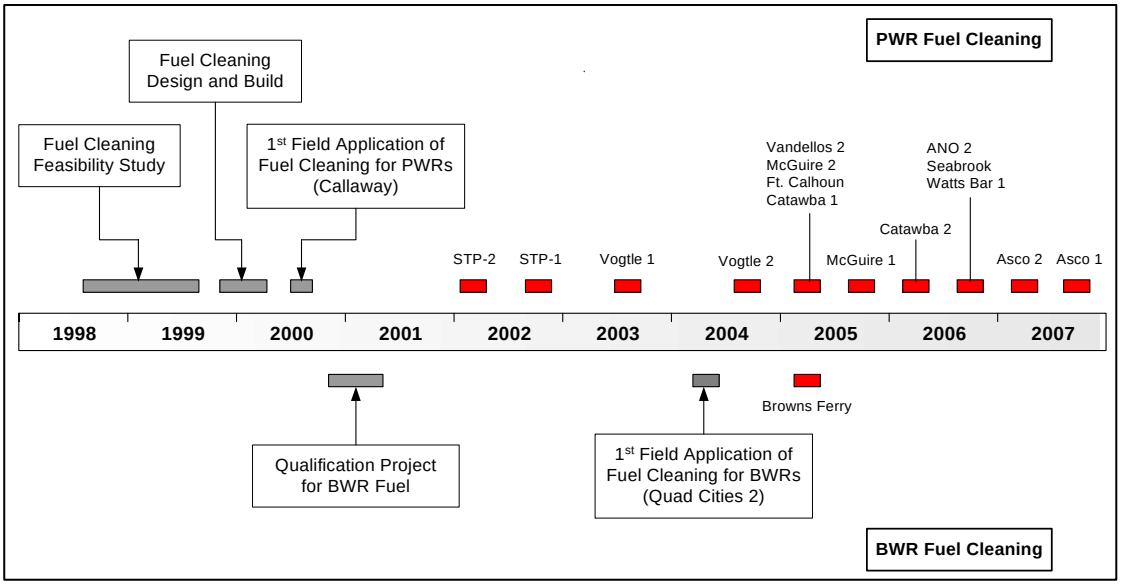

Fig 1. UFCS background

The cleaning fixture is comprised of two independent cleaning chambers that are attached at the bottom by a common baseplate and at the top by a common lifting frame. Each chamber contains a transducer basket which is essentially a 9-inch square box tube surrounded by ten or more ultrasonic transducers. With ten transducers per chamber, the coverage of the transducers is slightly more than the top half of the fuel assembly, since the thickest corrosion deposits typically form on the top half of fuel assemblies.

For full-length cleaning applications, sixteen transducers are used in each chamber spanning the entire length of the fuel assembly. A flow diverter valve is installed at the bottom of each cleaning chamber to ensure that the flow is directed to the chamber containing the fuel, and not through the empty chamber. The outlet of each chamber combines into a common header that provides a connection for a filtration system suction hose.

The filtration system consists of two redundant air-operated diaphragm pumps that draw suction from the cleaning fixture through one or both of two filter banks. Generally, only one pump is run at a time. Each filter bank consists of four filter housings, each containing a one-micron filter used to capture the corrosion products. The filter bank is selected by two manual valves, and each filter bank remains in service until either a radiation or differential pressure limit is reached. Then the other bank is manually lined up and the loaded bank removed from service. This allows the used filters to be replaced without interrupting the cleaning process. Filter system instrumentation includes water temperature, filter differential pressure, process flow, and both in-line and filter gamma dose rate.

In addition to the main recirculation diaphragm pumps, there are also two smaller auxiliary diaphragm pumps which are used to remove air bubbles which accumulate underneath the filters during operation. They draw a water/air mixture from underneath the filter housing and reinject it back into the main recirculation line just upstream of the large pumps.

Other cleaning system equipment includes an air regulator module, a transducer cabinet, and a control interface module. The air regulator module includes valves and regulators to control air flow to the positive-displacement pumps on the filter skid. The control interface module contains the microprocessor and instrumentation displays used to control and monitor the cleaning process. The control interface module provides connections for a keyboard and monitor that the operator uses to control the cleaning process via a Windows interface. The transducer cabinet contains a number of ultrasonic generators and a switching unit used to automatically switch the ultrasonic generator output

between the two cleaning chambers. The output of the switching unit is connected to each cleaning chamber by a transducer power cable, one for each chamber. In full-length cleaning applications, there are two transducer cabinets and two additional transducer power cables running to each cleaning chamber.

The cleaning chambers and filtration skid are typically installed in the spent fuel pool, cask loading pit, or other underwater locations, while the air regulator module, control module and transducer cabinets are located poolside near the cleaning equipment.

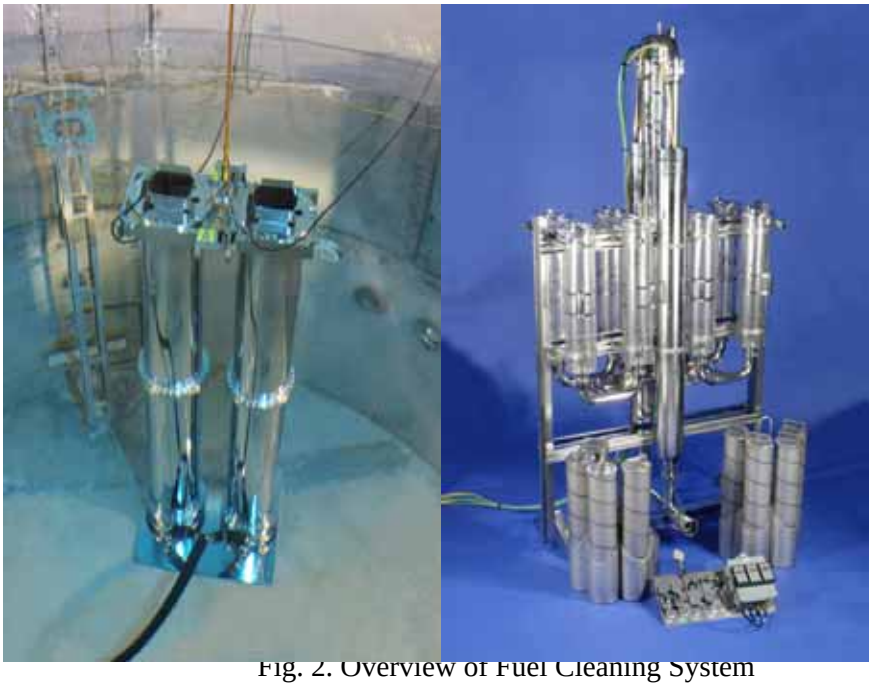

Fig. 2. Overview of Fuel Cleaning System

2. Results, efficiency and benefits

The average cycle time per assembly (preparation, handling and cleaning) is approximately 14 minutes. The cleaning typically is made during the core unloading and before inserting the assemblies into the storage rack.

Typical cleaning PWR rates are shown in figure 6. Typical average dose rates per assembly is 7 R/h.

In BWR fuel, the experience is lower, but two applications in BWR plants have demonstrated a dose rate between ten and twenty times higher.

Ultrasonic cleaning of reload fuel is expected to remove a major source of activated isotopes, thereby lowering shutdown personnel dose rates. Using UFCS the dose rate savings are predicted to range from 35 - 50 percent.

Data at NPP's show that twice-burned assemblies often produce larger dose rate increases than once and thrice-burned assemblies. There was no evident systematic variation depending on location in the core.

No impact to the fuel structure and configuration has ever been observed.

The system has demonstrated in all the applications a high efficiency removing cruds from fuel assemblies (see Fig 3, 4, 5, 6 & 7). This is affecting very positively in all parameters included in point 1 of this report.

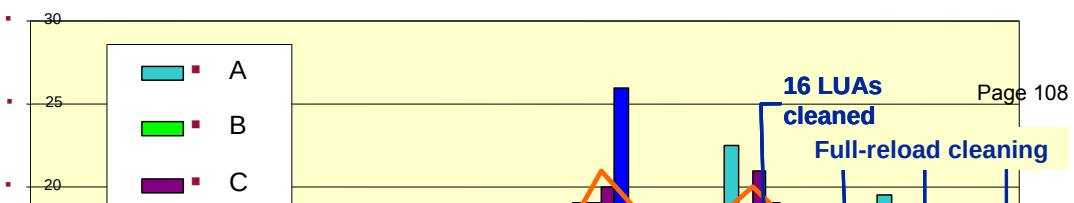

Fig 3. Typical SG Channel Head Dose Rate

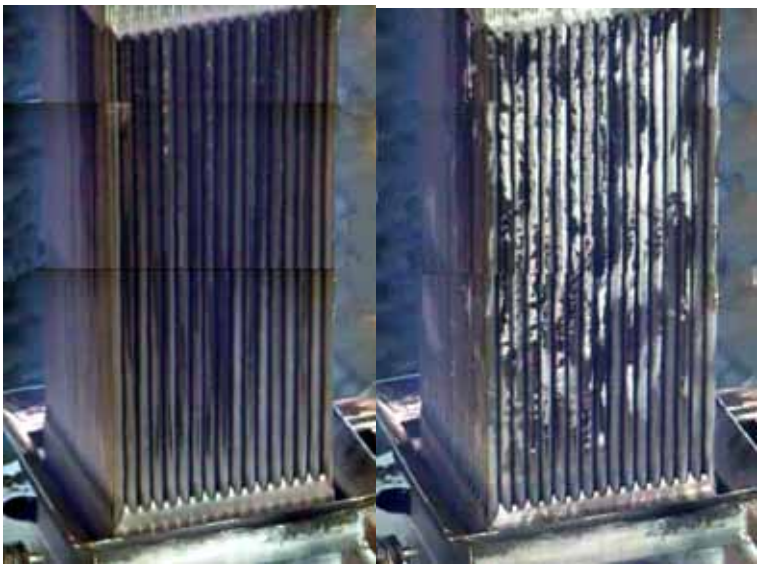

Before After

Fig 4. Cleaning efficiency PWR

Before After

Fig 5. Cleaning efficiency BWR

Fig 6, Crud removal core map

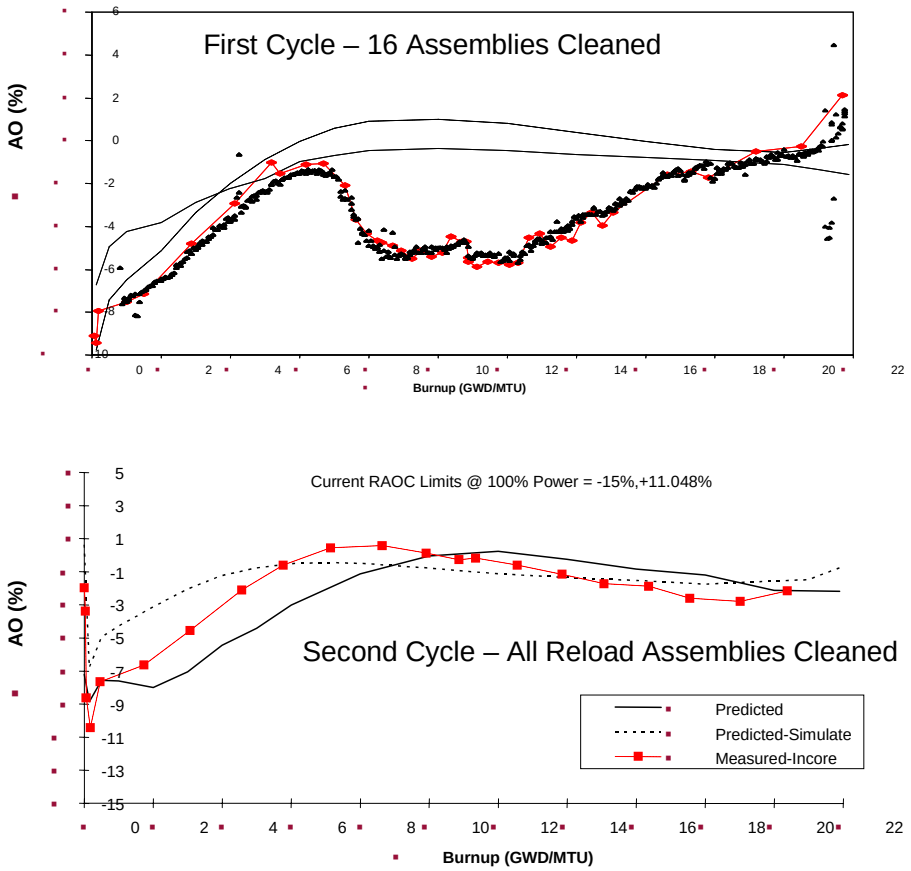

Fig 7. Axial Offset reduction

ANALYSIS OF CRDA IN A HIGH BURNUP FUEL CORE FOR COFRENTES NPP WITH RETRAN-3D

ANDRÉS GÓMEZ, I. COLLAZO, A. ORTEGO, C. MONTALVO, P. GARCÍA
GENU, IBERDROLA IGENIERÍA Y CONSTRUCCIÓN
Ave. Burgos, 8 B; 28036-Madrid (SPAIN)

P. MATA
COSNU, IBERDROLA GENERACIÓN
Tomás Redondo, 1; 28033 Madrid (SPAIN)

ABSTRACT

Within the Fuel Reliability Program, EPRI is developing RIA failure criteria for BWR CRDA at cold and hot zero-power (CZP and HZP) conditions and their dependence of the burnup. Under this project, Iberdrola Ingeniería y Construción (IBERINCO) has made with RETRAN3D a deep analysis calculating the power histories required for this development. After previous studies of CRDA with the fuel at regular burnups with conditions of CZP and HZP, (presented last year in 2005-WRPM, Kyoto), in this occasion it is studied the behaviour of the maximum fuel enthalpy and fuel temperature in conditions of high burnup.
An important part of the deposited enthalpy is because the delayed power tail associated to startup conditions at significant initial coolant subcooled coditions. From that characterization, EPRI will select specific result cases for use in a separate project for analysis of the fuel rod thermal-mechanical consequences and determination of the failure threshold and coolability limit.

1. Introduction

Within the Fuel Reliability Program, EPRI is planning to develop RIA failure criteria appropriate to BWR CRDA under cold zero-power (CZP) as well as hot zero-power (HZP) conditions. To achieve this objective, it is necessary to know the deposited energy and transient power histories that low, intermediate and high-burnup fuel rods would experience during such accidents.
Under this project Iberdrola Ingeniería y Construcción SAU (IBERINCO) has calculated power histories required for the development of RIA failure criteria by conducting a series of RETRAN CRDA calculations for a large BWR under CZP and HZP conditions.
The results of the RETRAN analyses provide a mapping of both the peak prompt enthalpy (enthalpy at the time of peak power plus one pulse width, Full Width Half Max) and the peak radially averaged maximum fuel enthalpy for the most energetic RIA rod drop accident. These enthalpies are plotted as a function of bundle and nodal average exposure for different initial coolant temperature states that are possible during reactor startup. A significant part of the total enthalpy is consequence of the delayed power tail associated to startup conditions with a significant initial coolant subcooling. From that characterization, EPRI will select specific result cases for use in a separate project for analysis of the fuel rod thermal-mechanical consequences and determination of the failure threshold and coolability limit.

2. Object

The object of these analyses is to apply the IBERDROLA's CRDA Methodology for performing a CRDA Dynamic Analysis in Cofrentes NPP with conditions of high burnup. These analyses will provide EPRI information of the thermal behaviour for high burnup fuel during the startup phase of a real reactor at different core inlet temperatures (20ºC, 80ºC, 160ºC, and 240ºC).

3. CRDA Description

The Control Rod Drop Accident (CRDA) is a Reactor Initiated Accident whose analysis is a part of the licensing basis accident analysis required for boiling water reactors (BWR). These analyses simulate the reactor coolant system, core, fuel rod, and fuel pellet response to the transient induced by a rapid positive reactivity insertion produced by the fall down of a control rod initially fully inserted. The immediate consequence of it is an overpower event that is characterized by an amount of stored energy that the fuel could not tolerate without damage. In fact the current Standard Review Plan (NUREG-800) sets forth an enthalpy limit for RIA safety analyses of 280 cal/g. When this limit was developed, only low burnup fuels were allowable, now this limit is to be modified in order to introduce a dependency of the burnup. Hence the necessity of performing realistic high burnup CRDA analyses.
The fuel damage can occur in two ways: PCMI failure or DNB depending of the thermal conditions of the core.

4. IBERDROLA's CRDA Methodology

The code utilized in the IBERDROLA's 3D dynamic analysis is RETRAN-3D [3], by using its 3D feature as standard method for the analysis of the BWR CRDA and other asymmetric accidents. The core design is performed with the CASMO/SIMULATE package. A set of 3D cross sections is generated from SIMULATE [4]. In order to do it, a methodology (SIMTAB) has been developed [5].This methodology collapses the kinetic information from SIMULATE and converts it to the format required by RETRAN. This figure summarizes the process used to generate the kinetic data. To verify the adequacy of the process before the RETRAN dynamic analysis is performed, the RETRAN -3D values of the relevant static variables are compared with the SIMULATE results.

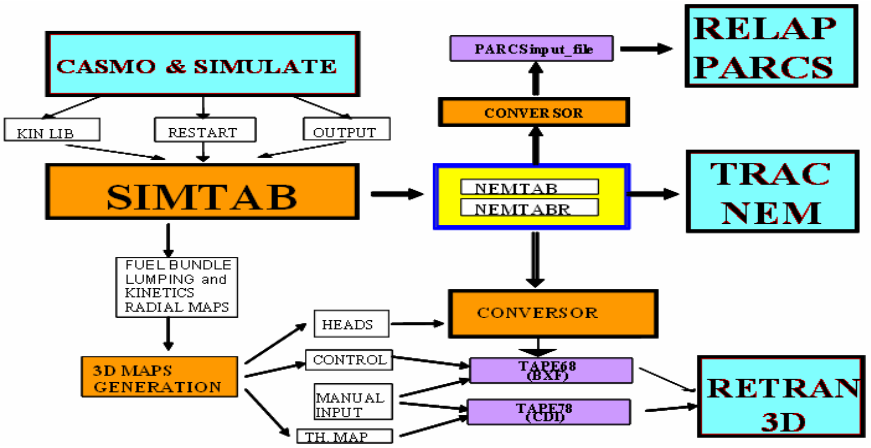

5. Methodology Validation

The 3D kinetic model of RETRAN-3D has been accepted for licensing purposes by the US-NRC and has been used in several 3D kinetics benchmarks [6]. IBERDROLA has additionally performed its own validation by reproducing the SPERT 81 and 86 tests and with comparisons with Cofrentes licensing CRDA analysis performed with RAMONA-3 code by Westinghouse. These comparisons have been presented in several events, and particularly in the Water Reactor Fuel Performance Meeting held in Kyoto in October 2005 [7].
The process to generate the cross section package from SIMULATE is validated for every RETRAN-3D case before performing the dynamic analyses. To verify the adequacy of the process the following relevant RETRAN-3D variables are compared with the SIMULATE results: Initial Keff values; Initial beta effective values; Initial power distributions; Dropped rod worth values
Typical differences obtained in these comparisons are: less than 1% DK in the Keff, less than 15% differences in the power peak values, axial offset and rod worth values and less than 5% in the beta effective.These differences are similar to those obtained in other methodologies where different codes are used for the static and dynamic RIA analysis and are covered by the conservatisms used in the licensing models [8],[9].

6. Analyses

In order to get a high burnup core, the analyses are performed at the end of an equilibrium cycle, at this EOC (including cycle extensions) point, critical conditions are searched following the startup

procedures for each one of the temperatures of analysis. The dynamic CRDA analyses are to cover the range of the possible temperatures during startup conditions (20ºC, 80ºC, 160ºC and 240ºC). With SIMULATE-3 the highest worth rod is searched, starting from each one of the critical conditions,(using the Iberdrola's licensed control rod worth search methodology[10]). In order to have the highest dropped rod worth as possible, the droping rod is assumed to do from fully inserted to fully withdrawn position, bypassing the Bank Position Withdrawal Sequence system (BPWS). This system determines the rod withdrawal sequence and is designed to minimize the rod worths during the plant startup and has to be bypassed in order to have significant enough rod worth values[11], in this case the worth obtained is around 3.5$, with the BPWS active, the rod worth would be limited to 1.7$

7. RETRAN-3D model

The CRDA dynamic analyses are performed with the RETRAN-3D code. The 3D core kinetic module of RETRAN is used. Since the CRDA is a core kinetic accident the modelization is limited to the core. A detailed 3D core model with boundary conditions is sufficient to characterize the simulation, as represented in the next figure .

The core model is formed by a cubic matrix of 28x28x25 active cells surrounded by the reflectors,

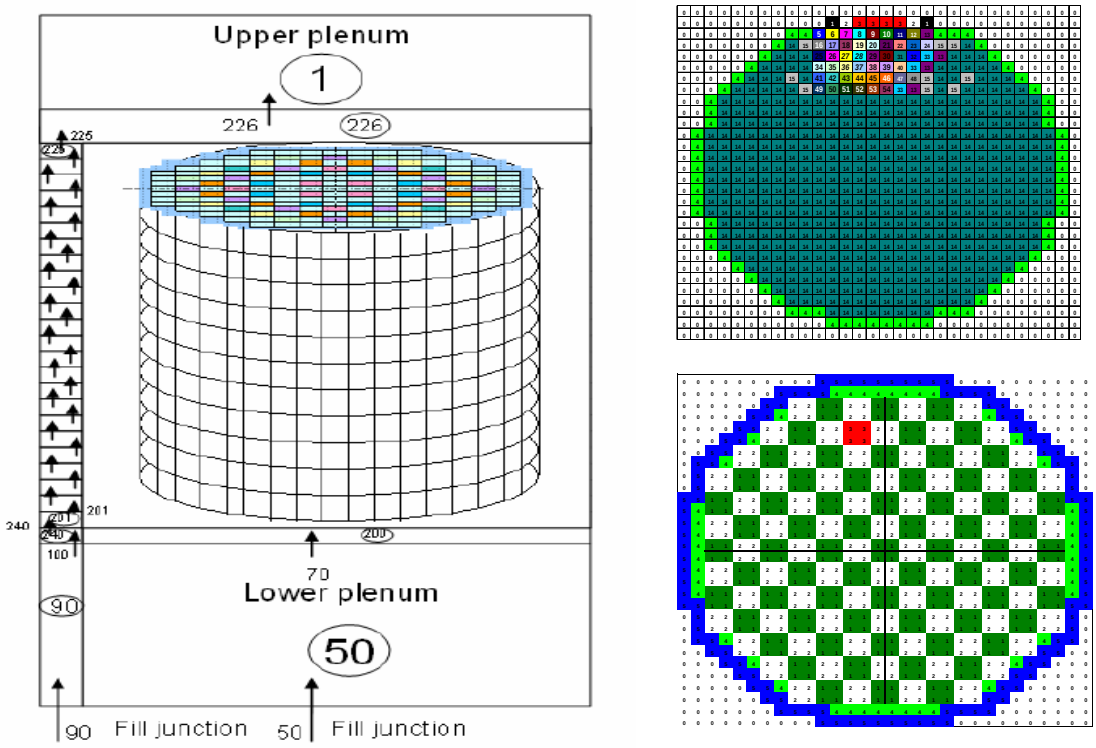

plus the bypass composed by 25 volumes. Both core and bypass are linked in the bottom by the lower plenum and in the top by the upper plenum.

The kinetic model is formed by 4353 different fuel compositions. These compositions result in 175 different kinetic elements as indicated in the previous figure. The kinetic cross sections are obtained from SIMULATE through the SIMTAB method as described.

The initial control rod pattern and rod grouping is illustrated in previous figure. There are three groups of rods in a checkerboard configuration typical of the 50% rod density. Group 3 represents the dropped rod. Group 1 represents the fully inserted rods and group 2 represents the withdrawn rods. The core is composed of 624 bundles of SVEA-96-Optima 2 fuel.

8. PCMI Failure results

The results obtained in the CRDA dynamic analysis indicate that for the cases with a significant initial subcooling, an important part of the total enthalpy rise during the accident is due to the existence of a power tail. It can be clearly distinguished the following evolution in the fuel enthalpy. A fast initial enthalpy rise is observed due to the power peak. A prompt enthalpy (enthalpy at the time of the peak

power plus one pulse width) is defined to quantify this effect. During this period of time the cladding temperatures are close to their initial values.

After the fast initial enthalpy increase there is a slower enthalpy rise due to the delayed power tail. During this period the cladding temperatures increase significantly.

In this figure, the prompt enthalpy and the total enthalpy values for all the bundles surrounding the dropped rod are represented vs. the initial subcooling. It can be clearly observed that the maximum prompt enthalpy decreases slowly with the initial subcooling (slightly lower rod worth value) but the maximum total enthalpy increases significantly with the initial subcooling.

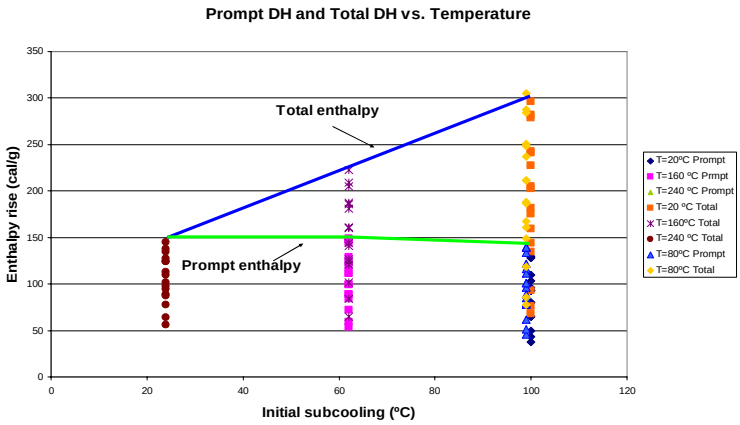

The significance of the prompt enthalpy and the total enthalpy in the potential cladding failure due to Pellet Cladding Mechanical Interaction (PCMI) will be quantified in a separate EPRI project.

9. DNB Failure Results

The typical temporal evolution of the cladding temperature with respect to the fuel enthalpy during the CRDA can be observed in this figure.

It can be seen that the prompt enthalpy rise is produced in a short time period and the cladding temperatures do not increase significantly during this period. This is due to the time needed to transfer the deposited energy from the fuel to the cladding. After that the delayed enthalpy rise occurs at a slower rate and the cladding temperatures follow the total enthalpy rise.

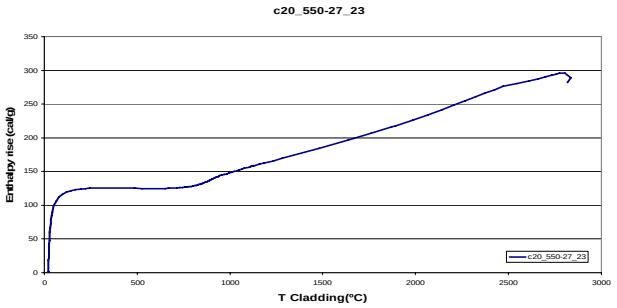

The maximum cladding temperature (PCT) is function of the total enthalpy rise. The relationship between the PCT and the total enthalpy rise is observed in this figure for the different bundles and at the different initial temperatures.

It can be seen that the enthalpy at which the cladding temperature starts to increase (departure from nucleate boiling-DNB enthalpy) is higher when the initial subcooling is higher. However the maximum cladding temperatures reached are relatively independent of the initial subcooling and strongly dependent on the total enthalpy. Only the cases with PCT below the cladding melting temperature (2000ºC) are shown in this figure.

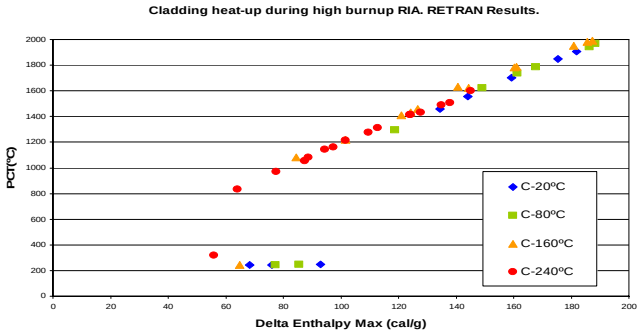

To verify the adequacy of the RETRAN models in the determination of the DNB phenomenon at CRDA conditions, a comparison with CDC-SPERT and Japanese-NSRR experiments has been made. Experiments with similar initial temperatures (20ºC) and rod geometry have been selected from the literature [12]. Rods with a ratio of initial gap width to pellet radius similar to the SVEA-96-OPTIMA 2 fuel rod have been selected (GEP rods in CDC and standard and JPDR-II rods in NSRR). This ratio determines the enthalpy

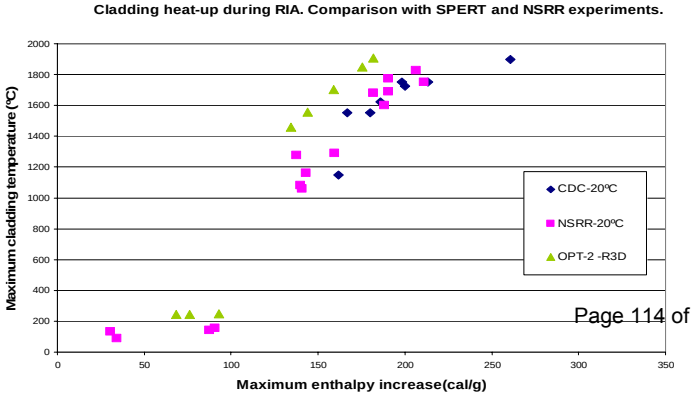

needed to close the gap between the fuel pellet and the cladding and therefore the initiation of the DNB phenomenon. The results are shown in this figure and indicate a good coincidence in the enthalpies needed to initiate DNB between RETRAN calculations and experimental results.

10. Conclusions

Detailed 3D kinetic analyses have been performed with the RETRAN-3D code for different initial temperatures expected at a BWR CRDA during the plant startup process.

Cases with a significant initial subcooling presents a significant power tail well after the power peak has passed. For these cases the power is not reduced until the scram rods are inserted. This power tail produces a significant delayed enthalpy rise.

The ratio between the prompt enthalpy rise and the total enthalpy rise is established as figure of merit to differentiate the different behaviour during CRDA. This ratio is strongly dependent on the initial subcooling (the higher the subcooling the lower the ratio), but is independent on the fuel burnup or the total enthalpy rise.

During the prompt enthalpy rise the cladding temperature remains relatively invariant and equal to the initial temperature. During the delayed enthalpy rise the cladding temperatures increase significantly increasing the cladding ductility. The significance of this phenomenon on the cladding failure due to PCMI will be determined in a separate EPRI project.

The phenomenon of DNB has been calculated at relative low enthalpy rise values, especially for the high temperature case. The significance of these results on the cladding failure due to ballooning and rupture will be determined in a separate EPRI project.

11. References

1 NUREG-800,"*USNRC Standard Review Plan"*, Office of Nuclear Reactor Regulation, Section 15.4.9, Spectrum od Rod Drop Accidents (BWR), Revision 2 July 1981.

2 "*Research Information Letter No 0401, An Assessment of Postulated Reactivity-Initiated Accidents for Operating Reactors in the U.S.*,March 31 2004

3 "*RETRAN-3D: A Program for Transient Thermal-Hydraulic Analysis of Complex Fluid Flow Systems*",EPRI, Palo Alto,CA, EPRI-NP 7450, October 1996.

4 "*SIMULATE-3: Advanced Three-Dimensional Two-Group Reactor Analysis Code"*, Studsvik/SOA-95/15 Rev.0 ,October 1995.

5 Andres J. Gomez et al. " *Validation of SIMTAB Cross Sections Generator Method for TRAC-NEM from SIMULATE-3"*, 2004 TUG Meeting, Gostport, May 2004.

6 Safety Evaluation by the Office of Nuclear Reactor Regulation Related to EPRI-NP-7450(P) "*RETRAN-3D- A Program for Transient Thermal-Hydraulic of Complex Fluid Systems*" EPRI Project No 669, January 25 2001.

7 Andres J. Gomez et al. " *Analysis of a Reactivity Initiated Accidetn (RIA) in Cofrentes NPP, Cold and Hot Conditions with RETRAN-3D"*, 2005 Water Reactor Fuel Performance Meeting,. Kyoto, Japan , October 2-6 2005.

8 Javier Riverola et al. "*Realistic and Conservative Rod Ejection Simulation in a PWR Core at HZP,EOC, with Coupled PARCS and RELAP"*, Proceedings of the 2004 International Meeting on LWR Fuel Performance, Orlando Florida, Sept. 19-22, 2004.

9 CENPD-284-P-A " *Control Rod Drop Accident Analysis Methodology for Boiling Water Reactors:Summary and Qualification"*, ABB Combustion Engineering Nuclear Operations, July 1996.

10 IT-COSNU-205 "*Methodology for the Licensing Analysis of Control Rod Drop Accident (CRDA) for Cofrentes NPP.* Control Rod Calculations, Rev.0 March 2004.

11 NEDO 21231 "*Banked Position Withdrawal Sequence*", C. J. Paone, January 1977.

12 NUREG/CR-0269, TREE-1237, "*Light Water Reactor Fuel Response During Reactivity Initiated Accident Experiments*", August 1978.

METHODOLOGY TO EVALUATE LIMITING CLADDING TEMPERATURES DURING DRY STORAGE OF SPENT FUEL

K. L. NISSEN[1], Y. PARMAR[2], W. GOLL[1], J. AFONSO[2]

[1]*AREVA NP GmbH*
Freyeslebenstr. 1, D-91058 Erlangen, Germany

[2] *Nordostschweizerische Kraftwerke (NOK) AG*
Parkstrasse 23, CH-5401-Baden, Switzerland

ABSTRACT

Dry storage of spent fuel assemblies in casks is established today as an intermediate step before final disposal or before future reprocessing. Various design objectives of the storage casks have to be considered (shielding, thermal, integrity of fuel assemblies etc.). In order to facilitate the cask design evaluation, a very straightforward methodology to derive limiting rod parameters for dry storage is presented in this paper. The evaluation specifically addresses limiting fuel rod cladding temperatures during dry storage of spent fuel using design criteria which ensure fuel rod integrity. A spectrum of maximum allowed cladding temperature vs. time curves are calculated depending on fuel type, fuel rod burnup and previous dwell time in wet storage, thereby accounting for the natural decay. The definition of such a matrix of limiting temperature curves gives the operator a high degree of flexibility in loading the dry storage casks. The fuel manufacturer has the EOL data of the fuel rods, such as cladding degradation, cladding oxidation, cladding hydrogen pick-up, hydride orientation and EOL gas pressure inside the fuel rods from experience feedback and design calculations. With an established creep model (CSAS) and some assumptions regarding the cladding temperatures, the compliance with required cladding stress and creep strain limits during dry storage is shown and hence the limiting temperature curves are derived.

1. Introduction

Dry storage of spent fuel elements in casks is still a maturing technology in the nuclear industry. Wet storage spent fuel pools are increasingly being filled up and dry storage in spent fuel casks is at present the main option for interim storage of spent fuel assemblies in many countries. Switzerland has at present, two facilities, ZWILAG and ZWIBEZ, for interim dry storage. On NOK's request AREVA NP initiated a project to evaluate and define the thermal limits for a safe and efficient storage of spent fuel assemblies in the storage casks. Such thermal limits will then be used by the cask designer when optimising the cask design. This methodology, developed to evaluate limiting fuel rod cladding temperatures during dry storage, is described in this paper. The paper also describes the regulatory background in Switzerland and the design limits for safe dry storage of the fuel. Furthermore, some important results are discussed. In Fig. 3 an example of limiting temperature decay curves for a safe and efficient storage of fuel rods is given. Similar curves have been evaluated for nearly all fuel types presently used by NOK, in Beznau Nuclear Power Plant (KKB) and Leibstadt Nuclear Power Plant (KKL), in order to improve the interface between fuel supplier (fuel design) and cask supplier (cask design and loading). If the maximum cladding temperature in the cask stays below the limiting temperature curve, the fuel rod integrity design limits are inherently fulfilled.

2. Regulatory background in Switzerland

Spent fuel storage casks must be designed to meet a number of safety objectives, including:

1. thermal performance (ensure that adequate heat dissipation is achieved)
2. radiological protection (ensure that dose-rates from the spent fuel in the casks are less than limits prescribed in the regulations)
3. confinement (ensure that there is adequate confinement and containment of the spent fuel under all credible conditions of storage)
4. sub-criticality (maintain sub-criticality under all credible conditions)
5. retrievability (allow the ready retrieval of the spent fuel from the casks)

In general, it must be assured that the spent fuel is maintained in the configuration that is analyzed in the Safety Analysis Report (SAR). The spent fuel cladding is the primary structural component that is used to ensure that the spent fuel is contained in a defined geometric configuration and in addition it forms a barrier to radioactivity release. Accordingly, cladding considerations must be addressed so as to provide reasonable assurance that spent fuel is maintained in the configuration that is analyzed in the storage SAR.

Up to the period that a Swiss regulatory guideline came into force in July 2003, the Swiss Regulatory Authority (HSK) required that the storage license applicant demonstrates that the clad temperature is not greater than 350-390°C. This was mainly on the basis of the diffusion-controlled cavity growth (DCCG) concern. The HSK Guideline focuses on casks (transport and storage) used in Switzerland for the interim storage of vitrified high-level radioactive waste and spent fuel. As part of the Swiss storage licensing process, the license applicant is required to submit an application for approval for storage of a cask type, based on the HSK regulatory guideline. This generally takes the form of a storage Safety Analysis Report (SAR) submittal which is then approved. This submittal is made prior to order/manufacture of cask.
In particular, with regard to storage of fuel assemblies, the Guideline requires that clad damage be prevented. In order to fulfil this requirement:

- the fuel manufacturer is required to specify the limiting criteria for clad integrity during the dry storage period.
- these criteria are then to be submitted to the HSK for approval as part of the SAR submittal.
- if the criteria identified is clad temperature related, then proof of compliance of this criteria must be provided, taking into account the storage concept as approved by the HSK as well as assuming that the facility is used up to its full capacity.

3. Design limits for safe dry storage of spent fuel rods

The safety functions of a dry cask storage system, such as ensuring subcriticality during and retrievability after storage, impose requirements to avoid degradation of the fuel assembly. This is achieved by maintaining the integrity of the fuel assembly structure and preventing systematic cladding failures. The applied engineering approach to ensure cladding integrity imposes a limit of 1% thermal creep hoop strain and 120 MPa hoop stress in the cladding during the entire storage process.

The strain criterion of 1 % thermal creep hoop strain was demonstrated by a series of creep rupture tests on irradiated cladding [2] (see Fig. 1).

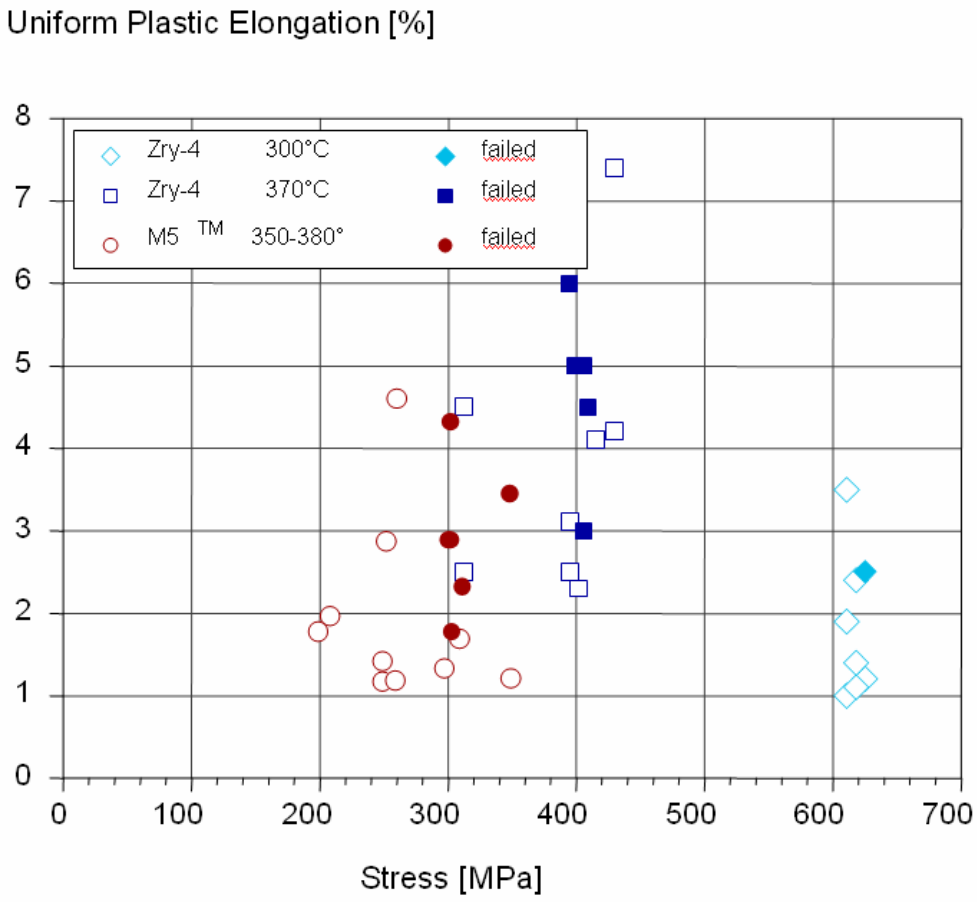

Fig 1. Irradiated cladding in creep rupture tests fails at hoop strains greater than 1 %

The limit of 1 % burst strain was derived from burst tests with medium-level burnup test sections. With increasing burnup and increasing hydrogen content in the cladding, the strain criterion is now verified for high burnup rods having a Zry cladding [1]. The tests were performed with hoop stresses of 400 to 600 MPa and showed that a uniform elongation of at least 1 % is achievable without causing a defect. The tests were done at temperatures of 300 to 380°C which is realistic for dry storage conditions allowing temperatures of up to 400°C. In these tests, the Zry-4 samples were cooled down at a stress of 100 MPa in order to assess the influence of hydrogen on cladding integrity. Although some hydride reorientation was observed, the cladding did not fail. In that respect, the stress criterion for avoidance of cladding failures due to hydride reorientation was also verified.

The applied stress criterion of 120 MPa excludes a substantial reorientation of precipitated Zr-hydrides in the cladding [2]. As a result thereof, the susceptibility to DHC (delayed hydrogen cracking) is practically eliminated.

4. Methodology to evaluate thermal clad limits

AREVA NP developed in collaboration with NOK, a methodology to evaluate bounding maximum temperature curves during dry storage for the fuel rods on the basis of the design criteria on cladding strain and stress. Input parameters to these calculations are; fuel rod design data, the burnup and the dwell time in wet storage. With this approach, the cask designer has the clad limits already available when performing cask design evaluation, thus optimising loading flexibility.

The iterative methodology applied is shown in Fig. 2. Two sets of input data are necessary for the procedure (see left hand boxes). The values for fuel rod internal gas mass and free volume are taken from fuel rod design calculations for in-reactor service (maximum inner rod gas pressure case).

The temperature of the fuel rod during dry storage is calculated starting from a decay heat generation vs. time curve for spent fuel of a specified burnup and fuel type (UO_2 or MOX) as a master maximum temperature vs. storage time curve. This curve takes into account the previous dwell time of the fuel assemblies in wet storage. A longer dwell time in wet storage leads to less slope in the decay curve of temperature. The master maximum cladding temperature decay curve can then be scaled (decreased or increased) by applying a scaling factor. The scaling factor is adjusted, and thereby the temperature curve, until the design criteria are just met when evaluated with the creep and stress model (within the specified convergence limit of 0.9 to 1.0 of the design limit). If the convergence criteria on the right hand side of Fig. 2 are fulfilled, the limiting temperature curve for clad temperature during dry storage is found for the specific rod burnup, the fuel type and the earlier dwell time in wet storage.

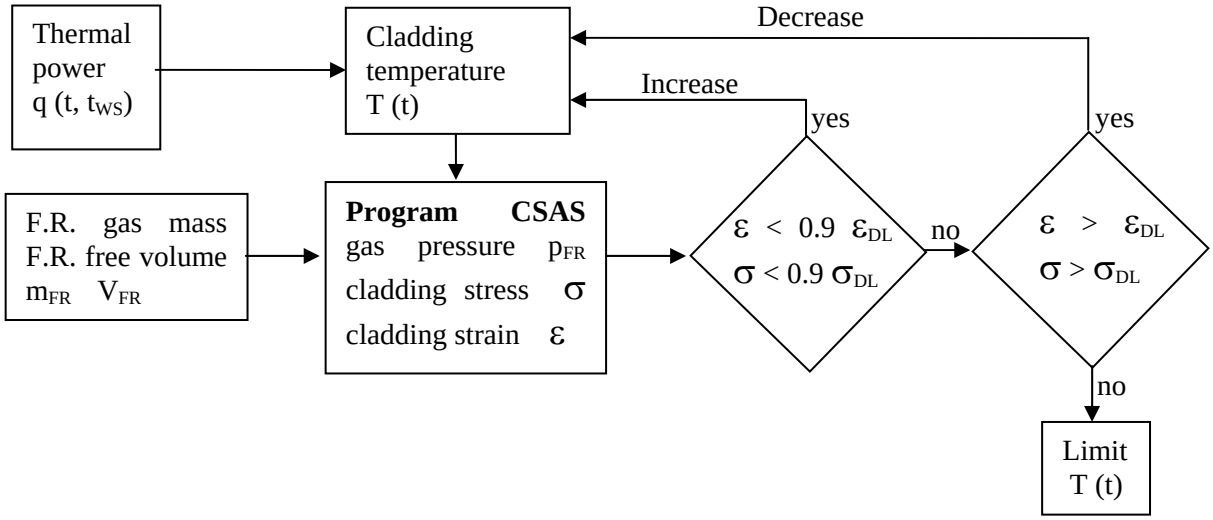

Fig 2. Iterative methodology to evaluate limiting cladding temperature curve T(t)
(F.R.=fuel rod, DL=design limit, t_{WS}=time in wet storage)

5. Calculation of cladding stress and strain during dry storage

The calculation of the cladding stress is dependent on the fuel rod inner gas pressure. With the knowledge of the free volume and the gas mass inside of the fuel rod, the gas pressure can be calculated from the fuel rod temperature with the ideal gas law. Temporal and axial variations of the temperature along the fuel rod during dry storage have to be considered. The master decay curve for the temperature is deduced from isotope decay calculations which give the heat produced by a fuel assembly vs. time. A proportionality factor based on the behaviour of results from typical cask temperature calculations can be deduced which is of the form of a heat transfer coefficient. The resulting master decay curve for the temperature can be increased or reduced simply by a scaling factor. In this manner, the typical decay behaviour of the temperature during dry storage of fuel elements is taken into account and serves as a realistic assessment of the yet to be calculated specific cask heat transfer behaviour. Characteristic behaviour of e.g. the slow MOX fuel rod temperature decay will be reproduced via the scaling of the original isotope decay calculations.

The hoop stress is the driving force for the thermal creep of the cladding during dry storage. Creep strain measurements on unirradiated cladding materials were performed extensively at various stress and temperature conditions [4]. The behaviour of unirradiated cladding material is a conservative estimate of the creep strain of irradiated cladding. The decreasing temperature and hoop stress during dry storage necessitate a computer calculation of the cladding hoop stress and strain with the program CSAS developed by AREVA NP.

6. Discussion of results

Fig. 3 gives exemplary results for limiting temperature decay curves for a BWR UO_2 fuel. The calculations were performed for a rod burnup of 70 MWd/kgU for four different dwell times in wet storage. For longer wet storage times prior to dry storage, the allowed temperature curves during dry storage exhibit less slope and as a result allow only a lower starting maximum temperature in the casks. Or in other words: For 5 years of wet storage we can start with a higher maximum temperature in the cask compared to the case with 40 years of wet storage. Nevertheless the overall heat produced by the fuel element with 40 years of storage will be much less than that of the element with 5 years of storage. The temperature curves of Fig. 3 are limiting curves and allow the cask loader to optimise the loading of the casks.

Fig. 4 gives the dependence on burnup in addition to the dependence on wet storage time. This is an example of an UO_2 fuel element for a PWR. Shown is the maximum allowed cladding temperature at beginning of dry storage. It again decreases with dwell time in wet storage for the reasons given above and also as expected with burnup due to the lower slope of the temperature decay curve for higher burnup.

7. Conclusions

Using this methodology it is demonstrated that for the various fuel rod types considered, clad integrity during the dry storage period is assured.

8. References

[1] W. Goll, H. Spilker, E. Toscano: Short-time creep and rupture tests on high burnup fuel rod cladding, Journal of Nuclear Materials, 289 (2001), 247-253

[2] W. Goll, A.C. Leger, K. McCoy: Spent Fuel Behavior under Dry Cask Storage Conditions, Topfuel, Würzburg, Germany, March 16-19, 2003

[3] D. O. Northwood, U. Kosasih: Hydrides and delayed hydrogen cracking in zirconium and its alloys, International Metals Reviews, 28 (1983), 92-120

[4] H. Spilker, M. Peehs, H.-P. Dyck, G. Kaspar, K. Nissen: Spent LWR fuel dry storage in large transport and storage casks after extended burnup, Journal of Nuclear Materials, 250 (1997), 63-74

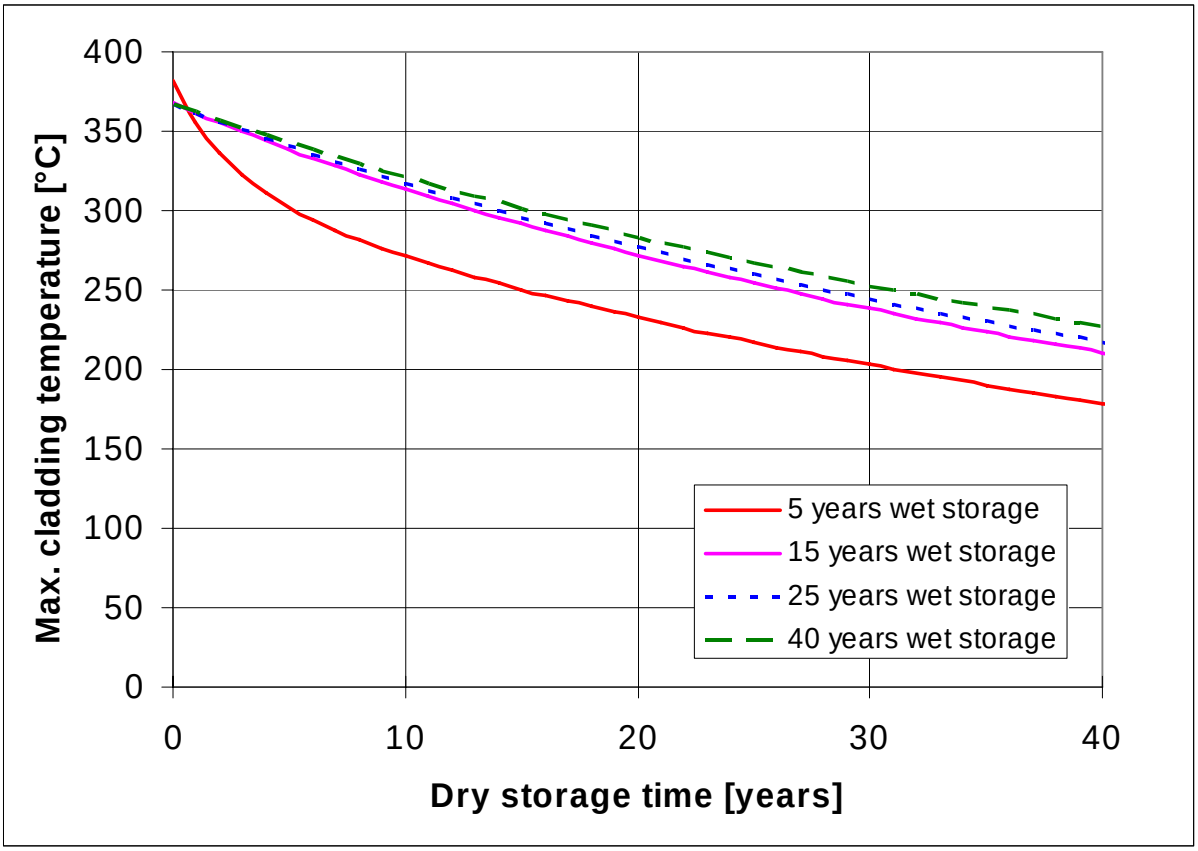

Fig 3. Limiting temperature decay curves for a BWR fuel rod (70 MWd/kgU) for 4 different dwell times in wet storage

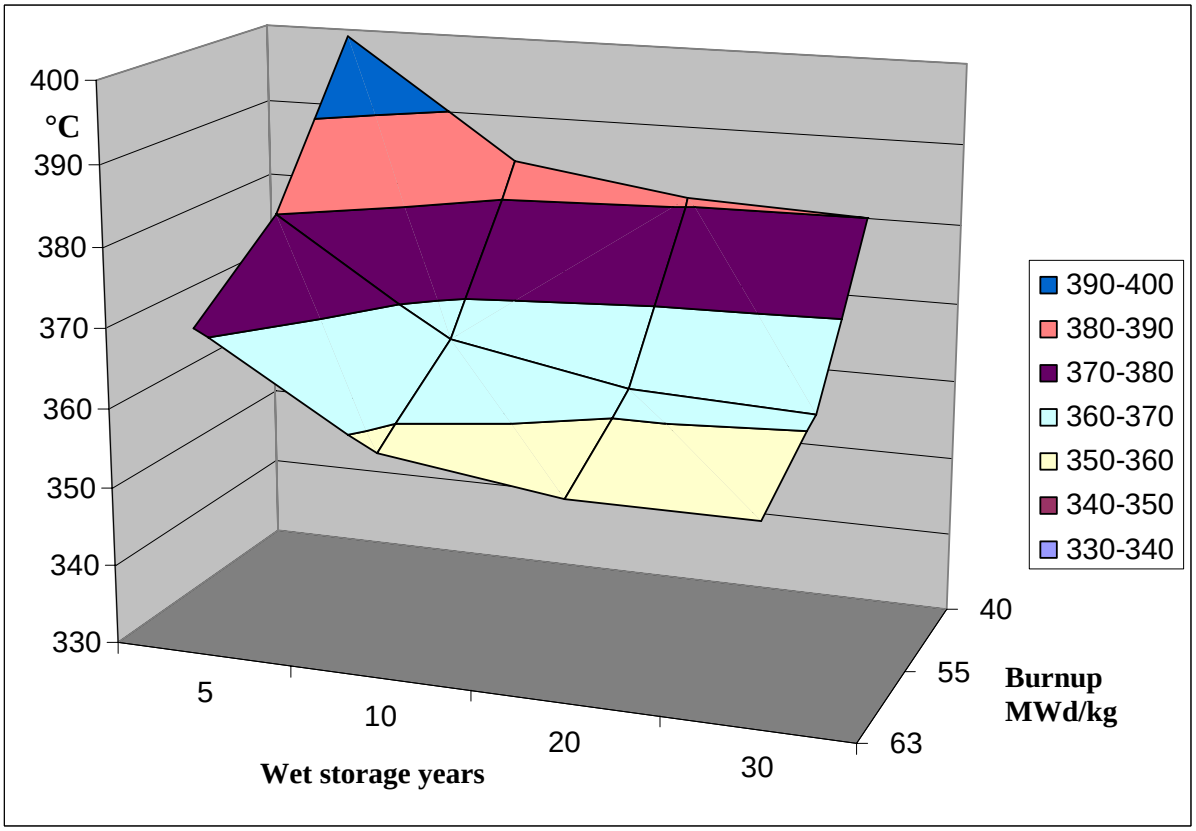

Fig 4. Maximum admissible cladding temperature at beginning of dry storage as a function of wet storage time and burnup for PWR UO_2 fuel

STUDY OF FUEL ROD CRITERIA FOR LOCA CONDITION IN THE LIGHT OF RECENT EXPERIMENTAL DATA

H.G. SONNENBURG
Thermal Hydraulics and Process Engineering Division,
Gesellschaft für Anlagen- und Reaktorsicherheit (GRS)mbH, Forschungsgelände, 85748 Garching

ABSTRACT

Recent investigations of the fuel rod performance under LOCA condition at Argonne National Laboratory (ANL) revealed that the fuel rod cladding looses its ductility at an oxidation level which is below the acceptance value. The actual regulatory rule for oxidation under LOCA requires that not more than 17% of the cladding thickness reacts with oxygen according to the equivalent cladding reacted (ECR) criterion. It turned out that Zry-4, M5 and Zirlo claddings have lost their ductility when oxidized at 1200°C to ECR values above 10% and subsequently quenched.
In order to assess the importance of the ECR criterion among the other core coolability criteria, which are applied in Germany, these criteria have been evaluated for a typical LOCA transient. The core coolability criteria applied are: a) ECR < 17%, b) Tcladding < 1200°C and c) Z_{failed} (number of burst fuel rods in core) < 10%. A screening of the fuel rods in a core with linear heat generation rate (LHGR) ranging from 300 W/cm to 600 W/cm has been accomplished in a generic study using both the thermal hydraulic code ATHLET and the fuel rod mechanics code TESPA-ROD.
According to this screening study, the activation of the criteria a) to c) can be reached at certain LHGR. On the other hand, depending on the LHGR of a fuel rod, specific LOCA phenomena like autocatalytic oxidation, excessive ballooning of cladding due to superplasticity, or severe embrittlement of ballooned cladding area may occur and threaten the core coolability. Thus, based on this fuel rod screening in LHGR the capability of each criterion to preserve the core coolability can be assessed.

1. Introduction

An improved corrosion resistance of the fuel rod cladding has been achieved relative to the conventional Zircaloy-4 cladding by adding niobium as alloying element (addition of 1% niobium in M5 cladding or in E110 cladding) or by protecting the cladding surface with a pure zirconium layer of some µm thickness (DUPLEX cladding). The price for the improved corrosion resistance under operational condition is a loss of cladding performance under loss of coolant accident (LOCA) condition.

Recent investigations at Argonne National Laboratory (ANL) reveal that the ductility of niobium containing cladding - in particular of the E110 cladding - might be totally lost if the fuel rod is heated up to 1200°C, oxidized, and subsequently quenched at 800°C to room temperature. During this LOCA like temperature transient it has been found that E110 cladding is susceptible to the hydrogen up-take. This hydrogen up-take leads to a severe embrittlement of the E110 cladding.

If the temperature transient is repeated for all cladding types under fuel rod internal pressure, the fuel rod starts to balloon and rupture. The hydrogen up-take close to the rupture opening of the cladding is so high that the cladding becomes totally brittle. This embrittlement mechanism occurs for each known type of cladding material. Because the ballooning and rupture of the cladding leads to both a large hydrogen partial pressure inside the burst fuel rod and a strained cladding condition which reduces the protective property of the oxide layer at the cladding surface. Large quantities of hydrogen enter into the cladding. For preserving a residual ductility in the cladding the 17% ECR criterion had

been defined in safety regulations. In view of the hydrogen up-take mechanism it becomes obvious that this safety criterion does no longer guarantee the residual ductility under LOCA condition.

The kinetics for both oxygen up-take and hydrogen up-take have been modelled and implemented into the code TESPA-ROD [SON 02]. The code predictions have been validated on the ANL data for hydrogen up-take and oxygen up-take. Prototypic LOCA transients have been calculated with this code for three different cladding types (Zry-4, M5 and DUPLEX). The linear heat generation rate (LHGR) has been varied from 300 W/cm to 600 W/cm which covers the LHGR range for a prototypic reactor core loading. Two burn-up levels have been assumed for these LOCA calculations, 30 MWd/kg as medium burn-up level and 80 MWd/kg as high burn-up level. The resulting cladding phenomena as calculated by TESPA-ROD will be discussed in the light of German safety criteria.

2. Oxidation and hydrogen up-take of the cladding

High temperature oxidation has been measured for the cladding materials Zry-4, Zry-2, E110, M5 and ZIRLO at ANL. E110, M5 and ZIRLO are 1% niobium containing materials. 25 mm long fuel rod samples of each material are exposed to a steam atmosphere under ambient pressure. Both the inner side and outer side of the samples are exposed. The oxidation temperature ranges from 1000°C to 1200°C [BIL 05]. It turns out that the oxygen mass up-take is best described with the correlation of Cathcart and Pawel (CP model) [CAT 77]:

$$\text{oxygen uptake}: \tau \text{ in } \frac{\text{kg O}}{\text{m}^2} \qquad \dot{\tau}\tau = \frac{\delta_\tau^2}{2} \qquad \tau = \delta_\tau \sqrt{t} \qquad \text{and} \qquad \frac{\delta_\tau^2}{2} = 18.09\, e^{\frac{-167074\,\text{J/mol}}{\text{R T[K]}}} \text{ in } \frac{\text{kg}^2\,\text{O}}{\text{m}^4\,\text{s}}$$

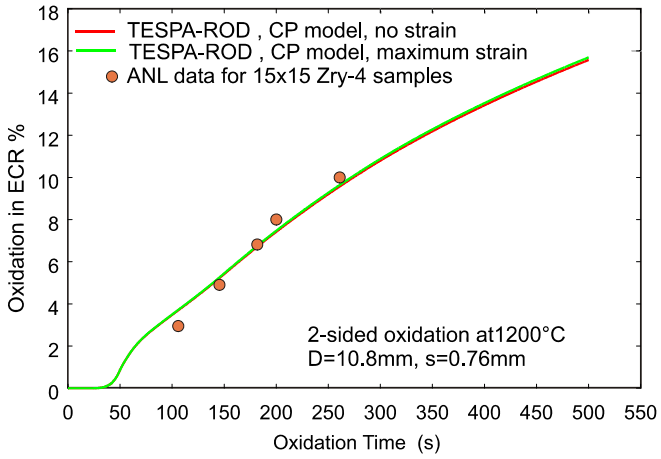

Fig. 1: TESPA-ROD prediction of ANL test for oxygen up-take measured in ECR-%

The TESPA-ROD model for oxidation also considers the straining of the cladding ε. If the cladding balloons due to internal pressure, the surface increase leads to an increase of the oxidation rate proportional to the enlarged cladding surface. The ECR value is determined from the oxygen mass up-take τ [kg O/m²] in the cladding assuming a stoichiometric relation of 2 mols O to 1 mol Zr:

$$\text{ECR} = \frac{\tau}{\rho_{Zr}\, s_0} \frac{91.2 \frac{\text{kg Zr}}{\text{kmol}}}{32 \frac{\text{kg O2}}{\text{kmol}}} 100 \qquad \text{in} \quad \% \qquad\qquad s_0 : \text{cladding thickness at design condition}$$

The ANL test OCL#11 (Zry-2 cladding) is a so-called integral test. The specimen is heated up to 1204°C. This temperature is kept constant for 5 minutes. During heat-up the internal pressure rises up to a maximum of 8.61MPa. The rod balloons and bursts. The temperature at burst is 680°C. Beyond the time of burst a 2-sided oxidation takes place reaching 18% ECR. The investigation of the cross-section at the burst level shows ECR-values from 13% to 36%. The post test prediction with TESPA-ROD for this ballooned rod leads to comparable ECR-values.

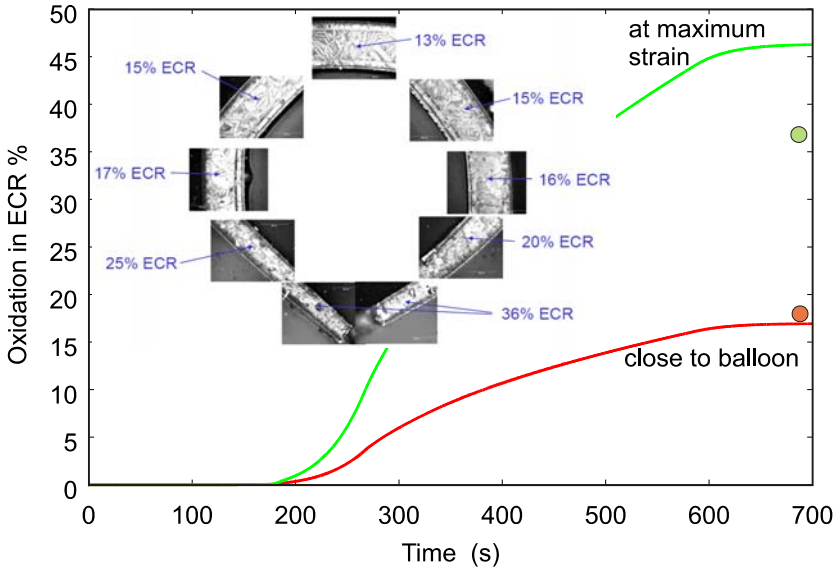

Fig. 2: TESPA-ROD prediction of ANL test OCL#11 for oxygen up-take measured in ECR-%

Close to the burst tip, the cladding strain measured reaches a maximum value of 50% strain. The TESPA-ROD prediction is 64% strain. Consequently, the corresponding ECR-value is over-predicted by TESPA-ROD with 46% compared to the measured value of 36%. This comparison illustrates that the calculation of ECR-values has to consider the actual geometry of the ballooned area of the fuel rod.

The hydrogen up-take η has been measured in the ANL test OCL#11. The hydrogen up-take varies along the axial position. The maximum of hydrogen up-take is about 70 mm in axial distance to the burst centre. About 3500 to 4000 wppm H have been found there. The hydrogen up-take becomes gradually smaller if the straining of the cladding vanishes with distance from the burst centre.

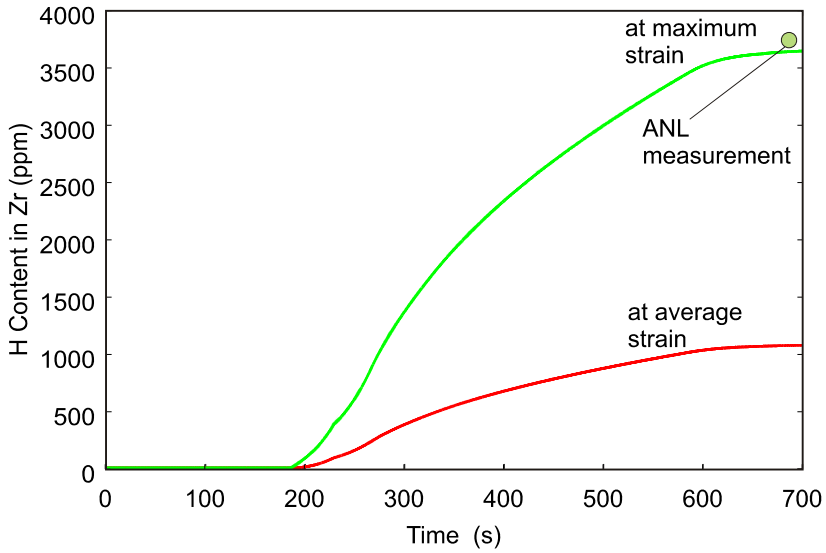

Fig. 3: TESPA-ROD prediction of ANL test OCL#11 for hydrogen up-take

The hydrogen up-take rate in TESPA-ROD is calculated proportional to both the oxygen up-take rate and the actual strain ε. s_0 is the design value of the cladding thickness.

$$\text{hydrogen uptake rate}: \dot{\eta} = \dot{\tau}\varepsilon \begin{cases} 16200 \frac{\text{wppmH}}{\text{kgO/m}^2} & \text{if } T < 1273\,\text{K} \\ 9050 \frac{\text{wppmH}}{\text{kgO/m}^2} & \text{if } T > 1273\,\text{K} \end{cases} \qquad \text{in } \frac{\text{wppm H}}{\text{s}}$$

The proportionality for O [kg O/m²] to H [wppm] has been identified for niobium containing cladding materials at FZK Karlsruhe [HOF 99]. The dependence on strain ε has been additionally introduced in the equation because the process of straining provides cracks in the protective oxygen layer thus hydrogen can reach the metallic surface of the cladding. The more the cladding is strained the more cracks will occur and the more hydrogen can be taken up. Consequently, this model predicts for oxidation tests with non strained claddings a negligible hydrogen up-take of the order of 10 to 50 wppm H. For the ANL integral test OCL#11 with a cladding strain of ε=0.6 (~60% strain), a hydrogen pick-up of 3650 wppm is predicted. This value is in relative good agreement with the measured hydrogen pick-up of 3500 wppm and 4000 wppm at about 70 mm distance from the burst centre.

3. Prototypic LOCA transients

As described above, the oxygen and hydrogen up-take has been modelled in TESPA-ROD. Prototypic LOCA transients have been evaluated with this code in order to identify the relevance of oxygen and hydrogen up-take during LOCA transients. The oxygen and hydrogen up-take depends on the time interval when the cladding temperature exceeds 700°C. The more efficient the emergency core cooling system (ECCS) operates the shorter this time interval is. The selected LOCA transient corresponds to a less efficient ECCS. The time interval, when cladding temperatures are above 700°C, is about 270 s. Depending on the LHGR the cladding temperature reaches values above 750°C (300 W/cm). At LHGR values close to 600 W/cm even the autocatalytic reaction can occur. Table 1 summarizes the cladding events calculated with TESPA-ROD for different cladding types in relation to LHGR values.

Cladding type	Burst of Fuel Rod	Cladding temperature of 1200° exceeded	Oxidation of 17% ECR exceeded	Autocatalytic reaction
M5	>360 W/cm	>550 W/cm	>590 W/cm	> 600 W/cm
Zry-4	>390 W/cm	>540 W/cm	>580 W/cm	>590 W/cm
DUPLEX	>340 W/cm	>520 W/cm	>570 W/cm	>580 W/cm

Tab. 1: Summary of cladding events during LOCA predicted with TESPA-ROD

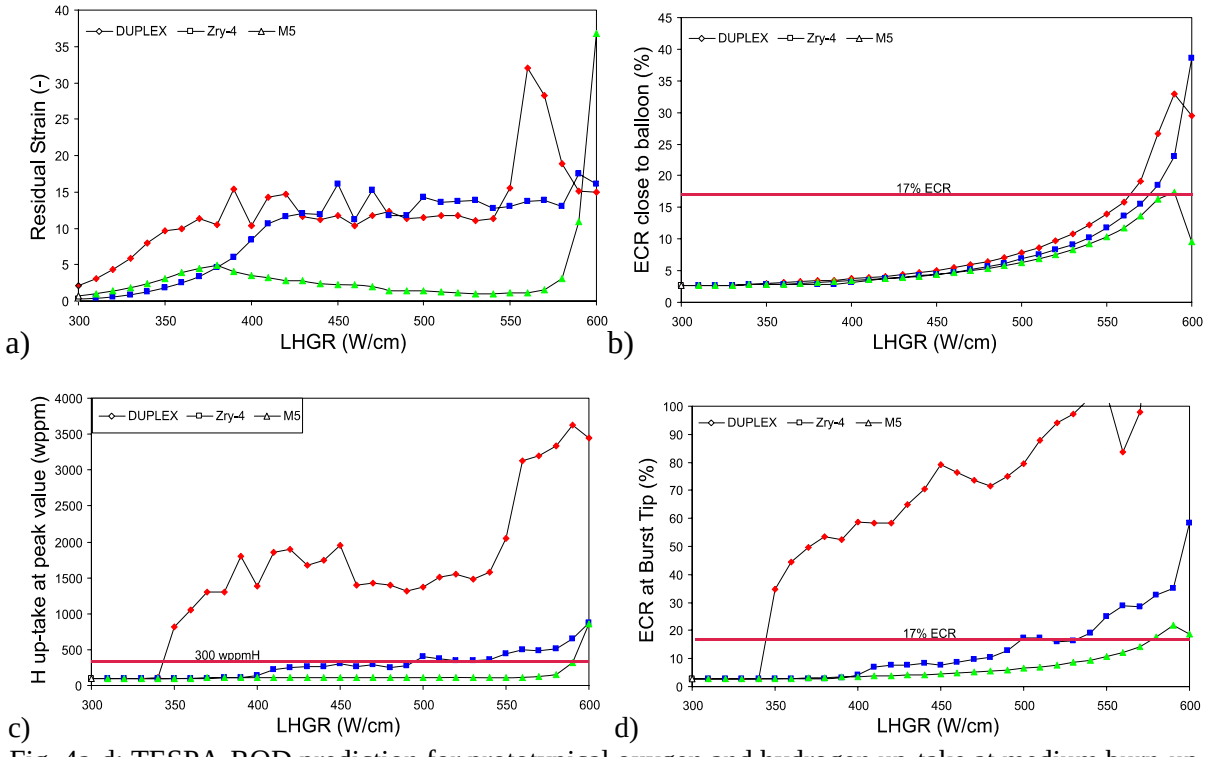

Fig. 4a-d: TESPA-ROD prediction for prototypical oxygen and hydrogen up-take at medium burn-up

The values for oxygen and hydrogen up-take as well as for cladding strain **at the end** of each LOCA transient are plotted in Fig. 4. Each plot in Fig.4 contains the results of 93 LOCA calculations.

4. Assessment of cladding ductility

Further ANL tests on hydrogen up-take reveal that the cladding ductility is lost if moderate oxidation of about 5% ECR occurs in combination with more than 300 wppm H. This hydrogen enhanced embrittlement occurs if the LHGR value exceeds **500** W/cm for Zry-4 (ECR close to balloon is ~7.5% and H up-take at peak value is ~300 wppmH), it occurs much earlier for DUPLEX at about **360** W/cm (ECR close to balloon is 3% and and H up-take at peak value is ~1100 wppm H) and relatively late for M5 at about **580** W/cm (ECR close to balloon is 16% and and H up-take at peak value is ~150 wppm H). In the light of the hydrogen enhanced embrittlement the presently applied embrittlement criteria (17% ECR and 1200°C) appear to be no longer applicable. If the 17% ECR criterion would have been applied to the strained burst tip, then the hydrogen enhanced embrittlement appears to be included, because the straining which reinforces the H up-take is considered. A residual ductility is preserved if the 17% ECR criterion is applied to the strained burst tip. The values of 500 W/cm (Zry-4), 360 W/cm (DUPLEX) and 580 W/cm (M5) agree with the 17% ECR value at burst tip, see Fig. 4d.

The same finding can be identified if the medium burn-up is shifted to high burn-up. The data are not shown here. The major difference to the medium burn-up is that the internal pressure in the fuel rod is increased. The ballooning at same LHGR values is more pronounced because of both higher internal pressure and hydrogen enhanced creep rate. The conclusion drawn is the same as for medium burn-up.

In addition to the embrittlement criteria, the fuel rod burst criterion has to be fulfilled in Germany, too. As can be seen from table 1, the event of fuel rod burst occurs at LHGR values which are about 200 W/cm less then those of the ductility criteria. If the fuel rod burst criterion ($Z_{failed} < 10\%$) is included in the safety assessment, the violation of the ductility criteria is of minor importance. Nevertheless, the ductility criteria need to be re-assessed because the burst criterion allows for 10% of the rods in a core to burst, for which the ductility still has to be proven.

5. References

[BIL 05] Billone, M.C.: LOCA Embrittlement Correlation, ANL report, NRC ADAMS, 08.04 2005

[CAT 77] Cathcart, J.V.; Pawel, R.E.; McKee, R.A.; Druschel, R.E.; Yurek, G.J.; Campbell, J.J.; Jury, S.H.: Zirkonium Metal-Water Oxidation Kinetics IV. Reaction Rates Studies, ORNL/ NUREG-17, 1977

[HOF 99] Hofmann, P.; Miassoedov, A.; Steinbock, L.; et al.: Quench Behavior of Zircaloy Fuel Rod Cladding Tubes. Small-Scale Experiments and Modelling of the Quench Phenomena, FZKA 6208, INV-COBE(98)-D018, ISSN 0947-8620, März 1999

[SON 02] Sonnenburg, H:G:; et al.: Development of methods for the analysis of the fuel rod behaviour in the high burn-up regime. Final Report, GRS-A-3079, 2002

DEVELOPMENT OF EXPERT SYSTEM FOR FAILED FUEL DIAGNOSIS UNDER WWER OPERATION CONDITIONS

V.V. LIKHANSKII, I.A. EVDOKIMOV, A.A. SOROKIN,
A.G. KHROMOV, V.D. KANUKOVA, O.V. APOLLONOVA

SRC RF TRINITI, 142190, Troitsk, Moscow Reg., Russia

V.B. IONOV, A.V. UGRYUMOV

JSC TVEL, 119017, 24/26 Bolshaya Ordynka st., Moscow, Russia

ABSTRACT

An analytical approach for diagnosis of WWER fuel failures under operation conditions is presented. The diagnosis is based on measurement of specific activity of reference nuclides in reactor primary coolant and application of a computer code for data interpretation. Analysis of coolant activity data comprises several steps: mass of tramp uranium is evaluated in the reactor core; failures are detected and characterized by iodine and caesium spiking; neural-network analysis is performed to get failure parameters in more detail. The expert system based on this approach provides the on-line evaluation of WWER failure characteristics – the number of failed fuel rods, fuel burnup and defect size.

1. Introduction

Fuel rod failures, progressively decreasing in frequency, are still possible events during operation of nuclear power plants (NPPs). Failures lead to release of radioactive fission products (FPs) into primary coolant. In case of a serious failure fuel washout and severe contamination of primary circuit may take place. Since regulatory authorities establish safety margins for primary coolant activity, all failed fuel bundles should be identified and characterized in course of refuelling outage. In several countries, e.g. Russia and France, failed fuel bundles with small leaks are allowed for further operation in reactor core.

Leakage tests during reactor outages are time consuming and involve high financial costs. To reduce expenses and a risk to miss a failure most NPPs use a preliminary evaluation of failure characteristics before the end of fuel campaign. The major failure parameters to be determined are the number and burnup of failed fuel rods as well as leak size. The state-of-the-art methods of failure evaluation under operation conditions are based on monitoring of primary coolant activity and application of computer codes for data interpretation. These methods can be integrated into a computer expert system for the on-line failure diagnosis at NPPs.

Several expert systems are reported in literature. The TIMS code based on RELWWER-2 calculations has been used at most WWER units, so far [1]. The TIMS works with only iodine activity in primary coolant. Other diagnostic systems use additional data on noble gas activity – the DIADEME [2] and the RING [3] codes, the PES-PEPA modules [4]. Caesium spiking data provide evaluation of failed fuel burnup [2]. Recently a new technique for failure analysis in BWRs and PWRs was developed [5]: activities of long-lived ^{133}Xe and short-lived ^{92}Sr or ^{89}Rb are compared to detect when a small or large (with fuel washout) failure occurs during operation.

At present time an integrated program on improvement of WWER failure diagnosis is in progress. The mechanistic code RTOP-CA has been developed as a part of this program [6]. The RTOP-CA code can be used for two purposes if failure characteristics are known. The first one is prediction of coolant activity in primary WWER circuits. The second one is modelling of defective fuel behaviour and degradation. The RTOP-CA code was extensively verified including NPP data on WWER primary coolant activity [7,8]. Currently the RTOP-CA verification database is being widened to cover issues of failed fuel performance at high burnups.

The RTOP-CA code provides the basis for constructing an advanced expert system for monitoring of fuel failures at operating WWERs. The expert system involves application of a neural-network approach for interpretation of primary activity data and evaluation of failure parameters. Key features of the neural-network approach are reported in papers [7,8].

The present paper is focused on adaptation of the neural-network approach to NPP conditions and its verification against NPP data. Verification database includes history of primary coolant activity and results of leakage tests in course of refuelling outages obtained at several WWER units. Analysis of coolant activity data by the expert system comprises several steps:

- mass of tramp uranium is evaluated in reactor core;
- failures are detected and characterized by iodine and caesium spiking;
- fuel washout is assessed for severe failures;
- neural-network analysis is performed to get failure characteristics in more detail.

2. General analysis of primary coolant activity

NPP data for failure analysis include activity of reference nuclides, history of reactor power and coolant purification rates (different for volatile and gaseous species). Russian regulatory instructions for WWERs prescribe measurement of iodine activity in primary coolant and do not mention gaseous FPs. For this reason, detailed data on gaseous activity is not always available at NPPs. The expert system being developed for WWER failure diagnosis accepts iodine radionuclides for the basis and takes gases into account when available.

The first step in data analysis is evaluation of tramp uranium mass in the reactor core. Contamination with tramp uranium forms a background activity in primary coolant. The evaluation is possible because of different mechanisms of FP release from failed fuel rods and from tramp uranium. In the former case FPs are generally released by diffusion and the release-to-birth ratio decreases for short-lived species. In the latter case the governing mechanism is recoil and the released fractions are lifetime independent. Consequently, activity of short-lived nuclides in primary coolant is mostly due to tramp uranium and contribution of fuel failures is negligible. A preferable nuclide for evaluation of tramp uranium mass is ^{134}I. It is fairly short-lived and susceptible of adsorption inside failed fuel rods [2]. ^{89}Rb suggested in [5] can also be considered for WWERs.

The same concept allows to detect failure occurrence and to gain a rough idea of its seriousness during reactor operation. Mass of tramp uranium is formally calculated using ^{131}I and ^{134}I activities assuming the recoil mechanism. If the both calculations give close results then the core is intact. Otherwise a failure has occurred. The higher is the ratio of ^{131}I to ^{134}I calculations the higher is defectiveness of the core. Severe failures can be also identified by growth of ^{134}I activity during the cycle that implies possibility of fuel washout.

The most reliable failure indicator is spiking in activity of long-lived nuclides (^{131}I, ^{134,137}Cs or ^{133}Xe) at power manoeuvres, reactor start-up or shutdown. Caesium spiking provides data for estimation of failed fuel burnup. Ratio of ^{134}Cs to ^{137}Cs activity in spikes is a function of burnup which

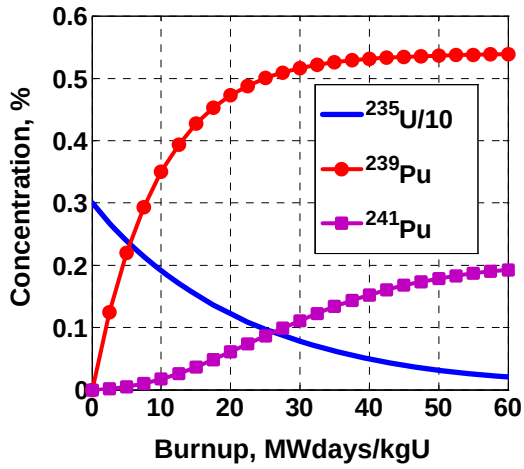

Fig.1. Evolution of fuel isotope composition, initial enrichment 3%.

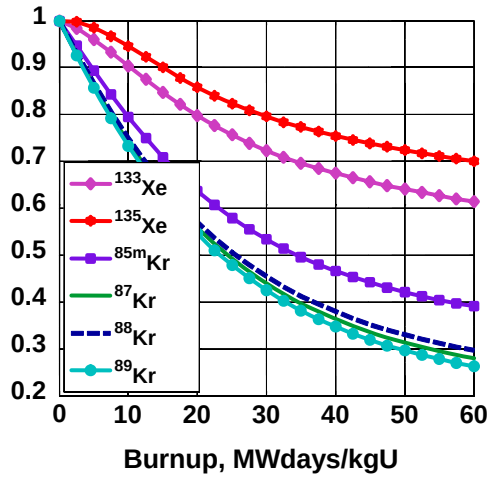

Fig.2. Relative changes in effective cumulative fission yields with burnup.

can be calculated for a given reactor type. For burnup estimation the measured values of the caesium ratio should be compared to the theoretical values. Due to long lifetimes ^{134}Cs and ^{137}Cs are accumulated in primary coolant from previous cycles and this method of burnup evaluation does not work under conditions of steady state operation.

For burnup estimation in nominal operation regime gaseous FPs can be used. Fission yields depend on fuel isotope composition which changes with burnup (Figs.1,2). Krypton (^{83m,85m}Kr, $^{87-90}$Kr) demonstrates more significant decrease of cumulative yields with burnup than xenon (^{133,135}Xe). So, the measured ratios of krypton to xenon activities indicate the burnup of failed fuel. The background activity should be taken into account in these assessments. The better results can be achieved with long-lived Kr-Xe pairs since they are less sensitive to level of tramp uranium.

There are some limitations on burnup estimation by noble gas activity and caesium spiking. The both methods can be applied directly only in the case of a few number of defective rods with nearly the same burnup. For several failures with different burnup additional analysis is necessary. Moreover, the gaseous radionuclides have much shorter lifetimes than ^{134}Cs and ^{137}Cs and their release into coolant varies with leak size, axial position and fuel heat generation rate. Therefore there is no universal relation between the ratio of krypton to xenon activities and fuel burnup and additional calculations are necessary even for a single failure.

3. The neural network approach to failed fuel diagnosis

For finding failure characteristics in more detail the neural network approach on the basis of the RTOP-CA code is developed [7,8]. Serial calculations with the RTOP-CA code for a single defective fuel rod at steady state power have been performed to configure and train a proper neural network. Leak size and axial position, fuel burnup, heat generation rate and the moment of failure occurrence were varied as input parameters. Since different failed fuel rods make additive contribution to primary activity, any defective core can be modelled by linear combination of the RTOP-CA calculations with different input. Contribution of tramp uranium to primary coolant activity is taken into account separately.

The neural-network program was verified in numerical tests. Some tests have been reported in papers [7,8]. To check the forecasting potential of the neural network approach additional tests have been performed. Primary coolant activity was modelled by a set of the RTOP-CA calculations which were not included into the network training database. The number of failed fuel rods in the core was limited to 10. Failures were subdivided into several groups: fuel with low (1-2 years of operation) or moderate (3-4 years) burnup, small or large leak, high or low power loading (relative to the nominal power). The boundary between small and large leaks was chosen to be 35 μm in equivalent hydraulic diameter – the value used by EdF [9]. The program objective was to evaluate the number of defective rods in each group.

The network predictions are illustrated in Fig.3 for one of the groups. In Fig.3*a* analysis was performed with iodine activity only, noble gases were added in Fig.3*b*. Actual number of failed fuel

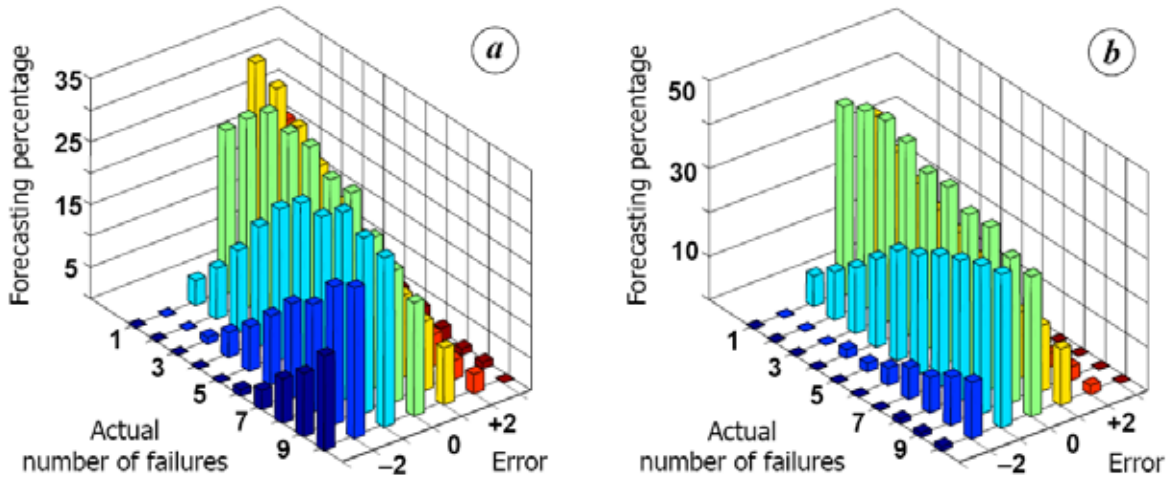

Fig.3. Neural network predictions: *a* – using iodine activity; *b* – using iodine + noble gas activity.

rods in the group (used in the RTOP-CA calculations) is shown on the left horizontal axes. The vertical axes show probability of different network predictions. For instance (Fig.3*b*), five defective rods in the group are properly identified with probability close to 40%, the program underestimates the actual number for one rod in ~ 30% cases and for two rods in ~ 5% cases; overestimations for one and two rods take place in ~ 20% and 5% cases, correspondingly. It can be seen, that noble gases give additional information to iodine activity and lead to better results. It is due to different chemical behaviour of noble gases and iodine inside failed fuel rods. Accuracy of predictions decrease with growing number of failures.

4. Application to NPP conditions

Data from several Russian WWER units have been used for testing the neural network approach. Table 1 shows the predicted number of failed fuel rods and leak size (small or large). The actual number of failed fuel bundles found in leakage tests is shown in the last column. In several cases the neural network seems to overestimate the number of failures. It is not a contradiction to experimental data since some fuel bundles may comprise several failed rods [10].

A separate neural network was developed for estimations of failed fuel burnup by noble gas activity. Results of analysis are demonstrated in Table 2. "Burnup" values are given in years of operation except of two burnup estimations by caesium spiking. The latter is given in MWdays/kgU and for both cases corresponds to three years of operation in WWER-1000. For other cycles no detailed data on caesium spiking were provided by NPPs. The operation period and number of failed fuel bundles found in leakage tests are shown in the last column of Table 2.

It can be seen that burnup estimations by noble gas activity are adequate if fuel failures are of nearly the same burnup (data scattering may lead to some uncertainty in predictions). If failures with different burnup are simultaneously present in the core then analysis by noble gases tends to give the lower boundary of the burnup range. On the contrary, analysis by caesium spiking tends to give the

NPP	Unit	Cycle	Mass of tramp uranium, g	Predicted number of failures		Found failures*
				small leak	large leak	
NPP A WWER-1000	*a*	9	11	5	14	9
	a	12	9	2	3	2
	b	7	1.5	0	1	1
	b	8	1	0	1	1
	b	9	1	0	1	1
	c	6	21	4	14	9
	c	7	17	2	3	3
	c	8	15	0	0	0
NPP B WWER-440	*a*	24	10	2	1	3

* *Number of failed fuel bundles found in leakage tests during reactor outage.*

Table 1. Examples of failure diagnosis at WWER units.

WWER-1000	Cycle	Mass of tramp uranium, g	Caesium spiking: *Bu*, MWdays/kgU	Gas activity*:	Leakage tests
NPP A Unit *a*	7	7	–	2-3	2(1)**, 3(3)
	9	11	35-38	2	2(4), 3(5)
	10	11	–	2-3	3(2)
	12	9	40-42	1-2	1(1), 3(1)
NPP B Unit *b*	18	4	–	3-4	4(1)
	19	3.5	–	4	4(1)

* *Burnup in years of operation.*
** *Burnup and number (indicated in brackets) of failed fuel bundles found in leakage tests.*

Table 2. Estimation of failed fuel burnup by noble gas activity.

upper boundary. This behaviour can be related to the following reasons.

Release of noble gases is higher for fresh fuel due to higher heat generation rates. Two identical leaks will show quite different release rates under steady state conditions if failure occurs at 1st or at 4th year of operation. Caesium is gradually accumulated in fuel and its content in fresh rods is low. When two rods with similar leaks but different operation period contribute to caesium spiking, the one with higher burnup will dominate. These differences can be used as additional tool for failure diagnosis. If lower burnup is predicted by noble gas activity than by caesium spiking it may be a signal of several failures with different burnup.

5. Conclusions

The expert system for WWER failure diagnosis is being developed on the basis of the RTOP-CA code. The RTOP-CA code is capable of prediction the primary coolant activity, behaviour and degradation of failed fuel rods under WWER operation conditions. The code is verified on a wide experimental database, at present time it is prepared for certification in regulatory authorities.

The WWER core state can be evaluated with the expert system providing the on-line data on mass of tramp uranium, fuel washout, the number, burnup and leak size (small or large) of failed fuel rods. Predictions of the expert system agree with results of leakage tests after reactor shutdown. The diagnosis is adequate for a few failures in the core but decrease in accuracy with increasing number of failures.

Even in its current version the expert system can help in making decisions on the scope of leakage tests during reactor outage and enhancing the reliability of testing (reduce risks of missing a failed fuel bundle). Development of the expert system will be continued including further verification on NPP data and optimization of the neural network module.

The work has been financed by JSC TVEL and partially supported by grant MK-9722.2006.8.

References

1. Slavyagin P., Lusanova L., Miglo V., “Regulation of the Fission Product Activity in the Primary Coolant and Assessment of Defective Fuel Rod Characteristics in Steady-State WWER-type Reactor Operation,” Proc. IAEA Int. Tech. Meeting on Fuel Failure in Water Reactors: Causes and Mitigation, 17-21 June 2002, Bratislava, Slovakia, pp.326-337.
2. Parrat D., Genin J.B., Musante Y. *et. al.*, «Failed Rod Diagnosis and Primary Circuit Contamination Level Determination Thanks to the DIADEME code», Ibid., pp.265-276.
3. Hózer Z., “Simulation of Leaking Fuel Rods,” Proc. 6th Int. Conf. WWER Fuel Performance “Modelling and Experimental Support", Albena, Bulgaria, Sept.19-23, 2005, paper 3B.9.
4. Barta O., et al. “The application of the PES-PEPA Expert System at the Dukovany Power NPP,” Proc. Tech. Meet. Fuel Failure in Normal Operation of Water Reactors: Experience, Mechanisms and Management, 26-29 May 1992, Dimitrovgrad, Russia, pp.100-105.
5. Ingemansson T., Rudling P., Lundgren K., “Assessment of Fuel Washout in LWRs – New Methodologies,” Proc. Int. Meet. LWR Fuel Performance, Orlando, Florida, September 19-22, 2004, pp.833-844.
6. V. Likhanskii, I. Evdokimov, *et. al.* “Modelling of Fission Product Release from Defective Fuel Rods under WWER Operation Conditions and in Leakage Tests during Refuelling,” Ibid., pp.798-812.
7. V. Likhanskii, I. Evdokimov, *et. al.* “Integrated Approach to Detection of Defective WWER Fuel Assemblies” Proc. Water Reactor Fuel Performance Meet., Kyoto, Japan, Oct. 2-6, 2005, p.382.
8. V. Likhanskii, I. Evdokimov, *et. al.* “Failed Fuel Diagnosis during WWER Reactor Operation using the RTOP-CA Code,” Proc. 6th Int. Conf. WWER Fuel Performance “Modelling and Experimental Support", Albena, Bulgaria, Sept.19-23, 2005, paper 1.13.
9. Dumont A., “FRAGEMA Fuel Reliability: from Detection of Fuel Failures to the Feedback on Design and Fabrication,” Proc. Tech. Meet. Fuel Failure in Normal Operation of Water Reactors: Experience, Mechanisms and Management, 26-29 May 1992, Dimitrovgrad, Russia, pp.46-50.
10. Chapot J., Suano R., Couto N., et al., “Fuel Failures at ANGRA-1: Causes and Mitigation,” Proc. IAEA Int. Tech. Meeting on Fuel Failure in Water Reactors: Causes and Mitigation, 17-21 June 2002, Bratislava, Slovakia, pp.92-116.

MECHANICAL PROPERTY EVALUATION OF HIGH BURN-UP NUCLEAR FUEL CLADDING USING THE RING TENSILE TEST

SUNKI KIM, JEGEON BANG, CHANBOCK LEE, DAEHO KIM, YONGSIK YANG, SANGBOCK AHN, DOSIK KIM, WANHO OH, HANGSUK SEO

P.O. Box 150, Yuseong, Daejeon, Korea, 305-600
Korea Atomic Energy Research Institute
Phone) +82-42-868-8661, E-mail) kimsk@kaeri.re.kr

ABSTRACT

Related to the degradation of the mechanical properties of Zr-based nuclear fuel cladding tubes under severe accident conditions such as RIA(Reactivity Initiated Accident) and LOCA(Loss of Coolant Accident), mechanical tests which can simulate the degradation of the mechanical properties properly are needed. Therefore, in this paper, modified ring tensile tests were performed in order to evaluate the mechanical properties of high burn-up fuel cladding under a hoop loading condition in a hot cell. On the basis of the ring tensile tests for a high burn-up Zircalay-4 cladding and un-irradiated Zircalay-4 cladding, the following conclusions were drawn. Firstly, the mechanical properties are abruptly degraded beyond 600°C, which corresponds to a design basis accident condition such as a RIA. Secondly, the un-irradiated fuel cladding showed ductile fracture behaviors such as 45° shear type fracture, while the high burn-up Zircalay-4 cladding showed a brittle fracture behavior even at the high temperatures (e.g. over 600°C) which are achievable during a RIA. Thirdly, in the case of the high burn-up Zircalay-4 cladding, the strength and ductility are strongly dependent on the material property itself which are degraded by oxidation and hydriding during an operation rather than the temperature.

1. Introduction

During a steady-state operation of light water reactors, the mechanical behavior of the zirconium-based fuel cladding degrades due to a combination of oxidation, hydriding, and radiation damage. In an effort to increase the operating efficiency through the use of longer fuel cycles, and to reduce the volume of waste associated with the core reloads, utilities have a strong incentive to increase the average discharge burn-up of the fuel assemblies. Further increases in the operating efficiency of power reactors can also be achieved by increasing the coolant outlet temperature. However, both of these changes in a reactor operation enhance the cladding degradation, which may increase the likelihood of a cladding failure during design-basis accidents. One such postulated design-basis accident scenario is the reactivity-initiated accident(RIA) in a pressurized water reactor (PWR) caused by the ejection of a control rod from the core, which would cause a rapid increase of the reactivity and the thermal energy in the fuel [1]. The increase in fuel temperature resulting from an RIA induces a rapid fuel expansion, causing a severe pellet-cladding mechanical interaction (PCMI). This PCMI forces the cladding to experience a multiaxial tension such that the maximum principal strain is in the hoop (i.e., transverse) direction of the cladding tube. The survivability of a

fuel cladding irradiated to a high burn-up under postulated RIA conditions is thus a response to a combination of the mechanics of a loading and the material degradation during a reactor operation. While such data is available for the axial deformation behavior of cladding tubes, relatively little has been reported in the open literature on the uniaxial tension behavior in the hoop direction of Zircaloy-4 cladding. Accordingly, it is essential to investigate the uniaxial tension behavior in the hoop direction of high burn-up Zircaloy-4 cladding. In this study, ring tensile tests are applied to obtain the data regarding the uniaxial hoop direction deformation behavior.

2. Experimental Procedure

The ring tensile specimen used in this study is a Westinghouse 17x17 type (Vantage-5H) Zircaloy-4 cladding irradiated for 3 cycles in the Ulchin Unit 2 pressurized water reactor, whose average burn-up was estimated to be approximately 65GWd/tU. The irradiated fuel rod was transferred to PIEF at KAERI, cut into approximately 13 cm length segments with a diamond low speed saw, and then the UO_2 pellet inside the fuel rod segment was removed by a mechanical grinding with a drill-attached defueling machine in a hot cell in IMEF. The specimens for the mechanical properties evaluation were fabricated with a diamond wheel grinder from the defueled cladding segments. The dimensions and shape of the ring tensile specimen were designed in order to ensure that any deformation is limited to the gage section of the specimen, so that the uniform uniaxial hoop strain in the gage section could be at its maximal. The dimensions of the ring tensile specimen are shown in Figure 1.

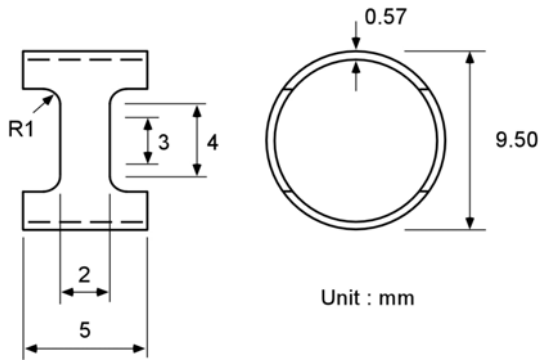

Figure 1. Dimensions of the ring tensile specimen

The gage sections of the specimens were oriented at the top and bottom of the half cylinder of the grip, such that a constant specimen curvature can be maintained during a deformation. The interface was lubricated with a graphite-containing vacuum grease lubricant at the beginning of each test to minimize a loss of the applied load. The ring tensile tests were performed in a hot cell with the Instron Servohydraulic System, Model 8562. The tests were performed at 25, 135, 200, 300, 350, 400, 600, and 800°C, and the initial strain rate was maintained at 0.01/s.

3. Results and Discussion

To obtain the mechanical strength, the 0.2% offset YS(Yield Strength) and UTS(Ultimate Tensile Strength) were evaluated, and the UE(Uniform Elongation) and TE(Total Elongation) were also evaluated as a measure of ductility. Figure 2 shows a comparison result of mechanical strength and ductility of irradiated Zircaloy-4 with the PROMETRA database. Open symbols and closed symbols represent the PROMETRA results and the results in this study, respectively. The values of

yield strength and ultimate tensile strength were almost similar regardless of temperature, which is reasonable results, considering that all of the Zircaloy-4 claddings in this study and in the PROMETRA test program were irradiated for 3 cycles. The evaluation results of the 0.2% offset YS and the UTS are shown in Figure 3. From the figure, it is confirmed that the 0.2% offset YS and the UTS abruptly decrease with an increasing temperature. The UTS was evaluated to be 942.70 MPa at RT, 678.83 MPa at 400°C, but, it is abruptly diminished to 282.64 MPa at 600°C, which is achievable in the RIA condition. Especially, it decreases to 58.30 MPa at 800°C, an extreme condition, which corresponds to 6% of the UTS at RT. This means that the mechanical strength of the high burn-up Zircaloy-4 cladding sharply decreases in the RIA-relevant temperature ranges. The evaluation results of the UE and TE are shown in Figure 4. The results show that both the UE and TE increase with an increasing temperature. Especially, they abruptly increase at 600°C, but become lower beyond this temperature. This peculiar behavior was also observed in the PROMETRA program[2] which is a mechanical property relevant test program in conjunction with the CABRI program simulating a RIA. It is believed that this behavior is caused by the elongation minimum phenomenon by the dynamic strain aging of the Zircaly-4 cladding material beyond 600°C.

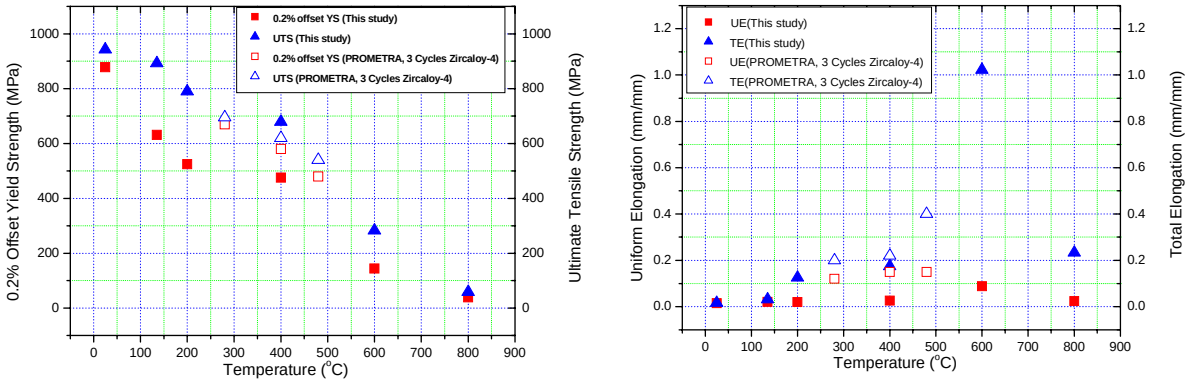

Figure 2. Comparison of mechanical strength and ductility with the PROMETRA database

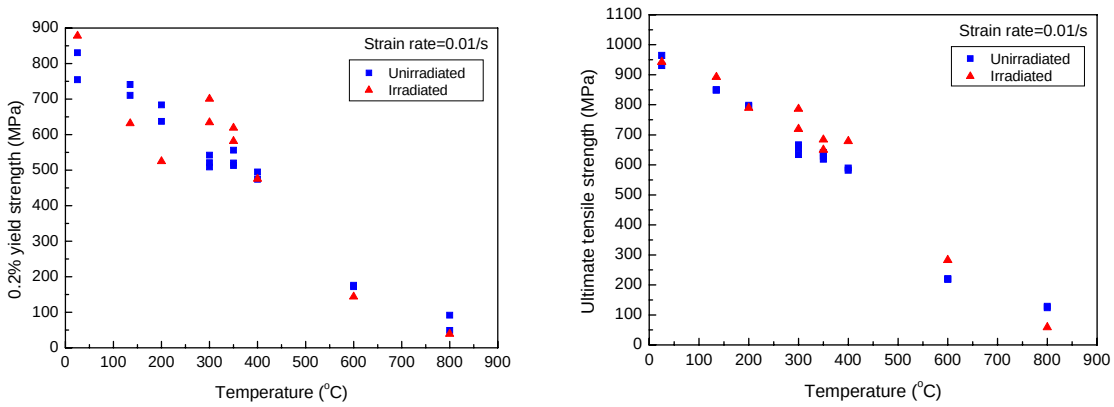

Figure 3. Yield strength and ultimate tensile strength of the un-irradiated and high burn-up fuel cladding

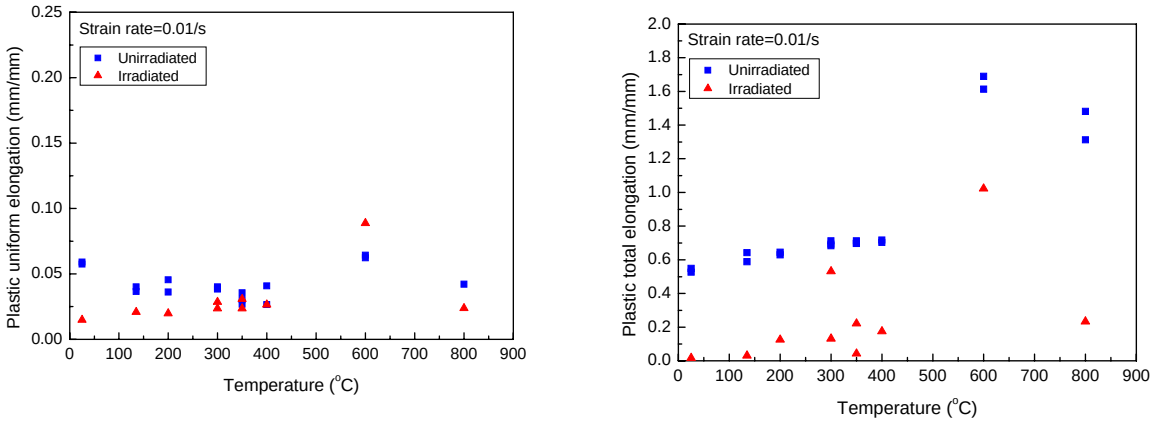

Figure 4. Total elongation of the un-irradiated and high burn-up fuel cladding

The stereoscope photographs of the specimens after the ring tensile test are shown in Figure 5. Figure 5 represents the fracture patterns of the non-irradiated and high burn-up Zircaloy-4 cladding specimens. As shown in the figure, the fracture patterns such as 45° shear type fracture were observed in the non-irradiated cladding at room temperature. On the contrary, the fracture pattern of the high burn-up Zircaloy-4 cladding showed completely different fracture patterns from the non-irradiated Zircaloy-4 cladding. The fracture type was observed to be vertical in the tensile direction without a necking at all of the test temperatures, which is convincing evidence of the brittle fracture behavior of high burn-up fuel cladding regardless of temperature. This means that even at a high temperature, 600°C or 800°C, the fracture pattern showed a brittle fracture behavior. Accordingly, it was found that the high burn-up Zircaloy-4 cladding becomes very brittle even at the high temperatures achievable during a design-basis accident.

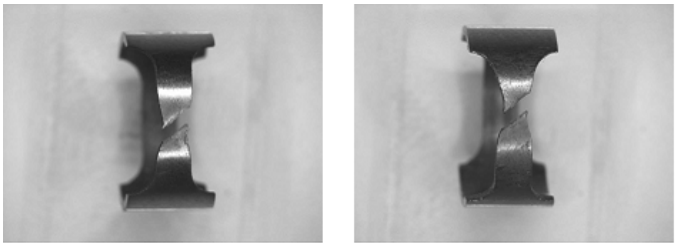

Un-irradiated Zircaloy-4 cladding

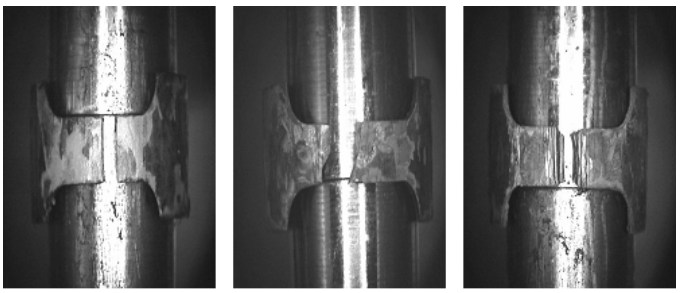

Irradiated Zircaloy-4 cladding(25, 400, 600°C)

Figure 5. Fracture Patterns after ring tensile tests

4. Conclusions

On the basis of the ring tensile tests for a high burn-up Zircalay-4 cladding from Ulchin Unit 2 and a as-received non-irradiated Zircalay-4 cladding, the following conclusions were drawn. Firstly, the mechanical properties are abruptly degraded beyond 600°C, which corresponds to a design basis accident condition such as a RIA. Secondly, the un-irradiated fuel cladding showed ductile fracture behaviors such as 45° shear type fracture, while the high burn-up Zircalay-4 cladding showed a brittle fracture behavior even at the high temperatures (e.g. over 600°C) which are achievable during a RIA. Thirdly, in the case of the high burn-up Zircalay-4 cladding, the strength and ductility are strongly dependent on the material property itself which are degraded by oxidation and hydriding during an operation rather than the temperature.

Acknowledgements

This work has been carried out under the Nuclear R&D Program supported by Ministry of Science and Technology in Korea

5. References

[1] Meyer, R. O. *et. al*., "A Regulatory Assessment of Test Data for Reactivity Initiated Accidents" *Nuclear Safety*, Vol. 37, No. 4, pp. 271-288, 1996.

[2] Averty, X. *et. al*., "Tensile tests on ring specimens machined in M5 cladding irradiated 6 cycles" IRSN 2003/50, 2003.

[3] Daum, R. S. *et. al*., "On the Embrittlement of Zircaloy-4 Under RIA-Relevant Conditions" *Zirconium in the Nuclear Industry : Thirteenth International Symposium, ASTM STP 1423*, PA, pp. 702-719, 2002.

SUBSTANTIATION OF WWER FUEL SAFETY IN DESIGN BASIS ACCIDENTS. EXPERIMENTAL SUPPORT

V.V. NOVIKOV, A.V. MEDVEDEV, A.V. SALATOV, O.A. NECHAEVA, P.V. FEDOTOV
FSUE A.A. Bochvar VNIINM, P.O. Box 369,123060 Moscow-Russia

V.L. MOLCHANOV, YU.V. PIMENOV
JSC "TVEL", Bolshaya Ordynka st. 24/26, 119017 Moscow-Russia,

V.P.SMIRNOV, A.V. GORYACHEV, V.A. OVCHINNIKOV, V.N. SHULIMOV
FSUE SRC RIAR, 433510 Dimitrovgrad 10-Russia,

V.I. NALIVAEV, V.S. KONSTANTINOV, D.N. IGNATYEV
FSUE SRI SIA "LUCH", Zheleznodorozhnaya st. 24, 142100 Podolsk-Russia,

ABSTRACT

The directions of modern experimental researches of WWER fuel rods behavior under design bases accident (DBA) conditions are determined by the following reasons: increase of design fuel burn-up; use of advanced materials (E110 sponge based alloy); the tendencies of safety criterions development. The experiments under LOCA conditions: corrosion behaviour of samples made from high burn-up fuel rod and made from E110 (sponge Zr) alloy claddings; thermomechanical and corrosion behaviour of single fuel rod simulators and assemblies in integral tests at the PARAMETER facility; integral steam-water loop test at the MIR reactor with assembly (19 fuel rods) containing 3 refabricated fuel rods. The experiment under RIA conditions: preliminary results of integral water loop tests with assembly (3 fuel rods) containing 2 refabricated fuel rods at the MIR reactor.

1. Purpose of experimental researches of WWER fuel behaviour under DBA conditions

The primary goals of experimental researches follow from general requirements to the safety substantiation of a fuel system in DBA /1-4/ (substantiation of an active zone cooling and radiological consequences after accident). They consist in following:

· the substantiation of limiting value for the equivalent degree of fuel rod claddings oxidation (ECR), this limit should not lead to excessive cladding embrittlement;

· the substantiation of limiting value for the enthalpy of fuel, this limit should guarantee the absence of a fuel rod fragmentation in design RIA;

· research of temperature-power conditions leading to fuel rod failure (a breach of cladding integrity of the gas leakage type or direct fuel-coolant contact) in design LOCA and RIA.

2. The experimental researches of fuel rods behaviour under LOCA conditions

The large complex of experimental researches of unirradiated claddings and standard WWER fuel rod claddings (burn-up 50 MW*d/кgU), was made early with the purpose of the substantiation of cladding embrittlement criteria for LOCA conditions /5, 6/.

The following activities already are executed or are still carried out:

1 Oxidation kinetics in temperature range of 800 - 1200 ^{o}C and mechanical characteristics of oxidized claddings, made from E110 (sponge Zr) alloy /7 /;

2 The universal model of flow stress for description of Zr-Nb alloy cladding deformation behavior under DBA conditions /8, 9/ ;

3 Integral LOCA experiments at the "PARAMETER" facility with single simulator of fuel rod and with WWER type simulators assembly: corrosion and deformation behavior and simulators failure under operating of internal pressure, cladding made from E110 alloys and E110 (sponge Zr) alloy /7, 9, 10, 11/;

4 Hot cell investigations of high temperature oxidation and heat resistance of samples made from standard WWER fuel rods , burn-up 65 MW*d/кgU;
5 Hot cell investigations of high temperature oxidation and heat resistance of samples made from E110 (sponge Zr) alloy claddings of WWER type fuel rods irradiated up to burn-up 50 MW*d/кgU at MIR research reactor(preparatory measures);
6 Integral LOCA test with WWER-1000 type assembly (19 fuel rods) containing 3 refabricated fuel rods (49 MW*d/kgU) at the MIR research reactor steam-water loop;
7 Halden reactor LOCA experiment with fuel rod refabricated from WWER-440 fuel rod, irradiated up to burn-up50 MW*d/кgU at Loviisa NPP (preparatory measures) /12/;
8 Integral LOCA test with WWER-1000 type assembly containing refabricated fuel rods (60 MW*d/kgU) at the MIR research reactor steam-water loop (preparatory measures).
The figure 1 shows results of high temperature oxidation and post compression tests (at 20 ^{0}C) of E110 (sponge Zr) alloy cladding samples. The samples keep plasticity above 1 % at 18 % ECR.
The experiments modelling conditions of the WWER LOCA first stage has been lead at the PARAMATER facility with single simulators of fuel rod. Depending on combination of temperature-pressure conditions instituted by fuel rod power and burn-up at the initial accident moment, both compression and ballooning (up to the failure) of cladding are possible (figure 2). The next direction - fuel rod assembly behaviour under conditions of LOCA second stage: influence of a temperature and pressure mode, influence of cross section temperature non-uniformity, influence of the first stage temperature mode on deformation and corrosion behaviour of claddings in the second stage. Effect of a temperature schedule of the first LOCA stage (heating up to 900 ^{o}C with rate about 100 ^{o}C /s, high temperature exposure during 5 s, cooling with rate 100 ^{o}C /s) hardens a cladding material. It results to (other conditions being equal) rise of cladding failure temperature and to appreciable decrease of cladding deformation at failure in the LOCA second stage (figure 3). Two experiments with WWER-1000 type assemblies (19 fuel rod simulators) were conducted under identical conditions (figure 4). One of the assembly had E110 alloy claddings, other – E110 (sponge Zr) alloy claddings. Both assemblies showed the equal deformation behaviour. Post-test researches are carried out now.
High temperature oxidation of samples refabricated from Balakovo NPP fuel rod (E110 alloy cladding, burn-up - 65,6 MW*d/kgU) was realized in hot cell. The characteristics of the reference specimen: the average oxide film thickness at external cladding surface - 7 μm; at internal surface -11 μm, estimation of ECR-1,5 %, hydrogen content - ≤ 120 ppm, the gap is absence, the fuel pellet fragmentation as a several radial cracks, rim-layer at the fuel periphery. It is important to note, that destruction oxidation was not observed (figure 5).
The integral test (BT-2) with WWER-1000 type assembly (19 fuel rods) containing 3 refabricated fuel rods (49 MW*d/kgU) at the MIR steam-water loop has modelled conditions of LOCA second stage: pressure drop in an active zone, drainage of its top part, fuel rods cooling by stream flow and reflow water cooling (figure 6,7). The «fresh» and refabricated fuel rod claddings strain is identical. The maximal hoop strain has made 25 -28%. The estimation of blockage – 26%, assembly has kept cooling geometry (figure 8). Post-test investigation of four fuel rods (5, 13, 14, 19) has shown the similarly corrosion conditions, the oxide layer on the external surface of claddings had many breaks caused by deformation until cladding failure. The maximal external oxide layer – 14 μm (14, 19), the maximal internal oxide layer (located in rupture area) - 20 μm (19), 50 μm (14).

3. The experimental researches of fuel rods behaviour under RIA conditions

The pulse tests of unirradiated and refabricated WWER type fuel rods with burnup 50 and 60 MW d / kg U at the IGR and BIGR facilities allowed to determinate the fuel enthalpy values guaranteed the absence of fuel rod distraction under RIA conditions /9,13/. The estimations of maximal radial averaged fuel enthalpy conforming to a fuel rod failure threshold under power pulse conditions (single fuel rod was placed into an ampoule containing water at atmospheric pressure and room temperature) are obtained also. The implementation of the experimental RIA program in the MIR water loop started some times ago. The purpose of the program is the analysis of fuel rod failure mode. The first test of experimental assembly (one unirradiated and two refabricated fuel rods burnup 48,3 MW d /kgU, E110 alloy claddings) was conducted in 2005. The measured parameters are neutron flux, fuel centerline temperature, unirradiated fuel rod cladding temperature, FGR, coolant temperature, flow rate and pressure. The initial conditions (exposure more than 40 hours): coolant pressure-16 MPa, rate-6,5 t/h, temperature (inlet)-275^{o}C; claddings temperature - 280-300^{o}C. Post-test investigations of

experimental fuel rods are carried out now (figure 9, 10). The main outcome - all fuel rods have kept tightness. Also the opening-up of following integral RIA experiments with assembly containing refabricated fuel rods (60 and 70 MW d / kg U) is prolonged.

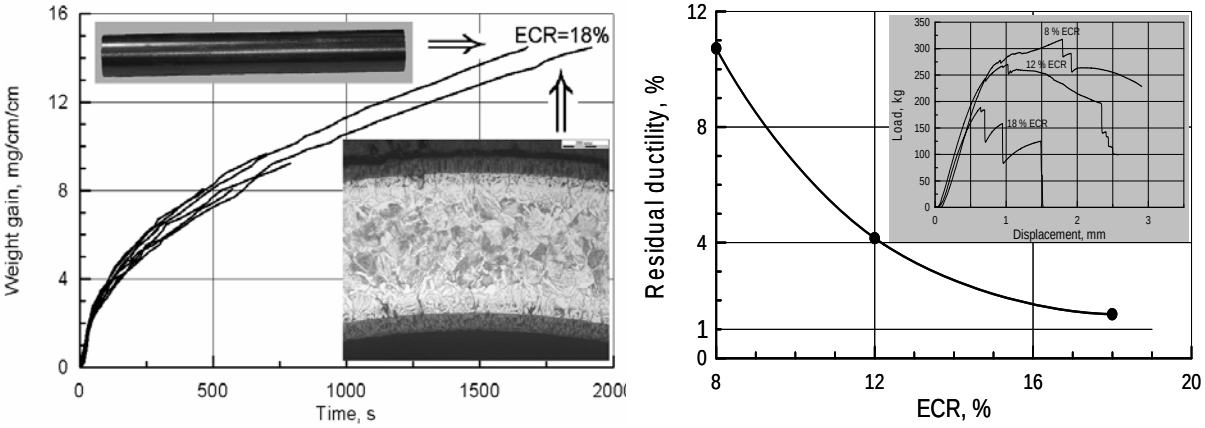

Fig 1. High temperature (1100 ºC) oxidation of E110 (sponge Zr) alloy samples

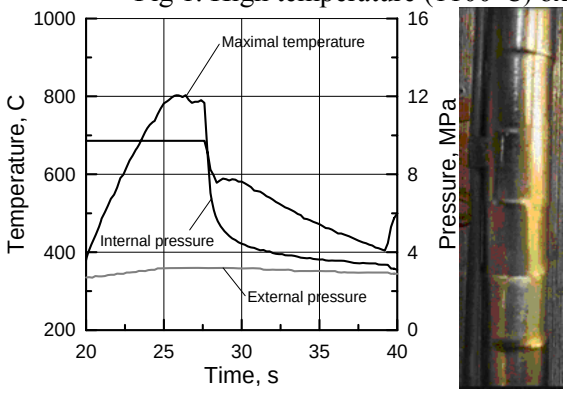

Cladding reduction on fuel

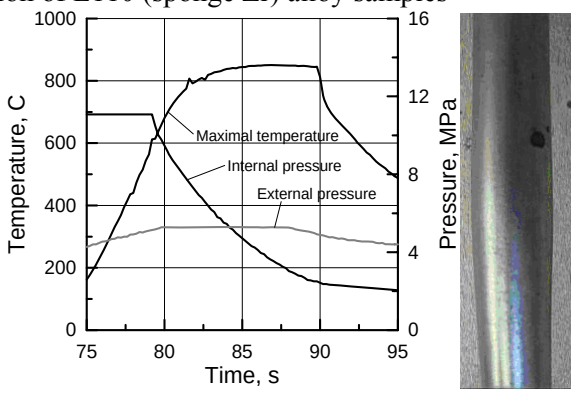

Maximal hoop strain is nearly 10 %

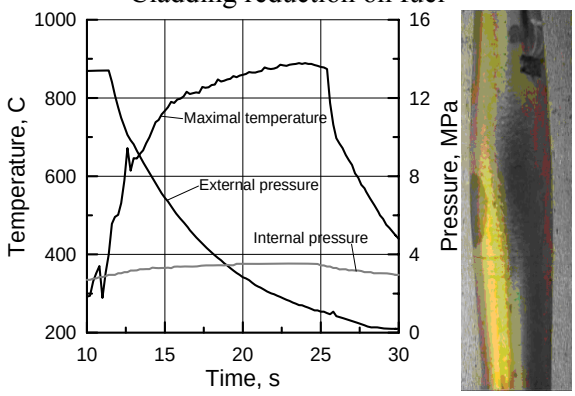

Maximal hoop strain is nearly 30 - 35 %

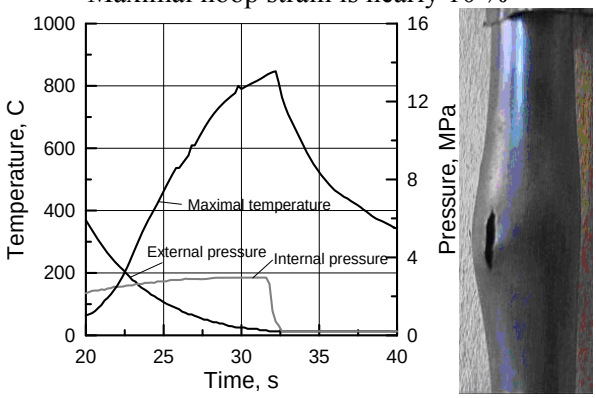

Maximal hoop strain is nearly 46 %

Fig 2. The WWER LOCA first stage experiments (single fuel rod simulators)

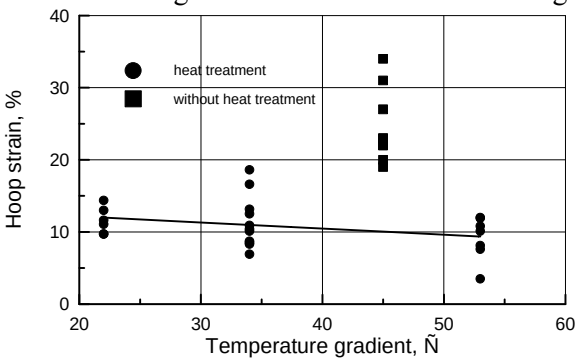

Fig 3. Hoop strain at failure section versus azimuthal temperature non-uniformity

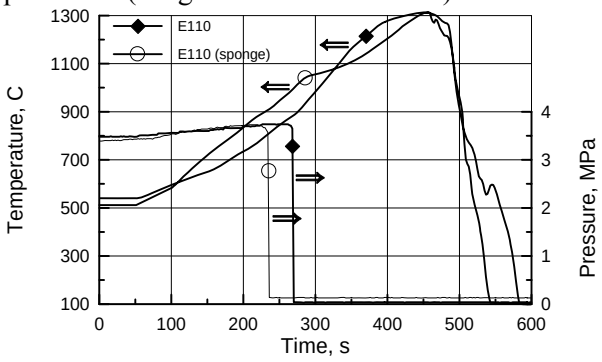

Fig 4. Experiments with WWER-1000 type assemblies, PARAMETER facility

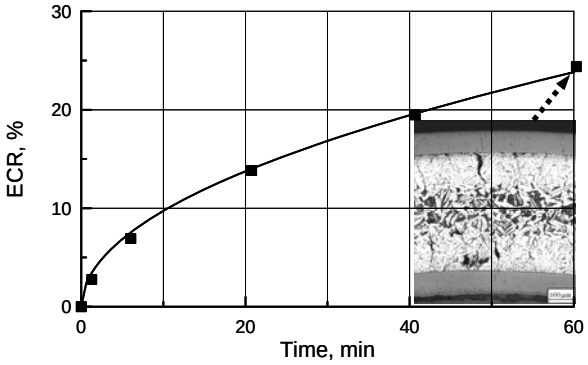

Fig 5. ECR of samples (burn-up - 65,6 MW*d/kgU) versus oxidation time

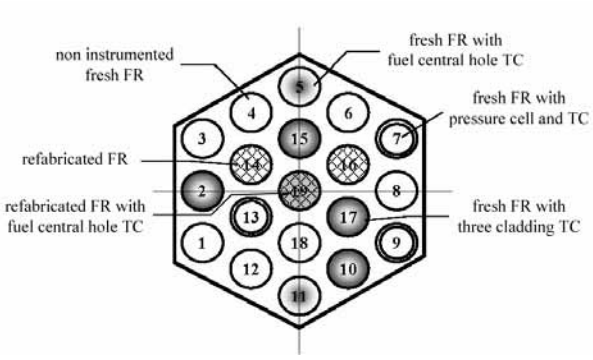

Fig 6. Configuration of BT-2 assembly

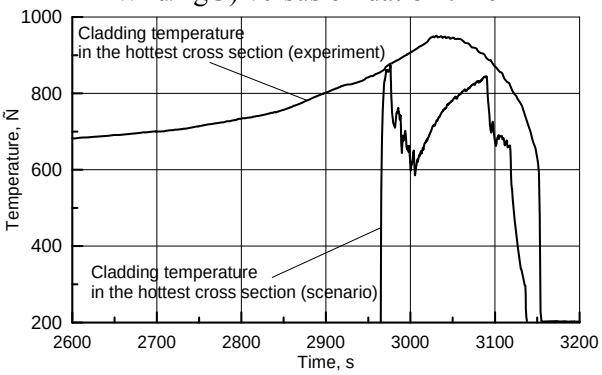

Fig 7. Cladding surface temperature, hottest cross section, BT-2

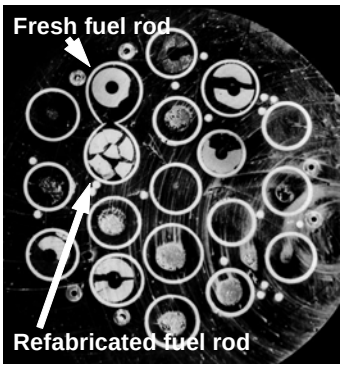

Fig 8. BT-2 assembly cross section

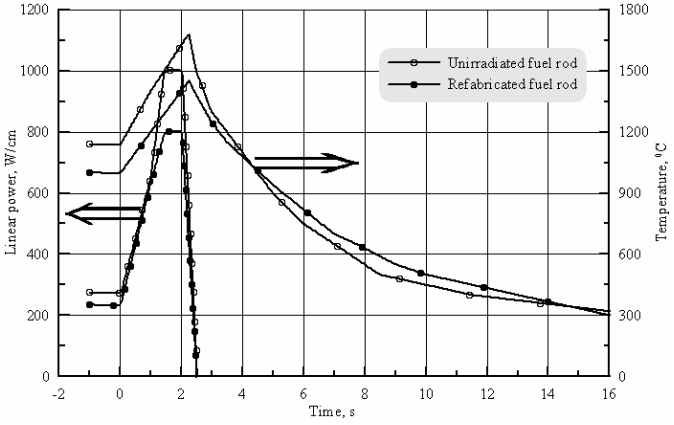

Fig 9. Parameters of RIA-MIR-1 experiment

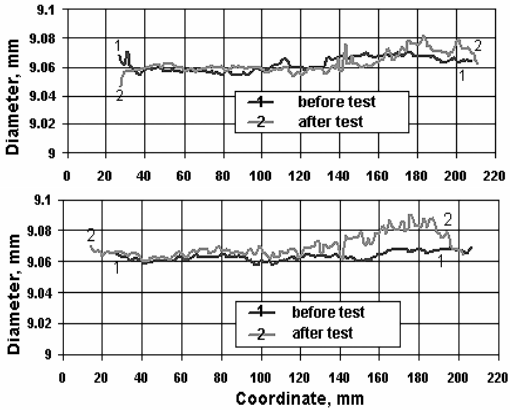

Fig 10. Profilometry results of refabricated fuel rod claddings

4. Conclusions

With the purpose of experimental support for licensing of perspective WWER in a part of the substantiation of fuel rods safety behavior under LOCA and RIA conditions the programs of experimental researches are realized:

1. Corrosion behavior and mechanical characteristics of oxidized claddings, made from E110 (sponge Zr) alloy;
2. Corrosion behavior and heat resistance of samples made from high burn-up WWER fuel rods and samples made from E110 (sponge Zr) alloy claddings of WWER type fuel rods irradiated at MIR research reactor;
3. Corrosion and deformation behavior and fuel rod claddings failure during integral LOCA experiments at the "PARAMETER" facility with single simulator of fuel rod and with WWER type simulators assembly;

4. Thermomechanical behavior of high burn-up WWER fuel rods during integral RIA experiments at the MIR research reactor steam-water loop.
The preparatory measures of LOCA experiments with high burn-up WWER fuel rods at Halden reactor and at the MIR research reactor are carried out.

5. References

1 Общие положения обеспечения безопасности атомных станций ОПБ-88/97. НП-001-97 (ПНАЭ Г-01-011-97)

2 Правила ядерной безопасности реакторных установок атомных станций. ПБЯ РУ АС-89. ПНАЭ-Г-1-024-90

3 "Standard Review Plan", Section 4.2 (Fuel System Design), NUREG–0800, Rev.3

4 Fuel Safety Criteria Technical Review, CSNI/R (99)25, OECD, Paris (2001)

5 Yu.K. Bibilashvili, N.B. Sokolov, L.N. Andreeva-Andrievskaya, V.Yu. Tonkov, A.V. Salatov, A.M. Morosov, V.P. Smirnov. Thermomechanical properties of zirconium-based alloys oxidized claddings in LOCA simulating conditions. Technical Committee Meeting on Fuel behaviour under transient and LOCA conditions, Halden, Norway, 10 - 14 September, 2001.

6 N.B. Sokolov, L.N. Andreeva-Andrievskaya, V.Yu. Tonkov, A.V. Salatov, A.M. Morosov, V.P. Smirnov, Thermo-mechanical properties of irradiated Zr1%Nb alloy claddings in LOCA simulating conditions. Proceedings of Fuel Safety Research Specialists' Meeting, Tokai, Japan, March 4-5, 2002, JAERI-Conf 2002-009.

7 P.V. Fedotov, O.A. Nechaeva, V.V. Novikov, A.V. Salatov, A.V Alekseev, A.V.Goryachev, I.V Kiseleva, I.V.Kuzmin, V.N. Shulimov, V.S. Konstantinov , V.I. Nalivaev, V.M Gukov, V.E.Donnikov,V.I. Latunin, Studies of VVER fuel rods behaviour under LOCA condition, current status, OECD LOCA Meeting, Paris, France, 27-28 June, 2006.P. Fedotov, O. Nechaeva, A. Salatov, L. Loshmanov, Universal model of zirconium alloys plastic deformation under WWER design basis accident (DBA) conditions, 6th International Conference on WWER Fuel Performance, Modelling and Experimental Support, Bulgaria, 19-23 September, 2005.

9 A.V. Kumachev, A.V. Medvedev, O.A. Nechaeva, V.V. Novikov, A.V. Onufriev, A.V. Salatov, V.L. Molchanov, Yu.V. Pimenov, A.V Alekseev, I.V Kiseleva, V.N. Shulimov, I.I. Fedik, V.I. Nalivaev, N.Ya. Parshin, V.S. Konstantinov, Estimation of Water-Water Energy Reactor Fuel Rod Failure in Design Basis Accidents, 2005 Water Reactor Fuel Performance Meeting, Kyoto, Japan, 2-6 October, 2005. Yu.K.Bibilashvili, N.B.Sokolov, A.V.Salatov, V.Yu.Tonkov, P.V.Fedotov, L.N.Andreeva-Andrievskaya, V.P.Deniskin, V.I.Nalivaev, N.Ya.Parshin, P.G.Afanasyev, V.S.Konstantinov, V.P.Semishkin, A.M.Shumski. VVER-1000 Type Fuel Assembly Tests on Electroheated Facilities in LOCA Simulating Conditions, Technical Committee Meeting on Fuel behaviour under transient and LOCA conditions, Halden, Norway, 10-14 September, 2001.

11 A.V. Salatov, P.V. Fedotov, P.G. Afanasyev, V.P. Deniskin, V.S. Konstantinov, V.I. Nalivaev, N.Ja. Parshin, E.B. Popov, I.I. Fedik, V.P. Semishkin, A.M. Shumsky, Modelling of behavior of 37 fuel rod assembly with Zr1%Nb-alloy simulators cladding under loss-of-coolant accident conditionson PARAMETR-M facility Fifth International Conference on WWER Fuel Performance, Modelling and Experimental Support, Bulgaria, 29 September - 3 October, 2003.

12 V. V. Novikov, A. V. Medvedev, A. V. Salatov, O. A. Nechaeva, P. V. Fedotov, J. V. Pimenov. Proposals at the choice of the LOCA script for the Halden Reactor experiment with refabricated WWER type fuel rod. Enlarged Halden Programme Group Meeting. Lillehammer, Norway, 16-17 October, 2005.

13 L.Yegorova, K. Lioutov, N. Jouravkova, O. Nechaeva, A. Salatov, V. Smirnov, A. Goryachev, V. Ustinenko, I. Smirnov, Experimental Study of Narrow Pulse Effects on the Behaviour of High Burnup Fuel Rods with Zr-1%Nb Cladding and UO_2 Fuel (VVER Type) under Reactivity-Initiated Accident Conditions, NUREG/IA-0213, Vol.1,2 (2006)

AREVA NP NEW UO_2 FUEL DEVELOPMENT AND QUALIFICATION FOR LWRs APPLICATIONS

C. DELAFOY[1], P. DEWES[2]
AREVA, AREVA NP - FUEL SECTOR - DESIGN AND SALES
[1]10, rue Juliette Récamier, 69456 Lyon Cedex 06 – France
[2]P.O. Box 3220, 91050, Erlangen – Germany

ABSTRACT

The increasing needs in plant manoeuvrability together with high expectations in terms of fuel performance and reliability appeal to remove the current Pellet Clad Interaction (PCI)-related constraints and to restore high burn-up safety margins on Light Water Reactors.
AREVA NP has been conducting for a long time research programs to develop products having robust margins to match with customer requirements. The most promising way relies on the development of a high burn-up and PCI remedy UO_2 fuel.
In particular, the AREVA NP optimised chromia-doped UO_2 fuel microstructure with enlarged grain size has already exhibited very promising performance regarding PCI resistance and high burn-up issue. The emphasis is now to go further on that fuel qualification with the purpose to produce a full set of consistent and valuable licensing data to respond to nuclear utilities' requests.
This paper presents the basis of this qualification designed to thoroughly assess the in-service performance of the chromia-doped UO_2 fuel. The process which will fulfil the PWR and BWR licensing requirements is based on:

- mastering the Cr_2O_3-doped UO_2 fuel fabrication technology,
- irradiating fuels in different LWRs operating conditions,
- performing power ramp tests in a wide range of conditions and post-irradiation examinations up to very high burn-up,
- developing modelling able to predict fuel behaviour under various operating conditions.

Finally, this paper gives a state of progress of the chromia-doped UO_2 fuel performance validation under irradiation.

1. Introduction

The will of utilities to upgrade the economics of their nuclear plants leads to increasing needs in reactor manoeuvrability together with high expectations in terms of fuel performance and reliability. AREVA NP is conducting research programs to develop products having robust margins to match with customer requirements. Key features to UO_2 fuel performance improvements addresses to the reduction of:

- **Fission gas release (FGR)** which can be a limiting phenomenon in terms of discharge burnup increase and operational flexibility. Having higher fission gas retention into fuel matrix, leads to lower the end of life internal pressure of fuel rods. Such feature is desired to operate fuel assemblies up to a burnup level of 70 GWd/t with increased operational margins. Higher fission gas retention within the fuel should contribute to improve fuel behaviour under accident conditions for high burnup safety criteria relating to LOCA and RIA. Finally, lower internal pressures in fuel rods give improved conditions for the back end of the fuel cycle, notably to ensure the integrity of irradiated assemblies during handling and long-term interim storage.

- **Pellet-clad interaction (PCI) effect** which is a potential mechanism for cladding ruptures during reactor operations. PCI failures might be normally induced following substantial local power variations: from load follow, frequency control and extended reduced power operation for PWRs, and from control blade movements in BWRs. The PCI mechanism involves a synergistic combination of mechanical and chemical interactions between the UO_2 pellets and the cladding (1). PCI-induced fuel failures can be mitigated by implementation of operating constraints. However, within a strongly competitive environment, the need to reduce the overall PCI-constraints is crucial, for example in France (2). The most promising way for that concern relies

on the development of PCI resistant fuel designs. The introduction of liner-cladding in BWRs has greatly reduced the incidence of PCI failures. Another or additional way of mitigation involves the use of softer UO_2 fuel pellet for both PWR and BWR applications.

For that double target, the ability of large grain doped UO_2 microstructures has been investigated by AREVA NP since the early 90's. High expectations are placed on the optimised chromia-doped UO_2 fuel which exhibit significantly higher performance compared to the reference UO_2 fuel (3). The emphasis is now to go further on that fuel qualification with the purpose to produce a full set of consistent and valuable licensing data to respond to nuclear utilities' requests.

2. Optimised Cr_2O_3 doped-UO_2 fuel characteristics

Chromium oxide at an optimum concentration of 0.16 wt.% proved to be a very effective additive for grain size enlargement and to improve the fuel mechanical properties (4). Typically, a matrix grain size of 50 to 60 µm can be reached (equivalent to ~80-90 µm in 3D calculations). As a consequence of that grain growth activation, a better densification of the UO_2 matrix occurs and high densities can be easily achieved, typically in a range of 96 to 97% TD or even more. Increasing the fuel density allows to improve fuel thermal conductivity and to decrease the in-service temperatures. That also gives an increase of the U235 mass per fuel assembly for implementing fuel management with longer cycle length, considering that Cr_2O_3 has a negligible impact on neutron absorption (4).

The wash-out behaviour of chromia-doped pellets in a defective fuel rod is assessed and compared to standard UO_2 through out-of-pile tests. The program comprises realistic conditions for PWR and BWR (pressure, temperature) in steam and water. Results indicate that the fuel oxidation proceeds in an intergranular mode with consequent oxidation of the grains and mechanical disintegration of the oxidised layer. The large-grain structure and the high density of the optimised Cr_2O_3-doped fuel cause a deceleration of the corrosion process. Accordingly, oxidation kinetics of the Cr_2O_3-doped fuel is significantly lower than that of the standard UO_2 fuel.

To master the Cr_2O_3-doped UO_2 fuel fabrication technology, an industrialisation program has been launched to study the evolution of the pellet characteristics in function of various parameters: U_3O_8 recycling, pellet sintering conditions, etc. Optimum manufacturing conditions have been defined to insure the reproducibility of the targeted microstructural changes while keeping the throughput of a fuel manufacturing process. Today, more than 4 tons of optimised Cr_2O_3 doped-UO_2 pellets are inserted in nearly 1200 fuel rods that are under irradiation in PWRs and BWRs.

3. Qualification process of the optimised Cr_2O_3 doped-UO_2 fuel

The addition of a dopant material, i.e. Cr_2O_3, in the UO_2 matrix modifying the fuel microstructure and its properties under irradiation, requires qualifying the fuel behaviour in all conditions this fuel has to sustain: normal, incidental (class 1&2 power transients) and accidental conditions. The key points of the qualification process defined by AREVA NP for the Cr_2O_3-doped fuel concern:

- The thermal behaviour of the fuel pellet. Even if it is interesting to assess the thermal diffusivity of fresh doped pellets compared to UO_2 fuel, from a licensing viewpoint, the pertinent data will be provided thanks to in-pile measurements of the pellet centre temperatures on irradiated fuel rods covering the range of relevant burnups, in order to analyse the end of life penalizing conditions and the high rod power conditions (high duty, transients), together with the beginning of life.

- The behaviour of fission gases in the fuel matrix. The microstructural changes in the fuel in particular; the grain size enlargement and the presence of Cr_2O_3 can modify phenomena governing the fission gas behaviour (fission gases location in the fuel matrix, gas coefficient diffusion, etc.). When considering the different FGR mechanisms identified today for normal and incidental conditions, the experimental data required for the calibration of design models, should necessarily establish a dependence with regard to temperature (i.e. power), burn-up and power transient conditions. For accidental situations, the stake is the evaluation of the envelope of gas fraction immediately available for release in case of LOCA and to predict the source term. The knowledge of that gas fraction allows also anticipating, in tendency, on the fuel behaviour during a RIA type accident. Here the approach will bring together gas release measurements during adapted annealing treatments and fine microstructural fuel examinations.

- The fuel rod overall behaviour. With regard to the physical models describing the specific and individual behaviour of the two main fuel rod components; clad and pellet, a strong interaction exists between the various phenomena. Accordingly, integral experimental data (rod growth, diametral deformation, internal pressure) must be acquired to qualify the whole thermomechanical behaviour of the fuel rod. The experimental data in support have to be established first in function of burnup but also regarding transient conditions for rod diametral deformation.
- The PCI behaviour of the fuel rod in power transients. The fuel rod qualification with regard to PCI is first based on a direct experimental demonstration through ramp testing. The ramp test conditions shall be define so as to determine the potential of PCI failure risk in cases considered as limitating, i.e. including high local power and fast power variations. In parallel, advanced modelling is requested to represent the complex and combined physical/chemical phenomena involved in PCI. The first objective with such development is to discriminate the behaviour of various fuel pellet materials and thus enhance the value of fuel products with PCI benefits. A second objective is to streamline the industrial qualification plan of the Cr_2O_3-doped fuel by optimising the power ramp tests to perform. Finally, advanced modelling will contribute to the reduction and/or suppression of PCI operating constraints following the progressive introduction of PCI remedy fuel in commercial LWRs (2).

To answer to all these requirements and needs, AREVA NP has launched qualification irradiation programs in LWRs plants in order to cover a wide range of operating conditions. In both cases, the irradiation campaigns are designed to produce data up to high burnup (70 GWd/tU), with an influence of variation in power histories: from high duty operation to moderate or low power in order to allow for later ramp testing at various stages of burnup.

The qualification program has started first in PWR with the irradiation in a 1300 MWe reactor of lead fuel rods with chromia-doped pellets loaded into M5^{TM} cladding tubes. This campaign, started in 2001, aims to acquire the data required to demonstrate the ability of this fuel to be a high burnup PCI remedy as a response to the need to significantly reduce in France the overall PCI operating constraints within improved fuel management. In 2005, a milestone was reached with the insertion in a 1300 MWe PWR unit of four lead test assemblies with all M5™ rods filled with chromia-doped pellets. In a second part, lead fuel rods with chromia-doped fuel into M5™ or Duplex claddings will be irradiated in 2007 in a high duty plant at maximum possible heat generation rates in order to cover future demands.

In 2005, the program has been widened to BWR units with base irradiation of fuel rods in lead assemblies of the ATRIUM^{TM}10XM up to high burnup (5). Besides steady state operation at continuously high linear heat generation rates, withdrawal of control blades in a critical exposure stage will be also investigated to promote transient fission gas release. For the purpose of later ramp testing from initial intermediate to low power conditioning power level, test fuel rods were manufactured with both liner cladding and non-liner cladding, and will be irradiated in ATRIUM^{TM}10 carrier assemblies in two reactors. The aim is to define the range of operational conditions in the BWR for application of chromia-doped fuel in combination with LTP2 non-liner cladding as an alternative to the present standard Fe-enhanced Zr liner cladding.

In parallel to the LWRs qualification program, important R&D efforts are conducted to characterise the properties of the Cr_2O_3-doped fuel pellets. For example, out-of-pile tests are carried out to assess the elasto-viscoplastic properties in order to define specific behaviour laws for PCI modelling purpose. Finally, the R&D CONCERTO program, launched in 1997 contributes to the acquisition of behaviour data for the Cr_2O_3-doped pellets, in base load, ramp testing and through the realisation of analytical experiments in MTR. In that 900 MWe PWR campaign, fuel rods made of Zy-4 cladding and chromia-doped pellets were irradiated up to ~57 GWd/tU after 5 annual cycles.

4. Irradiation experience

4.1 Base load irradiation

In the PWR programme CONCERTO (3) extensive PIE was carried out with regard to this optimised Cr_2O_3-doped UO_2 fuel. In comparison to standard Zy-4/UO_2 rods, non destructive examinations revealed a slightly higher fuel rod growth (Fig.1) and diametral rod deformation. An equivalent trend is also observed with Cr_2O_3-doped fuel in M5™ cladding after 3 long irradiation cycles (50 GWd/tU).

This behaviour is explained by an early in life pellet-clad contact considering that the Cr_2O_3-doped fuels exhibit a lower densification. The density measurements confirm the high dimensional stability of Cr_2O_3-doped fuel up to 62 GWd/tU with a very low initial densification and a swelling rate equivalent to un-doped UO_2 (Fig.2).

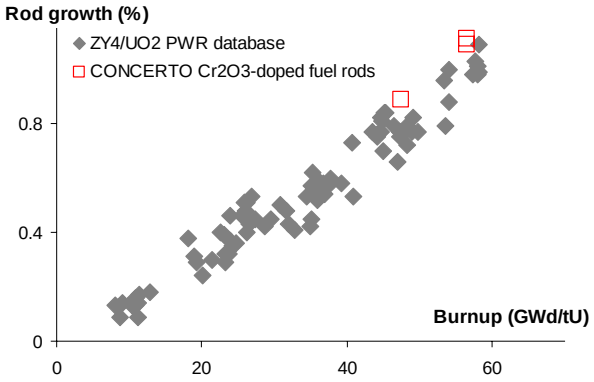

Fig 1. Rod growth in function of burnup

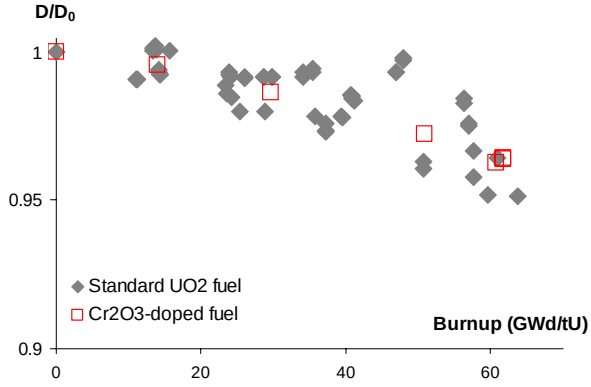

Fig 2. Fuel density in function of burnup

Rod punctures of the CONCERTO rods after 5 cycles revealed fission gas release values lower than 2%. The microstructural examinations showed an important precipitation of fission gases into intragranular bubble form and rather low precipitation of gas on grain boundaries. Such feature, opposite to un-doped UO_2 fuel, is expected to be very beneficial to reduce fission gas release in high power conditions. The microstructural examinations also show a great stability of the Cr_2O_3-doped fuel microstructure, in particular no grain growth has occurred during irradiation up to ~60 GWd/tU.

4.2 Ramp testing

Ramp testing was performed under PWR conditions on CONCERTO segmented rods after two and five annual cycles of exposure. None of the rods failed up to a maximum experienced peak final power of 535 W/cm, corresponding to a maximum power variation of 335 W/cm. Such results give impressive gains compared to standard UO_2-Zy4 PCI threshold (Fig.3).

Extensive PIE of ramped rods revealed intensive creep of the doped fuel into dishes and enhanced cracking of the pellet peripheral zone as possible mechanisms to decrease the local stress concentration factor exerted by the fuel on the cladding in power transient situations (6). Fission gas release measurements after the ramp tests confirmed the better retention capability of the large grain microstructure of the doped fuel. Compared to UO_2 standard fuel, Cr_2O_3-doped pellets exhibit a lower fission gas release with a gain at least equal to a factor 2. The better behaviour is due to the improved intragranular fission gas retention capability following the matrix grain size enlargement. Additionally, fission gas bubbles linkage on small-scale Cr_2O_3 inclusions contributes also to this improvement.

Under typical BWR conditions the cladding temperature is lower than in PWRs, which increases the risk for PCI failure. To investigate the potential of chromia-doped fuel to act as PCI remedy, segments from the CONCERTO program were also ramp tested under such severe conditions. The chromia-doped fuel rods did not fail even at a high power level of 480 W/cm (Fig.4), which is far above the failure threshold for standard BWR UO_2 fuel in non-liner cladding (7). The maximum increase in power during the ramp was 230 W/cm which is comparable to the capability of liner cladding. The positive results of the tests gave reason to promote use of chromia-doped fuel in BWR applications, also.

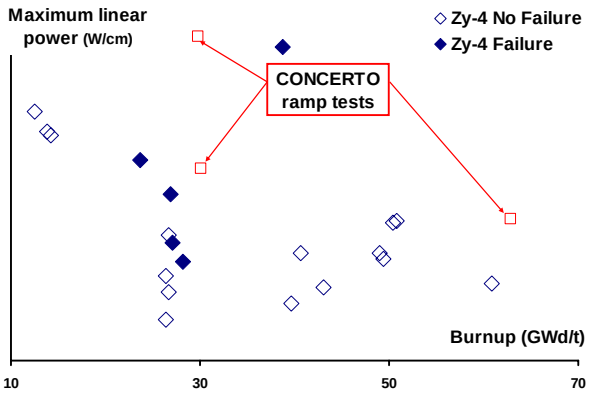

Fig 3. Ramp test results of PWR Zy-4 rods and of CONCERTO rods

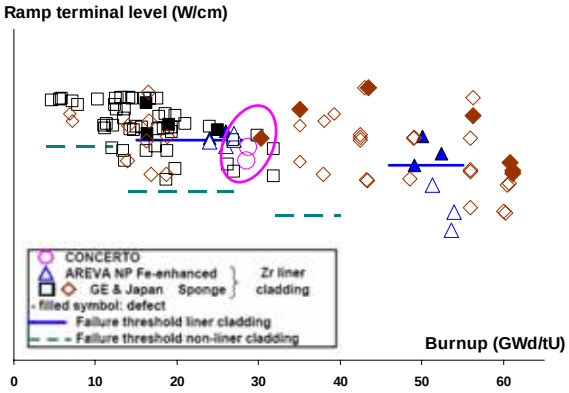

Fig 4. Ramp test results of BWR rods and of CONCERTO rods tested at reduced coolant temperature

5. Conclusions

Doping UO_2 with an optimum Cr_2O_3 concentration level provides significant improvements on PCI performance and fission gas retention. To thoroughly assess the margins of that optimised fuel towards safety criteria at high burn-up and the risk of PCI clad failure, PWR and BRW qualification programs are under progress to investigate a wide range of operating conditions, and to constitute a relevant experimental database for a proper modelling of the chromia-doped UO_2 fuel behaviour in-service .

6. References

(1) S. Yagnik: Effect of PWR restart ramp rate on pellet clad interaction, Proceeding of the 2004 IAEA meeting on Pellet-Clad Interaction in Water Reactor Fuels, Aix en Provence, France, March 9-11, 2004

(2) S. Beguin: PCI-related constraints on EDF PWRs and associated challenges, Proceeding of the 2004 IAEA meeting on Pellet-Clad Interaction in Water Reactor Fuels, Aix en Provence, France, March 9-11, 2004

(3) Ch. Delafoy, P. Blanpain, C. Maury, Ph. Dehaudt: Advanced UO_2 fuel with improved PCI resistance and fission gas retention capability, TOPFUEL 2003, Würzburg, March 16 – 19, 2003

(4) M. Zemek, Ch. Delafoy, G. Maier: How oxidic additives influence UO_2 fuel, IYNC 2006, Stockholm, Sweden – Olkiluoto, Finland, June 18-23, 2006

(5) P. Dewes, Ch. Delafoy: FRAMATOME LWR UO_2 fuel development for challenging operating environments, Proceedings of the Annual Meeting on Nuclear Technology, Aachen, Germany, May 16-18, 2006

(6) B. Julien, Ch. Delafoy, V. Rebeyrolle, S. Beguin: S. Lansiart, Performance of advanced fuel product under PCI conditions, Proceedings of the 2004 International Meeting on LWR Fuel Performance, Orlando, Florida, September 19-22, 2004

(7) P.B. Hoffmann, P. Dewes: Post-irradiation examination and ramp testing of fuel rods with Fe-enhanced Zr liner cladding at high burnup, Proceedings of the 2004 International Meeting on LWR Fuel Performance, Orlando, Florida, September 19-22, 2004

Acknowledgements

The development of chromia-doped fuel is performed in close cooperation with EDF and CEA. Their contributions and the release of segments from the CONCERTO program for BWR ramp tests are gratefully appreciated. The authors would also acknowledge all the STUDSVIK persons for their involvement to this work.

PELLET CONTINUITY AS PERSPECTIVE FUEL PROPERTIES.

I.LOKTEV
Department of Atomic Energy of Russian Federation, JSC"NCCP",
B.Khmelnitsky, 94, 6030110, Novosibirsk, Russia.

ABSTRACT

Pellets with chip defects, observed inside of fuel elements appear thanks to fragile destruction of ceramic fuel because of the technological reasons. It is possible that defective pellets were absent before their loading into cladding. There are some reasons of chip making, but most important of them is deferred propagation of cracks. Initial cracks be made by impact on a pellet edge as result of falling, for example. Another case of crack initiation is centreless grinding. Part of pellets after grinding can be with chips and rejected, another part makes chips under weak impact in another place, than grinding device - before loading into cladding, or after. There is probability, that some chipped pellets of last case come into fuel element. Different kinds of a matrix discontinuity are helping at first initiate of cracks, and then propagate them. The larger size of discontinuity, the weaker pellet resistance to the initiation of cracks. Technological causes of formation of different kinds of the pellet discontinuity is discussed in the report.

1. Introduction.

Pellets with chip defects, which may be observed inside of fuel elements appear thanks to fragile destruction of ceramic fuel because of the technological reasons. It is possible that defective pellets were absent before their loading into cladding. There are some reasons of chip making, but most important of them is deferred propagation of cracks. Initial cracks have been made by impact on a falling pellet, on edge, for example. Another case of crack initiation is centreless grinding. Part of pellets after grinding can be with chips and rejected, another part makes chips under weak impact in another place, than grinding device - before loading into cladding, or after. There is probability, that some chipped pellets in last case come into fuel element. Different kinds of a matrix discontinuity are helping at first initiate of cracks, and then propagate them. The larger size of discontinuity, the weaker pellet resistance to the initiation of cracks. Technological causes of formation of different kinds of the pellet discontinuity are discussed in the report.

Different kinds of matrix discontinuity play key role in substantial decreasing of pellet strength. Main of them is initial powder property: size distribution of powder particles, their phase composition and strength; condition of pressing: size and density of green pellets, dry or wet binding.

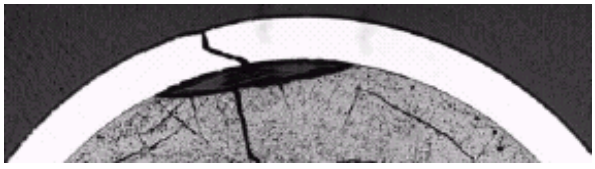

Fig. 1. Chipped pellet in fuel element with crackeg cladding (with chip).

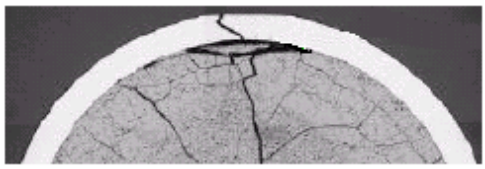

Fig. 2. Chipped pellet in fuel element with crackeg cladding (without chip).

2. Strength of ceramic products.

It can be taken two main levels of destruction of fuel pellets (and not only): first, level of loss of exploitation properties, second, loss of integrity.

If the first level connects with any inadmissible geometrical deviation, the second level means volume destruction or fragmentation on parts with dimensions, comparable to pellet dimensions.

Work of moving of two atoms in solid material against an interatom forces, from a to distance, on which these forces equal to zero, is *energy of material destroying.*

Theoretical strength of ceramic products σ_T with Young module E and specific energy γ can be received using this theoretical energy of failing:

$$\sigma_T = (E\gamma / a)^{1/2}. \quad (1)$$

However, experimental data give values, which much smaller, then for monocrystal, because of different kinds of structure imperfections of real products. However, it is need to know a concrete product behavior for solving different practical tasks in specific conditions. Interruption of atom connection and destroying of material can be result of two processes: straining of material and shifting along of sliding surface.
Theories, which connect state of limit stress of material with fragile destruction of this material, they name *theories of destruction.* Some of them are [3]: Coulomb-Navje theory, Mor theory, Griffith theory.

Griffith theory. Griffith supposed, real ceramics have a multiple microcracks with chaotic orientation. A propagation of crack is connected with energy spending. Distance of one propagation step of crack is in compliance with elastic energy, saved around space of initial microcrack. The Griffith criterion of the one-step propagation of crack is:

$$\sigma = (E\gamma / \pi a)^{1/2} \tag{2}$$

Some ceramics have certain plastic deformation, which require energy spending along a crack trace. Tip of crack creates stress field, where occurs a dislocate moving, a branching of cracks. A imperfections of material compels stopping or deflection of cracks from initial direction, fig. 3. Waviness of fraction surface can characterize uniformity of material or its rate of structure nonconformities, fig. 4.

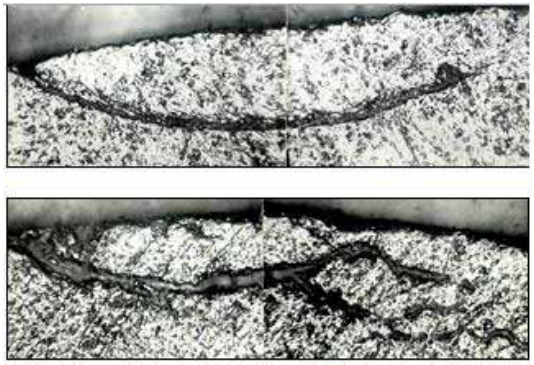

Fig. 3. Suspended chipping (on top) and branching of cracks (below) in fuel pellets with structure nonconformities.

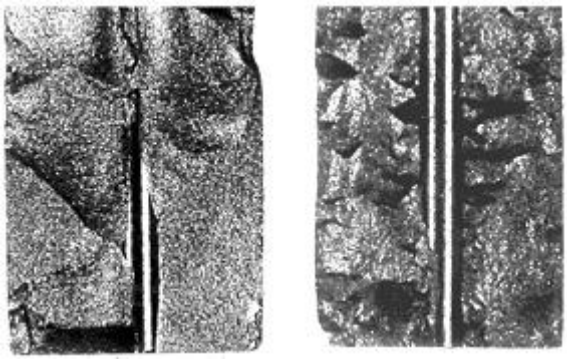

Fig. 4. Fraction surface of pellets before thermal cracking (on the left) and after that (on the right).

Waviness of fraction surface can characterize uniformity of material or its rate of a structure nonconformities fig. 4.Uranium dioxide is semi-plastic ceramic, so cracks in sintered pellets propagate step by step under slight influences and after some time they go out on pellet surface, fig.4.
Pores have dual influence on pellet durability, from one side, they suspend the crack propagating, fig. 3, from another side, they increase strength of pellet matrix. Influence of pore with size c follows to formula of Griffith theory (3):

$$\frac{\sigma_1}{\sigma_2} = \left(\frac{c_1}{c_2} \right)^{1/2} \tag{3}$$

Weibull statistic theory. Vivid description of real behavior of pellet (batch of pellets) under mechanical loading had been given by Weibull and by his theory of destruction. He suggested, destruction of specimen begins from weak spot. Role of weak spots in a ceramics play discontinuity of different kind [3, 6]. The more size of specimen and it unhomogeneity, the greater probability of destroying under one and the same load. The destroying probability B of pellet, from any batch, under loading σ is determined by Weibull distribution [6]:

$$B = \frac{V(\sigma - \sigma_u)^m}{\sigma_0^m} \tag{3}$$

where V – dimensional characteristic of specimen, σ_0, σ_u and m are Weibull parameters.

3. Kind of weak spots in fuel pellets.

They can name three main kinds of weak spots in fuel pellets: structural discontinues of ceramic matrix with and without microcracks, middle cracks because of grinding of pellets, middle and macro cracks from impacts on edges of pellets.

Fig. 5.1. Pore, densification out of local sintering centre

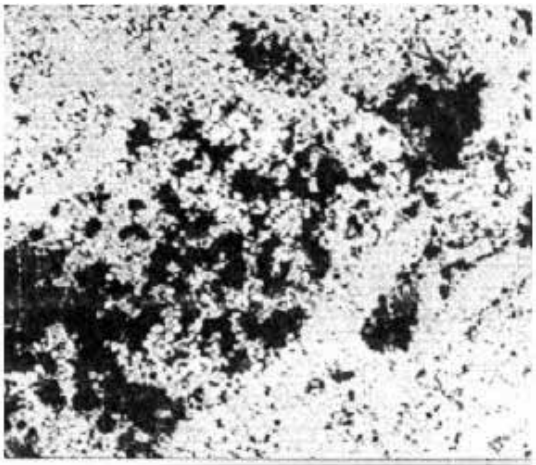

Fig. 5.2. Local porosity – effect of low density

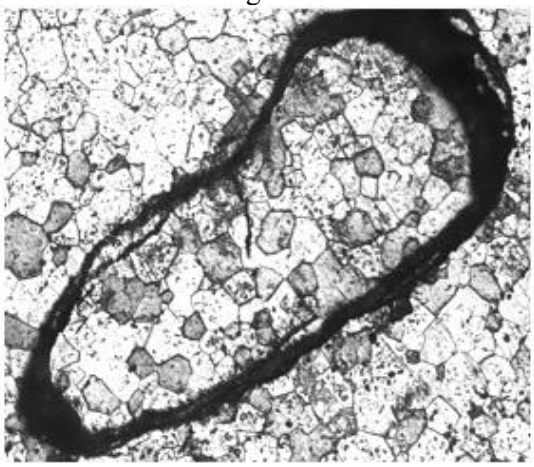

Fig. 5.3. Contour pore – effect of phase hetorogeneity

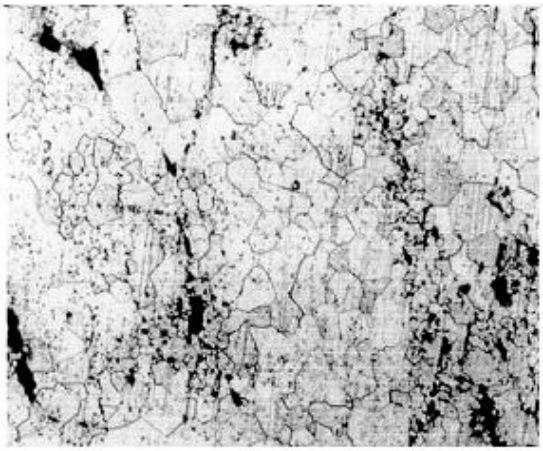

Fig. 5.4. Nonhomogen distribution of additivity.

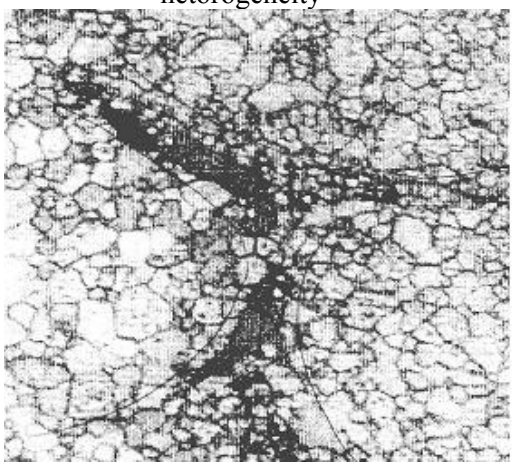

Fig. 5.4. Interparticle space – shadow effect for powder with strong particles

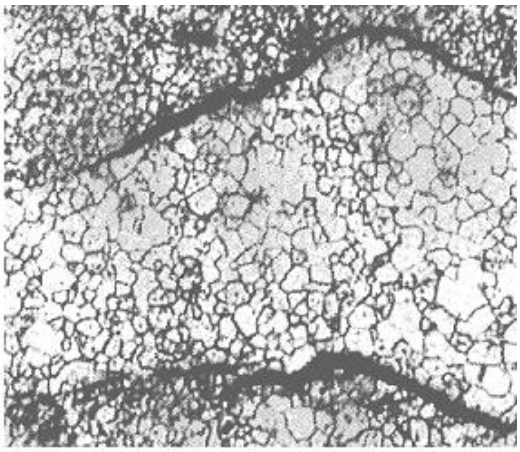

Fig. 5.5. Transverse elastic cracks - post-presser effect

Fig. 5. Kind of structural discontinues of pellet matrix.

Grinding of pellets connects with high level of loading. An alternating stress arise in volume of pellet, they initiate new or propagate existing microcracks. After grinding the pellet, they have micro- and macro-cracks and allowable or non-allowable chips.

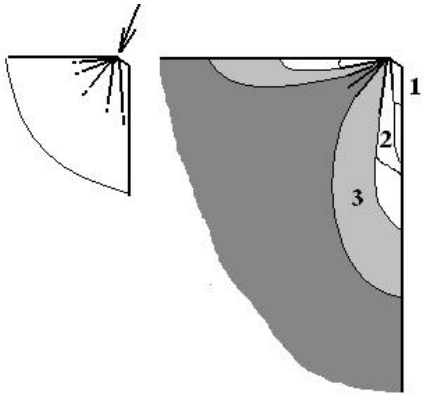

Fig 6. Cracks and chips coming from pellets edge after impact (point of impact is pointed by arrow), 1 - short chip, 2 - lengthened side chip, 3 - big side chip

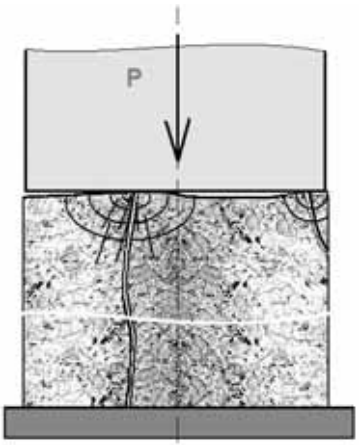

Fig. 7. Chipping and destroying during axial test on fracture of sintered piece of uranium dioxide.

Impacts on edges of pellets can make cracks going into body, fig. 6. Some of them will propagate and give chips. Similar picture can be present on top of pellet, fig. 6. Similar chipping can be during axial test on fracture of pellets, fig. 7. Chip №1, fig 6, on side or on upper surface, has a most probable appearance.
One test can be offered for control of pellet chip-making capacity, it is a group treatment of pellets on a vibrosieve. Under multiple collisions of pellets with each other, initial cracks propagate along path of least effort - to outside, fig. 6. Another test is drop of pellets on steel plate from height, for example, 100mm.
Total level of pellet defectiveness, because of chipping, is about one percent. If even reliability of appearance of chipped pellets, as on fig. 1, is one hundredth of total level of defectiveness, there are some chipped pellets with dangerous size and shape of chips in each of fuel assembling.

4. Chip-making of pellets under different conditions.

4.1 Chip-making of pellets with different density.

Special-made pellets, which had density from 10,10g/sm^3 to 10,70g/sm^3 was subject to the drop test from height 100mm 5-100 times. Results are shown on fig. 8; they allow making next conclusions.

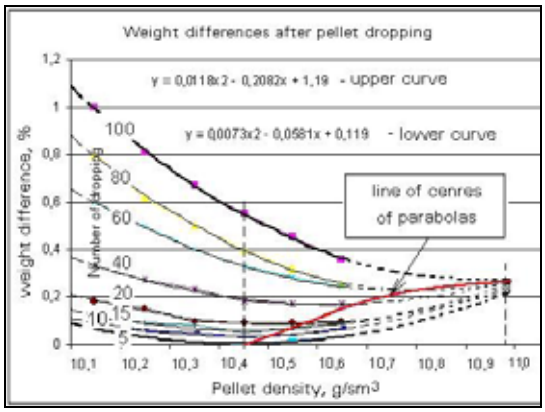

Fig. 8. Results of drop test of pellets, influence of pellet density.

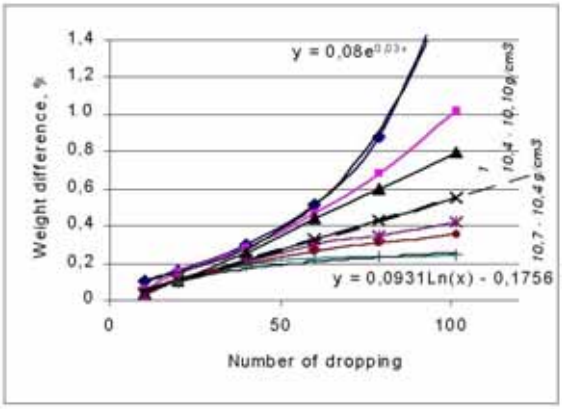

Fig. 9. Results of drop test of pellets, influence of number of dropping.

- for few fallings of pellets, weight differences, or chip-making of pellets have minimal value for density of 10,4g/cm^3, fig.9, dependence from number of falling is nearly linear;
- for few tens of fallings of pellets with density not more, than 10,4g/cm^3, weight difference depends from density exponentially, with density more than 10,4g/cm^3 - according to the logarithmic dependence;

This phenomenon becomes clear, if take into account that density of 10,4g/cm^3 is remarkable point in process of uranium dioxide densification - transition of open porosity to closed one. Obviously, open porosity promote propagation of a crack in the manner step by step, or in other words, the deferred creation of chips, closed porosity - not.

5. Summary

1. Pellets with chips, observed inside of fuel elements appear thanks to fragile destruction of ceramic fuel because of deferred, step by step process, crack propagation, which leads to chip-making after appearance control of fuel pellets and, in some cases, after loading of pellets into cladding.

2. General principles of decreasing of chip-making in total production cycle are: decreasing of structural heterogeneity and discontinue of pellets, exclude or decrease to minimum of impacts or loading of sintering pellets, including weak, but multiple ones, for example, vibration, overloading; making pellets near optimal density 10,4g/cm^3.

3. To test batch of pellets for deferred chip-making can be used methods on base of vibration or another testing by weak multiple impacts.

6. Reference

1. R.S.Reynolds, J.T.Willse, Recent Framatom ANP Fuel Experience. Proceeding of 2004 International Meeting on LWR Fuel Performance. Orlando, FL, September 22, 2004.

2. Rosa Yang, Odelli Ozer, Kurt Edsinger et al. Fuel Reliability Program. Proceeding of 2004 International Meeting on LWR Fuel Performance. Orlando, FL, September 22, 2004.

3. Cobl R.L. Parikh N.M. Destroing of polycristallic ceramic. Destroing. v.7. M. "Mir".

4. Stoks R.G. Microscope destroing of ceramic. Destroing. v.7. M. "Mir". 1976

5. Obert L. Brittle destroing of rocks. Destroing. v.7. M. "Mir". 1976.

6. Weibull W., Proc. Roy. Swedish Inst. Eng. Res., 151, 5-45 (1939).

7. Knudsen F.P. J. Am. Ceram. Soc. 42, 376 (1959).

European Nuclear Society
Rue de la Loi 57
1040 Brussels, Belgium
Telephone +32 2 505 3 50
Fax + 32 2 502 39 02
ens@euronuclear.org
www.euronuclear.org

Layout and Design: Marion Brünglinghaus, ENS